# DEVELOPMENT OF METAL OXIDES SUPPORTED SPEEK MATERIALS FOR HYDROGEN GENERATION AND PROTON EXCHANGE MEMBRANE (PEM) FUEL CELL APPLICATIONS

by

**SEGALE EMILY MAYETU MARTHA**

**(Student No: 45507910)**

submitted in accordance with the requirements for
the degree of

**DOCTOR OF PHILOSOPHY**

In the subject

**ENGINEERING**

in the

COLLEGE OF SCIENCE, ENGINEERING AND TECHNOLOGY

at the

UNIVERSITY OF SOUTH AFRICA

SUPERVISOR: **PROF RUDZANI SIGWADI**
CO-SUPERVISOR: **PROF TOUHAMI MOKRANI**
CO-SUPERVISOR: **PROF GABRIEL SUMMERS**

(**04 September 2025**)

# DECLARATION

Name: Emily Mayetu Segale

Student number: 45507910

Degree: **DOCTORAL DEGREE IN ENGINEERING**

**DEVELOPMENT OF METAL OXIDES SUPPORTED SPEEK MATERIALS FOR HYDROGEN GENERATION AND PROTON EXCHANGE MEMBRANE (PEM) FUEL CELL APPLICATIONS**

I declare that the above thesis is my own work and that all the sources that I have used or quoted have been indicated and acknowledged by means of complete references.

I further declare that I submitted the thesis to originality checking software and that it falls within the accepted requirements for originality.

I further declare that I have not previously submitted this work, or part of it, for examination at Unisa for another qualification or at any other higher education institution.

04 September 2025

SIGNATURE DATE

# KEY TERMS

Hydrogen evolution reaction
Sulfonated poly(ether ether ketone)
Cerium oxide
Sulfated zirconia
Silica
Nanocomposite
Fuel cells
Swelling ratio
Electrochemical
Fuel cell efficiency
Mechanical properties
Nanoparticles
Oxidative stability
Proton conductivity
Stress-strain
Tensile strength
Thermal stability
Water uptake
Zirconia

# LIST OF ABBREVIATIONS

AFC: Alkaline fuel cell
BET: Brunauer EmmettTeller
CA: Chronoamperometry
CV: Cyclic voltammetry
DMFCs: Direct methanol fuel cells
ECSA: Electrocatalytic surface area
EIS: Electrochemical impedance spectroscopy
FC: Fuel cell
FTIR: Fourier transform infrared
GE: Graphite electrode
HER: Hydrogen evolution reaction
IEC: Ion exchange capacity
LSV: Linear sweep voltammetry
MCFC: Molten carbonate fuel cell
OCV: Open circuit voltage
PAFC: Phosphoric acid fuel cell
PEEK: Poly ether ether ketone
PEM: Proton exchange membrane
PVP: Poly Vinyl Pyrrolidone film
PBI: Polybenzimidazole
PVA: Poly (vinyl alcohol)
RH: Relative humidity
RHE: Reversible hydrogen electrode
SEM: Scanning Electron Microscopy
SOFC: Solid oxide fuel cell
SPEEK: Sulfonated poly (ether ether ketone)
SR: Swelling ratio
SZr: Sulfonated zirconia
TGA: Thermal Gravimetric Analysis
TEM: Transmission Electron Microscopy
TOF: Turnover frequency

WU: Water uptake

XRD: X-ray diffraction

# DEDICATION

This thesis is dedicated to:

God Almighty, my creator, my strong pillar, and my source of inspiration, wisdom, knowledge, and understanding, has been the foundation of my strength throughout my studies. It is on His wings that I have soared. I also dedicate this work to my husband, my mom, my uncle Tebogo, and my one and only son (Rory), who have encouraged me every step of the way. Their support has motivated me to give my all and complete what I started. To my late sister, Dr. Seadimo Mojaki, your presence is missed every day, sisi.

My love for you all can never be quantified ♥

# ACKNOWLEDGEMENTS

I would like to thank the following people and organisations who supported and assisted me in their own special ways:

- My supervisors Prof Rudzani Sigwadi, Prof Touhami Mokrani and Prof Gabriel Summers for their immense support, encouragement, constructive science criticism, countless suggestions towards research challenges, and the opportunity to take a leading role.
- Dr Olayemi Fakayode, for instilling project organisation and result-driven skills that aided in moving the project forward, and the opportunity to explore new ideas.
- Kgaugelo Tapala (Chemistry); Pinky Mothibi and Nyiko Mathonsi (Chemical and Materials Engineering); Luleka Menzi (Physics) for analysis and other laboratory equipment.
- My “MCE” group thank you for making my laboratory sessions memorable.
- Dr Dieketseng Tsotetsi, Dr Keletso Mphahlele, Pinky Mothibi, Gertrude Mitilene-Bokaba, you rewrote the definition of sisterhood in and out of profession.
- To Dr Tumelo Seadira, Dr Kabelo Ledwaba, Dr Tau Ntelane, and Dr Olayemi Fakayode, your support and words of encouragement are highly appreciated. I cannot thank you enough.

The Almighty for giving me the strength, courage, and his amazing grace that guided and protected me throughout my studies.

# ABSTRACT

This study focuses on the synthesis and characterization of novel alternative non-platinum electrocatalysts for hydrogen generation and fuel cell applications using SPEEK nanocomposite membranes modified with mixed oxide fillers. Three different mixed oxide electrocatalysts were prepared, namely cerium-zirconium ($CeO_2$:$ZrO_2$), cerium-silica ($CeO_2$:$SiO_2$), and sulfated zirconia-silica (SZr:$SiO_2$). The cerium-zirconium oxide electrocatalysts were synthesized using the coprecipitation method and subsequently annealed with varying $CeO_2$:$ZrO_2$ ratios. Among the various compositions evaluated, the $CeO_2$:$ZrO_2$ nanocomposite demonstrated remarkable efficiency at a 1:1 ratio. A current density of -2000 mA/cm$^2$ was achieved on a geometrical area of 0.20 cm$^2$. The outstanding performance is attributed to the unique mixture of spherical and rod-like morphology and surface area characteristics of the nanocomposites, which have a BET surface area of 63.41 m$^2$/g and electrochemical active surface area (ECSA) of 4.4 cm$^2$. In this system, SPEEK binder plays a dual role as both a protective membrane (Ecorr = −0.33 V vs −0.29 V) and a binder for the inorganic materials. When compared to platinum (Pt), these electrocatalysts showed commendable performance, with only a 2.56% deviation in current. The hydrogen generation rate followed first-order kinetics, with a rate of $9.6 \times 10^{-5}$ A/s and a rate constant of 8.35 × 10−5 s$^{-1}$.

Graphite electrodes (GE) were modified with SZr and varying proportions of SZr:$SiO_2$ metal oxides. The GE/SZr:$SiO_2$ (1:1) electrode demonstrated exceptional performance, exhibited a hydrogen evolution current density of -1700 mA/cm$^2$ at -0.55 V vs. RHE based on ECSA dimension. Furthermore, the enhanced electrocatalytic activity and durability of $CeO_2$:$SiO_2$ mixed oxides were also studied. The SPEEK-promoted $CeO_2$: $SiO_2$ (2:1) exhibited the best HER activity, having a current density of -260 mA/cm$^2$ at -0.50 V vs. RHE, an electrochemical surface area of 2.0 cm$^2$, and a turnover frequency of -1.42 s$^{-1}$.

The above-mentioned synthesized fillers that exhibited the highest HER activity was utilized to modify the SPEEK membrane, enhancing the thermal stability, proton conductivity, and mechanical properties of the composite membranes. The recast method was used to prepare the composite membranes with varying weight% of fillers. The modified membranes with $CeO_2$:$SiO_2$ nanoparticles showed a significant improvement in water uptake, leading to enhanced hydrophilicity when compared to the pristine SPEEK membrane. The presence of $SiO_2$ enhanced proton conductivity, while $CeO_2$ helped reduce the chemical degradation of the membrane by scavenging free radicals. The proton conductivity of the SPEEK-$CeO_2$:$SiO_2$ (5 wt.%) nanocomposite membrane measured 0.037 S/cm, compared to only 0.004 S/cm for the bare SPEEK membrane under the same conditions. Additionally, oxidative stability tests conducted in 3 ppm $Fe^{2+}$ at 80 °C revealed that the membrane with 5% $CeO_2$:$SiO_2$ exhibited the highest oxidative stability of 81.6% after 250 minutes. Additionally, SPEEK-$CeO_2$:$ZrO_2$ nanocomposite membranes were also studied. SPEEK-$CeO_2$:$ZrO_2$ (10 wt.%) exhibited higher proton conductivity of 0.07 S/cm.

Lastly, composite membranes incorporated with varying amounts of sulfated binary metal mixed oxide (SZr:$SiO_2$) were prepared. SPEEK-SZr:$SiO_2$ (1wt%) membrane exhibited the highest antioxidant stability at 82.87%, surpassing the pure polymer matrix membrane, which had a stability of 77.24%. Furthermore, they also demonstrated the highest proton conductivity of 0.087 S/cm. For assessing fuel cell performance, all composite membranes that displayed the highest proton conductivity within their respective groups were selected for testing. The SPEEK-SZr:$SiO_2$ (1%) membrane outperformed the other composite membranes with the highest current density of 1370.77 mA/cm² and a peak power density of 54.9 mW/cm², demonstrating its superiority as a catalyst in fuel cells due to its high conductivity and stability. Overall, the SPEEK-SZr:$SiO_2$ (1wt%) composite membrane shows great potential for polymer electrolyte membrane fuel cell (PEMFC) applications.

# ARTICLES

---

1. **Segale, M.**, Seadira, T., Sigwadi, R., Mokrani, T. and Summers, G., 2024. A New Frontier Towards Development of Efficient SPEEK Polymer Membranes for PEM Fuel Cells Applications: A Review. *Materials Advances*, **5**, 7979-8006 (Impact factor: 5.2).
2. **Segale, M.**, Fakayode, O.J., Mokrani, T., Summers, G.J., Mothudi, B.M. and Sigwadi, R., 2025. Hydrogen evolution on graphite/sulfonated polyether ether ketone (SPEEK) surface using zirconium oxide-stabilized cerium oxide nanocomposites. *Journal of Power Sources*, *629*, p.235975 (Impact factor: 8.1).
3. **Mayetu Segale**, Olayemi J. Fakayode, Tumelo Seadira, Touhami Mokrani Bakang M. Mothudi, Gabriel Summers, Rudzani Sigwadi, Hydrogen evolution reaction by sulphated zirconia: silica mixed oxides, *Next Materials*, 12 (2026) 102092.
4. **Mayetu Segale**, Olayemi J. Fakayode, Tumelo Seadira, Touhami Mokrani Bakang M. Mothudi, Gabriel Summers, Rudzani Sigwadi, Cerium-silica mixed oxides as non-platinum electrocatalysts for hydrogen evolution reaction, International Journal of Electrochemical Science, 21 (2026) 101383 (Impact factor: 3.6)
5. **Mayetu Segale**, Koena Zamisa, Olayemi J. Fakayode, Tau Ntelane, Tumelo Seadira, Touhami Mokrani Bakang M. Mothudi, Gabriel Summers, Rudzani Sigwadi, The Proton Conductivity and Mechanical Properties of SPEEK-Ce: Zr Nanocomposite Membrane, Journal of Nano Research (JNanoR) (Accepted).
6. **Mayetu Segale**, Olayemi J. Fakayode, Tumelo Seadira, Touhami Mokrani Bakang M. Mothudi, Gabriel Summers, Rudzani Sigwadi, Enhanced Conductivity and Chemical Durability of SPEEK Membranes by Cerium-Silica Incorporation for Low-Humidity PEM Fuel Cells, Journal of Power Source, POWER-D-26-03297(Submitted).
7. Tsotetsi, D., Seadira, T., Fakayode, O.J., **Segale, M.,** Mothudi, B., Mbule, P. and Dhlamini, M., 2025. Molecular caffeine electrode for hydrogen

production using two or three electrode configurations in sulphuric acid electrolyte solution on a graphite's surface. *FlatChem*, p.100864.

8. Tau S. Ntelane, **Mayetu Segale**, Mokhotjwa Dhlamini, Nomcebo H. Mthombeni , Usisipho Feleni, Rudzani Sigwadi, Dieketseng Tsotetsi , Alex T. Kuvarega,Selective removal of cationic organic dyes from aqueous solution using dendritic fibrous nanosilica, Polyhedron 286 (2026) 117950
9. Olayemi J. Fakayode, Busisiwe P. Mabuea, Sisonke Sigonya, Dieketseng Tsotetsi, **Mayetu Segale**, Rudzani Sigwadi, Mokhotjwa Dhlamini, Bakang M. Mothudi, Biochar-supported $Cu_2O$ nanocrystallites as a platinum-free electrocatalyst for hydrogen evolution, International Journal of Electrochemical Science 21 (2026) 101339
10. Mantsopa Koena Zamisa, Tumelo Seadira, Dieketseng Tsotetsi, **Mayetu Segale**, Mokhotjwa S Dhlamini,Synthesis and characterization of Ti- and Fe-pillared clay catalysts for photodegradation of dyes. (Accepted)
11. Olayemi J. Fakayode, Dieketseng Tsotetsi, **Mayetu Segale**, Mantsopa Zamisa, Azwifunimunwe Tshikovhi, Bulelwa Ntsendwana & Bakang M. Mothudi, The Polymer-Water Nexus. Springer, Cham

# PRESENTATIONS

1. **Segale, M.,** Fakayode, O.J., Mokrani, T., Summers, G.J., Mothudi, B.M. and Sigwadi, R., F. 2025.Ce:$SiO_2$ Mixed Oxides for Efficient Hydrogen Evolution Reaction. Nanotech France 2025, June 25-27, Paris, France.
2. **Segale, M.,** Fakayode, O.J., Mokrani, T., Summers, G.J., Mothudi, B.M. and Sigwadi, R., F. 2025.SPEEK/$SiO_2$ as a Potential Nanocomposite for Hydrogen Evolution Process Electrocatalysis.Smart Materials & Surfaces conference 2025, October 29-31, Rome, Italy, (SMS 2025)

# TABLE OF CONTENTS

## CHAPTER 5: HYDROGEN EVOLUTION REACTION BY SULFATED ZIRCONIUM OXIDE NANOPARTICLES 148

## CHAPTER 6: ACIDIC WATER SPLITTING OF CERIUM-SILICA MIXED OXIDES FOR SUSTAINABLE ELECTROCATALYTIC HYDROGEN PRODUCTION. 168

# LIST OF FIGURES

# LIST OF TABLES

# CHAPTER 1: INTRODUCTION

## 1.1. Introduction

Energy is crucial for human civilization, enabling technological advancement in our daily lives. The majority of the world's energy is generated by fossil fuels such as coal, natural gas and oil (gasoline and diesel), because of their low cost and widespread availability [1]. However, rising energy demand in today's world has put a strain on the limited supply of these fossil fuels, which will eventually run out. Furthermore, the combustion of these fossil fuels emits greenhouse gases such as carbon dioxide, nitrogen oxides and oxocarbons, which contribute to global climate change and dilapidation of human health, animals and plant growth [2]. As a result, there is an urgent need to replace fossil fuels with alternative renewable, clean, and low-carbon energy sources.

Alternative renewable energy sources such as solar, wind, biomass, geothermal, and hydropower can be utilized to reproduce energy and are therefore extensively useful to combat energy crises. However, the major drawbacks of these energy sources are the high cost involved in construction of their respective energy plants as well as difficulties and limitations in operating those plants [3-5].

Among the various available renewable energy sources, fuel cells seem to offer a promising solution. This technology enables direct conversion of chemical energy into electrical energy, heat and water in high yield since it is not subjected to the limitation of a Carnot’s cycle. It is considered as a way to produce clean energy as the only by-product for $H_2/O_2$ fuel cell is water [6]. Some fuel cells use hydrogen as fuel and oxygen as oxidant whereas others uses hydrocarbons and alcohol [7]. There are several types of fuel cells currently under development namely; polymer electrolyte fuel cells also known as proton exchange membrane fuel cells (PEMFCs), direct methanol fuel cells (DMFCs), alkaline fuel cells (AFCs), molten carbonate fuel cells (MCFCs) and solid oxide fuel cells (SOFCs) and each has its advantages, limitations and potential applications [8, 9]. Of all types of fuel cells, PEMFCs and DMFCs are the most promising candidates for the next generation energy source for transportation, stationary and portable devices [10].

Proton Exchange Membrane Fuel Cells (PEMFCs) utilize a water-based, acidic polymer as their electrolyte and platinum as the primary electrode. They operate at very low temperatures, and their electrical output can be optimized to meet varying power demands On the other hand, Direct Methanol Fuel Cells (DMFCs) convert the chemical energy in methanol ($CH_3OH$) into useful electrical energy with minimal emissions [11]. However, precious metal-based electrodes in these fuel cells can suffer from deactivation due to low operating temperatures and issues like platinum poisoning. Consequently, PEMFCs typically use pure hydrogen as their fuel source, while DMFCs use methanol [12, 13]. Both types of fuel cells face several limitations, including catalyst poisoning from carbon monoxide (CO), challenges with membrane hydration, mechanical strength issues, and fuel crossover problems [14]. These limitations has led to an increase in research interests to develop membrane composites that can withstand high reaction temperatures (120 °C-150 °C) and remain chemically and mechanically stable [15]. Currently, the state-of-the-art Nafion membranes have been widely used as proton exchange membranes (PEMs) due to their outstanding properties such as high proton conductivity under humid conditions and long-term stability. However, drawbacks such as low proton conductivity at operating temperatures above 80 °C due to water evaporation, high fuel permeability, and high cost restricted their applications [16, 17].

So far, Sulfonated poly (ether ether ketone) (SPEEK) has demonstrated appropriate properties for fuel cell applications when compared to other non-perfluorinated membranes and perfluorinated membranes such as Nafion [18]. Due to their narrow and less connected hydrophilic channels, SPEEK-based membranes have been reported to have high proton conductivity, good thermal and mechanical stabilities and low cost [19]. SPEEK can be easily synthesized by sulfonating PEEK with concentrated sulfuric acid. Different properties of SPEEK are highly dependent on the degree of sulfonation (DS), which can be controlled by altering the reaction temperature, acid content, and sulfonation time [20]. The degree of sulfonation (DS) of SPEEK is an important parameter for its performance because the proton conductivity increases with DS, but the methanol crossover also increases, and the dimensional stability of the membrane deteriorates up to dissolution due to the ionomer's excessive hydrophilicity[18]. Above 80% DS, the membrane becomes excessively hydrophilic, resulting in significant swelling and eventual dissolution in water. Furthermore, it is possible to reduce the water swelling of SPEEK by adding inorganic nanofillers that may act as cross-linking agents [21].

To date, extensive work has been done to develop inorganic-organic composite SPEEK membranes. This includes the incorporation of inorganic nanofillers such as Titanium dioxide ($TiO_2$), Zirconium oxide ($ZrO_2$), metal oxides and carbon nanotube (CNT). Amongst these materials, metal oxides has not been given most attention due to its high thermal conductivity, excellent chemical resistance and low thermal expansion properties, as a nanofiller [22].

## 1.2. Problem Statement

The rising global demand for energy has resulted in increased combustion of fossil fuels, which emits toxic greenhouse gases that contribute to climate change, pollution, and health issues. Drought has recently affected the agricultural sector in South Africa, and there have been reports of fatalities as a result of heat strokes caused by extremely high temperatures caused by climate change. Most of the hydrogen in the world is produced by steam reforming and coal gasification processes; however, the drawbacks of these processes are that they both require high energy (thus making them expensive) and produce carbon dioxide as a by-product. Fuel cells have been identified as one of the most promising and potential clean energy technologies, meeting all of the requirements for energy security, economic growth, and environmental sustainability, and have received considerable attention as a potential replacement for power generation systems. PEMFC and DMFC are the most preferred fuel cells. Dihrab et al. described them as "the perfect melding of benefits from energy sources," as a result of their ability to emulate the ease of refuelling and continuous operation potential of internal combustion engines, as well as the highly efficient and quiet operation of batteries. As a result, fuel cells appear to be an ideal energy source [23]. With these promising achievements remain several challenges associated with working of PEMFC and DMFC in real life conditions. The main issues associated with these fuel cells are humidity management at the electrodes, CO poisoning of the anode (Pt) catalyst, slow cathode kinetics, mechanical strength, and the high cost of the platinum electrode catalyst.

For this reason, this research focuses on developing electrocatalysts for hydrogen generation, which can also be used as filler in SPEEK membranes for fuel cell applications. The electrocatalyst is designed to significantly boost current density and stability for hydrogen generation. Meanwhile, the electrocatalysts are engineered to optimize the oxygen reduction reaction, enhance CO tolerance, and streamline the hydrogen oxidation reaction in proton exchange membrane fuel cells (PEMFC), making them essential components in advancing fuel cell technology. Additionally, incorporating the inorganic metal oxide into the organic proton-conducting SPEEK membranes enhances proton conductivity, mechanical and thermal stability.

## 1.3. Aim of the study

This thesis aims to synthesize, characterize, and apply new alternative non-platinum electrocatalysts for hydrogen generation and the development of proton conductive membranes based on SPEEK. The approach involves using SPEEK nanocomposite membranes modified with synthesized mixed metal oxide as fillers. This aim was achieved by carrying out the following objectives:

## 1.4. Objectives and Research questions

### 1.4.1 Specific Objectives

a) Synthesis of electrocatalyst at varying ratios.
b) Synthesis of sulfonated polyether ether ketone (SPEEK) membrane.
c) Synthesis of SPEEK/inorganic metal oxide nanofiller composite membrane.
d) Characterization of the as-synthesized materials using conventional spectroscopic, and morphological instrumental techniques such as ultraviolet-visible (UV-Vis), Fourier transform infrared spectroscopy (FTIR), Powder X-ray diffractometry (XRD), Thermal gravimetry analysis (TGA), Brunauer Emmett Teller surface area, adsorption and porosity analyses (BET), Scanning electron microscopy (SEM), Energy dispersive X-ray (EDX), Transmission electron microscopy (TEM), and electrochemical approaches such as cyclic voltammetry (CV), linear sweep voltammetry (LSV), chronoamperometry (CA) and electrochemical impedance spectroscopy (EIS).
e) Evaluation of the as-synthesized electrocatalyst as viable working electrodes alongside with SPEEK binder for hydrogen generation.
f) Evaluate the conductivity of the as-synthesized SPEEK/Inorganic metal oxide filler.

g) Optimize and utility of membrane materials for fuel cell application through the construction of power density curves.

### 1.4.2. Research questions

a) How do varying synthesis ratios of the electrocatalyst affect its structural and electrochemical properties?
b) Can a stable, proton-conductive SPEEK membrane be synthesized effectively for fuel cell applications?
c) How does the incorporation of inorganic metal oxide nanofillers into the SPEEK matrix influence membrane morphology and performance?
d) What are the structural, morphological, thermal, and electrochemical characteristics of the synthesized materials as revealed by UV-Vis, FTIR, XRD, TGA, BET, SEM, EDX, TEM, CV, LSV, CA, and EIS?
e) How effective are the synthesized electrocatalysts, when used with a SPEEK binder, as working electrodes for hydrogen generation?
f) What is the proton conductivity of the SPEEK/inorganic metal oxide filler composite membranes, and how does filler loading affect it?
g) How can the membrane materials be optimized for fuel cell application, and what power density performance can be achieved under varying conditions?

## 1.6. Research gap

Despite extensive research on inorganic-organic composite SPEEK membranes for PEM fuel cell applications, no study has systematically investigated the incorporation of binary or mixed-metal oxide nanofillers (as opposed to single metal oxides) into the SPEEK matrix. Existing literature focuses predominantly on single metal oxide nanofillers such as $TiO_2$, $ZrO_2$, $SiO_2$, or $Al_2O_3$ incorporated into SPEEK. Binary or mixed-metal oxide systems have not been tested as fillers in SPEEK membranes. Furthermore, the dual functionality of such mixed-metal oxides serving simultaneously as electrocatalysts for hydrogen generation and as proton-conductivity-enhancing fillers in SPEEK has not been explored.

This research gap is significant because:

- Mixed-metal oxides often exhibit synergistic properties (e.g., enhanced thermal stability, improved charge transport, and tailored hydrophilicity) that single oxides lack.
- The same mixed-oxide material could potentially optimize both hydrogen evolution reaction (HER) activity and membrane proton conductivity, offering a unified materials solution.
- Without testing binary/mixed oxides, the full potential of SPEEK-based composite membranes remains unrealized.

Thus, this study explicitly addresses the gap by synthesizing mixed-metal oxide nanofillers at varying ratios, incorporating them into SPEEK, and evaluating their performance for both hydrogen generation and PEM fuel cell applications.

## 1.5. Scope of Study

This research focuses on the synthesis, characterization, and application of metal oxide-supported sulfonated poly(ether ether ketone) (SPEEK) materials for two interconnected energy applications: hydrogen generation and proton exchange membrane (PEM) fuel cells.

The scope is limited to:

Non-platinum-based metal oxide electrocatalysts will be synthesized at varying compositional ratios. These materials are intended to serve dual functions as working electrode materials for hydrogen generation and as nanofillers within SPEEK membranes. SPEEK will be synthesized via sulfonation of PEEK, with a controlled degree of sulfonation (DS) to balance proton conductivity and dimensional stability. Composite membranes will be prepared by incorporating the synthesized metal oxide nanofillers into the SPEEK matrix.

All synthesized materials (electrocatalysts, SPEEK, and composite membranes) will be characterized using Spectroscopic techniques (UV-Vis, FTIR), Structural techniques (XRD), Thermal analysis (TGA), Surface and porosity analysis (BET), Morphological techniques (SEM, EDX, TEM), and Electrochemical methods (CV, LSV, CA, EIS)

Evaluation of electrocatalysts (with SPEEK as binder) for hydrogen generation via water splitting or related electrochemical processes. Measurement of proton conductivity of SPEEK/metal oxide composite membranes. Optimization of membrane electrode assembly (MEA) and construction of power density curves to assess fuel cell performance under varying operating conditions.

The study is confined to *ex situ* laboratory-scale electrochemical testing. It does not extend to full-scale fuel cell stack fabrication, long-term durability testing beyond the experimental timeframe, or system-level economic analysis.

## 1.6. Justification

The justification for this research arises from the convergence of several critical gaps in current energy materials science, particularly concerning proton exchange membrane fuel cells (PEMFCs) and direct methanol fuel cells (DMFCs). While SPEEK has emerged as a promising low-cost, non-perfluorinated membrane alternative, its application is hindered by excessive swelling and loss of dimensional stability at high sulfonation degrees, which this study addresses by incorporating metal oxide nanofillers specifically $CeO_2$:$ZrO_2$, $CeO_2$:$SiO_2$, and SZr:$SiO_2$ as cross-linking agents to reduce swelling while maintaining or enhancing proton conductivity. These three mixed oxide systems were strategically selected for their complementary properties: $CeO_2$:$ZrO_2$ enhances oxygen vacancy concentration and electron transfer for the hydrogen evolution reaction (HER); $CeO_2$:$SiO_2$ combines radical scavenging ability (to prevent polymer degradation) with hygroscopic properties (to retain water and enhance proton conduction); and SZr:$SiO_2$ provides superacidic characteristics for high proton conductivity while silica prevents sulfate loss and offers mechanical reinforcement. Furthermore, the development of non-platinum metal oxide electrocatalysts is justified to replace expensive, CO-sensitive platinum-based electrodes, thereby reducing cost, enhancing CO tolerance, and improving reaction kinetics. Given that most hydrogen is currently produced via energy-intensive, $CO_2$ emitting processes such as steam reforming or coal gasification, this research contributes to a pathway for green hydrogen production through electrochemical water electrolysis. Uniquely, this study synthesizes a single class of metal oxide materials for two integrated roles as working electrode catalysts for hydrogen generation and as fillers in SPEEK membranes for fuel cell operation offering potential synergies in material design, reducing development redundancy, and providing a more holistic solution across the fuel cell value chain. Finally, the research is justified by its clear and systematic objectives, which determine how synthesis ratios affect electrocatalyst properties, how filler loading influences membrane conductivity and stability, and how optimized membranes perform in fuel cells via power density curves, thereby directly advancing PEMFC technology for portable, stationary, and transportation applications.

## 1.7. Thesis Overview

This thesis is divided into seven different main sections/chapters. The description of each chapter is briefly summarized below.

**Chapter 1: Introduction**

This chapter provides a background information about the thesis project. It describes briefly the problem statement, aim and objectives of the project.

**Chapter 2: Literature review**

This chapter describes a detailed literature review involving sources where background leading to the study originated from.

**Chapter 3: Experimental**

This chapter involves the briefly description of the methods and instrumentation techniques used in the project.

**Chapter 4: Hydrogen evolution on graphite/sulfonated polyether ether ketone (SPEEK) surface using zirconium oxide-stabilized cerium oxide nanocomposites.**

This chapter provides details on the use of zirconium oxide-stabilized cerium oxide nanoparticles for hydrogen generation.

**Chapter 5: Hydrogen evolution reaction by sulphated zirconium oxide nanoparticles.**

This chapter focuses on the use of sulphated zirconium oxides for hydrogen generation.

**Chapter 6: Acidic water splitting of cerium-silica mixed oxides for sustainable electrocatalytic hydrogen production.**

This chapter describes the use of $CeO_2$: $SiO_2$ mixed oxides for hydrogen generation.

**Chapter 7: Membrane synthesis and fuel cell applications**

This chapter describes the details of the preparation and characterization of the SPEEK membranes, both pristine and mixed oxide nanocomposites, and their fuel cell applications. The chapter is divided into three sections:

A: The proton conductivity and mechanical properties of SPEEK-Ce:Zr nanocomposite membrane.

B: Enhanced Conductivity of Sulfonated Poly(ether ether ketone) membrane by the Incorporation of cerium-silica as a nanofiller for fuel cells.

C: Enhanced proton conductivity and oxidative stability of SPEEK-SZr:$SiO_2$ composite membrane for fuel cell application.

**Chapter 8: Conclusion and recommendations**

This chapter gives a general conclusion based on the results of the experimental work and provides some recommendations for future study.

## 1.8. References

1. Solomon, S., G.-K. Plattner, R. Knutti, and P. Friedlingstein, *Irreversible climate change due to carbon dioxide emissions.* Proceedings of the national academy of sciences, 2009. **106**(6): p. 1704-1709.
2. Di Primio, R., B. Horsfield, and M.A. Guzman-Vega, *Determining the temperature of petroleum formation from the kinetic properties of petroleum asphaltenes.* Nature, 2000. **406**(6792): p. 173-176.
3. Qazi, A., F. Hussain, N.A. Rahim, G. Hardaker, D. Alghazzawi, K. Shaban, and K. Haruna, *Towards sustainable energy: a systematic review of renewable energy sources, technologies, and public opinions.* IEEE Access, 2019. **7**: p. 63837-63851.
4. Barbier, E., *Geothermal energy technology and current status: an overview.* Renewable and sustainable energy reviews, 2002. **6**(1-2): p. 3-65.
5. Yüksel, I., *Hydropower for sustainable water and energy development.* Renewable and Sustainable Energy Reviews, 2010. **14**(1): p. 462-469.
6. Couture, G., A. Alaaeddine, F. Boschet, and B. Ameduri, *Polymeric materials as anion-exchange membranes for alkaline fuel cells.* Progress in Polymer Science, 2011. **36**(11): p. 1521-1557.
7. Sharaf, O.Z. and M.F. Orhan, *An overview of fuel cell technology: Fundamentals and applications.* Renewable and sustainable energy reviews, 2014. **32**: p. 810-853.
8. Carrette, L., K.A. Friedrich, and U. Stimming, *Fuel cells: principles, types, fuels, and applications.* ChemPhysChem, 2000. **1**(4): p. 162-193.
9. Rozière, M.J., *Nano-structured Polymer Electrolytes based on Ionic Liquids for High-Temperature PEMFCs*. 2013, Citeseer.

10. Laberty-Robert, C., K. Valle, F. Pereira, and C. Sanchez, *Design and properties of functional hybrid organic–inorganic membranes for fuel cells.* Chemical Society Reviews, 2011. **40**(2): p. 961-1005.
11. Wang, Y., K.S. Chen, J. Mishler, S.C. Cho, and X.C. Adroher, *A review of polymer electrolyte membrane fuel cells: technology, applications, and needs on fundamental research.* Applied Energy, 2011. **88**(4): p. 981-1007.
12. Najafi, B., A.H. Mamaghani, F. Rinaldi, and A. Casalegno, *Fuel partialization and power/heat shifting strategies applied to a 30 kW el high temperature PEM fuel cell based residential micro cogeneration plant.* International Journal of Hydrogen Energy, 2015. **40**(41): p. 14224-14234.
13. Dutta, K., S. Das, D. Rana, and P.P. Kundu, *Enhancements of catalyst distribution and functioning upon utilization of conducting polymers as supporting matrices in DMFCs: a review.* Polymer Reviews, 2015. **55**(1): p. 1-56.
14. Winter, M. and R.J. Brodd, *What are batteries, fuel cells, and supercapacitors?* Chemical reviews, 2004. **104**(10): p. 4245-4270.
15. Rodriguez, P. and T.J. Schmidt, *Platinum-Based Anode Catalysts for Polymer Electrolyte Fuel Cells*, in *Encyclopedia of Applied Electrochemistry*. 2014, Springer. p. 1606-1617.
16. Chandan, A., M. Hattenberger, A. El-Kharouf, S. Du, A. Dhir, V. Self, B.G. Pollet, A. Ingram, and W. Bujalski, *High temperature (HT) polymer electrolyte membrane fuel cells (PEMFC)–A review.* Journal of Power Sources, 2013. **231**: p. 264-278.
17. Zhang, H. and P.K. Shen, *Recent development of polymer electrolyte membranes for fuel cells.* Chemical reviews, 2012. **112**(5): p. 2780-2832.
18. Cui, Y., Y. Liu, J. Wu, F. Zhang, A.P. Baker, M. Lavorgna, Q. Wu, Q. Tang, J. Lu, and Z. Xiao, *Porous silicon-aluminium oxide particles functionalized with acid moieties: an innovative filler for enhanced Nafion-based membranes of direct methanol fuel cell.* Journal of Power Sources, 2018. **403**: p. 118-126.
19. Prapainainar, P., N. Pattanapisutkun, C. Prapainainar, and P. Kongkachuichay, *Incorporating graphene oxide to improve the performance of Nafion-mordenite composite membranes for a direct methanol fuel cell.* International Journal of Hydrogen Energy, 2019. **44**(1): p. 362-378.

20. Parnian, M.J., F. Gashoul, and S. Rowshanzamir, *Studies on the SPEEK membrane with low degree of sulfonation as a stable proton exchange membrane for fuel cell applications.* Iranian Journal of Hydrogen & Fuel Cell, 2017. **3**(3): p. 221-232.
21. Tripathy, M., P.S. Kumar, and A.P. Deshpande, *Molecular structuring and percolation transition in hydrated sulfonated poly (ether ether ketone) membranes.* The Journal of Physical Chemistry B, 2017. **121**(18): p. 4873-4884.
22. Simari, C., C.L. Vecchio, V. Baglio, and I. Nicotera, *Sulfonated polyethersulfone/polyetheretherketone blend as high performing and cost-effective electrolyte membrane for direct methanol fuel cells.* Renewable Energy, 2020. **159**: p. 336-345.
23. Kayser, M.J., M.X. Reinholdt, and S. Kaliaguine, *Amine grafted silica/SPEEK nanocomposites as proton exchange membranes.* The Journal of Physical Chemistry B, 2010. **114**(25): p. 8387-8395.
24. Tahrim, A. and I. Amin, *Advancement in phosphoric acid doped polybenzimidazole membrane for high temperature PEM fuel cells: a review.* Journal of Applied Membrane Science & Technology, 2019. **23**(1).
25. Odeh, A., P. Osifo, and H. Noemagus, *Chitosan: a low cost material for the production of membrane for use in PEMFC-A review.* Energy sources, part A: recovery, utilization, and environmental effects, 2013. **35**(2): p. 152-163.

# CHAPTER 2: LITERATURE REVIEW

**PART I:** Published research paper: A New Frontier Towards Development of Efficient SPEEK Polymer Membranes for PEM Fuel Cells Applications: A Review. *Materials Advances*, 5, 7979-8006

## 2.1. Introduction

For decades, fossil fuels have been regarded as the primary sources of increased pollution levels in the environment due to the emission of harmful greenhouse gases such as COx, NOx, and SOx during their combustion [1-3]. There are increasing concerns about the long-term viability of fossil fuels, which are expected to deplete sooner rather than later. Consequently, sustainable, renewable, and environmentally friendly fuels will become necessary. To tackle these issues, extensive research and development efforts are underway to identify alternative sources of electricity that are efficient, renewable, and ecofriendly. Among the many technologies being explored, fuel cells stand out as a key solution that can support future sustainable hydrogen production, carbon-free cycles, and a circular economy [4, 5]. In the past two decades, the use of fuel cells has increased significantly as engines and as sources of stationary and portable power [6, 7]. Mohammed et al.[8] described a fuel cell as an electrochemical device that converts the chemical energy of a fuel, such as methanol, ethanol, or ethylene glycol, into electrical energy without combustion. In this process, the fuel undergoes direct oxidation, generating electricity, heat, and water vapor. The electrochemical reactions within the fuel cell can be summarized as follows: When hydrogen flows through the anode, it is transformed into hydrogen ions, while electrons are released. These electrons travel through an external circuit to the cathode, producing electrical current [9]. The membrane electrode assembly (MEA) is the main component of a fuel cell and consists of a gas diffusion layer, a catalyst, and an electrolyte (membrane). Protons migrate through the electrolyte to the cathode, where they combine with oxygen and electrons to produce water and heat. Fuel cell technologies are distinguished by the type of electrolyte they use. The electrolyte is a crucial part of the fuel cell, as it defines the cell's properties and operating conditions [10, 11]. There are six distinct types of fuel cells: (i) Alkaline Fuel Cell (AFC), (ii) Direct Methanol Fuel Cell (DMFC), (iii) Molten Carbonate Fuel Cell (MCFC), (iv) Phosphoric Acid Fuel Cell (PAFC), (v) Proton Exchange Membrane Fuel Cell (PEMFC), and (vi) Solid Oxide Fuel Cell (SOFC). Each of these fuel cells operates under different reaction conditions and utilizes various electrolytes. Among these six, two fuel cells, the Hydrogen Fuel Cell ($H_2$-FC) and the Direct Methanol Fuel Cell (DMFC), use a polymeric membrane as their electrolyte. In contrast, the others are based on different electrochemical principles. The components, fuel types, and performance characteristics of the various types of fuel cells are presented in Fig. 2.1.

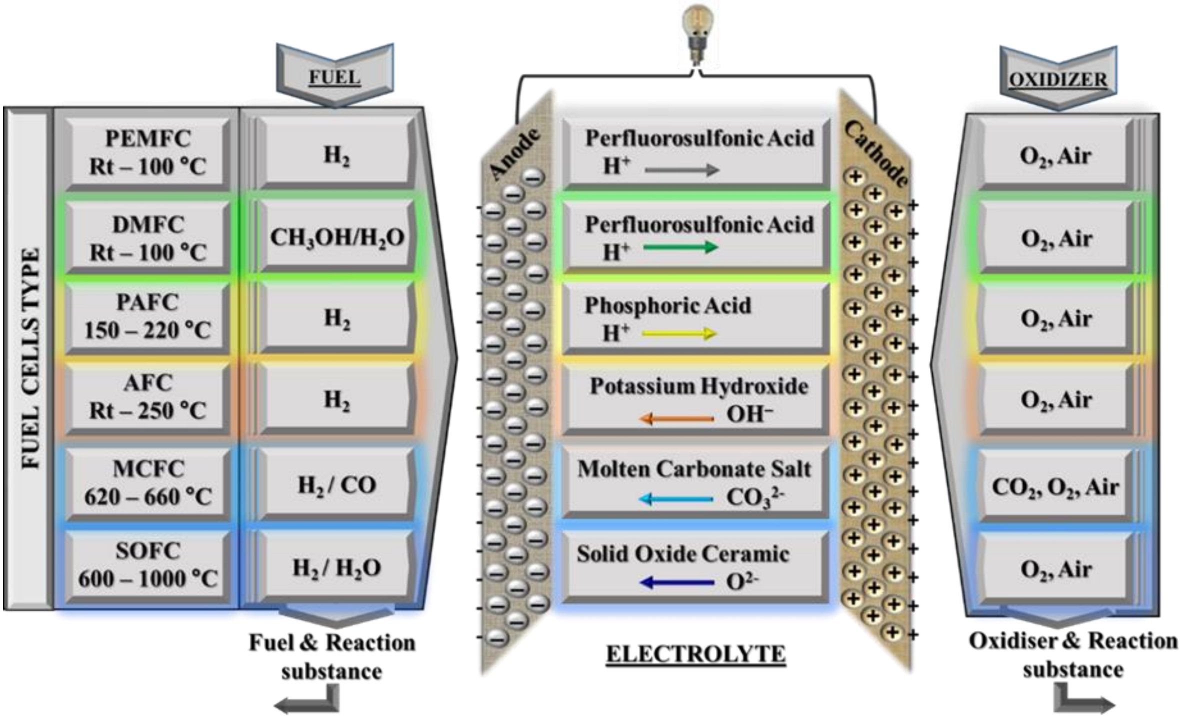

**Fig. 2. 1:** Schematic representation of different types of Fuel Cells and their properties

Among the fuel cells mentioned, proton exchange membrane fuel cell (PEMFC) technology is a significant focus of global research [12]. Its high energy density and efficiency, along with the potential for low emissions, make it a promising clean energy solution. The proton exchange membrane (PEM) serves as a barrier between the fuel gas and the electrodes, allowing protons to transfer from the anode to the cathode of the PEMFC. The reactions that take place in the PEMFC are as follows:

Anode side: $2H_2 \rightarrow 4H^+ + 4e^-$ **(2.1)**

Cathode side: $O_2 + 4e^- + 4H^+ \rightarrow 2H_2O$ **(2.2)**

Overall cell reaction: $2H_2 + O_2 \rightarrow 2H_2O + Heat + Electrical\ energy$ **(2.3)**

In the anodic reaction, hydrogen gas flows through the gas diffusion layer before dissociating into two electrons and two protons within the catalyst layer (as described in equation 2.1). The two protons travel through the proton exchange membrane (PEM) to reach the catalyst layer at the cathode, while the two electrons flow through the external circuit to the cathode [13, 14]. The cathodic reaction, similar to the anodic reaction that produces heat and water, occurs when air enters the catalyst layer through the gas diffusion layer. In this reaction, air reacts with two electrons and two protons (as described in equation 2.2). The most commonly used membranes in proton exchange membrane (PEM) fuel cells are fluorinated membranes, with perfluorosulfonic acid (PFSA) polymers, such as Nafion membranes, being the most prevalent type. Nafion is a sulfonated polymer featuring a perfluorinated backbone and sulfonated side chains. It is widely used in PEM fuel cells because it performs effectively at temperatures below 100 °C. The perfluoroether component in Nafion contributes to its chemical stability, while the sulfonated side chains aggregate and help maintain proper hydration [15]. Owing to its high ionic conductivity of approximately 0.1 S/cm when fully hydrated, along with its thermal and chemical stability, the Nafion membrane has been selected as the standard for polymeric electrolyte fuel cells [16]. However, Nafion membranes have certain limitations, such as a decrease in ionic conductivity and low humidity at high temperatures, which complicates their commercialization. To address these issues, alternative proton-conducting membranes utilizing either partially fluorinated or hydrocarbon-based polymers with ionic transfer sites have been created to enhance fuel cell performance. The chemical structure of Nafion is illustrated in Fig. 2.2.

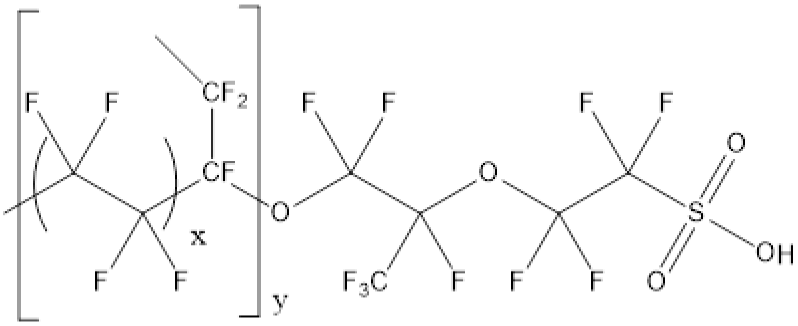

**Fig. 2. 2:** Chemical structure of Nafion.

In this context, many studies have focused on developing proton exchange membranes (PEM) with enhanced performance characteristics, including low cost, ease of synthesis, good thermal and mechanical stability, and eco-friendliness. One approach to creating partially fluorinated PEM is by synthesizing block copolymers that include a fluoropolymer. These partially fluorinated membranes, similar to fully fluorinated membranes, have shown high proton conductivity. However, they tend to be expensive due to the use of costly fluorinated materials. Additionally, the commercialization of these membranes has faced challenges stemming from high costs and a shortage of trifluorostyrene monomers [16].

Non-fluorinated membranes are composed of polymer materials that feature aromatic structures and functional groups in either the polymer backbone or side chains. These membranes are being utilized in proton exchange membranes (PEMs) as substitutes for perfluorinated membranes. One significant advantage of hydrocarbon membranes is that their polymeric structure can be easily designed to possess the desired characteristics for fuel cell applications [17]. Different types of monomers are utilized to manage the reaction conditions during the preparation of hydrocarbon membranes with outstanding properties. Additionally, the cost of the monomers used in the production of hydrocarbon-based polymers is generally lower than that of fluorinated membranes, which presents a significant advantage for commercialization [15, 18]. Hydrocarbon-based polymers typically have a carbon backbone and polar groups, resulting in high water uptake across a wide temperature range. While these polymers exhibit increased proton conductivity, they may also suffer from poor dimensional stability in membranes, leading to the formation of water channels [19]. Rigid structures, such as aromatic rings, are incorporated directly into the polymer backbone to enhance the stability and properties of membranes. These aromatic rings provide rigidity, which contributes to both thermal and mechanical stability. Consequently, a variety of hydrocarbon-based polymers, including polyether ketones (PEK), poly(arylene ethers), polyether ether ketone (PEEK), polyesters, and polyimides (PI), have been actively researched and developed for applications in fuel cells [20-23]. Among the various alternative aromatic polymers available, polyether ether ketone (PEEK) stands out as the most promising material for proton exchange membrane (PEM) applications in fuel cells. PEEK is a semicrystalline thermoplastic polymer characterized by its ether and ketone functional groups. This polymer offers an excellent combination of mechanical properties, cost-effectiveness, and exceptional thermo-oxidative stability [22]. PEEK polymer features an aromatic, non-fluorinated backbone consisting of 1,4-disubstituted phenyl groups linked by ether (—O—) and carbonyl (—C=O) groups, as illustrated in Fig. 2.3 below. This structure contributes to its properties as a high-performance, thermostable engineering polymer [24].

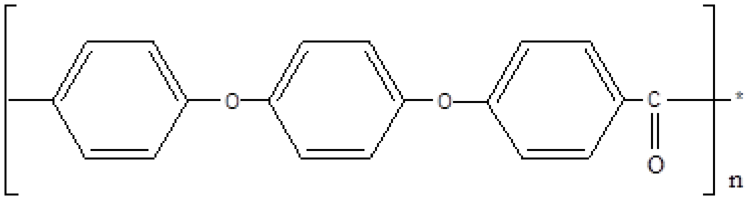

**Fig. 2. 3:** General structure of PEEK [24].

The polymer's natural hydrophobicity is usually addressed by chemically modifying its polymer chains. Sulfonic acid groups can be readily introduced onto the aromatic backbone of poly(ether ether ketone) (PEEK). The resulting sulfonated poly(ether ether ketone) (SPEEK) is a semi-crystalline, amorphous polymer that demonstrates high chemical and thermal stability, thanks to its aromatic rings [25]. It is produced by polymerizing various monomers using the following synthesis techniques: (i) displacement reaction; (ii) nickel-catalysed coupling polymerization; (iii) ring-opening polymerization with monomers containing sulfonic acid groups; and (iv) Friedel-Crafts acylation [26]. The degree of sulfonation (DS) significantly affects the properties of sulfonated poly(ether ether ketone) (SPEEK). This degree can be controlled by adjusting the reaction conditions, including the reaction temperature, acid concentration, and duration of sulfonation. SPEEK exhibits excellent chemical durability at low DS, showing greater dimensional, mechanical, and thermal stability compared to Nafion. However, it has lower water uptake and proton conductivity [27]. At higher degrees of sulfonation (DS), membrane swelling in aqueous solutions leads to the formation of interconnected channels filled with hydrophilic clusters. This results in high proton conductivity comparable to Nafion; however, it also presents undesirable mechanical properties, excessive dimensional swelling, increased fuel permeability, and consequently, low durability. Numerous studies have been conducted to modify sulfonated poly(ether ether ketone) (SPEEK) membranes to enhance fuel cell performance [28, 29].

Intensive research into the development of modified sulfonated poly(ether ether ketone) (SPEEK) membranes, particularly for fuel cell applications, plays a crucial role in advancing this specific field. Significant efforts have been made to enhance SPEEK membranes, and this review focuses on the development of proton exchange membranes (PEMs) based on these polymers. The paper discusses the physicochemical properties and characteristics of pure SPEEK membranes and explores various strategies for improving the performance of the SPEEK matrix. Additionally, it summarizes and analyzes the results of different types of modified SPEEK membranes. The review concludes by addressing the challenges and opportunities encountered during the development of SPEEK-based membranes for fuel cell applications.

## 2.2. Mechanism of proton conduction in PEM

Proton conduction is a crucial factor to consider when evaluating membranes for potential fuel cell applications. In the operation of a Proton Exchange Membrane Fuel Cell (PEMFC), the membrane must facilitate the systematic movement of water and ions, prevent the passage of electrons, and enable the dissociation of reactant gases. Maintaining sufficient hydration levels in the proton exchange membrane (PEM) is essential for ensuring high proton conductivity during fuel cell operation. Two primary mechanisms contribute to proton transfer at the molecular level: electro-osmotic drag (where water molecules help transport protons) and proton hopping (known as the Grotthuss mechanism) [30]. A schematic diagram illustrating the Grotthus, and vehicular mechanisms is presented in Fig. 2.4.

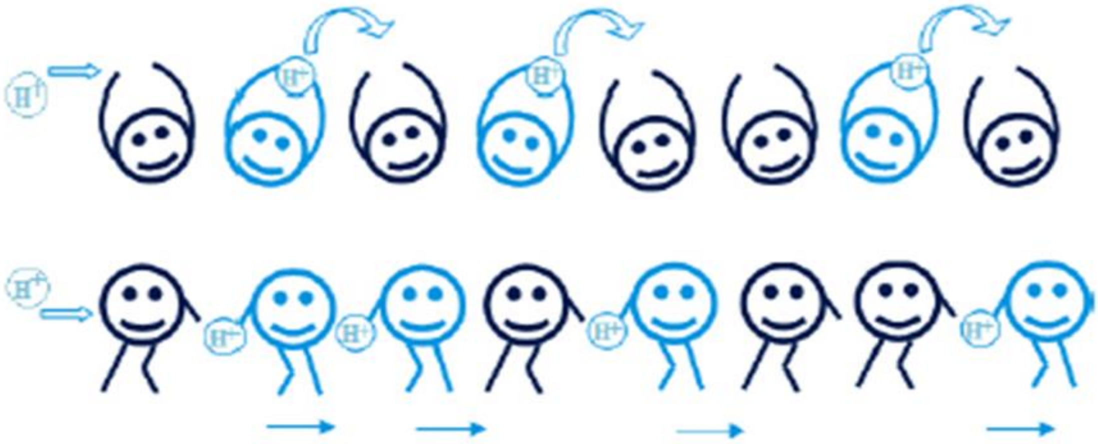

**Fig. 2. 4:** A schematic representation of the Grotthus and vehicular mechanisms [30].

In the proton hopping (Grotthus) mechanism, protons move between hydrolyzed ions ($SO_3^-$, $H_3O^+$) through polymeric matrices. The activation energy necessary for proton conductivity in this mechanism ranges from 0.1 to 0.4 eV. Protons are drawn from hydronium ions by adjacent water molecules, which facilitates the cycle of movement. In this process, the ion area forms a specific hydrophilic cluster that expands in the presence of water. As a result, protons undergo percolation phenomena. The Grotthus mechanism plays a significant role in the conductivity of perfluorinated sulfonic acid membranes, such as Nafion [31].

The ion exchange capacity (IEC) value influences the Grotthus-type transfer, as it indicates the number of ionizable groups present in the fuel cell membrane. In this membrane, electro-osmotic drag facilitates the transport of hydrogen ions ($H_3O^+$) through the aqueous medium. Consequently, water and methanol molecules function as proton transporters within the polymeric membrane. An activation energy greater than 0.5 eV is required to initiate proton conductivity [32]. In this mechanism, hydrated protons (hydronium ions) move through an aqueous medium due to electrochemical differences. Protons attach to carriers such as water or methanol before they diffuse into the medium, forming cationic complexes like $H_3O^+$, $H_5O_2^+$, $H_9O_4^+$, and $CH_3OH_2^+$. The presence of free volumes within the polymeric chains of proton exchange membranes is crucial for this vehicular mechanism. Water enhances proton conductivity in these membranes by affecting the size, stability, formation, clustering, and connectivity of ion pathways. In aqueous conditions, an increase in cluster size leads to a corresponding increase in proton conductivity with respect to humidity. Additionally, in polymeric membranes, selecting inorganic additives can improve proton conductivity at high temperatures and low relative humidity by utilizing this mechanism [33].

## 2.3 Sulfonation of PEEK

Poly(ether ether ketone) polymers exhibit chemical resistance and are thermally and mechanically stable. However, due to their entirely hydrophobic segments, they are unsuitable for direct use in fuel cell applications [29]. Adding a sulfonic acid group to PEEK polymer enhances its hydrophilicity, solubility in polar solvents, and ion exchange capacity. The solubility of the sulfonated form, known as SPEEK, varies with different degrees of sulfonation (DS). Specifically: (a) a sulfonation degree of approximately 30% allows solubility only in hot DMF (dimethylformamide), DMAc (dimethylacetamide), DMSO (dimethyl sulfoxide), and NMP (N-methyl-2-pyrrolidone), (b) a sulfonation degree of 40% to 70% enables solubility at room temperature in these same solvents: DMF, DMAc, DMSO, and NMP, (c) a sulfonation degree above 70% allows solubility in methanol and (d) a sulfonation degree of 100% results in solubility in hot water.

This improved solubility facilitates various applications of SPEEK in different environments [34]. There are three synthetic methods that can be employed to prepare sulfonated poly(ether ether ketone):

(a) Direct copolymerization reactions of sulfonated monomers with appropriate monomers.

(b) Direct sulfonation reactions after polymerization of poly(ether ether ketone).

(c) Sulfonation reactions of poly(ether ether ketone)s introduce pendant sulfonate groups into the polymer chains.

### 2.3.1 Direct sulfonated monomer copolymerization reactions with suitable monomers.

A sulfonated dihalogenated diaryl ketone monomer or a sulfonated bisphenol derivative can be directly copolymerized with a suitable dihalogenated diaryl ether monomer unit to produce random (statistical) sulfonated poly(ether ether ketone) [35]. By carefully controlling the reaction stoichiometry, the sulfonate group can be introduced specifically along the polymer backbone. This is achieved through a step-growth copolymerization reaction that utilizes sulfonated monomers [36]. Electrophilic aromatic substitution reactions using various sulfonating agents can produce sulfonated dihalogenated diaryl ketone or bisphenol monomer derivatives [37]. Nguyen et al. [38] synthesised a sulfonated di-halogenated diaryl ketone monomer by treating 4,4'-difluorobenzophenone with 25.3% fuming sulfuric acid, resulting in 100% yield and high purity disodium-3,3'-disulfate-4,4'-difluorobenzophenone (Fig. 2.5).

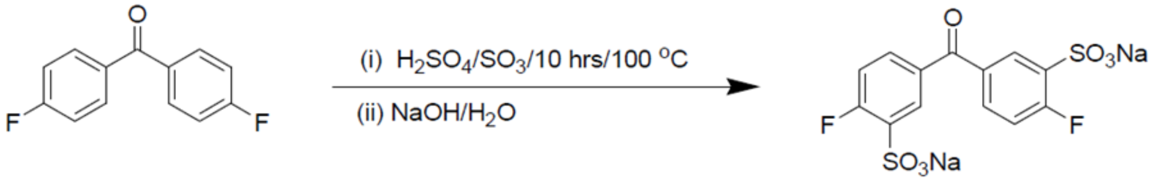

**Fig. 2. 5:** The reaction formula of a sulfonated di-halogenated diaryl ketone monomer [38].

A series of sulfonated poly(ether ether ketone) polymers were synthesized through a base-catalyzed nucleophilic aromatic polycondensation reaction involving 4,4'-difluorobenzophenone and the pure sulfonated monomer, disodium-3,3'-disulfate-4,4'-difluorobenzophenone, along with hexafluoroisopropylidene diphenol (see Fig. 2.6) [39]. The resulting high molecular weight polymers demonstrated thermal stability up to 260 °C. These sulfonated poly(ether ether ketone) polymers were subsequently utilized as proton exchange membranes in fuel cells.

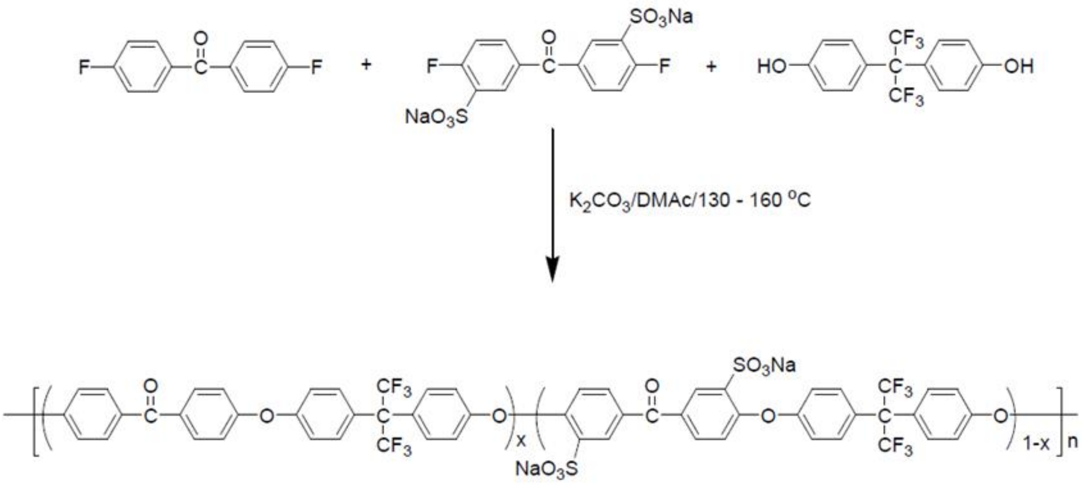

**Fig. 2. 6:** Reaction mechanism for preparation of Sulfonated poly (ether ether ketone) by the base catalyzed nucleophilic aromatic polycondensation [39].

### 2.3.2 Direct post-polymerization sulfonation reactions with poly (ether ether ketone)

Poly(ether ether ketone) is a highly effective polymer that is insoluble in most organic solvents. The incorporation of a sulfonic acid group along the polymer backbone reduces crystallinity and enhances solubility [40]. Direct sulfonation of poly(ether ether ketone)s with various sulfonating agents is not region-specific due to the lack of control over the degree and location of sulfonation during the process [40]. In addition, polymer degradation and various side reactions have been observed. The sulfonation of poly(ether ether ketone)s occurs through an electrophilic substitution reaction mechanism, using sulfonating agents like sulfuric acid ($H_2SO_4$), as illustrated in Fig. 2.7. The ether linkage activates the phenyl rings in the polymer chain for these electrophilic substitution reactions, allowing the sulfonating group to be introduced into the hydroquinone segment of the polymer chain [41, 42]. Typically, one sulfonic acid group is added per unit because the carbonyl group attracts electrons, lowering the electron density of the other aromatic rings [40, 43]. However, disulfonation reactions can occur at elevated temperatures or with prolonged reaction times. Sulfonation reactions involving poly(ether ether ketone)s are usually performed using sulfonating agents such as chlorosulfonic acid or sulfuric acid [44]. The reaction time, temperature, and acid concentration all play a crucial role in the sulfonation process using sulfuric acid. In their study, Daud et al. [45] prepared sulfonated poly(ether ether ketone) (PEEK) using Victrex and 95-97% concentrated sulfuric acid along with chlorosulfuric acid at room temperature. This approach was chosen to prevent the degradation of PEEK and to avoid cross-linking reactions. They conducted the reaction over a range of time periods and achieved a degree of sulfonation of 80%. In another study, Muthu Lakshmi et al. [46] examined the effects of temperature and reaction duration on the degree of sulfonation of Gatone, as well as on the characteristics of the sulfonated polymers. Their sulfonation process was carried out at temperatures between 35-50 °C for 3-5 hours, resulting in a degree of sulfonation between 50-80%. The resulting sulfonated poly(ether ether ketone) derivatives were utilized in fuel cells and electrodialysis processes as electrochemical devices.

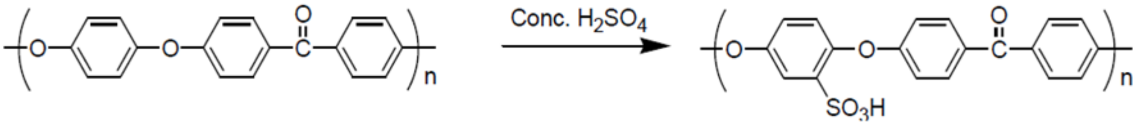

**Fig. 2. 7:** Sulfonation reactions of Gatone poly (ether ether ketone) [46].

To simplify the incorporation of a sulfonic acid group into the polymer chain, standard organic reactions are often employed to functionalize poly(ether ether ketone)s. Reactive sites can be introduced directly along the polymer backbone or by adding an appropriate functional group as a pendant to the chain before the polymer precursor undergoes sulfonation functionalization.

Xu et al. [41]. utilized dihydroxy functionalized poly(ether ether ketones) as substrates to synthesize a series of new sulfonated poly(ether ether ketones). They employed a base-catalyzed nucleophilic aromatic substitution polymerization method to create the corresponding poly(ether ether ketone) derivative based on dihydroxynaphthalene. The sulfonated poly(ether ether ketone) was produced through a base-catalyzed nucleophilic reaction between the dihydroxynaphthalene-based poly(ether ether ketone) and 1,4-butane sulfone (see Fig. 2.8). The resulting sulfonated poly(ether ether ketone) derivative demonstrated high proton conductivity, making it suitable for direct methanol fuel cell (DMFC) applications.

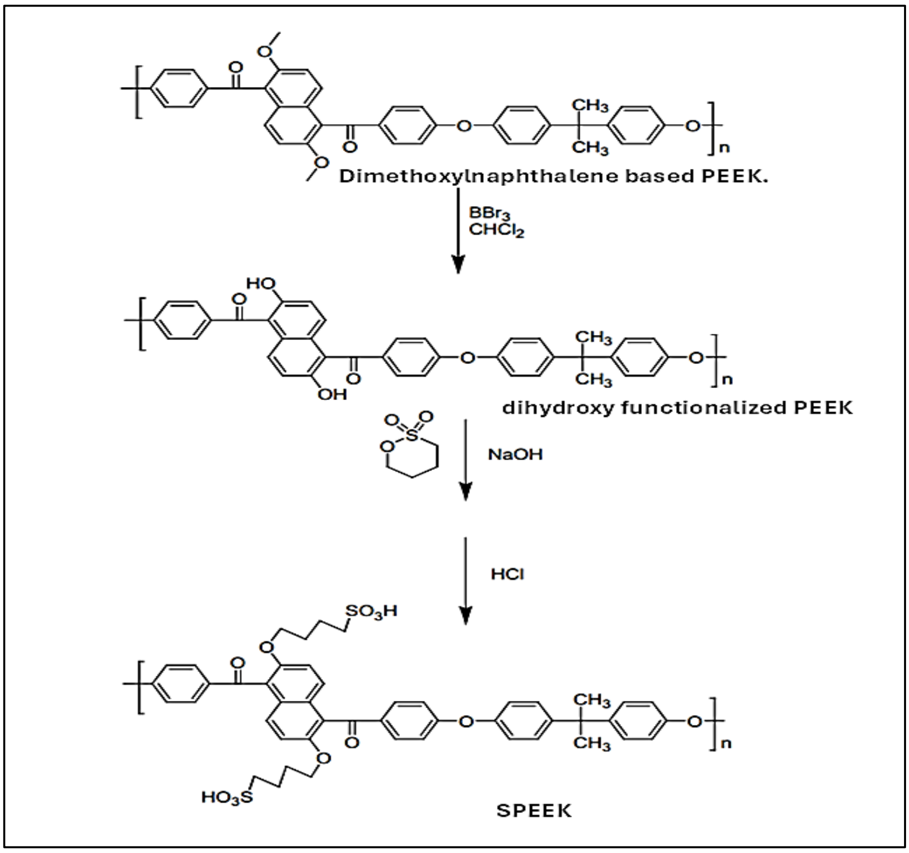

**Fig. 2. 8:** Nucleophilic reaction of dihydroxynaphthalene-based poly(ether ether ketone) with 1,4-butane sulfone [41].

Another synthetic method for creating sulfonated poly(ether ether ketone)s with the sulfonic acid group pendant to the polymer chain was created by Tsai et al. [47]. In order to produce pristine sulfonated poly(ether ether ketone), poly(ether ether ketone) was first treated with concentrated sulfuric acid. This was done by treating the resulting sulfonated poly (ether ether ketone) with 1,1'-carbonyl-diimidazole (CDI). Novel main-chain and side-chain sulfonated poly(ether ether ketone) with enhanced nano-phase separation morphology were formed after reaction with 2-aminoethanesulfonic acid (see Fig. 2.9). The addition of the new sulfonated group pendant to the polymer chain resulted in well-defined nano-phase separation morphology and improved the properties of the proton exchange membrane in DMFC applications.

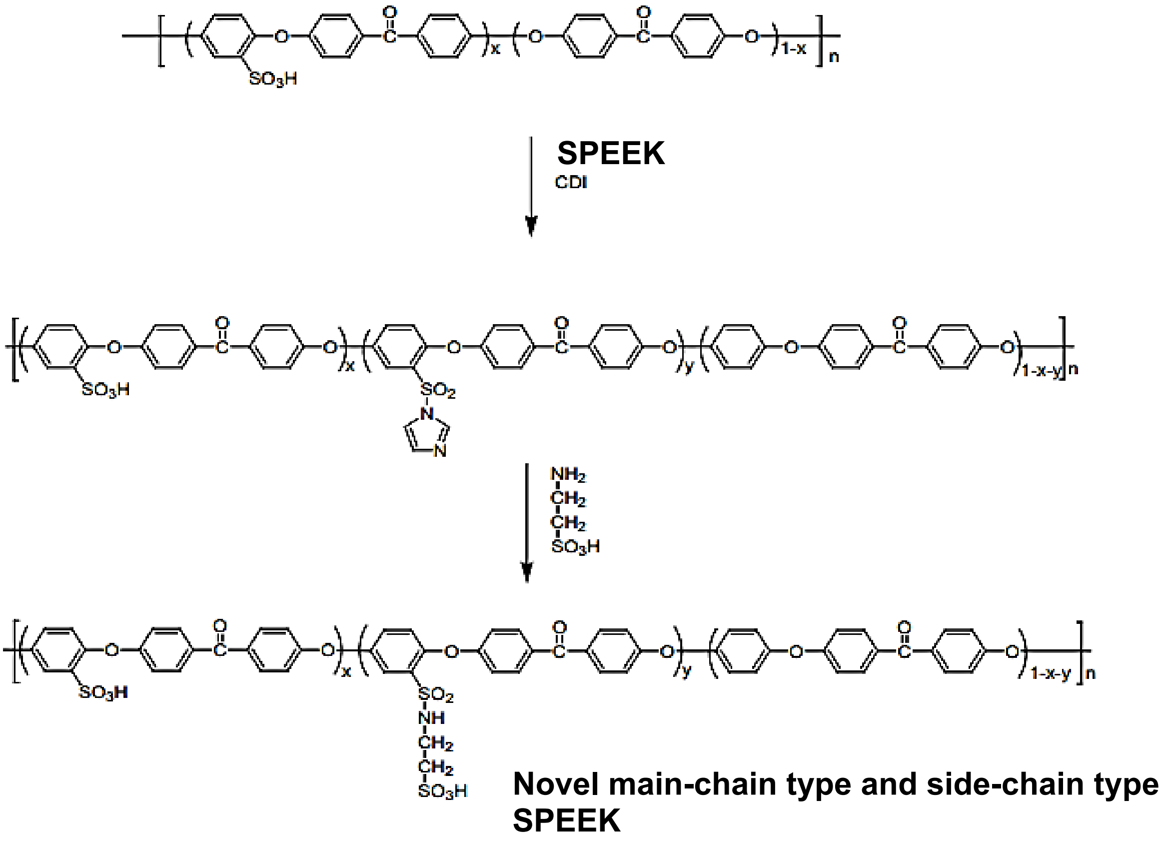

**Fig. 2. 9:** Sulfonated poly(ether ether ketone) synthesis route using 1,1'-carbonyl-diimidazole (CDI) [47].

The sulfonic acid group can also be introduced to the poly(ether ether ketone) chain through the thiol-ene reaction, which comprises the following steps:

(i) The synthesis of a poly(ether ether ketone) precursor derivative containing an unsaturation site on the polymer chain.

(ii) The double bond site of unsaturation reacts with a mercapto compound that contains a sulfonate group through the classic thiol-ene reaction.

Li et al. [48] utilized the thiol-ene method to synthesize poly(aryl ether ketone) ionomers that feature pendant sulfonic acid groups attached to the polymer backbone, as shown in Fig. 2.10. They achieved quantitative yields of sulfonated poly(ether ether ketone) by treating the propenyl derivative of poly(ether ether ketone) with sodium 3-mercapto-1-propane sulfonate and AIBN in a mixed solvent of NMP and DMSO. The resulting sulfonated poly(ether ether ketone) materials were used as substrates for polymeric membranes in fuel cell technology.

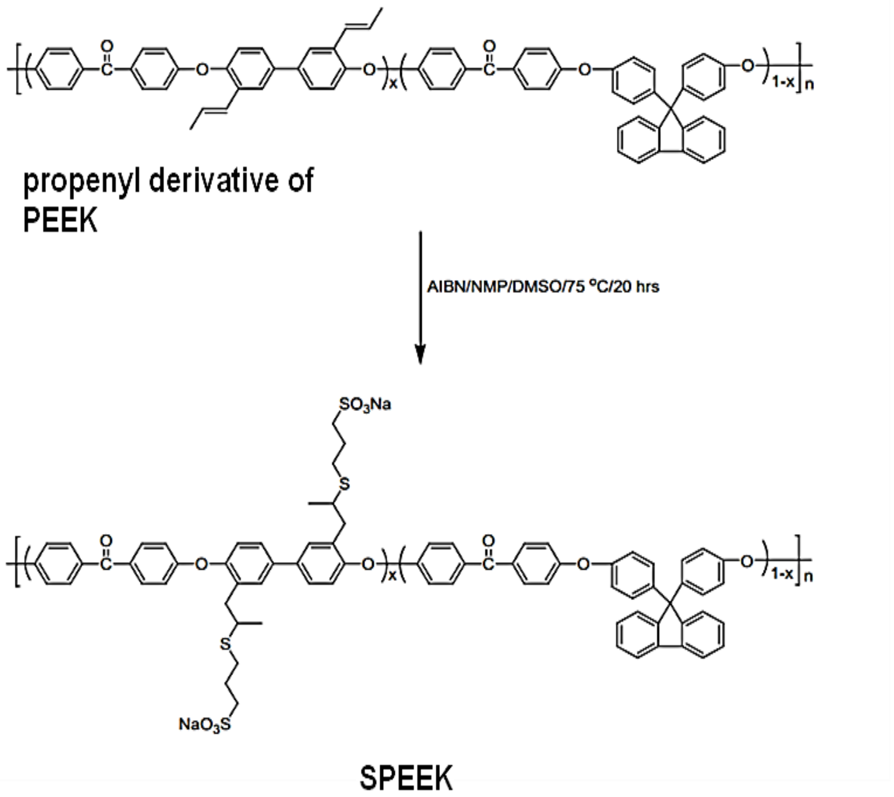

**Fig. 2. 10:** Synthesis of Sulfonated poly(ether ether ketone) using the Thiol-ene method [48].

## SPEEK modification methods

The sulfonation of SPEEK polymer is significantly influenced by various reaction conditions, including reaction time, temperature, and the presence of an inert atmosphere. If these conditions are not properly controlled, the degree of sulfonation (DS) may either increase or decrease. A higher DS in the SPEEK material leads to increased swelling at elevated temperatures before it dissolves in water. Furthermore, a higher DS is often associated with enhanced ion exchange capacity (IEC) and proton conductivity. As a result, several modification techniques, such as blending and cross-linking, have been explored to develop effective SPEEK membranes [49].

## 2.4 Membrane crosslinking

### 2.4.1 Electron beam (EB) radiation

Radiation-induced crosslinking with electron beam (EB) technology is now widely utilized for processing polymer materials because of its inherent advantages over UV and thermal curing methods. This radiation crosslinking approach is a straightforward and effective way to reduce methanol permeability and enhance the thermal and dimensional stability of membranes, as well as improve their mechanical properties, all while maintaining proton conductivity [49]. Xiang et al. [50] utilized a combination of cross-linking agents, including trimethylolpropane triacrylate (TMPTA), polyester acrylate, 2-(2-ethoxy-ethoxy)ethyl acrylate (EOEOA), and 1,6-hexanediol diacrylate (HDDA), to introduce electron beam (EB) cross-linking in the sulfonated poly(ether ether ketone) (SPEEK) structure. Their study showed that the degree of cross-linking and structural density was directly influenced by the exposure dose when different EB irradiation samples were treated at a dose rate of 6 kGy $min^{-1}$. Higher doses of EB irradiation led to improved thermomechanical and dimensional stability. They found that the cross-linked polymer membranes exhibited a higher cluster transition temperature compared to the Nafion 117 membrane, suggesting that the cross-linked membranes could be more advantageous in high-temperature fuel cells. Small-angle X-ray scattering (SAXS) analysis indicated that the ionic sites remained active during the cross-linking reaction, leading to increased proton conductivity, particularly at elevated temperatures (90 °C). Additionally, the membranes demonstrated enhanced proton conductivity and dimensional stability at 80 °C under fully humidified conditions, allowing for a maximum power density of 0.225 W/$cm^2$ at a higher EB irradiation dosage of 200 kGy. Xiaomin et al. [51] synthesised 1,6-bis(4-vinylphenyl) hexane (BVPH), an unhydrolyzable cross-linker, to enhance the dimensional stability, mechanical strength, and methanol crossover resistance of SPEEK membranes through electron beam (EB) irradiation at room temperature. By incorporating BVPH at varying concentrations between 5% and 15% by weight and applying a constant irradiation dose of 350 kGy with a dose rate of 6 kGy $min^{-1}$, a higher degree of cross-linking was achieved. The membranes with 15% BVPH exhibited superior performance compared to pristine SPEEK membranes, showing improved dimensional and chemical stability, as well as greater mechanical strength. Moreover, the SPEEK membranes containing 15% BVPH demonstrated enhanced oxidative resistance, achieving a tensile strength of 93 MPa (when dry) and sustaining 38 hours in a 3% $H_2O_2$ solution with 2 ppm $Fe^{2+}$ at 80 °C. However, it is important to note that the increased hydrophobicity and reduced water sorption, along with fewer active ionic sites, led to a slight decrease in the proton conductivity of the cross-linked SPEEK membranes.

### 2.4.2 UV radiation

Before Hayes published a patent claiming that UV crosslinking enhances the environmental stability and reduces the gas permeability of polyimide materials, the crosslinking of polymer materials through ultraviolet (UV) irradiation had been studied for a long time but received little attention in the field of proton exchange membranes (PEM) research [52]. Since then, several studies have examined polymer membranes that have been cross-linked through UV irradiation in order to improve their properties. While many photo initiators and crosslinking agents are available on the market, they can often be highly unstable or quite expensive [53]. Chemical crosslinking may reduce the efficiency of polymer chain packing, which can lead to increased gas permeability and alterations in the properties of membranes [54]. As a result, most researchers have focused on incorporating photo initiators and suitable crosslinking sites into the polymer backbone. The UV-crosslinked hybrid SPEEK membrane, when combined with a biodegradable polymer, reduces the elasticity of the polymer chains by forming a denser network. Ramly et al. [55] investigated SPEEK with methylcellulose (MC) and UV radiation, employing benzoin ethyl ether (BEE) as a photo-initiator. Radiation-induced demethylation, chain cleavage, acid group production, and carbonyl in MC all contributed to increased hydrophilicity. When the non-crosslinked membrane was crosslinked with BEE under UV light for 30 minutes, the proton conductivity at 30 °C rose from 0.004 S $cm^{-1}$ to 0.008 S $cm^{-1}$. Because of its denser structure, the UV membrane demonstrated greater dimensional stability after crosslinking. Teruel-Juanes et al. [56] used UV irradiation to crosslink polystyrene-ethylene-butylene block copolymers (SEBS) with DVB, rather than sulfonation followed by crosslinking. The hardened membranes were then post-sulfonated with trimethylsilyl chlorosulfonate solutions in 1,2-dichloroethane (DCE). The dielectric relaxation spectrum (Fig. 2.11) indicated two major relaxations: the glass transitions of the ethylene-butylene (EB) and styrene (S) blocks, and sub-Tg intramolecular non-cooperative dielectric relaxation. In addition to affecting the fragility of both styrene (S) and ethylene-butylene (EB) blocks, photo-crosslinking and post-sulfonation operations have an impact on the dielectric relaxation spectrum. They concluded that membrane behaviour can be estimated and reengineered depending on changes to desired cell performance due to a correlation discovered between relaxation processes and membrane performance in $H_2/O_2$-PEM single cells.

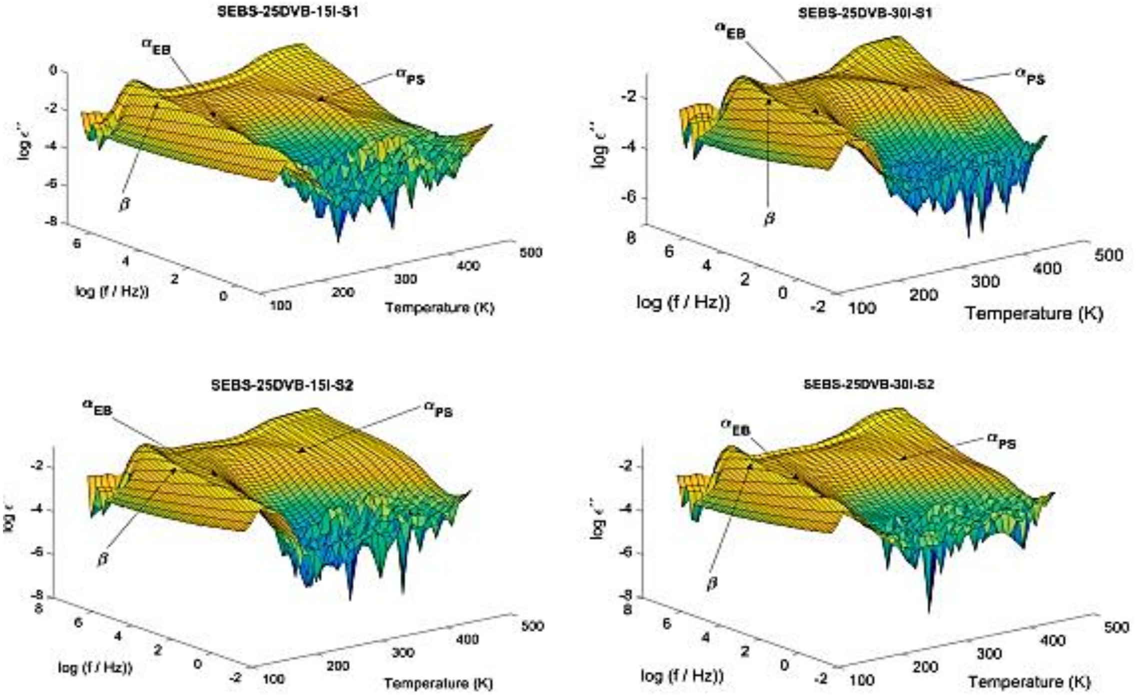

**Fig. 2. 11:** Dielectric relaxation spectrum [56].

### 2.4.3 Chemical cross-linking

Chemical additives can also be used to initiate polymer crosslinking during the membrane casting process. The literature identifies a large range of unique additions, such as sulfonic acid groups and "free" hydrocarbon sites on the polymer chain, each with a distinct crosslinking process.

Polyatomic alcohols like glycerol, ethylene glycol, and meso-erythrite can be utilized as crosslinking agents to improve or preserve the flexibility of the SPEEK membrane (Fig. 2.12) [41]. This is owing to the fact that the sulfone bond formed by thermal crosslinking of two sulfonic acid groups is less flexible than the sulfonic ester bond formed by condensation with polyatomic alcohol. The flexibility of macromolecular chains allows them to align into hydrophilic and hydrophobic domains, which improves conductivity [57]. Kumari et al. [58] examined the influence of polyatomic alcohol linker length. They employed ethylene glycol (PEG) with varying molecular weights (MW/Da: 200 to 10000) and investigated the effect of molecular weight on the membrane's ultimate qualities. The scientists discovered that PEG 400 could create many small hydrophilic and hydrophobic clusters, which were more practicable than bigger clusters formed by PEG with a MW less than 600. They discovered this using atomic force microscopy (AFM) and small-angle X-ray scatting (SAXS). The findings also showed that there was an ideal linker length for stacking macromolecular chains into hydrophobic and hydrophilic domains.

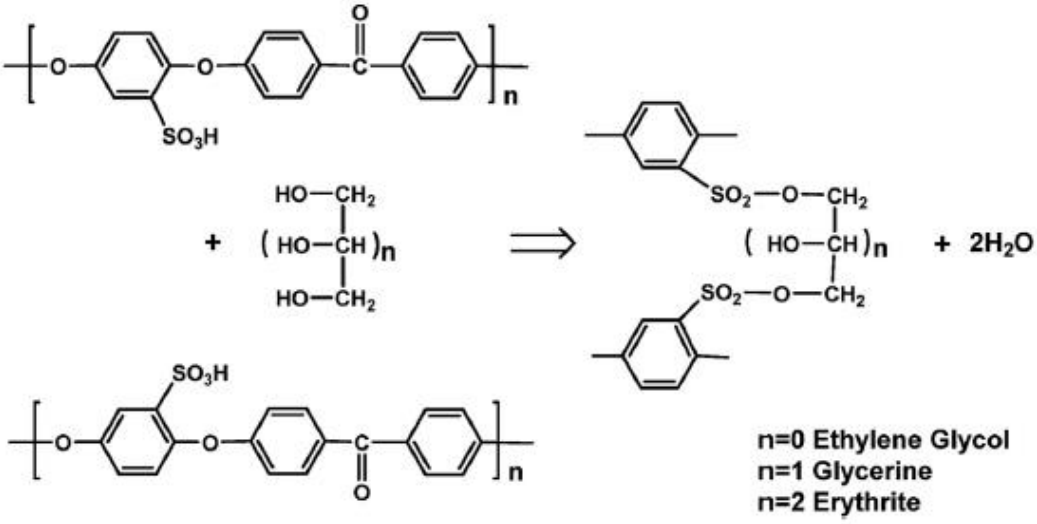

**Fig. 2. 12:** Reaction scheme of SPEEK cross-linked with polyatomic alcohol [41].

In a separate investigation, Gupta et al. investigated the flexibility of diol crosslinking agents [59]. To crosslink the SPEEK membrane, cyclohexane di-methanol (CDM) was used as the stiff crosslinking reagent and PEG (MW 200) as the flexible crosslinking agent. According to their findings, the optimal polymer-to-crosslinker ratio was determined to be 3:1 after completing conductivity and water uptake trials with various crosslinking agent ratios. Furthermore, membranes crosslinked with the rigid CDM had worse characteristics as compared to membranes crosslinked with the flexible PEG. When crosslinking SPEEK, it is also important to consider the flexibility of the crosslinkers.

## 2.5 SPEEK blend polymer membrane

Blending is a simple way for defining and regulating phase separation in the microstructure of homopolymers, assuming that the second polymer is entirely compatible with the original polymer [59]. Hydrogen bonds and ionic interactions, the two most frequent physical interactions amongst polymers, can be exploited to strengthen blend membranes.

### 2.5.1 Acid-base polymer blend

When benzimidazole side groups are added to the polysulfone backbone and blended with SPEEK, they generate an acid-base blend membrane [60]. The benzimidazole group uses basic nitrogen as a medium to transport protons between SPEEK's sulfonic acid groups, which supports both the hopping-type and vehicle-type processes. In PEMFC at 60-100 °C, the blended membrane surpasses the Nafion and pristine SPEEK membranes [61]. Numerous researchers selected Poly(amide imide) (PAI) to blend with SPEEK due to the effectiveness of sulfonated polyimides in preventing methanol diffusion. The addition of PAI to the membrane structure decreases swelling ratio and methanol permeability while boosting mechanical, thermal, and oxidative properties. As expected, proton conductivity decreased as PAI content increased. Raja et al. [62] incorporated BaCeO3 nanoparticles into SPEEK/poly (amide-imide) (PAI) matrices to enhance mechanical properties. The inclusion of BaCeO3 nanoparticles increased conductivity, ion exchange, and water uptake (WU) capabilities while retaining regulated stability due to the nanoparticles' strong interfacial contact with the polymer. The polymer was shown to have stronger methanol barrier characteristics, making it appropriate for DMFC.

.

### 2.5.2 Acid-acid polymer blend

Introducing hydrogen bonding between polymer chains in a blend PEM is a promising strategy for reducing methanol permeability and increasing DMFC durability. Li et al. [63] blended fully aromatic polyamide (fa-PA) with SPEEK with a sulfonation degree of 76%. There are numerous electronegative sites, such as carbonyl, amine, and sulfonate groups, that can generate dense morphologies and produce H-bonds between polymer chains, as illustrated in Fig. 2.13a. At 25 °C, fa-PASP-20 (20 weight percent completely aromatic polyamide) outperformed pristine SPEEK in terms of mechanical strength and swelling behaviour.

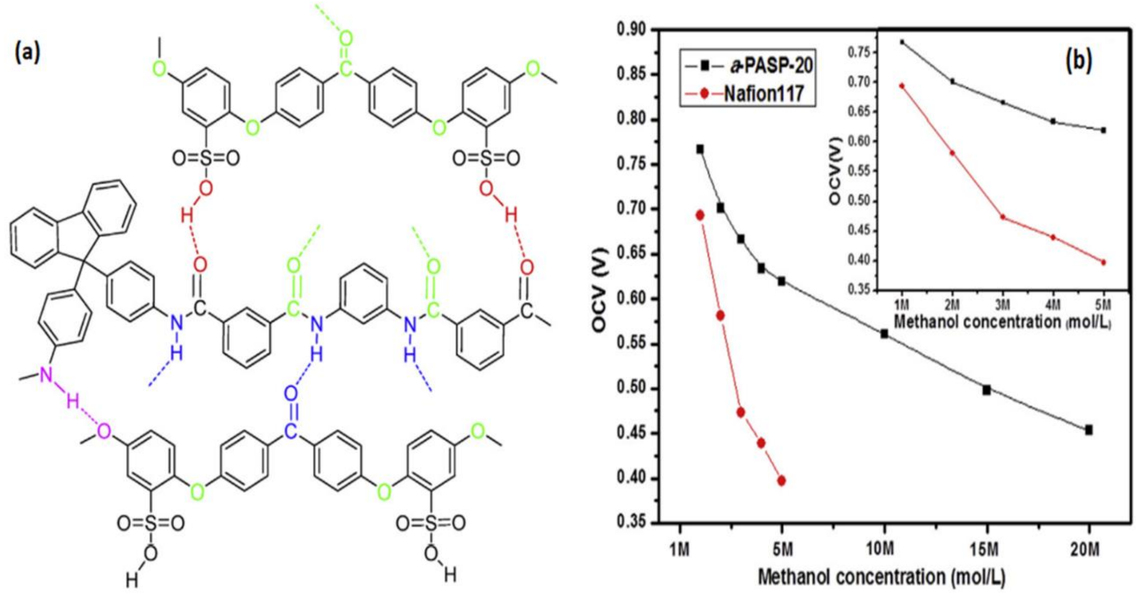

**Fig. 2. 13:** Expected hydrogen bonding between the blend of sulfonated poly (ether ether ketone) with fully aromatic polyamide (fa-PA), and (b) OCV of fa-PASP-20 blend and Nafion 117 membranes at different methanol concentrations [63].

Additionally, in an aqueous methanol solution (2 M) at ambient temperature, faPASP-20 had a comparatively low methanol permeability of 1.29 x $10^{-7}$ $cm^2/s$, whereas SPEEK's values were 3.06 x $10^{-7}$ $cm^2/s$. Figure 2.13b shows the open circuit voltage (OCV) values of fa-PASP-20 and Nafion 117 as a function of methanol concentration, revealing that the blend PEM has good methanol resistance even at high concentrations.

Haragirimana et al. [64] used acid-acid blending and sulfone bridges to achieve a synergistic effect in SPEEK and SPAES. In their investigation, they created a series of PEEK/SPAES polymer blends using a three-component technique. Ductile and dense membranes were effectively constructed using simple solution mixing and casting due to the good compatibility and fine dispersion of both copolymers inside the membrane. The inclusion of SPAES into SPEEK improved membrane water-swelling behaviour and oxidative stability significantly, especially at high temperatures. The SPAES and SPEEK chains formed strong hydrogen bonds and interfacial interactions (π-π interactions).

### 2.5.3 Blending with Perfluorosulfonic acid (PFSA) membrane.

PEMs can be created by combining PFSA polymers and SPEEK. The SPEEK nanofiber mat was first electrospun, then impregnated with PFSA polymers [65].

Dimensional stability and mechanical qualities improved, while proton conductivity dropped when compared to the original membrane. Fluoropolymers, such as poly(-vinylidene fluoride) (PVDF) or poly(vinylidene fluoride-cohexafluoropropylene) (PVDF-HFP), can easily be combined with SPAEKs or SPAESs to form composite membranes [66]. The addition of PVDF or PVDFHFP reduced proton conductivity while increasing water absorption, swelling ratio, and methanol barrier characteristics. In another noteworthy investigation, Nayak et al. [67] blended non-fluorinated blend membranes, SPEEK, and fluorinated blend membranes. Sulfonated poly (ether-ether-ketone)/poly (vinylidene fluoride-co-hexafluoropropylene)/silica (SPEEK/PVdF-HFP/SiO2) composite proton exchange membranes have been created for fuel cell applications. The SiO2 (7.5 wt.%) polymer membrane with SPEEK (80 wt.%) and PVdF-HFP (20 wt.%) had the maximum proton conductivity of $8 \times 10^{-2}$ $S.cm^{-1}$. Furthermore, a maximum power density of 1.5 $mW/m^2$ was found. This study suggests that adding SiO2 to polymer composite membranes could result in a distinct PEM.

Cali et al. [68] created a high ionic conduction sulfonated poly(ether ether ketone)/poly(vinylidene fluoride) (SPEEK/PVDF) blend membrane doped with boron phosphate. At 0.6 V, SPEEK/ PVDF/10BP demonstrated the highest current density (0.4 $A.cm^{-2}$) and power density (0.242 $W.cm^{-2}$). At 80 °C, the SPEEK/PVDF/10BP sample had a proton conductivity of 39 $mS.cm^{-1}$. The combination of boron phosphate and the SPEEK/PVDF mix membrane produced encouraging results for future fuel cell operations.

### 2.5.4 Blending with non-fluorinated membrane

PVA-SSA/SPEEK composite membranes were prepared using sulfosuccinic acid crosslinked with polyvinyl alcohol (PVA-SSA), according to Wang et al. [69]. Despite their high tensile strength, the blended polymers had lower ion exchange capacity (IEC) and water uptake (WU) than the pure membrane. Low DS and PVA crosslinking may inhibit the PVA-SSA reaction when SPEEK is present. The presence of SPEEK in the blend, as well as the crosslinking of PVA and SSA, appear to improve thermal stability. When hydrated, PVA-SSA/SPEEK (70:30) has a proton conductivity of 0.070 $S.cm^{-1}$. Liu et al. [70] produced a combination of SPEEK and sulfonated poly (phthalazinone ether sulfone ketone) (SPPESK). The disclosed SPPESK/SPEEK membrane has an excellent water absorption rate and a low swelling ratio. At 80 degrees Celsius, the mix membrane's proton conductivity was estimated to be 0.212 S.cm$^{1}$.

### 2.5.5 The modification of SPEEK membranes with other polymers

Most polymers contain carbon atoms covalently bonded to additional elements such as hydrogen, oxygen, or nitrogen. These organic compounds can be referred to as polymers. Thus, mixing a polymer with SPEEK might result in the creation of acid-base interactions or hydrogen bonds between polymer chains, which can significantly alter the mixture's properties. SPEEK coupled with other polymers is a regularly used approach in composite membrane manufacturing, providing good proton conductivity and acceptable mechanical properties. Blends of SPEEK with various polymers, including polyacrylonitrile (PAN) [71], polybenzimidazole (PBI) [72], poly(ether sulfone) (PES) [73], polyimide (PI) [74], polyphenylene oxide (PPO) [75], polytetrafluorethylene (PTFE) [76], vinylidene fluoride [77] [87], polyvinylpyrrolidone (PVP) [78] and poly(tungstophosphoric acid (TPA) [79] . According to Peng et al., the performance of a SPEEK membrane can be improved by changing its microstructure using either dibutyl phthalate (DBP) porogen or Nafion resin applied as a layer atop polypropylene. A modified membrane structure made up of SPEEK membrane layers covered with polydopamine (PDA) has been shown to improve mechanical strength and selectivity. All of these technologies enhance performance and suggest the usage of composite SPEEK membranes in PEMFC applications.

Phosphonate membranes have recently gained popularity as a viable substitute for PEMFC applications.

The acid form of phosphorylated polysulfone (PPSU-As) with phosphonation (DP) values of 0.4, 0.75, and 0.96 was effectively synthesized and blended by Abu-Thabit et al. [80] using SPEEK with a DS of 0.75. The phosphoryl group ($-PO_3H_2$) could make strong hydrogen bonds with acidic SPEEK polymers, minimizing swelling while sacrificing little proton conductivity. When compared to pure SPEEK, the SPEEK/PPSU membrane had lower methanol permeability, higher mechanical strength, and water uptake without losing proton conductivity. Proton conductivity was higher in the mix membrane (30PPSU-A-0.96) compared to the pristine SPEEK membrane. At 120 degrees Celsius, the maximal proton conductivity of 0.124 S.cm$^{-1}$ was achieved and maintained. Sultan et al. [81] developed a novel hybrid membrane poly (trimellitic anhydride chloride-co-4,4'-methylenedianiline) (SPEEK/PTCMA) with PTCMA loadings ranging from 10% to 50% and a DS of 53%. At room temperature, SPEEK/PTCMA (50 wt.%) had an 11% reduced water uptake due to the acid-base interaction of the amine and sulfonate groups. At 90 degrees Celsius, the composite membrane SPEEK/PTCMA (20 wt.%) had a greater proton conductivity of 0.004 $S.cm^{-1}$. PTCMA was added to boost proton conductivity since its nitrogen atom can be protonated and contribute to proton transfer. Overall, the study found that the proton conductivity value reduced as the PTCMA level increased. As a result, the number of sulfonic acid groups in the composites decreases, increasing crystallinity and reducing water uptake, a critical stage in proton transfer.

Han et al. [82], Han et al. [83] developed SPEEK/PBI composite membranes by dissolving the two polymers in DMAc before casting the membrane. The combination of the -NH groups in PBI with the $-SO_3$ groups in SPEEK creates a three-dimensional network polymer structure that is beneficial for proton transport. At 80 °C, the PEM showed outstanding proton conductivity, with a value of 0.14 $S\ cm^{-1}$, comparable to Nafion 117 (0.142 $S\ cm^{-1}$). Methanol has a permeability of $2.38 \times 10^{-8}\ cm^2.\ s^{-1}$, which is significantly lower than that of Nafion. In addition to mechanical characteristics, thermal stability is crucial. This type of polymer membrane design is effective and almost ready for application in DMFCs. A sandwich-shaped PI/SPEEK/PI nanofiber composite membrane with straightforward manufacturing procedures was proposed by Wei et al. [74]. Proton performance was greatly enhanced by the development of an acid-rich layer and the firm support of PI nanofibers on the SPEEK matrix. The new hybrid membranes PI/SPEEK with PI loadings of 3% and PI/SPEEK/PI with PI loadings of 1.5% have poorer methanol permeability than SPEEK membranes because of the acid-base interaction between tertiary amide groups and sulfonated groups. Excellent conductivity of 0.178 $S.cm^{-1}$ at 60 °C was shown by the sandwiched membranes, which is significantly higher than that of the neat SPEEK membrane. The performance of the fuel cell can reach 0.152 $W.cm^{-2}$. At 60 °C and 100% relative humidity, the PI/SPEEK nanofiber composite membrane's swelling ratio and water uptake are 24.3% and 50.8%, respectively, indicating the sandwiched PEM's exceptional dimensional stability. The polymers' outstanding performance suggests that the PI/SPEEK membrane, with its balanced proton conductivity, stability, and durability, is a viable option for commercial PEM. Other applications for the sandwich-structure membrane concept include gas separation membranes and vanadium redox flow batteries.

Chitosan is another promising membrane with excellent hydrophilicity and strong chemical resistance. Hidayati et al. [83] recommended combining SPEEK with the natural polymer chitosan. SPEEK has been used to remove hydroxyl and amine groups from chitosan that has strong conductivity and low methanol permeability. In comparison to pristine chitosan, the SPEEK/Chitosan composite membrane demonstrated improved methanol permeability of $2.46 \times 10^{-6}$ $cm^2.s^{-1}$ at normal temperature. High proton conductivity is the result of higher SPEEK/Chitosan IEC values. According to reports, SPEEK/Chitosan exhibited inconsistent results for DMFC, suggesting that further study is necessary.

## 2.6. Modification of SPEEK membranes with inorganic materials

SPEEK polymer modification with inorganic components such as silica, clays, metal oxides, HPA, carbon nanotubes, and others is currently being explored for fuel cell applications. The addition of inorganic compounds to PEMs has been shown to improve proton conductivity, mechanical strength, and composite membrane durability [84]. Inorganic components can prevent methanol crossover and excessive water swelling while also improving the mechanical and thermal properties of composites [85]. These subtopics will go over a variety of SPEEK additions, including graphene, silica, metal oxides, heteropolyacids (HPAs), carbon nanotubes, metal organic frameworks (MOFs), and clay. Table 2.1 shows the influence of various additives on the SPEEK matrix, as well as their impact on SPEEK performance with an emphasis on fuel cells.

**Table 2. 1:** The influence of different additives on the SPEEK polymer matrix

| Additive Type | Temperature (°C) | IEC (meq g $^{-1}$) | Water Uptake (%) | Proton conductivity (S cm$^{-1}$) | Power density (mW cm$^{-2}$) | Ref |
|---|---|---|---|---|---|---|
| **$SiO_2$@CNT** | 25 | - | 43 | 4.1x10$^{-2}$ | - | [86] |
| **SWCNT-fly ash** | 90 | 1.59 | 27.3 | 3.4x10$^{-2}$ | 672 | [87] |
| **SsCNT-5** | 90 | 2.19 | 43.85 | 4.31x10$^{-2}$ | - | [88] |
| **CCNF** | 80 | - | 32.3 | 5.6x10$^{-2}$ | - | [89] |
| **β-CD-DHNTS/HPW** | - | 1.04 | 30 | 9.0x10$^{-2}$ | - | [90] |
| **Cs-HPAs** | 80 | - | 40 | 2.25x10$^{-3}$ | 247 | [91] |
| **Pt-$Cs_{2.5}H_{0.5}PW_{12}O_{40}$** | 60 | 1.96 | 46 | 6.82x10$^{-2}$ | - | [92] |
| **PEOS/PWA/$SiO_2$** | 100 | - | - | 6.25x10$^{-3}$ | 25 | [93] |
| **Cs-TPA** | 80 | 1.5 | 37 | 1.3x10$^{-1}$ | - | [94] |
| **Pd-GO-L-Tyr** | - | 2.05 | 50.6 | 2.56x10$^{-3}$ | - | [129] |
| **PANI-GO** | - | 1.83 | 40 | 8.4x10$^{-3}$ | 13.51 | [96] |
| **SPBI/PrSGO** | 90 | 2.02 | - | 1.7x10$^{-1}$ | 820 | [97] |
| **SPVdF-HFP-$SiO_2$** | 90 | 1.83 | 36.5 | 7.9x10$^{-2}$ | 110 | [98] |
| **HPW@KMSNs** | 60 | - | 31.5 | 2.43x10$^{-1}$ | - | [99] |
| **PVA/TEOS** | 80 | 2.02 | 76 | 8.1x10$^{-2}$ | 336 | [100] |
| **IL/SHMO** | 200 | - | - | 4.6x10$^{-3}$ | - | [86] |
| **Bentonite/clesite30** | 80 | - | 18.4 | 1.24x10-$^{5}$ | - | [101] |
| **fGO/halloysite** | - | 0.35 |  | 4.7x10$^{-4}$ | 72.2 | [102] |
| **$SiO_2$-montmorillonite** | 100 | - | 25 | 1.58x10$^{-1}$ |  | [103] |
| **$BaZro_3$** | 90 | 1.96 | 41.5 | 3.12x10$^{-1}$ | 183 | [104] |
| **Al-$CeZrO_4$/HPW** | 80 | 1.65 | 8.1 | 1.3x10$^{-3}$ | 1001 | [105] |
| **NBO** | 90 | 1.80 | 38.4 | 2.9x10$^{-2}$ | 601 | [106] |
| **ZCO** | 90 | 1.46 | 20.3 | 2.0x10$^{-2}$ | - | [107] |
| **HPW@ML** | 60 | 1.54 | 50 | 1.36x10$^{-1}$ | - | [108] |
| **MOF-C-$SO_3H$** | 80 | 1.63 | 28.7 | 1.1x10$^{-1}$ | 82 | [109] |
| **Co-MOF-74/[$IM_2$][$H_2PO_4$]** | 120 | 6.5 | 90 | 2.6x10-$^{2}$ | - | [110] |
| **Cu-MOF** | 80 | 2.46 | 36.7 | 7.1x10$^{-2}$ | - | [111] |
| **ZIF-8/CNT** | 120 | 1.48 | 40.2 | 5.0x10$^{-2}$ | - | 112] |
| **ZIF-67** | 120 | 0.3 | 40 | 1.4x10$^{-2}$ | 28 | [113] |

### 2.6.1 Carbon nanotubes as fillers for SPEEK membrane

Carbon nanotubes (CNTs) are one-dimensional tubular-like hexagonal graphene sheets produced by sp2 bonding between carbon atoms. CNTs have extraordinarily high mechanical properties because to their bonding structure, which is stronger than the sp3 bonds found in diamonds. CNTs can be either single walled (SWCNT) or multiwalled (MWCNT), with diameters ranging from 1 nm to more than 100 nm, as illustrated in Fig. 2.14. The electrical conductivity of CNTs is significantly affected by the graphene sheet's rolling-up direction. This is because the chirality vector describes the hexagonal lattice of carbon atoms. However, because to their larger surface flaws and poorer electrical conductivity, MWCNTs are preferred over SWCNTs for usage in PEM [114]. Carbon nanotubes (CNTs) have gained a lot of attention as a reinforcing material for polymers because of its stiffness, low density, high aspect ratio, optical characteristics, and extraordinary tensile strength of around 63 GPa, which is 50 times stronger than steel [115].

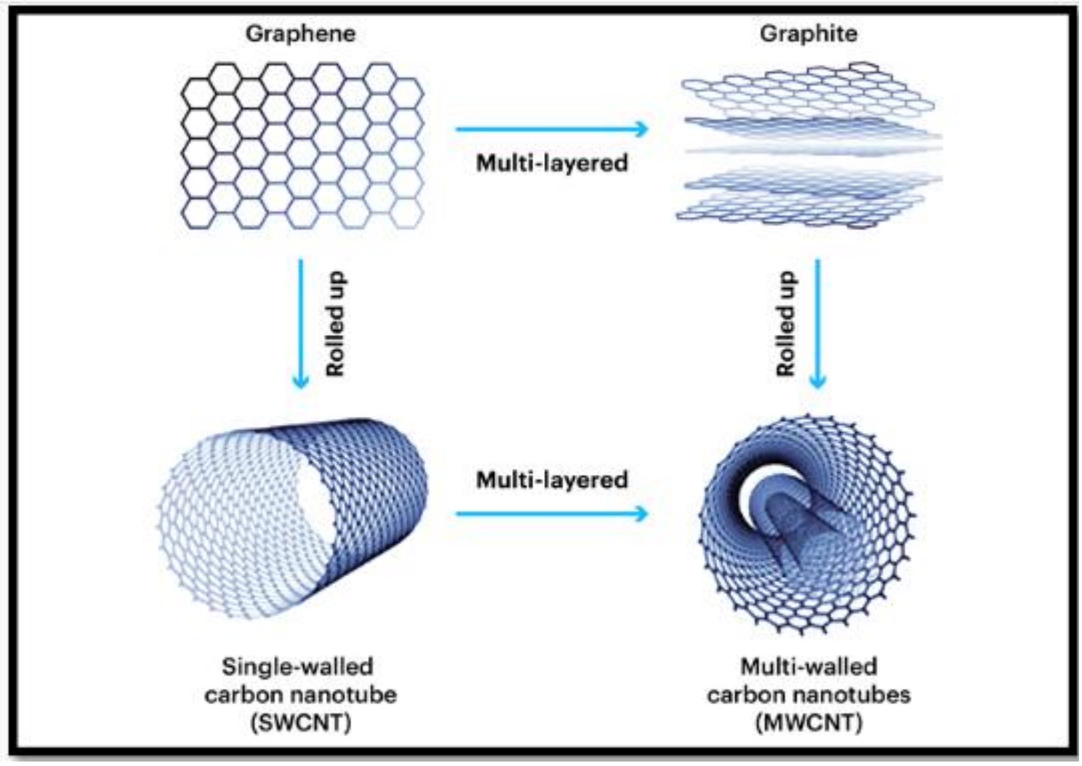

**Fig. 2. 14:** Single walled and multiwalled carbon nanotubes [115].

Carbon nanotubes (CNTs) are a cutting-edge nanomaterial used in the creation of high-performance polymer composites. SPEEK has recently used carbon nanotubes as fillers to overcome DS-dependent difficulties. Nonetheless, CNTs have a detrimental impact on proton conductivity since they are an electron conductor rather than a proton conductor, and this may offer a considerable risk of short-circuiting on PEMs in fuel cells. Cui et al. [86] effectively produced silica-coated CNTs ($SiO_2$:CNTs) using a simple sol-gel process and then utilized them as a novel component to SPEEK-based composite membranes, which benefit from silica's remarkable water retention and electronic shield capabilities. Not only did the hydrophilic and insulated silica coating on the CNTs' surface prevent short circuiting, but it also improved the CNTs' interfacial interaction with the SPEEK matrix, resulting in uniform dispersion. Additionally, compared to the pure SPEEK membrane (3.42 x $10^{-7}cm^2.s^{-1}$), the methanol permeability of the SPEEK/SiO:CNT composite membrane with a $SiO_2$:CNT loading of 5% was almost an order of magnitude lower at 4.22 x 10-8 $cm^2.s^{-1}$. The conductivity of protons was still more than $10^{-2}$ S.cm 1 at normal temperature. SPEEK/$SiO_2$:CNT membranes can be employed as high-performance PEMs in direct methanol fuel cells, as shown by the obtained results.

Sivasubramanian et al. [87] successfully synthesised Sulfonated poly (ether ether ketone) (SPEEK-based polymer nanocomposite membranes that incorporated single-walled carbon nanotubes (SWCNTs) and fly ash as inorganic fillers using the solution casting method. The degree of sulfonation in the poly(ether ether ketone) was evaluated using proton nuclear magnetic resonance spectroscopy and was found to be 64%. The researchers investigated and analysed the physicochemical characteristics of the produced membranes and their potential applications in fuel cells. At 90°C, the SP-CNT-FA-8 membrane exhibited the highest proton conductivity at 3.4 x $10^{-2}$ S $cm^{-1}$, compared to the pristine membrane, which had a conductivity of 3.1 x $10^{-2}$ S $cm^{-1}$. In addition to their favourable proton conductivity, the electrolyte membranes also demonstrated remarkable thermal and mechanical stability. These findings suggest that the composite membranes utilizing SPEEK, SWCNTs, and fly ash could be promising options for electrolyte membranes in fuel cell applications.

Gahlot et al. [88] employed solution casting to produce functionalized carbon nanotubes (f-CNT) that are electrically aligned with SPEEK. CNTs were functionalized by carboxylation and sulfonation. During the membrane's drying process, the CNTs were aligned with a continuous electric field of 500 $V.cm^{-1}$. The proton conductivity and methanol crossover resistance were measured at temperatures ranging from 30 °C to 90 °C to establish their suitability for direct methanol fuel cell applications. According to the findings, adding aligned carbon nanotubes (CNTs) reduces methanol permeability while boosting ion exchange capacity, water retention, and proton conductivity. The SsCNT-5 nanohybrid PEM had the highest proton conductivity (4.31 x $10^{-2}$ S.cm$^{-1}$), and it was more resistant to methanol crossover. The storage modulus rose proportionally to the concentration of s-CNTs in the SPEEK matrix (Fig. 2.15). The S-sCNT-5 membrane had the greatest modulus value of 2503 MPa, about 2.4 times greater than the SPEEK membrane. The increased storage modulus of S-sCNT membranes suggests strong bonding due to the existence of a common sulfonic acid group in CNT and PEEK, as well as the effect of an electric field on CNT alignment in the SPEEK matrix. The electrically oriented functionalized CNT/SPEEK membranes performed better than the randomly aligned composite membranes.

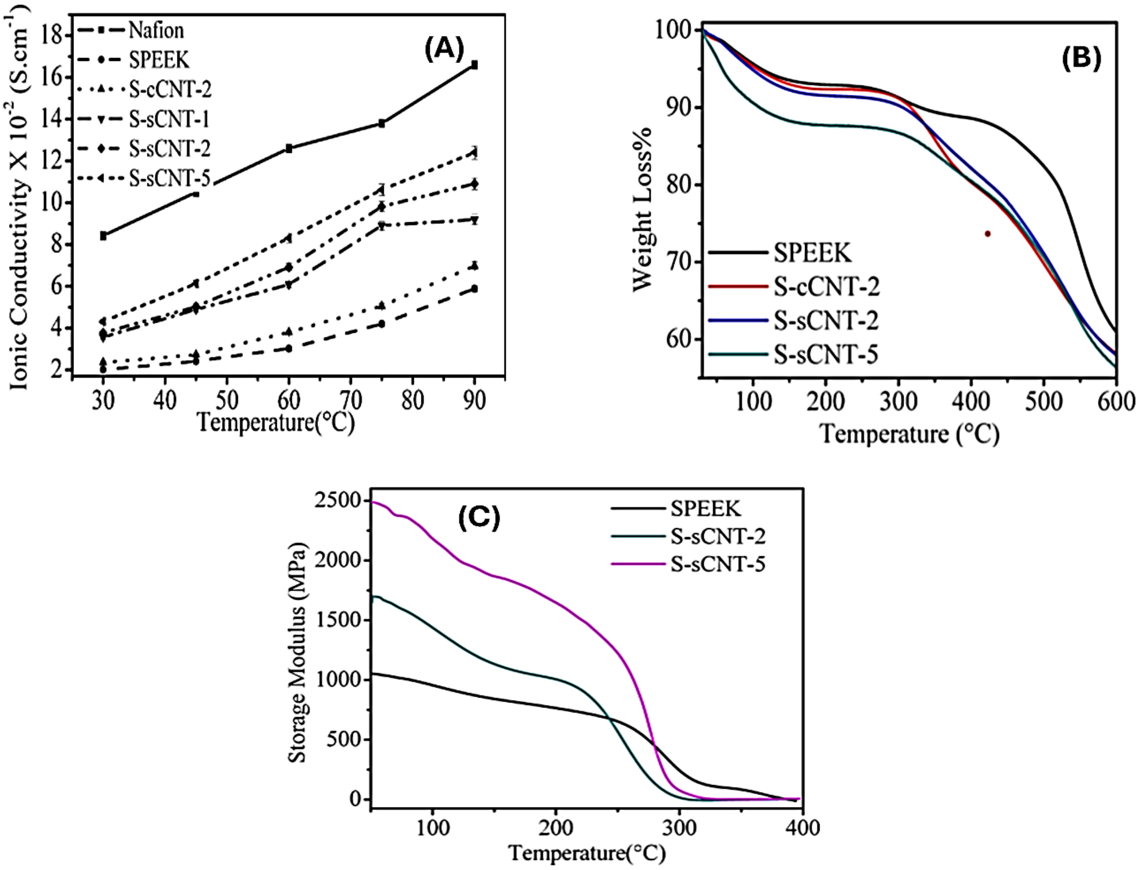

**Fig. 2. 15:** (a) Proton conductivity vs temperature (b) TGA thermographs and (c) DMA of SPEEK, S-sCNT-2, and S-sCNT-5 membranes [88].

Zhao Guodong et al. [89] created a PEM-compatible composite membrane by integrating continuous carbon nanofibers (CCNFs) into SPEEK. The CCNFs were equally distributed in an electrolyte polymer membrane after being easily mixed with the SPEEK matrix. The analysis of the composite membranes reveals that all dense composite membranes have low methanol permeability, strong proton conductivity, good mechanical performance, and great water swelling. The composite membrane with 0.51 weight percent (wt.%) CCNFs was fully hydrated and had a proton conductivity of 0.056 $S.cm^{-1}$ at room temperature. Furthermore, the hybrid membrane with 2.52 weight percent CCNFs showed 1.5 times the relative selectivity of a pure SPEEK membrane. These findings demonstrated that polyelectrolyte membranes for fuel cells with CCNF support (SPEEK) are a promising option.

### 2.6.2. Heteropolyacids (HPAs) as fillers for SPEEK membrane

HPAs are crystalline inorganic materials that are both thermally stable and extremely conductive. HPAs salts are made of MOx polyhedral, where M represents polyatoms such as Molybdenum (Mo), Niobium (Nb), Tantalum (Ta),Tungsten (W), and Vanadium (V), and x represents heteroatoms such as Iron (Fe), Phosphorus (P), Silicon (Si), and Cobalt (Co) through an oxygen-atom coordination bridge [115]. They are often identified by Wells-Dawson, Keggin, or lacunar structural arrangements (Fig. 2.16). By varying the core metal ion and addenda atoms, new salts with distinct structures and properties can be produced. HPAs are soluble in polar solvents, forming the Keggin structure ($XM_{12}O_{40}$), a heteropolyacid anion structure with a condensation ratio of 1:12. The huge size of the polyanion causes a low delocalized charge density, which accounts for HPAs' high acidity. HPAs are used for a variety of applications, including chemical analysis, ion selective membranes, sensors, chemical cleansers, catalysts, and additives in fuel cell component materials. Phosphotungstic acid (PWA) is a viable inorganic addition for PEM composites because of its strong proton conductivity and thermal stability.

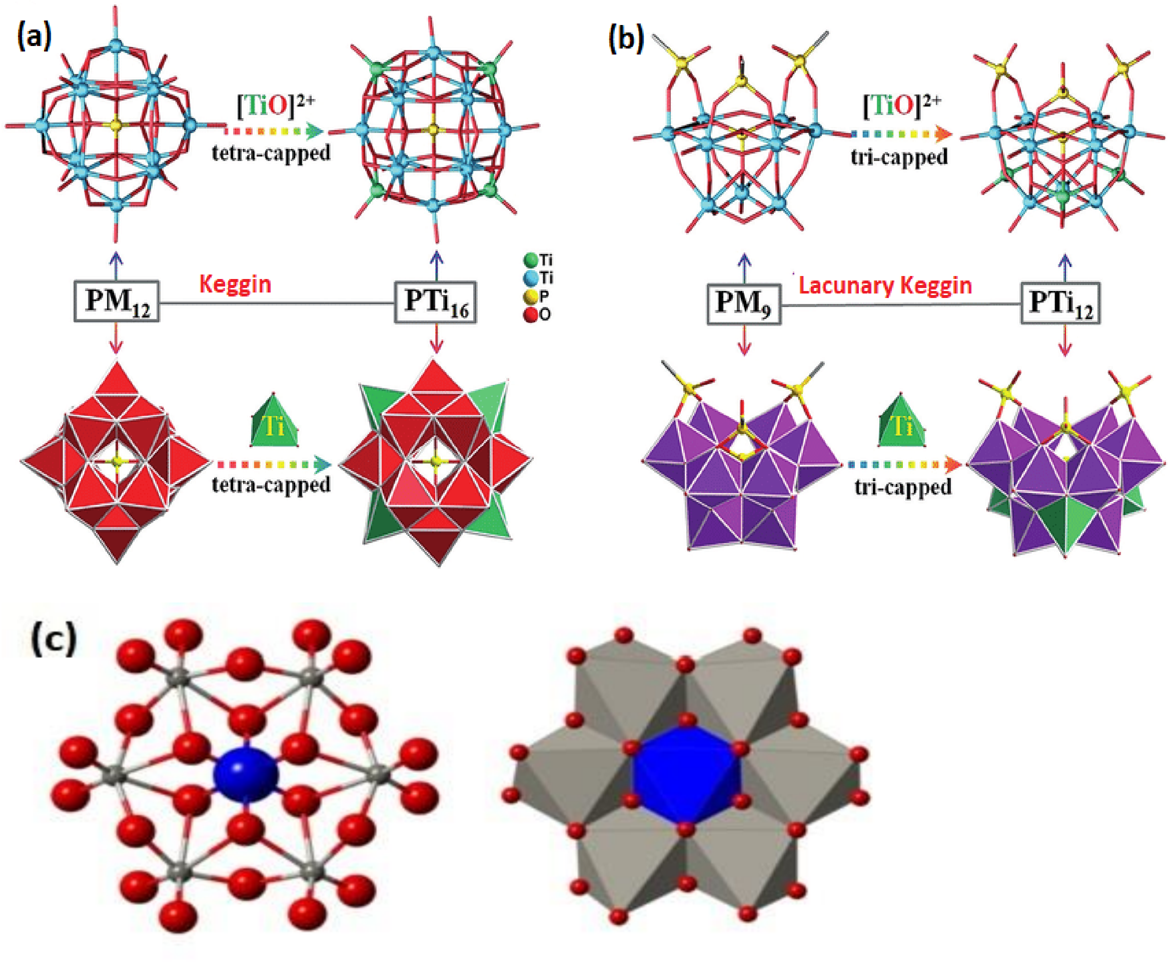

**Fig. 2. 16:** Structures of (a) Keggin,(b) Lacunary Kegging [116][88] and (c) Wells-Dowson [117].

HPA can be partly substituted with cesium (CsHPA) to improve its surface acidity [118].[89]. This substitution can improve interaction with the polymer matrix by decreasing salt solubility in water while increasing surface area. Silica-based salts improve the membrane's conductivity and mechanical qualities. Metal oxides (silica, titania), functional metal oxides [119] clay [120], aluminium phosphate (ALP) [121] , and zeolites [122] have been used to modify the SPEEK membrane as a water retainer.

Using polydopamine coating, He et al. [90] effectively added cyclodextrin (-CD) to halloysite nanotubes (HNTs) to create water-insoluble -CD-DHNTs. Traditional solution casting was then used to create SPEEK/-CD-DHNTs/HPW composite membranes. It has been observed that the hydrogen bonding complexation between $[PW_{12}O_{40}]^{3-}$ and β-CD caused both HPW and β-CD-DHNTs to be evenly distributed in the SPEEK matrix. The proton conductivity of the SPEEK/β-CD-DHNTs/HPW composite membranes rose as the HPW concentration increased (0.090 S cm$^{-1}$), increasing by up to 120% in comparison to the SPEEK membrane. Oh et al. [91] created composite membranes by adding Cs-HPAs to the SPEEK matrix. These membranes showed the highest power density values (245 and 247 mW/cm$^{2}$) and increased conductivity of about 2.25 x 10$^{-3}$ S cm$^{-1}$ at 80 °C under 80% RH. Zhang et al. [123] and Peighambardoust et al. [92] achieved essentially identical findings when $Cs_{2.5}H_{0.5}PW_{12}O_{40}$ was embedded on Pt in a SPEEK matrix. Zhang et al. measured a proton conductivity of 5.3 x 10$^{-2}$ S cm$^{-1}$ at 60 °C and 100% relative humidity, although Peighambardoust et al. measured roughly 6.82 x 10$^{-2}$ S cm$^{-1}$, which is estimated to be greater than Nafion 117. Colicchio et al. [93] studied SPEEK, polyethoxysiloxane (PEOS), and PWA ($H_3PW_{12}O_{40}$) with 20% silica ($SiO_2$). According to the data, this combination's proton conductivity is twice that of pure SPEEK at 90% relative humidity and 100 °C. Overall, the HPA-modified SPEEK membranes demonstrated greater stability and increased proton conductivity (6.25 x 10$^{-3}$ S.cm$^{-1}$) than the normal SPEEK membrane (2.21 x 10$^{-3}$ S.cm$^{-1}$). As a result of their superior proton conductivity and long-term stability, HPA/SPEEK composite membranes are promising candidates for replacing Nafion-based membranes in PEM fuel cells.

Dogan et al. [94] developed cesium salt of tungstophosphoric acid (Cs-TPA) particles by mixing aqueous solutions of tungstophosphoric acid and cesium hydroxide, as well as combining Cs-TPA particles with sulfonated polyether ether ketone (SPEEK). They investigated the impact of Cs-TPA on SPEEK membranes, focusing on the sulfonation degrees of SPEEK and the concentration of Cs-TPA. The performance of the composite membranes was evaluated based on several factors, including water uptake, ion exchange capacity, proton conductivity, chemical stability, hydrolytic stability, thermal stability, and methanol permeability. It was found that the Cs-TPA particles tended to aggregate as the sulfonation degree of SPEEK increased from 60% to 70%. Specifically, the SPEEK (DS: 60%)/Cs-TPA membrane with a 10% Cs-TPA concentration exhibited a reduced methanol permeability of $4.7 \times 10^{-7}$ cm$^{2}\cdot$s$^{-1}$. At a temperature of 80 °C and a relative humidity of 100%, the membrane achieved an acceptable proton conductivity of $1.3 \times 10^{-1}$ S cm$^{-1}$. The authors also noted that weight loss at 900 °C increased with the addition of inorganic particles, which was expected. Moreover, the inclusion of Cs-TPA particles in the SPEEK/Cs-TPA-based composite membranes enhanced their hydrolytic stability. The study revealed that the

SPEEK60/Cs-TPA composite membranes exhibited greater hydrolytic stability compared to the SPEEK70/Cs-TPA composite membranes. Additionally, the SPEEK60 composite membranes demonstrated lower permeability values for methanol, water vapor, and hydrogen in comparison to Nafion.

### 2.6.3. Graphene as fillers for SPEEK membrane

Graphene, a two-dimensional carbon sheet, has captivated the world with its remarkable chemical, physical, and thermal properties, paving the way for a wide range of applications [114]. One of its most significant uses is as an electrode material in various electrochemical applications, thanks to its large surface area, which is highly valued in energy storage systems. Graphene is a carbon allotrope characterized by a honeycomb lattice of sp2-hybridized monolayers [124] When compared to graphite and carbon nanotubes (CNTs), graphene boasts a larger surface area of 2629 $m^2$/g, while CNTs have a surface area of 1315 $m^2$/g. This makes graphene a fundamental building block for graphitic materials [125] Additionally, graphene exhibits excellent electronic properties, including a half-integral quantum Hall effect, even at room temperature [126, 127]. . Graphene was first isolated from graphite using a simple scotch tape method and garnered the Nobel Prize in 2010 for its discovery [128]. Since then, many researchers have redirected their focus toward graphene, particularly in the synthesis, functionalization, and application of this material in various electrochemical devices, such as fuel cells, solar cells, batteries, and ultra-capacitors.

Das et al. [95] synthesised solution-cast palladium graphite oxide-grafted amino acid nanocomposites (Pd-GO-L-Tyr) in sulfonated poly(ether ether ketone) (SPEEK). The composite membrane exhibited enhanced proton conductivity compared to the pristine SPEEK membrane due to its increased hydrophilicity, improved surface wettability, and greater ion exchange capacity, which are attributed to the higher presence of hydroxy and carboxyl groups. The SPEEK/Pd-GO-L-Tyr membrane achieved a high proton conductivity of 2.56 mS.$cm^{-1}$ and demonstrated low methanol crossover, resulting in significantly higher selectivity ($5.57 \times 10^{-3}$ S $cm^{-3}$ $s^{-1}$) compared to the SPEEK membrane ($4.8 \times 10^{2}$ S $cm^{-3}$ $s^{-1}$) and Nafion 117 membranes ($2.78 \times 10^{3}$ S $cm^{-3}$ $s^{-1}$). Additionally, incorporating Pd-GO-L-Tyr into the SPEEK membrane matrix created a physical barrier that effectively prevented methanol crossover. Based on these factors, the authors concluded that the composite membranes (Pd-GO-L-Tyr-

SPEEK) are better candidates for direct methanol fuel cell (DMFC) applications compared to standard Nafion 117 membranes. Graphene oxide (GO) and conductive polyaniline decorated graphene oxide (PANI-GO) were synthesized by Yogarathinam et al. [96] and applied to a sulfonated poly(ether ketone) (SPEEK) nanocomposite membrane in order to reduce methanol crossover. Analysis of surface morphology and crystallinity confirmed that PANI-coated GO nanostructures had formed (Fig. 2.17).

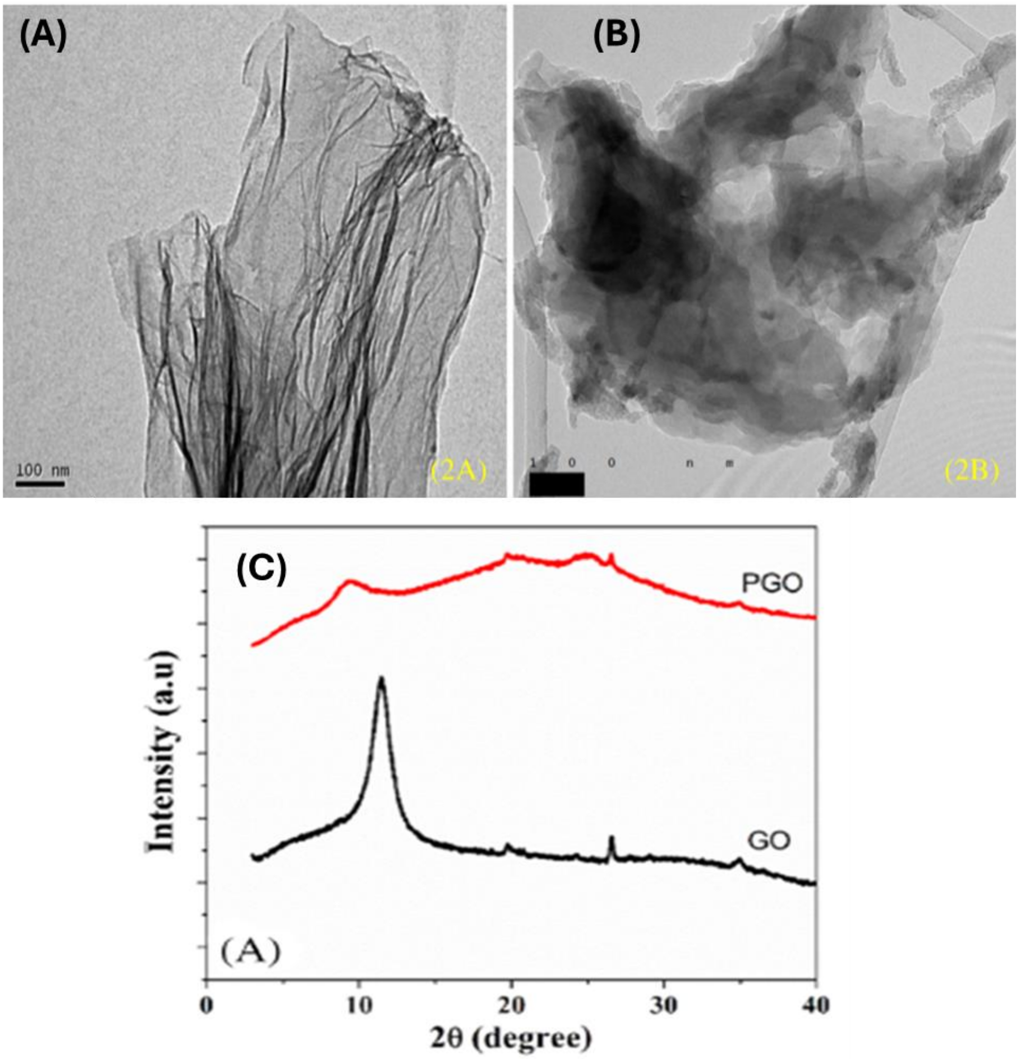

**Fig. 2. 17:** (A) Transmission electron microscopy (TEM) morphology of GO, (B) TEM morphology of PANI-GO nanocomposites and (C) X-ray diffractometer (XRD) patterns of GO and PANI-GO nanocomposites [96].

The analysis of membrane topography and morphology verified that PANI-GO and GO were evenly distributed across the surface of the SPEEK membrane. With a water uptake of 40% and an ion exchange capacity of 1.74 meq $g^{-1}$, the 0.1 wt.% PANI-GO modified SPEEK nanocomposite membrane demonstrated the highest performance. The nanocomposite membranes' oxidative stability was also improved. The modified SPEEK membrane containing 0.1 wt.% PANI-GO exhibited a lower methanol permeability of 4.33 x 10-7 $cm^2$ $.s^{-1}$. The incorporation of acidic and hydrophilic groups from PANI and GO enhanced the proton conductivity of the PANI-GO modified SPEEK membrane. Additionally, the selectivity of the PANI-GO modified SPEEK membrane was measured at $1.94 \times 10^4$ S $cm^{-3}$. $s^{-1}$. Overall, the PANI-GO modified SPEEK membrane shows promise as a potential material for direct methanol fuel cell (DMFC) applications. Maiti et al. [97] developed a unique technique for advancing proton exchange membranes by adding propylsulfonic acid-functionalized graphene oxide in crosslinked acid-base polymer blends, as well as its applicability in fuel cells. Different PrSGO loadings were used in the molecular dynamics (MD) simulations of the SPEEK/SPBI, XSPEEK/SPBI, and cross-linked SPEEK/SPBI composite systems. After increasing the amount of SPBI and PrSGO filler in the polymer matrix and cross-linking the polymer composites, the glass transition temperature (Tg) was raised. It was also found that the mechanical, chemical, and thermal stability of the XSPEEK/SPBI/PrSGO nanocomposite membranes increased dramatically with an increase in PrSGO loading, due to the strong interfacial connection between PrSGO and the XSPEEK/SPBI matrix. The proton conductivity of the XSPEEK/SPBI/PrSGO nanocomposite membrane increased dramatically to 0.17 $S.cm^{-1}$ at 4 weight percent PrSGO loading at 100% relative humidity (RH) and 90°C. Furthermore, at 100% RH and 80 °C, the XSPEEK/SPBI/PrSGO nanocomposite membrane showed exceptional fuel cell (FC) performance, with a maximum power density of 0.82 W.cm $^2$. Because of the hygroscopic nature of PRs GO, the authors noticed a higher number of sulfonic acid groups and a good interaction between the acid functionalized fillers and the cross-linked SPEEK/SPBI matrix. The addition of PrSGO nanofillers to the polymer matrix improved the membranes' overall performance as well as other essential features such as proton conductivity.

### 2.6.4. Silica as fillers for SPEEK membrane

The widespread research on silica-based nanoparticles is due to their inexpensive cost, superior mechanical and water retention qualities. However, because to their low organic compatibility and non-conductive qualities, $SiO_2$ particles clump in the polymeric matrix, reducing PEM conductivity [130]. Higher silica loading in the membrane causes considerable dilution of the membrane's ion-exchangeable groups [131]. As a result, as the concentration of pure silica increases, the membrane's ion exchange capacity diminishes [132]. However, various experiments have been carried out to increase membrane IEC by functionalizing silica filler with sulfonic group derivatives. Optimal silica loading increases membrane strength [133]. Higher silica content in the matrix, on the other hand, has a negative impact on the mechanical characteristics of the polymer because it causes more filler-filler to contact than filler-polymer interaction, destroying membrane homogeneity and causing the membrane to become brittle. As a result, a perfect combination of inorganic material and membrane can produce nanocomposites with enhanced mechanical properties [134]. Using the solvent cast process, Martina et al. [98] produced sulfonated silica (S-$SiO_2$) nanoparticles that were mixed with sulfonated poly (ether ketone) (SPEEK) and sulfonated poly (vinylidene fluoride-co-hexafluoropropylene) (SPVdF-HFP). They asserted that the mechanical, IEC, and water-uptake characteristics of SPEEK were enhanced by the addition of S-$SiO_2$. Maximum proton conductivity and current density were $7.9 \times 10^{-2}$ $S.cm^{-1}$ and 354 mA $cm^{-2}$, respectively, at 90 °C and 100% relative humidity using sulfonated silica with an 80-weight percent SPEEK-20 weight percent SPVdF-HFP nanocomposite membrane. Because S-$SiO_2$ is present, the proton conductivity is increased. The hydrophilic nature causes the membrane to enlarge and encourages the ion channels, which improves proton conductivity.

Meng et al. [99] studied how amino-modified mesoporous silica nanospheres influenced the characteristics of SPEEK/phosphotungstic acid (HPW). They claim that, while immobilizing acids is problematic, adding acid proton carriers to a polymer matrix is an effective way for enhancing proton conductivity. They found that incorporating aminated mesoporous silica nanoparticles (K-MSNs) and HPW into SPEEK improved proton conductivity and dimensional stability. The composite membrane's proton conductivity was 243 mS/cm at 60 °C and 1 weight percent K-MSN loading, suggesting that SPEEK/HPW/K-MSNs composite membranes have a lot of promise for use in methanol fuel cells. Tetraethyl orthosilicate (TEOS), PVA, and SPEEK were used to create a blending polymer by Sahin et al. [100]. In order to improve proton transport and oxidative and hydrolytic stability when TEOS is added, the author showed how adding PVA could increase the number of modifiable groups. The author's findings corroborated this conclusion, demonstrating that the SPEEK/PVA/TEOS blend performed better in terms of oxidative and hydrolytic stability than the other samples (pure SPEEK, PVA, and SPEEK/PVA composite). Water resistivity was enhanced by the addition of TEOS, which also decreased the quantity of -OH groups and boosted hydrolytic stability. Furthermore, the membrane exhibits superior cell performance metrics in contrast to Nafion 117. The results show the membranes' potential as PEMFC application candidates.

In a study conducted by Li et al. [86] composite membranes were successfully synthesized by incorporating ionic liquid (IL) into a sulfonated hollow mesoporous organosilica (sHMO) within a SPEEK polymer backbone. The research involved a comparative analysis of various SPEEK/IL/sHMO composites with different weight percentages (x) of 2.5, 5.0, 7.5, and 10 wt.%, alongside SPEEK/IL/HMO. The authors reported that the SPEEK/IL-30/sHMO-7.5 membrane exhibited a conductivity of 1.13 mS/cm at 200 °C, which is double that of the SPEEK/IL-30/HMO-7.5 membrane, which had a conductivity of 0.60 mS/cm under the same conditions.

### 2.6.5. Clay as fillers for SPEEK membrane

Clay is a commonly used nanofiller in various applications. Both natural and synthetic clays, including talc, mica, layered double hydroxide (LDH), laponite (LAP), sodium aluminosilicate (SAP), and montmorillonite (MMT), serve this purpose. The structures of laponite clay, layered double hydroxide, and montmorillonite are illustrated in Fig. 2.18 [135]. Among these, montmorillonite (MMT), with the chemical formula $(Na,Ca)_{0.33}(AlMg)_2(Si_4O_{10})(OH)_2nH_2O$, has garnered significant attention and is widely used as a nanofiller in many applications, including fuel cells. MMT is a cation clay that features a 2:1 crystal structure composed of one layer of octahedral aluminium hydroxide or magnesium hydroxide sheets, along with two interconnected tetrahedral silicon oxide sheets. Layered double hydroxide (LDH) consists of a positively charged brucite-type metal hydroxide sheet, with various anions and water molecules located in the galleries to balance the charge [136]. In addition to LDH, laponite (LAP) is another component of synthetic clay belonging to the 2:1 phyllosilicate structural group. LAP, with the chemical formula $Na_{0.7}(Si_8Mg_{5.5}Li_{0.3})O_{20}(OH)_4$, has a structure and composition similar to that of natural clay hectorite minerals [135]. It comprises octahedral magnesium oxide and two parallel sheets of tetrahedral silica, forming two-dimensional layers. A single layer of LAP has a diameter of 25 nm and a thickness of 1 nm, featuring positive charges on the edges and negative charges on the faces. Clay is abundant in nature and can be synthesized easily. It possesses a high ion-exchange capacity, chemical stability, and favourable rheological properties. The thin platelet structure of clay contributes to its high aspect ratio [137]. Due to its unique morphology, size, structure, and ionic nature, clay nanofiller demonstrates exceptional performance as an electrolyte, particularly in composite membranes for fuel cells.

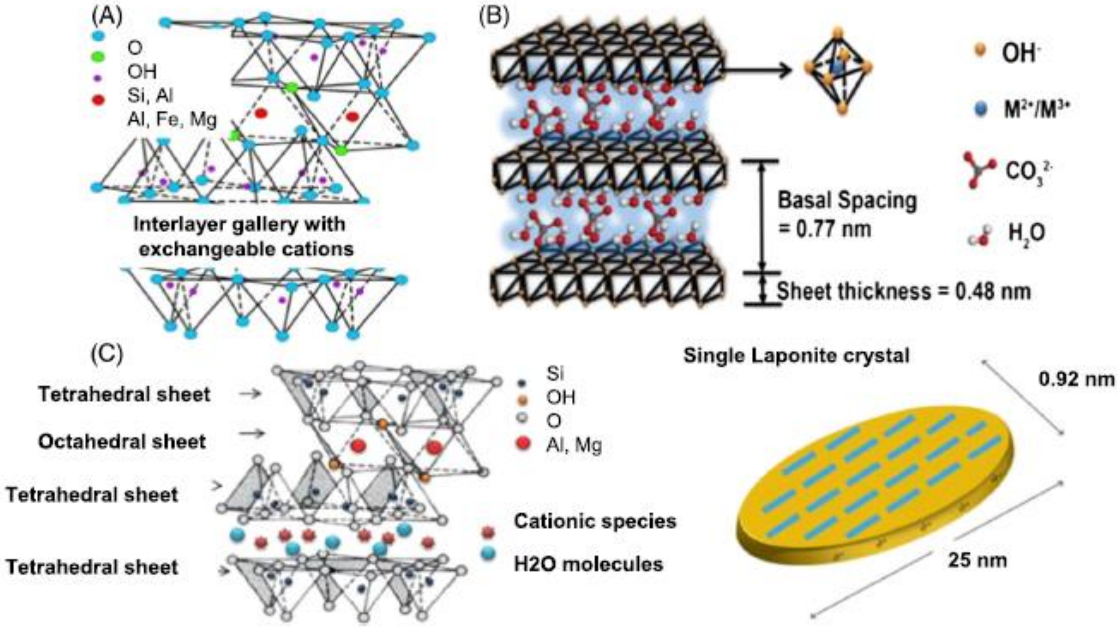

**Fig. 2. 18:** Structures of (A) montmorillonite (MMT), (B) layered double hydroxides (LDH), and (C) laponite (LAP) clays with single laponite crystal [135].

He et al. [138] compared the performance of unmodified clays ($CH_3(CH_2)17N(CH_3)_2^+$) (OC) and I.44P ($Na^+$ montmorillonite changed by I.24TL ($Na^+$ montmorillonite modified by $HOOC(CH_2)17NH_3^+$) (HC)) with that of unmodified clays ($Na^+$ montmorillonite) (IC). When less than 10 wt.% of HC is loaded, SPEEK/HC membrane performs better overall than all other SPEEK/clay composite membrane types and attains higher selectivity than pure SPEEK membrane. Proton conductivity and methanol permeability have been found to be enhanced by these SPEEK/HC composite membranes. Combining the HC carboxylic acid group improved dispersibility because of increased proton conductivity and HC bonding between membrane ion groups without sacrificing membrane stability. When the amount of filler in SPEEK/IC and SPEEK/OC hybrid membranes increases, proton conductivity also decreases. Kumar et al. [101] developed sulfonated polyether ether ketone (SPEEK) composites using bentonite and Cloisite 30B nanoclays. They observed an enhanced glass transition temperature and a change in membrane morphology in the pristine SPEEK membrane (Fig. 2.19), indicating the presence of nanoclays. However, compared to the pristine membrane, the addition of 0.5 weight percent of bentonite and Cloisite to SPEEK resulted in decreased proton conductivity and water uptake. The authors suggested that this decline could be attributed to blocked ionic micro-structure channels caused by the nanoclay particles, which reduce the presence of ion exchange carriers. The incorporation of Cloisite and bentonite into the SPEEK polymer matrix limits the available nanometric channels for the migration of polar molecules, such as hydrogen ions and water. Additionally, the increased rigidity of the Cloisite and bentonite layers complicates proton transport, which contributes to the decreased conductivity. Gokulakrishnan et al. [102] synthesised membranes of functionalized graphene oxide (f-GO) nanocomposites with varying concentrations of halloysite nanoclay using the dry phase inversion method. Their study found that the sulfonic acid group in SPEEK and the silane functionalization of graphene oxide led to an increase in ion exchange capacity from 0.22 to 0.35 meq/g, enhancing proton conductivity. In comparison, the pure SPEEK membrane exhibited a proton conductivity of 0.31 mS $cm^{-1}$ and a power density of 28 mW $cm^{-2}$.

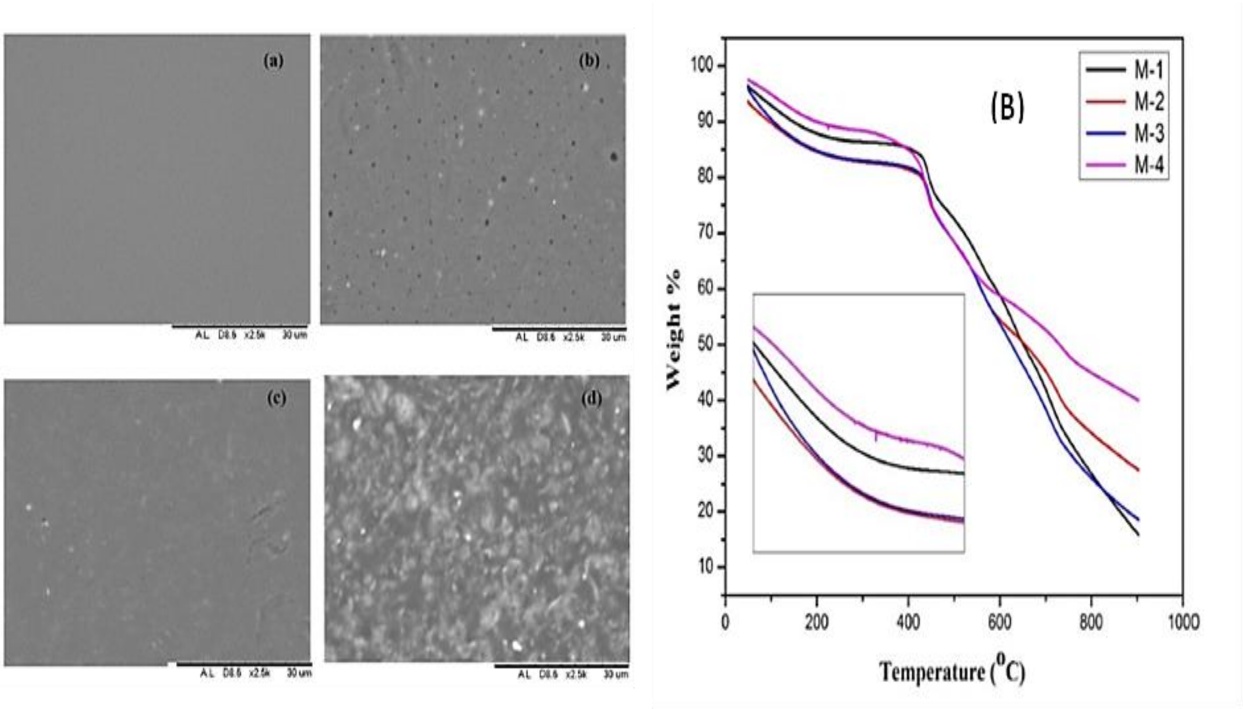

**Fig. 2. 19:** SEM images of various membranes: (a) SPEEK, (b) SPEEK/bentonite, (c) SPEEK/cloisite and (d)SPEEK/bentonite/cloisite, (B) TGA thermograms of SPEEK 1), SPEEK/cloisite (M-2), SPEEK/bentonite(M-3) and SPEEK/cloisite/bentonite (M-4) [101].

Conversely, the composite membrane containing 3 wt.% halloysite nanoclay and 2 wt.% f-GO achieved values of 0.47 mS cm$^{-1}$ and 72.2 mW cm$^{-2}$. The membranes comprising 2 wt.% f-GO and 3 wt.% halloysite with SPEEK showed improved proton conductivity, making them significant for direct methanol fuel cell (DMFC) applications. Charradi et al. [103] employed a porous $SiO_2$-montmorillonite heterostructured material filled with delaminated clay particles and a synthetic Mg-Al layered double hydroxide (LDH) swapped with sulphate anions to build composite membranes with varying nanofiller contents. The resulting composite electrolyte membranes seem to have better water retention and thermal stability when Mg-Al LDH and $SiO_2$-montmorillonite fillers are added to the SPEEK. Si-montmorillonite had a greater proton conductivity (0.158 S.cm$^{-1}$) at 120°C and 100% relative humidity than both Mg-Al LDH and plain SPEEK (0.070 and 0.023 S.cm$^{-1}$, respectively). Fuel cell membrane performance at high temperatures may be enhanced as a result.

### 2.6.6. Metal Oxide as fillers for SPEEK membrane

Interfacial interactions between membranes and catalysts, which are essential components of Membrane Electrode Assemblies (MEAs), play a crucial role in the effective operation of fuel cells. These interactions are strongly associated with the structures of both the catalysts and the membranes, as well as with the methods used to prepare the MEA [138]. Metal oxides, including $ZrO_2$, $SiO_2$, $Al_2O_3$, and $TiO_2$, are categorized into various types, each possessing distinct properties. The conductivity of protons in the membrane is often enhanced when metal oxides are added as additives in composite polymers for several reasons:

1. The presence of defects at the interface occurs when metal oxides occupy the polymer matrix, leading to the formation of distance charge sheets.
2. Metal oxide nanofillers are particularly effective in amorphous conditions, as they promote proton transport and increase the free volume within the polymer matrix.
3. There is an increase in ion dissociation within the polymer electrolyte membrane.

However, the water intake and conductivity of Proton Exchange Membranes (PEMs) are influenced by the properties and interactions of various metal oxides, such as strontium cerate, silica, titania, zeolite, and zirconia. Due to their large aspect ratio and surface area, metal oxide nanofibers are superior to other additives for improving composite materials. The addition of $Fe_3O_4$ to PEEK, SPEEK, SPES, and Nafion has been shown to enhance proton conductivity by facilitating efficient water hopping mechanisms. Additionally, molybdenum oxide ($MoO_3$) exhibits excellent conductivity and favorable physicochemical properties, making it a suitable choice for applications in energy-related fields.

Alumina, also known as aluminium oxide, is a widely used nanofiller in composite materials. Its chemical formula is $Al_2O_3$, and it can be sourced from various minerals, including bauxite, diaspore ($Al_2O_3H_2O$), and gibbsite ($Al_2O_{33}H_2O$) [139, 140]. Alumina can exist in different crystalline structures, but $Al_2O_3$ is the most thermodynamically stable form. Due to its large surface area and high catalytic activity, it serves as an effective nanofiller. Another metal oxide frequently utilized as a nanofiller in fuel cells is silicon oxide, commonly referred to as silica ($SiO_2$). There are several techniques employed to produce nanoparticle silica, including sol-gel processes, microemulsions, fuming, and precipitation. The hydrophilic properties of silica are attributed to the formation of siloxane and silanol groups on its surface, which contribute to its three-dimensional network structure. Surface-modified $SiO_2$, available in various forms such as mesopores, spheres, fibers, and rods, has been used as a nanofiller in fuel cell membranes. Common methods for producing silica/polymer composites include sol-gel processes, in situ polymerization, and simple blending. Among these, simple blending is the most popular technique due to its ease of controlling parameters like sonication time and temperature, which are essential for achieving high homogeneity in the polymer composite [141].

Selvakumar et al. [104] used the barium zirconate ($BaZrO_3$) solvent casting technique to generate sulfonation PEEK membranes. Adding 6 wt.% $BaZrO_3$ filler increased the polymer electrolyte's proton conductivity to $3.12 \times 10^{-1}$ $S.cm^{-1}$ at 90 °C. They discovered that the values of proton conductivity increase with rising temperature. Proton conduction occurs when $BaZrO_3$ nanoparticles dissolve protons from water in moist settings. The composite membrane has a current density of 280 mA $cm^{-2}$ and power density of 183 mW $cm^{-2}$. The author concluded that the 94 wt.% SPEEK/6 wt.% $BaZrO_3$ polymer composite membrane is a suitable alternative for PEM fuel cells.

Wang et al. [105] successfully synthesized a sulfonated poly(ether ether ketone) (SPEEK) nanocomposite membrane by incorporating phosphotungstic acid (HPW) and aluminium-doped cerium-based oxides (Al-$CeZrO_4$) into the SPEEK matrix. The inclusion of Al-$CeZrO_4$ boosted the chemical stability of the SPEEK membrane while retaining conductivity, while the addition of HPW increased proton conduction through acid-base interactions. The SPEEK/Al-$CeZrO_4$ nanocomposite membrane outperformed the SPEEK/HPW nanocomposite membrane in terms of proton conductivity by 15.5%. As a result, Al-$CeZrO_4$/HPW is thought to be a valuable inorganic nanofiller for improving the chemical stability and proton conductivity of SPEEK membranes, and further research into the hybrid composite membrane is warranted.

Gandhimathi et al. [106] produced sulfonated PEEK membranes by casting niobium oxide in a solution. With a high weight ratio of 10% niobium oxide (NBO) filler, the proton conductivity of the polymer electrolyte significantly increased to $2.9 \times 10^{-2}$ S $cm^{-1}$ at 90 °C, compared to $1.8 \times 10^{-2}$ S $cm^{-1}$ for the pure SPEEK membrane. Additionally, the thermal stability of the composite membranes was greatly enhanced by the incorporation of NBO. The SP-NBO-10 nanocomposite membrane achieved a maximum power density of 601 mW $cm^{-2}$, whereas the pristine membrane attained only 497 mW $cm^{-2}$. This increase in current density and power density of the composite membrane may be attributed to the vehicular proton transport mechanism of the sulfonic acid-based ionomeric membrane, which leads to the adsorption and retention of more water molecules. Based on the electrochemical results, the authors concluded that the SP-NBO-10 polymer composite membrane is a promising material for proton exchange membrane (PEM) fuel cell applications. Prathap et al. [107] successfully developed a new set of polymer composite membranes that used a linear sulfonated poly(ether ether ketone) (SPEEK) polymer and zinc cobalt oxide (ZCO) as an inorganic filler and were evaluated for fuel cells.

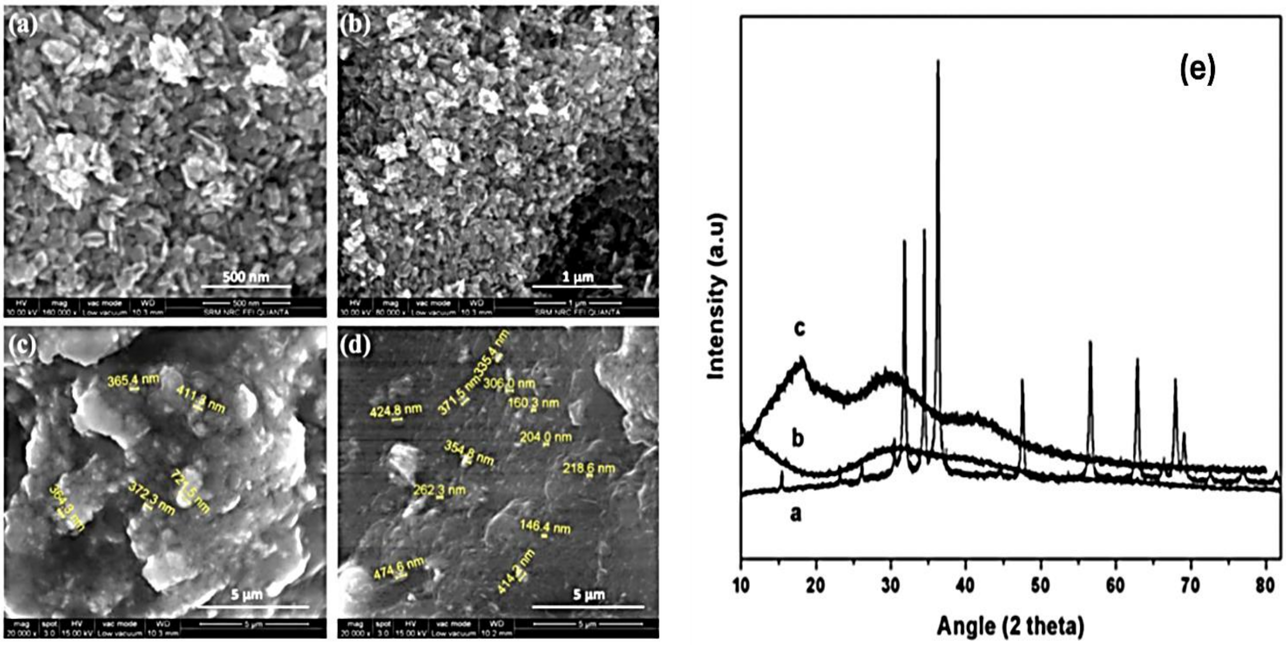

**Fig. 2. 20:** FESEM images of (a), (b) ZCO, (c) SP-ZCO-5, and (d) SP-ZCO-10, (e) XRD spectra of SPEEK and SP-SZO nanocomposites [107].

SPEEK was made by immediately sulfonating PEEK with strong sulfuric acid and then putting enough ZCO into it to make polymer composites. Proton nuclear magnetic resonance studies revealed a 55% sulfonation of SPEEK, whereas XRD and morphological analysis verified the successful incorporation of inorganic fillers into the polymer matrix, as shown in Fig. 2.20. Furthermore, the authors reported that the composite membranes loaded with 2.5 to 10 wt. % of ZCO displayed values in the range of 1.2 x $10^{-2}$–2 x $10^{-2}$ S $cm^{-1}$ at 30°C, whereas the pristine SPEEK membrane had a proton conductivity of 9 x $10^{-3}$ S $cm^{-1}$. The measured ion exchange capacities of the membranes ranged from 1.26 to 1.46 meq $g^{-1}$. Up to 370°C, the composite membranes showed exceptional thermal stability. The membranes developed in this study could therefore significantly aid in the development of novel proton conducting SP-ZCO composite membranes for application in PEM fuel cells.

### 2.6.7. Metal-organic frameworks (MOFs) as fillers for SPEEK membrane

Metal-organic frameworks (MOFs) are highly porous materials with variable pore size and chemical properties. They are formed by connecting metal ions or clusters with organic linkers. MOFs' organic linkers give higher loading than other additives because they are more compatible with organic polymers [142, 143]. The successful modulation of MOF composition and pore size can be accomplished by selecting the right precursors, adjusting synthesis parameters (reagent molar ratio, temperature, etc.), or performing post-synthesis chemical changes. MOFs' variable functionality, along with their large porosity and surface area, makes them ideal for applications that need interactions with guest species [144]. Zeolite imidazolate frameworks, or ZIFs, are an important subclass of metal-organic frameworks (MOFs) that provide high surface area and thermal stability because of their structural resemblance to zeolite and the structural diversity that MOFs offer through characteristics like chemical functionality and pore size tunability [147]. For small molecules, such as hydrogen, the huge internal cavities promote rapid diffusion, while the tiny pores at the entry provide a molecular sieve action [148, 149]. It has been demonstrated that a number of ZIF-polymer composite membranes comprising ZIF-7, ZIF-8, ZIF-22, ZIF-90, ZIF-100, and other components greatly enhance hydrogen separation; however, given its greater stability and superior resistance to acidic and alkaline environments, ZIF-8 has been successfully commercialized and is now widely used [150].

Zhang et al. [108] developed a membrane called SPEEK/HP-MIL by combining amino-modified chromium MIL-101 with heteropolyacid (HPW) to create nano-hybrid membranes for proton exchange membrane fuel cell (PEMFC) applications. The HPW was anchored using hydrogen bonds to reduce leakage and improve overall compatibility. As a result of the effective anchoring of MIL-101(Cr)-$NH_2$ on HPW and the formation of a hydrogen bond network with both HPW and SPEEK, the proton conductivity of the SPEEK/HPW-MIL composite membrane increased by 26%. Huang et al. created a sulfonated spindle-like carbon derived from a metal-organic framework, referred to as MOF-C-$SO_3$H, which was employed as a filler for the SPEEK membrane [109]. When 3 wt.% of MOF-C-$SO_3$H was added, the resulting MOF-C-$SO_3$H/SPEEK membrane exhibited enhanced properties as a proton exchange membrane (PEM) for direct methanol fuel cells (DMFCs). They found that the MOF-C-$SO_3H$/SPEEK membrane had higher proton conductivity and significantly lower methanol permeability compared to Nafion 115. The high performance of the MOF-C-$SO_3H$/SPEEK membrane was largely attributed to its unique porous and sulfonated carbon structures. The effective dispersion of MOF-C-$SO_3H$ within the SPEEK matrix reduced the membrane's methanol permeability and swelling ratio while simultaneously enhancing proton transport and improving proton conductivity. The authors reported a maximum power density of 83.91 mW $cm^2$, which is approximately 50% higher than that of Nafion 115. The superior stability of the MOF-C-$SO_3H$/SPEEK membrane, in contrast to Nafion 115, suggests that it is a viable option for use as a proton exchange membrane in fuel cells.

In a study conducted by Sun et al. [110], the researchers used the solution casting method to incorporate Co-MOF-74/phosphate-4-phenylimidazole into SPEEK ternary composite membranes, resulting in Co-MOF-74/[$IM_2$][$H_2PO_4$]/SPEEK membranes. They observed minor agglomeration on the surface of the Co-MOF-74/[$IM_2$][H2PO$_4$]/SPEEK composites. Scanning electron microscopy (SEM) revealed a gear-like structure in the cross-section of the prepared composite membrane, which correlated with increased Co-MOF-74 content. The metal-organic framework (MOF) effectively encapsulated the ionic liquid (IL) through hydrogen bonding, reducing IL loss and enhancing the proton conductivity of the Co-MOF-74/[$IM_2$][$H_2PO_4$]/SPEEK membrane. The study found that a loading of 2.5 wt.% Co-MOF-74/[$IM_2$][$H_2PO_4$]/SPEEK resulted in a proton conductivity increase of 25.96 $mS \cdot cm^{-1}$ at 120 °C, along with a decrease in the IL loss rate. It was further proposed that the Co-MOF-74/[$IM_2$][$H_2PO_4$]/SPEEK ternary composite membrane could operate at temperatures up to 320 °C. These findings suggest that encapsulating the IL within the MOF not only increases the proton conductivity but also enhances the thermal stability of the SPEEK membrane. Aparna et al. [111] fabricated Cu-MOF-anchored SPEEK and SPEEK/PI composite membranes for proton exchange membrane fuel cell (PEMFC) applications. This membrane exhibited high mechanical, thermal, and physicochemical properties. A 3 wt.% loading of Cu-MOF resulted in a maximum proton conductivity of 0.0711 S/cm, an ion exchange capacity (IEC) of 2.35 meq/g, and a water uptake of 38.18%. The experimental results demonstrated that these membranes serve as efficient proton exchange membranes for PEMFCs. Sun et al. also synthesized a novel two-dimensional (2D) zeolite structure, ZIF8/CNT hybrid crosslinked networks (ZCN), using an in-situ growth procedure, as shown in Fig. 2.21 [112]. The introduction of ZCN into the SPEEK matrix significantly improved proton conductivity while inhibiting methanol permeability. The proton conductivity of the SPEEK/ZCN composite membrane reached 50.24 mS/cm at 120 °C and 30% relative humidity, which was 11.2 times greater than that of the recast SPEEK membrane, which had a conductivity of 4.50 mS/cm under the same conditions. Furthermore, it was discovered that the proton conductivity of the membrane was greatly enhanced by the hybrid structure.

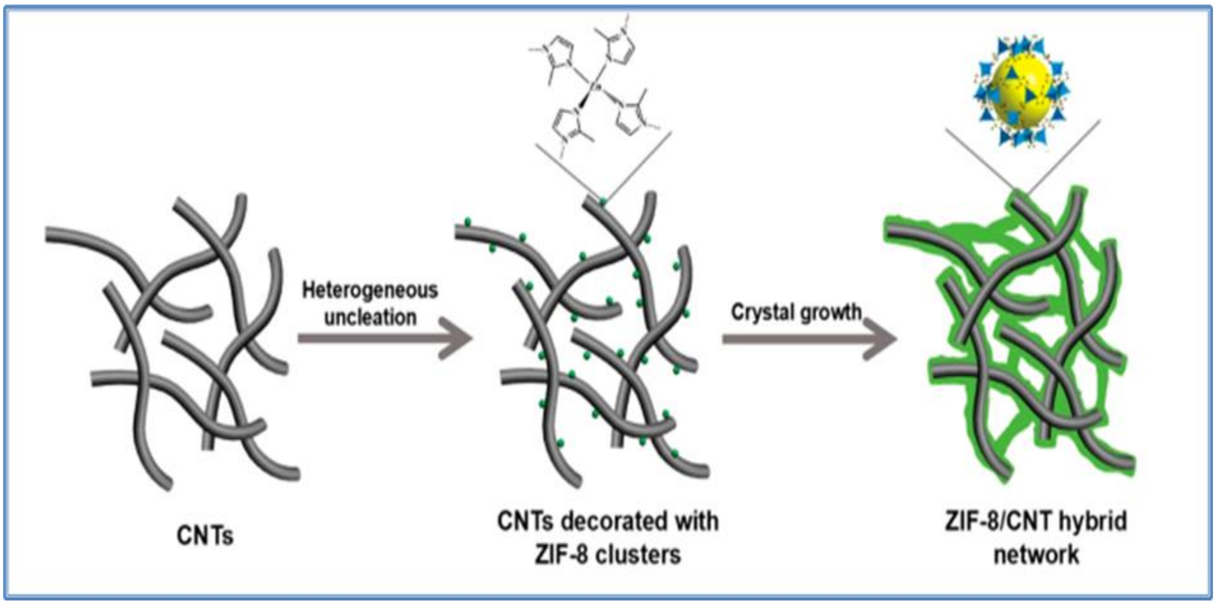

**Fig. 2. 21:** Schematic illustration of the synthesis process of ZCN through in situ growth procedure [112].

Barjola et al. [113] created nanocomposite membranes by casting a 1, 3, and 5 wt.% (SPEEK-Z1, SPEEK-Z3, and SPEEK-Z5) cobalt-based zeolitic imidazolate framework (ZIF-67) into a sulfonated poly(ether ketone) (SPEEK). The addition of 1 wt.% ZIF-67 to SPEEK improved both thermal stability and proton conductivity significantly. SPEEK-Z1 composite membrane had a proton conductivity of 0.014 S cm$^{-1}$. Despite promising results from Polymer Electrolyte Membrane Fuel Cells (PEMFC) performance trials at intermediate temperatures above 100 °C, the authors suggest that a rigorous optimization process is still required.

## 2.7. Conclusion and future perspectives

Undoubtedly, the expanding fuel cell market will serve as a strong catalyst for further investigation into non-fluorinated PEMs, which are less costly and outperform pricey Nafion membranes. Sulfonated poly (ether ketone)-based polymers may find application as fuel cell electrolyte membranes. The most recent developments in the design of several SPEEK-based electrolyte membranes for PEMFC and DMFC applications were reviewed in this review articleDespite their advantages, there are still some challenges associated with the use of SPEEK membranes in practical applications. These include: 1. SPEEK membranes cannot match the exceptional performance of the C-F chemical bonds found in PFSA membranes without modifications, 2. Higher degrees of sulfonation (DS) in SPEEK membranes often lead to excessive swelling and reduced thermal stability, although they enhance proton conductivity and 3. While cross-linked SPEEK membranes, formed through covalent bonds, can improve dimensional and chemical stability, they tend to decrease proton conductivity. To address these challenges, other polymers and fillers are being incorporated into the fabrication of SPEEK membranes. A key focus for future research will be to design and develop SPEEK membranes with an appropriate structure that effectively incorporates these additional materials. When compared to Nafion® membranes, SPEEK's organic-inorganic composite membranes present promising potential for superior performance. The inclusion of inorganic fillers may enhance the mechanical and electrical properties of the membranes, making them more suitable for fuel cell applications. Nonetheless, several issues still require further exploration:

a) To enhance the proton conduction mechanisms towards the hopping mechanism, it is essential to produce more hopping sites through the composite process. This improvement will increase methanol permeability and proton conductivity, especially at higher temperatures (preferably around 120 °C).
b) To strengthen the bond between the filler and the polymer, selecting the appropriate inorganic filler and modifying their interface is crucial.
c) Understanding the morphology and structure of polymer electrolyte membranes (PEMs) requires dynamic simulations that utilize mathematical models and computer software. This approach facilitates the design of modifications to sulfonated poly(ether ether ketone) (SPEEK) and inorganic fillers, as well as the optimization of their combinations.

The SPEEK composite membrane offers significant advantages, such as low methanol crossover and high proton exchange capability. Most SPEEK-related composite materials exhibit proton conductivity on the order of $10^{-2}$ S $cm^{-1}$, which is sufficient for use as membranes in hydrogen-oxygen fuel cells. This review also addresses the effects of various metal oxides on the SPEEK matrix, concluding that SPEEK-based membranes are among the best polymer electrolytes for proton exchange in fuel cells.

Further research is needed to select the right inorganic particles and to enhance the affinity of membranes towards water, thereby improving proton conductivity. Looking ahead to PEM development, it is unrealistic to expect that a single type of PEM will fulfil all requirements for a wide range of applications, including stationary, mobile, and automotive fuel cells. Research priorities will differ based on specific application goals; therefore, collaboration among specialists in various fields such as physics, electrochemistry, polymers, composite materials, and simulation will be essential. We hope this review provides a comprehensive overview of the advancements in SPEEK-based PEMs and offers suggestions for creating high-performing non-fluorinated PEMs in the future.

# PART II: Electrocatalysts for Hydrogen Evolution Reaction (HER)

## 2.8 Introduction

The ongoing and impending energy crisis, as well as the imminent threat posed by climate change, necessitate the world's reliance on alternative sources of sustainable and clean energy. Environmental difficulties caused by fossil fuels have sparked widespread concern, and numerous initiatives are currently ongoing to discover a cheap, carbon-free, and abundant energy substitute [145, 147]. Hydrogen energy is emerging as a key source of sustainable energy due to its efficiency in conserving energy and lowering pollution. Hydrogen fuel cell vehicles are a major application of this clean energy source, with hydrogen generation playing an important part in their uptake [148, 149]. Molecular hydrogen gas can be created by the electrochemical hydrogen evolution process (HER) in the presence of a catalyst using renewable energy sources such as solar energy, wind, geothermal heat, tides, biomass, and so on. It is the most cost-effective and efficient approach to produce high pure hydrogen in huge amounts [150].

Due to its great energy density and environmental friendliness, hydrogen has received a lot of attention as a potential renewable energy [151]. Platinum group metals (PGM) are known to be the most effective electrocatalysts for HER ($2H+ 2e^-= H_2$) [152, 153]. Metallic platinum (Pt) exhibits favourable activity for HER in acidic and alkaline environments [154], but its high cost and restricted availability necessitate the use of alternate and less expensive catalysts [155, 156]. In this context, it is critical to produce low-cost, high efficiency HER electrocatalysts for Pt replacement, and the purpose of this review is to summarize significant efforts in generating highly active and resistant HER without Pt for economic hydrogen production.

## 2.9 Fundamental mechanism for HER

The initial half-reaction of the electrochemical cell used to generate hydrogen in water electrolysis occurs at the cathode and involves the transfer of two electrons, which is highly reliant on environmental conditions, influencing the mechanism of HER. The HER response in acidic medium has three possible steps [156].

$$H^+ + e^- \longrightarrow H_{ad} \qquad \textbf{(2.4)}$$

$$H^+ + e^- + H_{ad} \rightarrow H_2 \tag{2.5}$$

$$2H_{ad} \rightarrow H_2 \tag{2.6}$$

$H_{ad}$ denotes adsorbed hydrogen atoms. The initial stage includes the Volmer process (2.4), which generates adsorbed hydrogen. The hydrogen evolution reaction can then proceed through the Heyrovsky step (2.5), the Tafel step (2.6), or a mix of the two to produce $H_2$ [157]. As shown in the equations, the HER reaction in alkaline conditions consists of two primary steps: the Volmer step (2.7) and the Heyrovsky step (2.8).

$$H_2O + e^- \rightarrow OH^- + H_{ad} \tag{2.7}$$

$$H_2O + e^- + H_{ad} \rightarrow OH^- + H_2 \tag{2.8}$$

HER is a two-step reaction in both processes, with the reaction rate determined by the Volmer step (adsorption) or the Heyrovsky/Tafel step (desorption). In particular, the pH of the electrolytes has a significant impact on the mechanism. In acidic solutions, proton adsorption and electrochemical conversion dominate reaction kinetics in the Volmer step; nonetheless, under neutral or alkaline circumstances, $H_2O$ dissociation and OH-desorption also play an important role in determining reaction kinetics. Furthermore, a Tafel slope is tightly linked to reaction kinetics and serves as a signal of the rate-determining step. The Tafel slopes of 120, 40, and 30 mV · dec-1 mirror the Volmer, Heyrovsky, and Tafel steps in particular. Interestingly, for a high hydrogen coverage over 0.6, 120 mV.dec$^{-1}$, the Tafel slope is also seen for the Heyrovsky step, indicating the potential and coverage dependence of the Tafel slope [158].

## 2.10 Catalysts for HER

The catalyst should exhibit high intrinsic activity for the hydrogen evolution reaction (HER), meaning it can effectively facilitate the splitting of water into hydrogen and oxygen. It should also have a low overpotential, which is the extra voltage required to drive the reaction compared to the thermodynamic potential. A lower overpotential indicates better energy efficiency [159, 160]. Additionally, the catalyst should support rapid reaction kinetics to ensure that the HER occurs at an adequate rate under practical operating conditions. Stability is essential for long-term performance in electrocatalysts [161]. The catalyst should remain stable under the acidic or alkaline conditions commonly used in electrochemical water splitting. To be considered high performing, an electrocatalyst must achieve a maximum current density and a minimal Tafel plot. Ideally, the catalyst should be made of abundant, low-cost materials to allow for widespread adoption and scalability. Additionally, the catalyst needs to have good electronic conductivity to effectively transfer electrons during the hydrogen evolution reaction (HER) [162]. [90]. A high surface area is important as it increases the number of catalytic active sites available for the reaction, thereby enhancing overall catalytic activity [163]. Some catalysts can demonstrate synergistic effects when composed of multiple components, leading to improved performance compared to individual components. By optimizing these characteristics, researchers aim to develop HER electrocatalysts that can efficiently and sustainably produce hydrogen for various applications, including renewable energy storage and fuel cell technology [164, 165].

Numerous methods are being developed to enhance the performance of noble-metal electrocatalysts, particularly platinum (Pt)-based catalysts, while also reducing costs. For example, alloying platinum with inexpensive transition metals can improve platinum utilization and create a synergistic effect that alters the electronic environment, thus enhancing catalytic activity [166,167]. Additionally, combining platinum with water-splitting promoters is an effective strategy to improve hydrogen evolution reaction (HER) activities in alkaline conditions, which has significant market applications. There has also been considerable interest in the development of non-noble metal HER electrocatalysts, primarily due to their low cost and abundance. In the following sections, we will first discuss selected examples of noble metal catalysts. Next, we will focus on various categories of non-noble metal-based electrocatalysts that have shown significant advancements in the field of electrocatalytic HER, including transition metal phosphides, transition metal carbides, and transition metal chalcogenides. Detailed descriptions of different types of HER electrocatalysts are provided below.

### 2.10.1 Platinum-based catalysts

Platinum group metals (PGMs), which include Platinum, Palladium, Ruthenium, Iridium, and Rhodium, are noble metals known for their exceptional catalytic activity in the hydrogen evolution reaction (HER). Platinum (Pt) is positioned at the peak of the volcanic curve shown in Fig. 2.22 [168].  PGMs excel as electrocatalysts for HER due to their efficiency. When combined, Platinum and HER exhibit a modest Tafel slope and an almost negligible onset overpotential, placing them near the volcano's peak [169, 170]. According to the Sabatier principle, Pt’s high effectiveness as a HER catalyst is attributed to its ideal conditions for hydrogen adsorption and desorption on its surface, which is reflected in its moderate metal-hydrogen bond strength. However, the cost and maintenance requirements of noble platinum catalysts limit their practical applications. To address this issue, earth-abundant electrocatalysts such as transition-metal nitrides, sulfides, and phosphides have shown significant potential as effective HER catalysts [171].

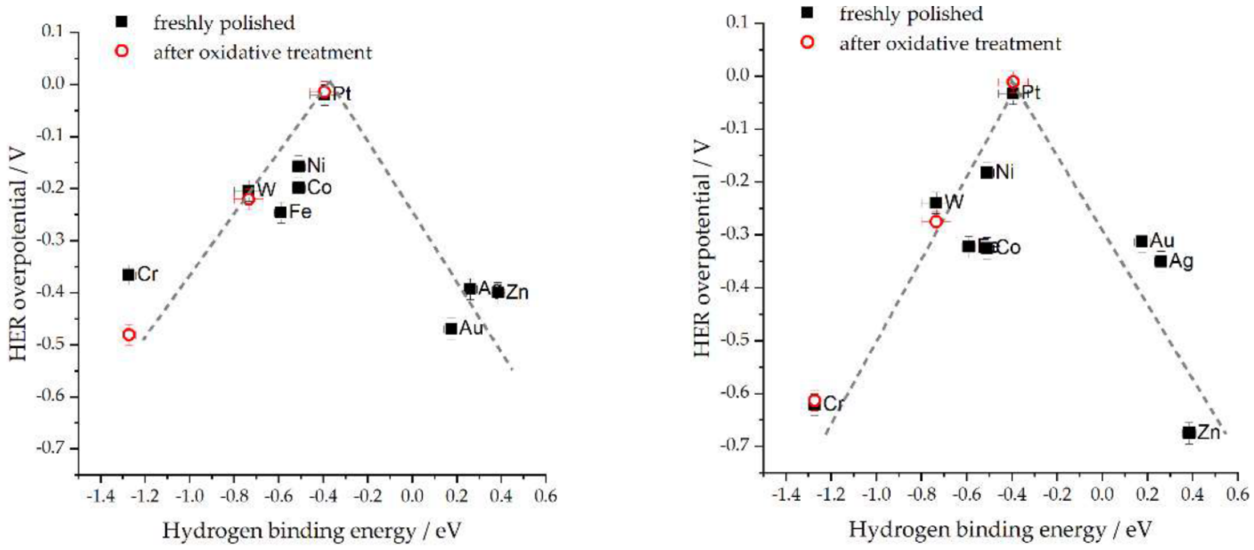

**Fig. 2. 22:** Hydrogen evolution reaction (HER) volcanoes in acid medium [168].

Currently, the most advanced hydrogen evolution reaction (HER) catalysts that demonstrate exceptional activity are based on platinum (Pt). However, since platinum is an expensive noble metal, research efforts have focused on reducing its loading capacity or enhancing its efficiency. This can be achieved by forming alloys with other elements, increasing the catalyst's exposed surface area, or by promoting the exposure of higher-index crystal planes [172, 173]. Forming stable Pt alloys with high HER performance can decrease the required amount of Pt while simultaneously improving its efficiency. Extensive research has been conducted on Pt alloys for HER performance, and platinum has been alloyed with various transition metals such as copper (Cu), cobalt (Co), nickel (Ni), and iron (Fe), as well as with other noble metals like ruthenium (Ru), rhodium (Rh), and iridium (Ir) [167,174, 175]. These modifications aim to optimize the strength of the Pt-H bond for HER by adjusting the d-band centre of platinum [176].

Chen et al. [177] combined solvothermal and high-temperature calcination techniques to create PtCo/PtSn heterojunction catalysts. XPS profiles indicated that PtCo and PtSn had electrical interactions on their heterogeneous crystalline surfaces (Figure 2a-b). DFT simulations show that the PtCo/PtSn heterojunction modulates the electronic structure of Pt surfaces, enhancing $H_2O$ dissociation capacity while decreasing Pt-Had bond strength. The ideal H* Gibbs free energy (ΔGH*) was achieved under these conditions (Figure 2c-d). PtCo/PtSn has high intrinsic activity and HER stability in alkaline electrolytes, resulting in the development of heterogeneous formations. The overpotential was 25 mV at 10 mA cm$^{-2}$, with a Tafel slope of 24 mV dec$^{-1}$. By leveraging the benefits of Pt-based alloys and heterojunctions, it is possible to efficiently tune the electronic structure of the Pt surface to reduce the d-band centre of Pt, increase electron transfer capability, and ultimately improve the intrinsic activity and stability of the catalyst. Sun et al. [178] grew a Ni nano sheet array coated with ultrafine Patni nanoparticles onto carbon cloth (PtNi-NiNA/CC) with a very low Pt loading concentration (7.7%) in situ and demonstrated improved HER activity with a very low overpotential of 38 mV than the Pt/C (20%). This growth was accomplished with a current density of 10 mA cm$^{-2}$ in 0.1 M KOH. A 90-h catalytic activity cycle test confirms its long-term effectiveness. The higher HER activity of PtNi-Ni NA/CC is rationally linked to Pt's centre of d-band down shift.

Cai et al. [179] used selective chemical etching and quick melting-quenching to create a highly active bifunctional np/$Pt_1Ru_1$–$Ni_{0.85}Se$ electrode. Single atoms of Pt and Ru were evenly co-embedded in a $Ni_{0.85}Se$ nanoporous structure. In situ Raman spectroscopy and DFT calculations show that the strong intracrystalline electronic metal-support interaction in the np/$Pt_1Ru_1$–$Ni_{0.85}Se$ electrode lowers the energy barrier for $H_2$ generation on Pt sites and water dissociation on Ru sites while increasing the charge density on Pt and Ru atoms. Additionally, the Pt-Ru dual atoms enhance the intrinsic activity of the np/$Pt_1Ru_1$–$Ni_{0.85}Se$ by activating the Ni sites in $Ni_{0.8}5Se$.

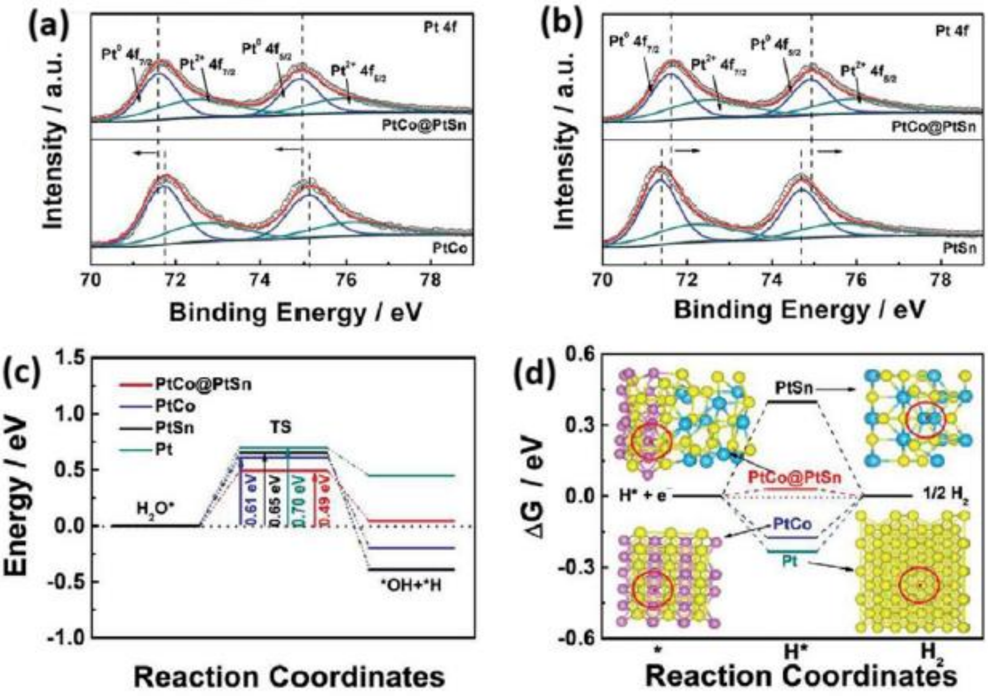

**Fig. 2. 23:** (a-b) XPS profiles of Pt 4f of PtCo/PtSn, PtCo, and PtSn. (c) Reaction energy diagram presenting the water dissociation process (d) ΔGH***** calculated at the adsorption sites for all catalysts [177].

## 2.10.2 Non-noble metal catalysts

The pursuit of efficient and cost-effective catalysts for the hydrogen evolution reaction (HER) is vital for advancing water electrolysis and facilitating the widespread adoption of hydrogen as a clean and sustainable energy source [180]. Although noble metals like platinum (Pt) and palladium (Pd) demonstrate outstanding HER performance, their scarcity and high prices create serious obstacles to large-scale use. This has sparked a significant interest in non-precious metal-based catalysts as viable alternatives. Transition metals such as iron (Fe), cobalt (Co), nickel (Ni), tungsten (W), and molybdenum (Mo) offer promising solutions due to their abundance in the earth's crust and greater affordability compared to their noble metal counterparts [181, 182]. Embracing these alternatives can pave the way for a more sustainable and economically viable hydrogen economy.

### 2.10.2.1 Iron (Fe) non-noble metal catalyst

The iron (Fe) atom is rich in d-band electrons, making it effective in modifying the electronic structure of parent catalysts. So far, most studies on Fe-doped, non-noble metal-based catalysts have concentrated on substituting Fe for substrate metal atoms like cobalt (Co) and nickel (Ni), which have similar electronic structures and atomic sizes. Typically, Fe doping is achieved by adding a specific amount of iron salt as a precursor during the synthesis process. Generally, the enhanced catalytic performance observed with Fe doping can be attributed to two main mechanisms: i) alterations in the local electronic structure that influence hydrogen adsorption free energy (ΔGH*), and ii) improvements in the electrical conductivity of the catalysts.

By computing the ΔGH* and the associated TOF values, Chan et al. [183] developed a number of models for doped transition metal phosphides (TMPs), such as CoP, $Fe_{0.25}Co_{0.75}P$, $Fe_{0.5}Co_{0.5}P$, $Fe_{0.75}Co_{0.25}P$, and so forth, in order to clarify the doping influence on the catalytic activity. The volcano plot's highest point was $Fe_{0.5}Co_{0.5}P$, which has been shown to have a catalytic capability comparable to Pt/C. This study demonstrated the TMP activity caused by various metallic dopants and offered a solid theoretical foundation for creating Fe-doped catalysts with high performance. The potential of Fe doped TMPs catalysts for high-performance HER catalysis is confirmed by the subsequent experimental studies [184, 185].

In another study, Yang et al. [186] found that introducing Fe into NiS nanosheets (β-INS) resulted in the creation of hexagonal α-INS with metallic properties and a change in the electronic structure of the active centres, causing $H_2$ molecules to preferentially form at the Fe sites. The Fe-doping and localized electronic structural modification reduced the energy barrier of the Heyrovsky step from 0.19 eV for NiS to 0.01 eV for α-INS, resulting in a significant increase in reaction rate. Yan et al. go on to show that Fe(III) doping in Fe-$NiS_2$ enhanced $NiS_2$'s electrical conductivity while simultaneously lowering the activation energy for hydrogen generation. Similarly, the Fe-$Co_9S_8$ nanosheet grown on carbon cloth (Fe-$Co_9S_8$ NSs/CC) benefited from the strong charge interplay caused by Fe doping. The Fe-$Co_9S_8$ NSs/CC demonstrated excellent catalytic performance throughout a wide pH range, with an overpotential as low as 83 mV required to obtain 10 mA $cm^{-2}$ and an effective specific double-layer capacitance, Cdl, of 373.19 mF $cm^{-2}$ achieved in 1.0 m KOH.

Based on the examples provided, it is clear that iron (Fe) doping can reduce the overpotential and enhance the durability of non-noble metal-based materials. This is achieved by modulating the hydrogen adsorption free energy, altering the local electronic structure, particularly around the active centres and improving the electrical conductivity of the catalysts. Despite the demonstrated effectiveness of Fe doping in certain non-noble metal-based hydrogen evolution reaction (HER) catalysts, there is still a lack of systematic studies exploring the relationships among doping levels, local doping structures, and catalytic performance. More comprehensive research in these areas is urgently needed. Additionally, while it is known that substrates or host materials, such as graphene, carbon nanotubes (CNTs), graphitic carbon nitride (g-$C_3N_4$), and metal-organic frameworks (MOFs), also influence the performance of Fe-doped catalysts, further investigation into how these substrates contribute to catalytic performance is necessary.

#### 2.10.2.2 Nickel (Ni) non-noble metal catalysts

Nickel's propensity to trigger HER in basic settings has been known for nearly a century. Numerous hypotheses with empirical results suggest that Nickel holds a significant HER interchange rate and the minimum energy content for adsorbed hydrogen (ΔGH*value) across numerous major elements.

Wang et al. [187] used a kinetically regulated selenium reaction to create Ni-doped $MoSe_2$ films with rough surfaces. The hydrogen binding energy at the Se-edge was significantly decreased upon the addition of Ni, rendering the Se-edge active for HER. As a result, the overpotential decreased by 30 mV in comparison to $MoSe_2$ due to the high density of active edge sites in Ni-$MoSe_2$. Ni doped $Mo_2C$ nanowire arrays supported on Ni foam were created by Xiong et al. [188] using a hydrothermal and post-carburization technique. In comparison to the undoped electrocatalysts, the Ni$Mo_2C$/NF provided a small Tafel slope (36.8 mV $dec^{-1}$) and a low onset potential (21 mV) in alkaline solution. According to DFT calculations, the addition of Ni to $Mo_2C$ caused the charge density to redistribute, hence lowering the |ΔGH*|. Wu et al. [189] presented an acid-etching approach for generating ultrathin $Ni(OH)_2$ nanosheets, followed by topotactic phase engineering to produce nonlayered NiSe nanosheets (Fig. 2.24a-b). The ultrathin structure's template effect resulted in the intact transformation of layered $Ni(OH)_2$ to nonlayered NiSe. The Rs and Rct values of the NiSe electrode are lower than those of $Ni(OH)_2$, showing that charge transfers quickly in NiSe. NiSe has a lower overpotential of 177 mV at 10 mA $cm^{-2}$ in basic medium than $Ni(OH)_2$ (278 mV), making it an effective HER catalyst. In a separate study, Xiang et al. [190] reported a one-step hydrothermal method for preparing $NiTe_x$ nanosheets, specifically NiTe, $Ni_{2.6}Te_2$, and $Ni_{2.86}Te_2$. The theoretical results indicated that the d-band centre of the nonstoichiometric $Ni_{2.86}Te_2$ approaches the Fermi level, which enhances the adsorption of hydrogen intermediates on the catalyst surface. Additionally, the electronic states near the Fermi level were significantly increased, indicating a higher charge carrier density, as well as improved charge transfer and conductivity of $Ni_{2.86}Te_2$ for hydrogen evolution reaction (HER). Furthermore, the Gibbs free energy change (ΔG H*) for $Ni_{2.86}Te_2$ was found to be 0.6 eV, which is lower than the 0.8 eV for NiTe. This suggests that $Ni_{2.86}Te_2$ can significantly enhance HER activity. When used as a HER catalyst, $Ni_{2.86}Te_2$ demonstrated excellent performance, with overpotentials of 166 mV and 253 mV required to achieve current densities of 10 mA/cm² and 100 mA/cm², respectively, in the presence of $H_2SO_4$. These overpotential values are lower than those of NiTe, which is 297 mV.

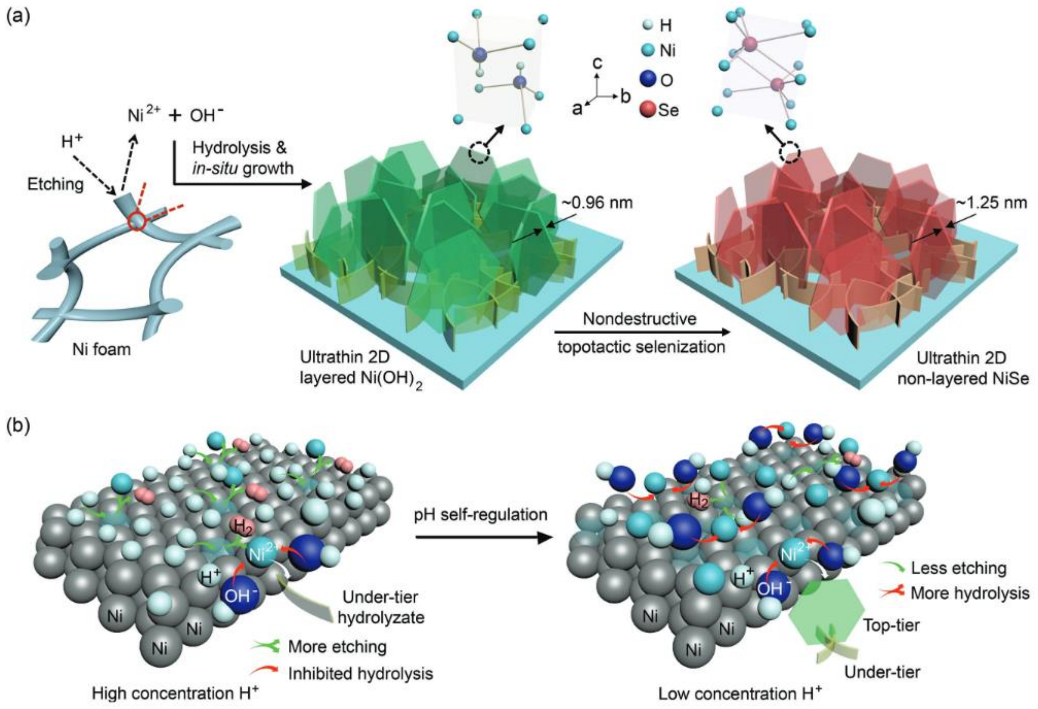

**Fig. 2. 24:** (a) Structural evolution of ultrathin 2D layered $Ni(OH)_2$ nanosheets and ultrathin 2D non-layered NiSe nanosheets through combinatorial acid etching and topotactic salinization, (b) Schematic illustration of two-tiered nanosheet formation via in situ self-regulating acid etching [189].

### 2.10.2.3 Cobalt (Co) non-noble catalysts

The cobalt (Co) element's moderate H-bonding energy has made it a viable HER catalyst. It is possible to effectively change the electronic structure of catalysts by introducing a trace amount of Co into their lattice [191]. A suitable doping level is beneficial to enhance intrinsic conductivity and lower ΔGH*, and the reported investigations showed that the catalytic performance is highly dependent on the Co doping levels. Co-doped non-noble metal-based catalysts' catalytic performance is heavily impacted by a number of other factors, including the substrates, coordination environments, and host catalysts. This section covers the impact of substrates on HER catalysis in particular, in addition to the improvement in catalytic performance brought about by the co-doping effect.

A potential class of HER catalysts are transition metal chalcogenides (TMCs), and co-doping has proven to be a successful tactic for boosting their catalytic activity. Wang et al. [192] developed a highly active and stable catalyst composed of cobalt-doped, earth-abundant iron pyrite ($FeS_2$) nanosheets hybridized with carbon nanotubes ($Fe_{1-x}Co_xS_2$/CNT hybrid catalysts) for hydrogen evolution reaction (HER) in acidic solutions. Electrochemical measurements demonstrated a low overpotential of approximately 0.12 V at a current density of 20 mA/cm², a small Tafel slope of about 46 mV/decade, and long-term durability over 40 hours of HER operation using bulk quantities of $Fe0.9Co_{0.1}S_2$/CNT hybrid catalysts at high loadings of around 7 mg/cm². Density functional theory calculations revealed that the high catalytic activity is primarily due to a significant reduction in the kinetic energy barrier for hydrogen atom adsorption on the $FeS_2$ surface when cobalt is doped into the iron pyrite structure. The enhanced HER catalytic activity of $Fe_{0.9}Co_{0.1}S_2$ is also attributed to the hybridization with carbon nanotubes, which facilitates strong heteroatomic interactions between the CNTs and $Fe_{0.9}Co_{0.1}S_2$. By employing controllable interface engineering and Co metal ions doped into $MoS_2$ nanosheets, Xu et al. [193] successfully demonstrated the synergistic regulations of both interface structural and electronic conductivity in their nanoflower-like Co–$MoS_2$/NiCoS structure supported on reduced graphene oxide (rGO), which was logically developed via a straightforward hydrothermal route. The interface coupling effect between $MoS_2$ and the Ni–Co–S phase, the 3D flower-like nanostructure with enormous active sites, and the ability of Co-doped $MoS_2$ to modify its surface electronic density are all attributed to this. The ideal Co–$MoS_2$/NiCoS/rGO hybrid has a low Tafel slope (46 mV $dec^{-1}$), a tiny overpotential (η10, 84 mV) at 10 mA $cm^{-2}$, and outstanding stability. It also shows great HER activity in 1.0 M KOH.

.These cases illustrate that co-doping is an effective method to enhance the hydrogen evolution reaction (HER) catalytic activity of non-noble metal-based catalysts by altering their electronic structure and increasing electrical conductivity. It's important to note that the choice of substrates plays a crucial role in improving catalytic activity alongside the co-dopants. Generally, substrates enhance catalytic activity in several ways:

a) They provide new nucleation sites and serve as nanostructure templates, helping to shape the catalysts into a highly active morphology.

b) They create additional strain or confinement effects that promote the growth of catalysts in an active non-equilibrium state.

c) They facilitate stronger heteroatomic interactions, which enhance charge and mass transfer around the active centers.

d) They maintain a more open structure that allows for easier access to reaction centers and faster diffusion of electrolytes.

e) They aid in the formation of interfacial defects and active centers.

f) They contribute additional stability and durability to the catalysts.

The effects of substrates are relevant to nearly all types of electrocatalysts and warrant comprehensive investigation in the near future.

#### 2.10.2.4 Molybdenum (Mo) non-noble catalysts

Mo is positioned on the right side of the curve in the volcano plots. The hydrogen adsorption energy can be modified by incorporating the Mo element into the lattice that includes the metal on the left side of the "volcano plots." In this context, a moderate metal-H bonding could be beneficial for the hydrogen evolution reaction (HER). It is crucial to consider the appropriate dosing of Mo during the catalyst design process, as the amount of Mo doping, similar to other non-noble metal dopants, significantly influences catalytic performance. Moreover, studies have shown that Mo doping notably alters the shape of the original catalyst, often resulting in a catalyst with a larger specific surface area [194] .However, if the Mo concentration is too high, phase separation will occur, compromising the activity. As a result, it is extremely difficult to precisely regulate the level of Mo doping while achieving uniform distribution and high concentration doping.

Using $MoO_3$/ZIF-67 as the precursor, Zhuo et al. [195] created CoP/$Mo_2C$-NC nanorods using a continuous calcination and phosphating procedure (Fig. 2.25a). The catalyst required only a 55.7 mV overpotential to achieve a current density of 10 mA $cm^{-2}$ (Fig. 2.25b). The electron transfer from Co to Mo via the Co-P-Mo link, which produced $Co^{3+}$ and $Mo^{2+}/Mo^{3+}$ active sites, is responsible for the high catalytic activity. Furthermore, the combination of CoP, $Mo_2C$, and N-doped carbon cloud effectively optimizes the ΔGH*, which is neither too high as for NC nor too low as for CoP and $Mo_2C$, achieving a balance for the adsorption/desorption of hydrogen, according to density functional theory (DFT) calculations. In another study, Huang et al. [196] created Ni-doped Ni-Mo-based sulfide (N-NiMoS) as chalcogenide systems and shown good HER performance. The N-NiMoS catalyst outperformed the Ni-NiS catalyst with a η of 68 mV at 10 mA/cm$^2$ and a Tafel slope of 86 mV/decade. Additionally, it demonstrated outstanding long-term stability for 1000 h. Instead of single metal sulfides, bimetal Ni-Mo based sulfides showed extensive interfaces formed by nickel sulfides (NiS and $NiS_2$) and molybdenum sulfides ($MoS_2$), which can serve as excellent active sites. Furthermore, it was confirmed that N doping in NiMoS improves electron transport and electrical conductivity by modifying electronic characteristics. The doping of molybdenum (Mo) can also be effective for other non-noble metal chalcogenides. Jaramillo et al. [197] introduced S to the surface of MoP via post-sulfidation of MoP at 400 °C under a 10:90% $H_2S$:$H_2$ gas mixture. The produced MoP|S largely reduced the overpotential of HER to 86 mV in 0.5 m $H_2SO_4$.

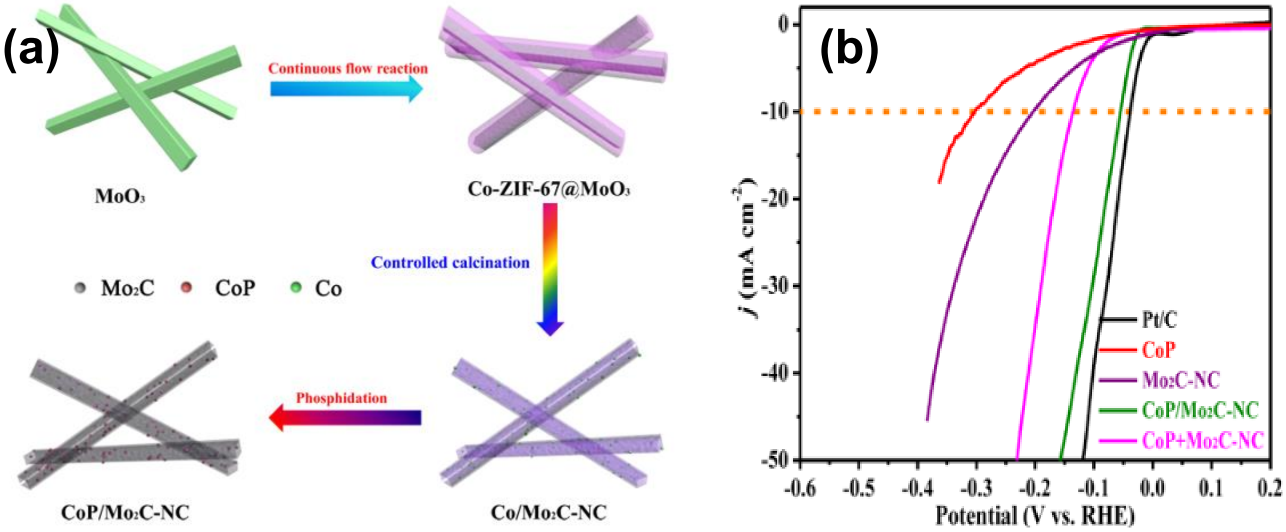

**Fig. 2. 25:** (a) fabrication of CoP/Mo2C-NC (Illustration), (b) CoP/Mo2C-NC HER polarization curves [195].

It was suggested that the implantation of S atoms obviously slows down the oxidation of MoP surface in air or during the catalytic process, thus ensuring the stability of the catalyst in an acid medium. S-doped $MoSe_2$ ultrathin nanosheets with more edge sites and rich plane defects were studied for HER. Owing to that S-doping increased unsaturated active sites and enhanced the electric conductivity, the S-$MoSe_2$

exhibited a much lower overpotential(156 mV at 30 mA cm$^{-2}$) than that for pristine $MoSe_2$.

#### 2.10.2.5 Tungsten (W) non-noble catalysts

W and its compounds share similar properties as Mo for HER. In addition, single-atom catalysts and atomic clusters have outstanding catalytic activity compared to their bulk counterpart [198]. Li et al. [199] developed a cobalt tungsten phosphide as an effective electrocatalyst for HER by creating hollow polyhedrons with a tuneable composition using the metal-organic frameworks (MOFs) template process. The as-prepared catalyst, which has a composition of Co0.9$W_{1.1}P_2$/C, was found to be able to achieve a current density of 10 mA cm$^{-2}$ at over potentials of 35 and 54 mV and in alkaline and acidic media, respectively. The surface W-doping enhances the free energy of hydrogen absorption and the kinetics and thermodynamic barriers for water dissociation, which, when combined with the hollow structure of Co-W phosphides, contributes to the remarkable HER catalytic efficiency. In a study conducted by Chen et al. [200]. Highly mesoporous tungsten phosphide was fabricated using a mesoporous model to create cationic tungsten positions within organized mesoporous tungsten phosphide (WP) nanostructures. The synthesized catalyst, referred to as WP-Mesoporous, demonstrated superior catalytic efficiency compared to catalysts without mesopores, attributed to the presence of tungsten vacancies and an ordered mesoporous structure. The WP-Mesoporous catalyst exhibited an overpotential of 229 mV in alkaline media and 175 mV in acidic media at a current density of 100 mA cm$^{-2}$, maintaining its performance for 48 hours without structural damage. Durability is a crucial factor when evaluating electrocatalyst performance, and after 48 hours, WP-Mesoporous showed improved stability compared to WP-Nano (Fig. 5a-b). In both alkaline and acidic environments, the WP-Mesoporous catalyst consistently generated hydrogen ($H_2$) at the same density for 48 hours, with only an 18 mV increase in applied bias in alkaline media and a 9 mV increase in acidic media. Remarkably, the polarization curves of the used WP-Mesoporous catalyst were nearly identical to those of the fresh catalyst, showing only a slight positive shift (Fig. 5c-d). The mesoporous structure and its crystallinity were preserved in both acidic and alkaline media after 48 hours, demonstrating the strong corrosion resistance and structural stability of the mesoporous catalyst.

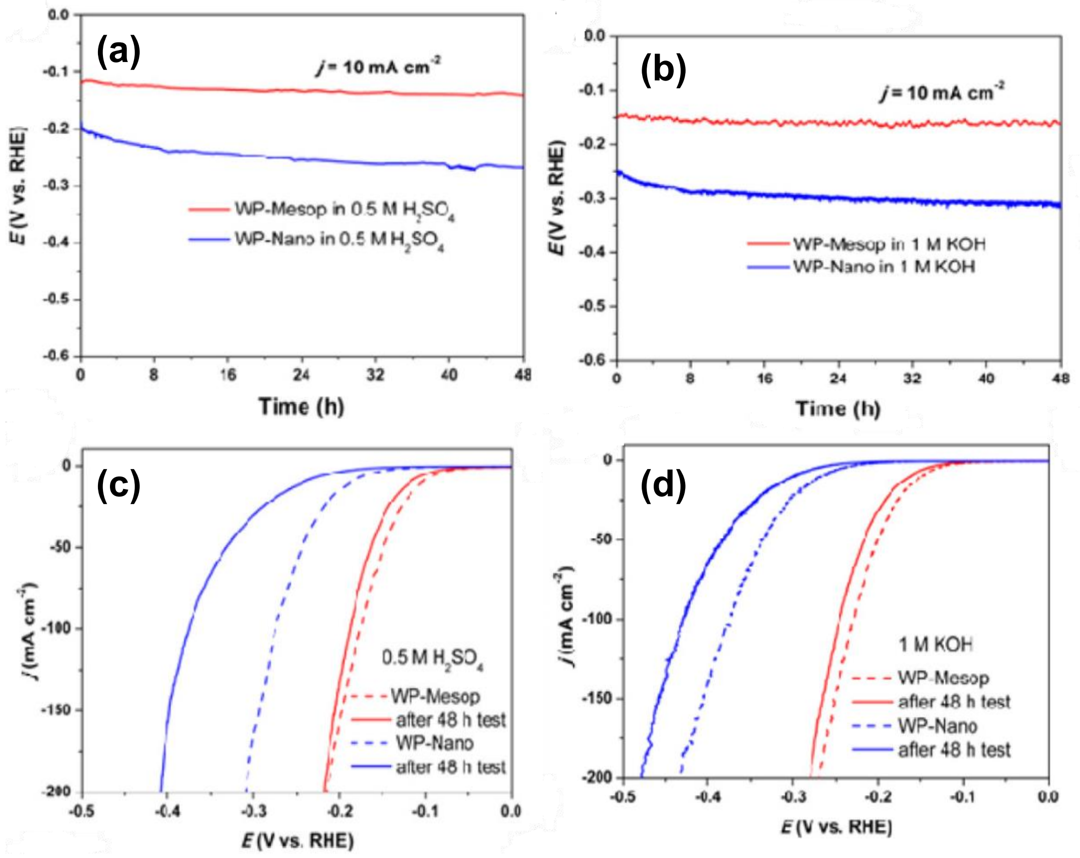

**Fig. 2. 26:** Chronopotentiometry curves of WP-Mesoporous and WP-Nano in (a) 0.5 M $H_2SO_4$ solution, (b) 1M KOH and LSV curves before and after a 48-hour evolution in (c) 0.5 M $H_2SO_4$ solution and (d) 1M KOH [200].

## 2.11 Emerging material for HER

### 2.11.1 2D materials

In recent years, there has been an astonishing breakthrough in 2D materials, ranging from fundamental investigations to the creation of next-generation technologies and materials engineering. Among them, 2D transition metal dichalcogenides (TMDs) have been extensively studied in various fields of research over the last few decades, and these 2D TMDs, which are semiconductors of the type $MX_2$, where M is a transition metal atom (such as Mo or W) and X is a chalcogen atom (such as S, Se, or Te), provide an advantageous alternative. 2D monolayer TMDs are distinguished by their unusual physical and chemical features, which include atomic-scale thickness, direct band gap, strong spin-orbit coupling, and favourable electrical and mechanical properties.

Thus, monolayer 2D TMDs have been recognized as the most promising low-cost replacements to noble metals (such as Pt and Pd) as catalysts for the HER because of their low cost and strong electrochemical stability in acidic circumstances [201, 202]. Recently, 2D transition metal dichalcogenide (TMD) materials have been shown to significantly enhance hydrogen evolution reaction (HER) activity, establishing them as promising alternatives to platinum due to their exceptional catalytic performance. These 2D TMDs possess unique characteristics that are crucial for electrochemical HER processes. The atomically thin layered structure provides numerous exposed active sites at the edges and a high specific surface area, facilitating effective HER [203].

Monolayer TMDs demonstrate in-plane resistivity that is lower than their resistivity through the basal planes. This property allows electrons to transport more easily along the basal plane to reach the catalytic sites located at the edges [204]. Consequently, these materials can serve as substitutes for platinum based HER catalysts, enabling sustainable hydrogen evolution at a lower cost and in scalable quantities. To leverage the catalytic activity of 2D TMDs for hydrogen evolution, effective conducting pathways are essential. These pathways accelerate the transport of electrons from the solvent to the system, initiating HER. Phase engineering, which converts the 2H phase into a metallic 1T phase, is one approach to enhance intrinsic electrical conductivity due to the higher electron density in the d-orbitals of the metals. However, the high cost and labour-intensive nature of phase engineering pose challenges for producing large quantities of 2D materials for industrial applications. Monolayer TMDs, such as $WS_2$, $MoS_2$, $WSe_2$, and the 2H phase of these materials, as well as their nanosheets, have been extensively studied for their excellent HER catalytic properties [205, 206]. This is largely due to three factors: (i) their increased surface area with active catalytic sites at the W-/Mo-edges or S-/Se-edges, (ii) effective electron transfer along the basal plane to the active catalytic sites, thanks to the lower resistivity of TMD nanosheets compared to the inert basal planes, and (iii) variations in the electronic structures of TMDs resulting from the d-orbitals of different transition metals. It is noteworthy that 2D 2H-$MoS_2$ and other 2H-TMD catalysts, among the earliest studied electrocatalysts, have shown remarkable enhancements in their electrocatalytic activity over the past decade. While the catalytic activity is primarily attributed to the edge sites, it is important to recognize that in-plane domains are generally considered inert. Comprehensive investigations into their HER catalytic mechanisms have provided valuable insights for the development of new HER catalysts [207]. The pure 2H-$MoS_2$ (particularly the 2D monolayer) has been shown to be a potential catalyst and energy storage material due to its inexpensive cost, abundance on Earth, specific hydrogen binding energy, and ease of electron acceptance. Fig.2.27 [207] depicts the detailed reaction steps and mechanisms involved in the HER process on the surface of a pristine 2D monolayer $MoS_2$ TMD.

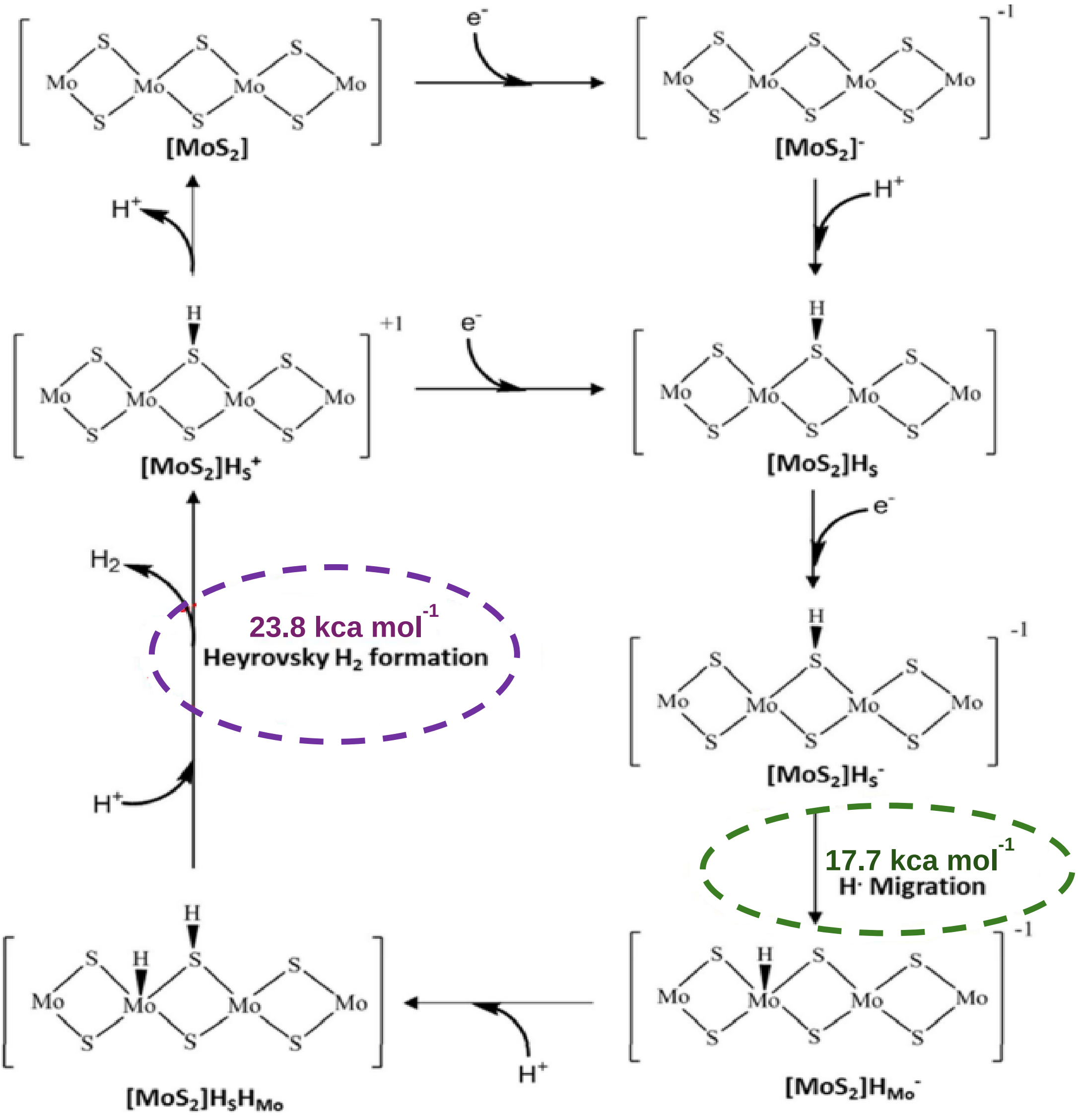

**Fig. 2. 27**: Overall chemical reaction mechanism for $H_2$ evolution on the surface of 2D monolayer $MoS_2$ material using the M06-L DFT method, and this M06-L method has shown to give accurate energies for the reaction barriers involving in the reactions on the surfaces of TMDs [207].

### 2.11.2 Metal organic framework (MOFs)

Pristine metal-organic frameworks (MOFs) have limited effectiveness as electrocatalysts for the hydrogen evolution reaction (HER) due to their instability and low conductivity in both alkaline and acidic environments. To enhance their conductivity and overall catalytic performance, various modifications have been explored for these pristine MOFs. MOFs can be applied to electrodes either by coating them onto the working electrode or by mixing them with conductive materials like graphite or acetylene black, which allows the MOFs to participate directly in the electrocatalytic process. To further improve conductivity during electrocatalysis, electrically conductive components can be incorporated while maintaining the structural integrity of the MOFs. Using MOF-based catalysts reduces the hydrogen free energies at the electrodes, enabling HER to occur in both acidic and alkaline media through different mechanisms. In acidic media, the reaction proceeds via the Volmer pathway, where a proton from the electrolyte combines with an electron from the electrode surface. Hydrogen is produced by combination of existing hydrogen atom with another adjacent hydrogen atom as per the Tafel pathway. As per the Heyrovsky pathway hydrogen molecule can be produced by combination of proton from electrolyte and electrons from electrode surface [208]. The Heyrovsky and Tafel processes are used to create hydrogen because protons are lacking in alkaline media, which causes water to dissociate (Vomer pathway) [209].

Shi et al. [210] using trinuclear and octanuclear nickel clusters as secondary building blocks that were joined by 4-connected ligands (Fig. 2.28a).The two metals' synergistic catalytic utility allowed $Cu_xNi_{1-x}$-NKU-101 to outperform other $M_xNi_{1-x}$-NKU-101 catalysts in acidic media in terms of HER electrocatalytic performance. The as-prepared $Cu_{0.19}Ni_{0.81}$-NKU-101 had the maximum exchange current density (j0) and the smallest charge transfer rate, reaching an overpotential of 324 mV at 10 mA $cm^{-2}$ and a Tafel slope of 131 mV $dec^{-1}$ (Fig. 2.28b-c) [211].

Chen et al. [212] used a simple template-based solvothermal reaction and redox post-processing strategy to create ultrathin tetragonal composites of a conductive copper-based MOF (Cu-MOF) with high carrier mobility and excellent conductivity loaded on the surface of iron hydroxide [$Fe(OH)_x$] nanoboxes (Fig. 2.28d). The produced Fe $(OH)_x$/Cu-MOF showed good HER catalytic activity, with an overpotential of 112 mV at 10 mA $cm^{-2}$ (Fig. 2.28e) and a small Tafel slope of 76 mV $dec^{-1}$

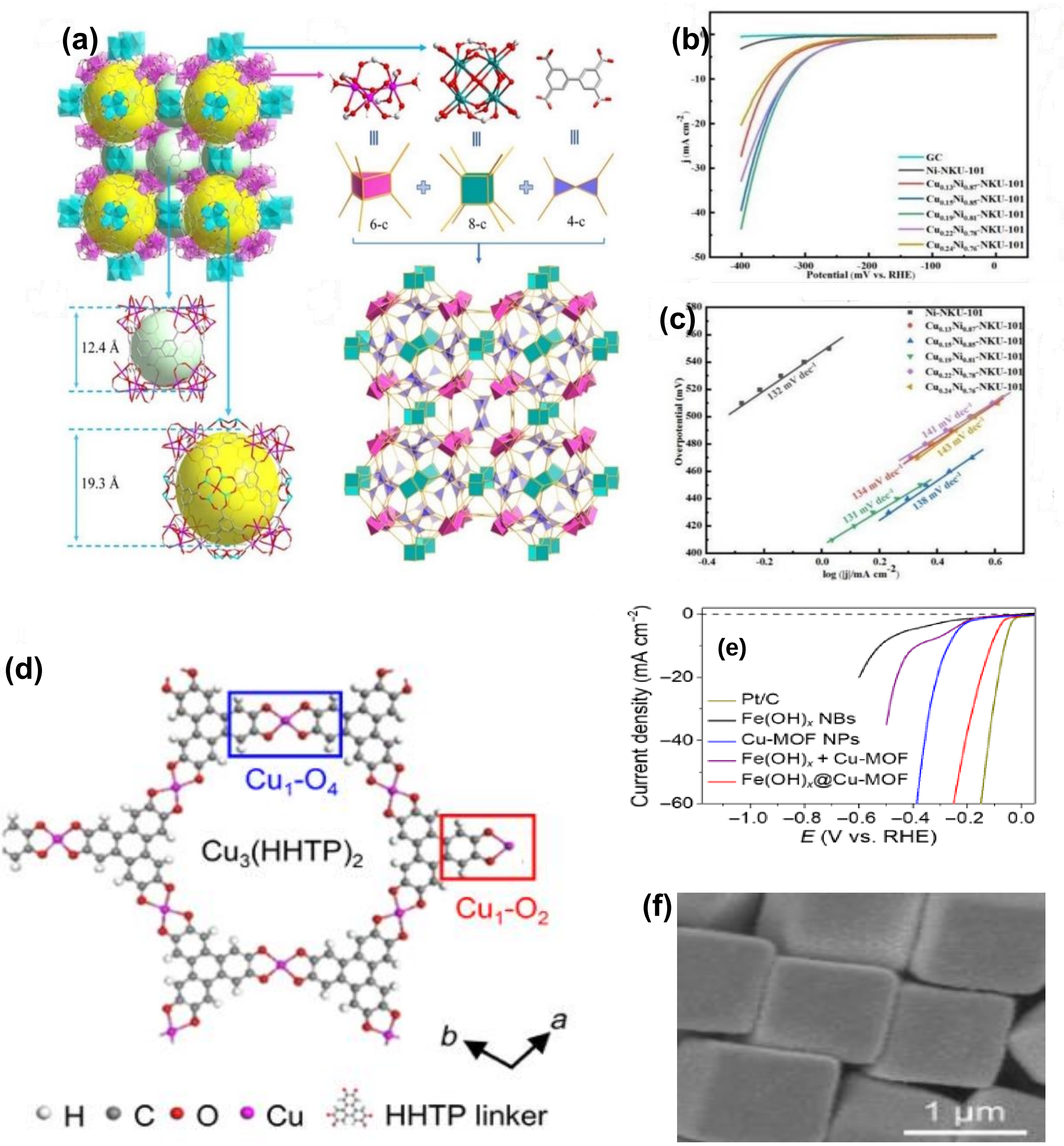

**Fig. 2. 28**: MOF-based HER electrocatalysts. (a) crystal structure of Ni-NKU-10, (b) LSV curves of CTGU-5, CTGU-6 (c) Tafel plots with other comparison samples for HER tests in 0.5 M $H_2SO_4$ [211], (d) Crystal structure of unsaturated Cu-MOF [$Cu_3(HHTP)_2$], (e) LSV curves of Pt/C, $Fe(OH)_x$ NBs, Cu-MOF NPs, $Fe(OH)_x$ + Cu-MOF, and $Fe(OH)_x$/Cu-MOF NBs in 1.0 M KOH and (f) FESEM images of sample $Fe(OH)_x$@Cu-MOF NBs [212].

### 2.11.3 Metal Oxide Nanoparticles

Metal oxides have attracted considerable attention from the research community due to their compositional and structural diversity, flexible tunability, low cost, abundance, and environmental friendliness, making them suitable for use as electrocatalysts [213, 214]. however, pristine metal oxides have not proven satisfactory for practical applications, particularly in the hydrogen evolution reaction (HER), because of unfavorable intermediate binding strength and stability issues. To address these challenges, mixed metal oxides have emerged as a promising strategy to fully utilize the unique properties of metal oxides for HER electrocatalysis [215]. These mixed metal oxides can achieve optimized adsorption energies and potentially surpass the limits of intrinsic catalytic activity found in heterostructure forms, leading to improve HER efficiency. Moreover, the stability of these electrocatalysts in aqueous environments and alkaline electrolytes has been significantly enhanced. Compared to other mixed metal-based ceramic materials, heterostructured mixed metal oxides represent a potential approach for affordable electrocatalysts in industrial applications, thanks to their easy synthesis methods and reduced dependence on noble metals [216, 217]. Despite these advantages, clear guidelines for the use of mixed metal oxides as HER electrocatalysts are still lacking.

Wei et al. [218] created $NiO/Co_3O_4$ concave surface microcubes using a metal-organic framework (MOF) precursor ($Ni_3[Co(CN)_6]_2$). The MOF precursor promotes uniform dispersion of $NiO/Co_3O_4$ on the cubes. X-ray diffraction (XRD) investigation confirmed the presence of both NiO and $Co_3O_4$ in the sample. Furthermore, the step-by-step annealing produces a concave surface that permits electrolyte penetration and increases surface area. The catalyst facilitated electrolyte penetration and HER kinetics, with a Tafel slope of 119 and an overpotential of 169.5 mV, resulting in a current density of 10 mA $cm^{-2}$. The flexible transition valence state between $Ce^{4+}$ and $Ce^{3+}$ [219, 220] has demonstrated potential electrocatalytic activity in cerium oxide ($CeO_2$). Zhang et al. [221] have used the concept to create a $TMO/CeO_2$ heterostructure rich in oxygen vacancies (VO). $CeO_2$ and TMOs, such $Co_3O_4$, can interact to adjust the electrical structure and lower HBE. Moreover, an abundance of VO may be produced on the surface by the presence of $Ce^{3+}$ and $Ce^{4+}$ as well as $Co^{2+}$ and $Co^{4+}$. In order to attain a 10 mA $cm^{-2}$ current density and a Tafel slope of 48 mV $dec^{-1}$, the $Co_3O_4/CeO_2$ catalyst demonstrated a high HER performance of 88 mV overpotential. The flexible transition valence state between $Ce^{4+}$ and $Ce^{3+}$ [220] has demonstrated potential electrocatalytic activity in cerium oxide ($CeO_2$). Zhang et al. [221] have used the concept to create a TMO/$CeO_2$ heterostructure rich in VO. $CeO_2$ and TMOs, such $Co_3O_4$, can interact to adjust the electrical structure and lower HBE. Moreover, an abundance of VO may be produced on the surface by the presence of $Ce^{3+}$ and $Ce^{4+}$ as well as $Co^{2+}$ and $Co^{4+.}$ To attain a 10 mA $cm^{-2}$ current density and a Tafel slope of 48 mV $dec^{-1}$, the $Co_3O_4/CeO_2$ catalyst demonstrated a high HER performance of 88 mV overpotential.

By adding oxygen vacancies to the catalyst, Singh et al. [222] were able to increase the HER activity of a $TiO_2/ZrO_2$ composite and achieve an overpotential value of 160 mV at 10 mA $cm^{-2}$ and a Tafel slope value of 87 mV $dec^{-1}$. A charge imbalance on the heterostructure could be caused by the $ZrO_2$ induced grain boundary defects. Consequently, an additional proton attaches itself to the oxygen atom linked to the charge imbalance, generating an excess of -OH groups on the surface and raising the acidity of the surface. Additionally, the density of state calculation demonstrated that adding oxygen vacancies to the resulting composite heterostructure results in the creation of new electronic states and a decrease in the bandgap from 3.18 to 0.52 eV, which raises the catalyst's electronic conductivity.

## 2.12 Key Performance Parameters for HER

### 2.12.1 Exchange current density and Tafel slope

The Tafel slope can be calculated using impedance data, polarization curves, or the electrochemical workstation. The voltage utilized here is the same as for the LSV test. The Tafel slope is calculated by re-plotting polarization data as overpotential vs. current density. At large overpotential values, current density typically deviates from the linear relationship. Therefore, at low over-potentials using the Tafel equation:

$$\eta = b. \log j + a \qquad \textbf{(2.9)}$$

where b is the Tafel slope, h is the overpotential, and j is the current density. Lastly, Tafel slopes are derived from the impedance data by linearly fitting the Rct v/s over-potential plots [223]. Tafel slope provides information about HER kinetics, as previously explained. The experimental temperature, electrode surface, and electrolyte composition all affect exchange current density. The favorable HER kinetics are demonstrated by the high magnitude of this current density.

### 2.12.2 Over potential

The Nernst equation indicates that, under normal circumstances, the Nernst potential (E_HER) of the hydrogen electrode is defined as zero, which refers to the standard hydrogen electrode [224]. However, to overcome barriers resulting from increased activation energy, a higher reference potential for the hydrogen electrode is required. The overpotential of the catalyst (η) represents the difference between the Nernst potential and the potential needed to drive the hydrogen evolution reaction (HER). Therefore, the expression for the applied potential can be written as $E = E_{HER} + \eta$. Additionally, the internal resistance of the electrocatalyst, the resistance of the solvent, as well as the resistance in wires, equipment, and the electrochemical system itself generate internal resistance. This internal resistance causes an ohmic potential drop in the current flow of the measurement system, necessitating adjustments in potential-current density [225, 226].

To compare the performance of different catalysts, three specific η values are typically used, which correlate with the current density values of $\eta_1$ (1 mA/cm²), $\eta_{10}$ (10 mA/cm²), and $\eta_{100}$ (100 mA/cm²). The onset overpotential is referred to as $\eta_1$, which indicates the starting point of the HER. Furthermore, a solar water-splitting device operating at a current density of 10 mA/cm² achieves an efficiency of 12.3%. Therefore, a useful method for comparison is to examine the overpotential required to achieve this current density of 10 mA/cm². When comparing the activity of different catalysts in HER, $\eta_{10}$ is typically utilized. A minimum of $\eta_{10}$ signifies greater activity; however, since the amount of active material loaded on the electrode can vary significantly even with the same geometrical area, it is improbable that $\eta_{10}$ values can be directly used to compare catalyst activity. Researchers strongly recommend standardizing the quality and amount of catalyst, such as using 0.1 mg loaded on a glassy carbon electrode with a standard area of 0.071 cm², to accurately compare catalyst activity and evaluate the potential of HER for further study [227]. For practical evaluation of the catalyst, $\eta_{100}$ is also an important factor.

### 2.12.3 Turn over frequency (TOF)

The number of product molecules produced per active site in a given amount of time is known as the turnover frequency (TOF) (Equation 2.10) [228]. The definition states that in order to determine the quantity of $H_2$ molecules, $H_2$ must be collected. Using Faraday's laws of electrolysis Eq. (2.10), where n is the amount of substance (mol), I is the current (A), z is the number of electrons transferred per molecule, and F is the Faraday constant (96485 C mol$^{-1}$), the theoretical number of $H_2$ can be determined from the charge passing through the circuit assuming a 100% Faradic efficiency. Eq. (2.10) and Eq. (2.11) then allow for the achievement of a TOF vs overpotential curve Eq. (2.12). As a result, calculating TOF is largely dependent on determining the number of active sites, which can be evaluated using a variety of methods such as the copper underpotential deposition method, calculating the number of molecules on the exposed surface, or quantifying using cyclic voltammetry (CV) tests. To create a reasonable TOF or TOF-overpotential curve, it appears that the number of active sites must be defined and evaluated [229]. It is notable that the overpotential value should always be indicated when reporting the TOF values, because TOF increases with rising overpotentials.

$$\mathrm{TOF} = \frac{\text{number of molecules reacted}}{\text{number of active sites} \times \text{time}} \tag{2.10}$$

$$n = \frac{I_t}{zF} \tag{2.11}$$

$$\mathrm{TOF} = \frac{\mathrm{I} \times \mathrm{N_A}}{\mathrm{zF} \times \text{number of active sites}} \tag{2.12}$$

### 2.12.4. Stability

It is the most critical parameter of an electrocatalyst utilized in HER. CV and chrono-potentiometry are employed to test this stability. Cyclic voltammetry is used to measure the current in electrochemical cells when a voltage is applied [230]. The current that results from altering the working electrode's potential where our catalyst is being used is measured. Kinetics, stability, and oxidation-reduction reactions are all studied using this method. By comparing the polarization curves before and after cycles, this stability is determined after 500–10000 cycles of CV [231]. The pace at which the working electrode's potential changes is measured in chrono-potentiometry with a constant current. Chrono-potentiometry (current-time) curves are also employed to assess the electro catalyst's stability.

## 2.13. Conclusion and Future Perspectives

The hydrogen evolution reaction (HER) plays a crucial role in the future of renewable energy, making the search for inexpensive and practical electrocatalysts an active area of research. These findings highlight the urgent need for efficient and affordable catalysts to support the transition to sustainable energy sources. This demand stems from hydrogen's potential as a clean energy carrier, which can help meet global energy needs and address climate change challenges. Researchers have explored a wide range of catalytic materials with varying compositions and properties. While noble metal catalysts, such as platinum, are highly efficient, their use is limited due to their high cost and scarcity. This review emphasizes innovations in non-noble and emerging material catalysts that aim to maintain efficiency while reducing dependence on expensive metals. Transition metal catalysts are gaining attention for their abundance and versatility, with materials like transition metal nitrides and molecular catalysts showing promising performance in the HER. Additionally, advancements in nanostructured catalysts, metal oxide nanoparticles, and metal-organic frameworks (MOFs) have revealed unique properties that enhance their catalytic performance, marking a significant shift in catalyst design and application.

Despite recent progress, there are still a number of obstacles to overcome in the development of catalysts for the synthesis of hydrogen. Since many high-performance choices need intricate synthesis techniques that are difficult to implement on a wide scale, scalability and cost-effectiveness of these catalysts are major challenges. The stability and durability of these catalysts, especially in acidic or alkaline environments, are still significant problems that affect their usefulness. These difficulties highlight the necessity of more research to guarantee catalysts' practical application in energy systems.This review identifies several promising research directions that could revolutionize hydrogen production. One key area is the integration of catalytic systems with renewable energy sources, which can significantly enhance the sustainability and scalability of hydrogen production, making it a viable alternative energy source. The broader implications of advancements in catalysis for hydrogen production extend beyond this specific application. By improving hydrogen production processes, these innovations could pave the way for a cleaner energy landscape, reduce reliance on fossil fuels, and mitigate greenhouse gas emissions. Furthermore, exploring diverse catalyst materials and innovative designs holds potential for breakthroughs in other catalytic applications across various industries. This interdisciplinary research effort, which bridges material science, engineering, and computational modelling, highlights the importance of collaboration in addressing global energy challenges and supporting sustainable solutions.

Despite the promising advancements in catalysis for hydrogen production, several research gaps still need to be addressed. A critical area of investigation is the long-term stability of catalysts, particularly transition metal and carbon-based catalysts, under real-world conditions. Additionally, there is a pressing need for scalable and cost-effective synthesis methods to produce high-performance catalysts, as this will facilitate their widespread use in industrial applications. Furthermore, advanced in situ characterization techniques are necessary to study the dynamic behavior of catalysts during reactions. Such techniques would enable more focused design improvements. Upon reviewing and summarizing the extensive information on material functionalization discussed in the article, one gains insights into the robust design and development of electrocatalysts for efficient hydrogen production through the hydrogen evolution reaction (HER). It is important to note that our understanding of catalytic mechanisms, active sites, and the structure of catalysts remains limited. These factors can vary dynamically during electrochemical reactions, especially at high current densities. The environmental impact of catalyst production is also a significant concern, highlighting the need for eco-friendly and earth-abundant materials in future research. Finally, integrating catalytic systems with renewable energy sources is crucial for optimizing hydrogen production in response to intermittent energy supplies. The field of catalysis for hydrogen production is rapidly evolving, offering hope for a sustainable energy future. Continued interdisciplinary cooperation and more funding for research are necessary to overcome present obstacles and investigate novel opportunities in this game-changing field. These initiatives will play a key role in ensuring that hydrogen production is sustainable and feasible, which will advance the larger objective of a clean and robust energy infrastructure.

## 2.14. References

1. Singh, P. and D. Yadav, Link between air pollution and global climate change, in Global Climate Change. 2021, Elsevier. p. 79-108.
2. Al Shaikh, R., A. Al-Othman, M. Tawalbeh, A. Shamayleh, and P. Nancarrow, *Development of MXene incorporated PVDF based membranes for an enhanced performance in higher temperature PEM fuel cells.* Process Safety and Environmental Protection, 2024. **189**: p. 985-994.
3. Al-Othman, A., M. Tawalbeh, A. Ka'aki, I. Shomope, and M.F. Hassan, *Novel zirconium phosphate/MXene/ionic liquid membranes for PEM fuel cells operating up to 145° C.* Process Safety and Environmental Protection, 2024. **189**: p. 1368-1378.
4. Ali, A.A., A. Al-Othman, and M. Tawalbeh, *Exploring natural polymers for the development of proton exchange membranes in fuel cells.* Process Safety and Environmental Protection, 2024. **189**: p. 1379-1401.
5. Nimir, W., A. Al-Othman, and M. Tawalbeh, *Unveiling zirconium phytate-heteropolyacids-ionic liquids membranes for PEM fuel cells applications up to 150° C.* International Journal of Hydrogen Energy, 2024.
6. Abdelkareem, M.A., K. Elsaid, T. Wilberforce, M. Kamil, E.T. Sayed, and A. Olabi, *Environmental aspects of fuel cells: A review.* Science of The Total Environment, 2021. **752**: p. 141803.
7. Nazir, H., N. Muthuswamy, C. Louis, S. Jose, J. Prakash, M.E. Buan, C. Flox, S. Chavan, X. Shi, and P. Kauranen, *Is the H2 economy realizable in the foreseeable future? Part III: H2 usage technologies, applications, and challenges and opportunities.* International journal of hydrogen energy, 2020. **45**(53): p. 28217-28239.
8. Mohammed, H., A. Al-Othman, P. Nancarrow, M. Tawalbeh, and M.E.H. Assad, *Direct hydrocarbon fuel cells: A promising technology for improving energy efficiency.* Energy, 2019. **172**: p. 207-219.
9. Suter, T.A., K. Smith, J. Hack, L. Rasha, Z. Rana, G.M.A. Angel, P.R. Shearing, T.S. Miller, and D.J. Brett, *Engineering Catalyst Layers for Next‐Generation Polymer Electrolyte Fuel Cells: A Review of Design, Materials, and Methods.* Advanced Energy Materials, 2021. **11**(37): p. 2101025.

10. Wang, Y., K.S. Chen, J. Mishler, S.C. Cho, and X.C. Adroher, *A review of polymer electrolyte membrane fuel cells: technology, applications, and needs on fundamental research.* Applied Energy, 2011. **88**(4): p. 981-1007.

11. Zhang, H. and P.K. Shen, *Recent development of polymer electrolyte membranes for fuel cells.* Chemical reviews, 2012. **112**(5): p. 2780-2832.

12. Xiao, F., Y.C. Wang, Z.P. Wu, G. Chen, F. Yang, S. Zhu, K. Siddharth, Z. Kong, A. Lu, and J.C. Li, *Recent advances in electrocatalysts for proton exchange membrane fuel cells and alkaline membrane fuel cells.* Advanced Materials, 2021. **33**(50): p. 2006292.

13. Gao, X., J. Chen, R. Xu, Z. Zhen, X. Zeng, X. Chen, and L. Cui, *Research progress and prospect of the materials of bipolar plates for proton exchange membrane fuel cells (PEMFCs).* International Journal of Hydrogen Energy, 2023.

14. Shabani, B., M. Hafttananian, S. Khamani, A. Ramiar, and A. Ranjbar, *Poisoning of proton exchange membrane fuel cells by contaminants and impurities: Review of mechanisms, effects, and mitigation strategies.* Journal of Power Sources, 2019. **427**: p. 21-48.

15. Ogungbemi, E., O. Ijaodola, F. Khatib, T. Wilberforce, Z. El Hassan, J. Thompson, M. Ramadan, and A. Olabi, *Fuel cell membranes–Pros and cons.* Energy, 2019. **172**: p. 155-172.

16. Kim, D.J., M.J. Jo, and S.Y. Nam, *A review of polymer–nanocomposite electrolyte membranes for fuel cell application.* Journal of Industrial and Engineering Chemistry, 2015. **21**: p. 36-52.

17. Gagliardi, G.G., A. Ibrahim, D. Borello, and A. El-Kharouf, *Composite polymers development and application for polymer electrolyte membrane technologies—A review.* Molecules, 2020. **25**(7): p. 1712.

18. Walkowiak-Kulikowska, J., J. Wolska, and H. Koroniak, *10. Polymers application in proton exchange membranes for fuel cells (PEMFCs).* Polymer Engineering, 2017: p. 293-348.

19. Park, C.H., C.H. Lee, M.D. Guiver, and Y.M. Lee, *Sulfonated hydrocarbon membranes for medium-temperature and low-humidity proton exchange membrane fuel cells (PEMFCs).* Progress in Polymer Science, 2011. **36**(11): p. 1443-1498.

20. Ghita, O., E. James, R. Trimble, and K.E. Evans, *Physico-chemical behaviour of poly (ether ketone)(PEK) in high temperature laser sintering (HT-LS).* Journal of Materials Processing Technology, 2014. **214**(4): p. 969-978.
21. Huang, Z., J. Liu, Y. Liu, Y. Xu, R. Li, H. Hong, L. Shen, H. Lin, and B.-Q. Liao, *Enhanced permeability and antifouling performance of polyether sulfone (PES) membrane via elevating magnetic Ni@ MXene nanoparticles to upper layer in phase inversion process.* Journal of Membrane Science, 2021. **623**: p. 119080.
22. Luo, H., G. Vaivars, and M. Mathe, *Double cross-linked polyetheretherketone proton exchange membrane for fuel cell.* international journal of hydrogen energy, 2012. **37**(7): p. 6148-6152.
23. Kausar, A., *Progression from polyimide to polyimide composite in proton-exchange membrane fuel cell: a review.* Polymer-Plastics Technology and Engineering, 2017. **56**(13): p. 1375-1390.
24. Gil, M., X. Ji, X. Li, H. Na, J.E. Hampsey, and Y. Lu, *Direct synthesis of sulfonated aromatic poly (ether ether ketone) proton exchange membranes for fuel cell applications.* Journal of membrane science, 2004. **234**(1-2): p. 75-81.
25. Mahimai, B.M., G. Sivasubramanian, K. Sekar, D. Kannaiyan, and P. Deivanayagam, *Sulfonated poly (ether ether ketone): efficient ion-exchange polymer electrolytes for fuel cell applications–a versatile review.* Materials Advances, 2022. **3**(15): p. 6085-6095.
26. Govinna, N.D., T. Keller, C. Schick, and P. Cebe, *Melt-electrospinning of poly (ether ether ketone) fibers to avoid sulfonation.* Polymer, 2019. **171**: p. 50-57.
27. Sarirchi, S., S. Rowshanzamir, and F. Mehri, *Simultaneous improvement of ionic conductivity and oxidative stability of sulfonated poly (ether ether ketone) nanocomposite proton exchange membrane for fuel cell application.* International Journal of Energy Research, 2020. **44**(4): p. 2783-2800.
28. RS, R.R., W. Rashmi, M. Khalid, W. Wong, and J. Priyanka, *Recent progress in the development of aromatic polymer-based proton exchange membranes for fuel cell applications.* Polymers, 2020. **12**(5): p. 1061.
29. Beyraghi, F., S.H. Mirfarsi, S. Rowshanzamir, A. Karimi, and M.J. Parnian, *Optimal thermal treatment conditions for durability improvement of highly sulfonated poly (ether ether ketone) membrane for polymer electrolyte fuel cell applications.* international journal of hydrogen energy, 2020. **45**(24): p. 13441-13458.

30. Ren, S., H. Lei, L. Wang, Q. Bu, S. Chen, and J. Wu, *Thermal behaviour and kinetic study for woody biomass torrefaction and torrefied biomass pyrolysis by TGA.* Biosystems engineering, 2013. **116**(4): p. 420-426.
31. Gilois, B., F. Goujon, A. Fleury, A. Soldera, and A. Ghoufi, *Water nano-diffusion through the Nafion fuel cell membrane.* Journal of Membrane Science, 2020. **602**: p. 117958.
32. Wang, G., Z. Liu, C. Liu, and W. Chen, *Molecular Study of Nonequilibrium Transport Mechanism for Proton and Water in Porous Proton Exchange Membranes.* International Journal of Energy Research, 2023. **2023**.
33. Haider, R., Y. Wen, Z.-F. Ma, D.P. Wilkinson, L. Zhang, X. Yuan, S. Song, and J. Zhang, *High temperature proton exchange membrane fuel cells: progress in advanced materials and key technologies.* Chemical Society Reviews, 2021. **50**(2): p. 1138-1187.
34. Dong, X., D. Lu, T.A. Harris, and I.C. Escobar, *Polymers and solvents used in membrane fabrication: a review focusing on sustainable membrane development.* Membranes, 2021. **11**(5): p. 309.
35. Mukeba, K.M., *Step-growth polymerization of perfluoro-vinyl ether,-cycloalkenes, and-acyclic alkenes with bisphenols containing variable polycyclic aromatic cores*. 2022: Mississippi State University.
36. Bossion, A., K.V. Heifferon, L. Meabe, N. Zivic, D. Taton, J.L. Hedrick, T.E. Long, and H. Sardon, *Opportunities for organocatalysis in polymer synthesis via step-growth methods.* Progress in Polymer Science, 2019. **90**: p. 164-210.
37. Yang, Y., Y. Wang, M. Zhu, J. Zhao, D. Cai, and H. Cao, *Valorization of lignin for renewable non-isocyanate polyurethanes: a state-of-the-art review.* Materials Today Sustainability, 2023. **22**: p. 100367.
38. Nguyen, M.D.T., S. Yang, and D. Kim, *Pendant dual sulfonated poly (arylene ether ketone) proton exchange membranes for fuel cell application.* Journal of Power Sources, 2016. **328**: p. 355-363.
39. Fulcrand, H., L. Rouméas, G. Billerach, C. Aouf, and E. Dubreucq, *Advances in Bio-based thermosetting polymers.* Recent Advances in Polyphenol Research, 2019. **6**: p. 285-334.
40. Sun, Y., S. Zhou, G. Qin, J. Guo, Q. Zhang, S. Li, and S. Zhang, *A chemical-induced crystallization strategy to fabricate poly (ether ether ketone)*

*asymmetric membranes for organic solvent nanofiltration.* Journal of Membrane Science, 2021. **620**: p. 118899.

41. Xu, M., H. Xue, Q. Wang, and L. Jia, *Sulfonated poly (arylene ether) s based proton exchange membranes for fuel cells.* International Journal of Hydrogen Energy, 2021. **46**(62): p. 31727-31753.
42. Nor, N.A.M., M.A. Mohamed, and J. Jaafar, *Modified sulfonated polyphenylsulfone proton exchange membrane with enhanced fuel cell performance: A review.* Journal of Industrial and Engineering Chemistry, 2022.
43. Khomein, P., W. Ketelaars, T. Lap, and G. Liu, *Sulfonated aromatic polymer as a future proton exchange membrane: A review of sulfonation and crosslinking methods.* Renewable and Sustainable Energy Reviews, 2021. **137**: p. 110471.
44. Harun, N.A.M., N. Shaari, and N.F.H. Nik Zaiman, *A review of alternative polymer electrolyte membrane for fuel cell application based on sulfonated poly (ether ether ketone).* International Journal of Energy Research, 2021. **45**(14): p. 19671-19708.
45. Sayed Daud, S.N.S., M.N.A. Mohd Norddin, J. Jaafar, and R. Sudirman, *High degree sulfonated poly (ether ether ketone) blend with polyvinylidene fluoride as a potential proton-conducting membrane fuel cell.* High Performance Polymers, 2020. **32**(1): p. 103-115.
46. Muthu Lakshmi, R., V. Choudhary, and I. Varma, *Sulphonated poly (ether ether ketone): Synthesis and characterisation.* Journal of materials science, 2005. **40**: p. 629-636.
47. Tsai, S., *Introduction to composite materials*. 2018: Routledge.
48. Li, Z., R. Yu, C. Liu, J. Zheng, J. Guo, T.A. Sherazi, S. Li, and S. Zhang, *Preparation and characterization of side-chain poly (aryl ether ketone) anion exchange membranes by superacid-catalyzed reaction.* Polymer, 2021. **222**: p. 123639.
49. Wong, C.Y., W.Y. Wong, K.S. Loh, W.R.W. Daud, K.L. Lim, M. Khalid, and R. Walvekar, *Development of poly (vinyl alcohol)-based polymers as proton exchange membranes and challenges in fuel cell application: a review.* Polymer reviews, 2020. **60**(1): p. 171-202.
50. Xiang, Z., H. Liu, P. Deng, M. Liu, Y. Yin, and X. Ge, *The effect of irradiation on morphology and properties of the PET/HDPE blends with trimethylol propane trimethacrylate (TMPTA).* Polymer bulletin, 2009. **63**: p. 587-597.

51. Xiaomin, G., L. Yonghua, and L. Jinlong, *Review on modification of sulfonated poly (-ether-ether-ketone) membranes used as proton exchange membranes.* Materials Science, 2015. **21**(4): p. 574-582.

52. Hayes, S., C. Boote, C.S. Kamma-Lorger, M.S. Rajan, J. Harris, E. Dooley, N. Hawksworth, J. Hiller, N.J. Terill, and F. Hafezi, *Riboflavin/UVA collagen cross-linking-induced changes in normal and keratoconus corneal stroma.* PloS one, 2011. **6**(8): p. e22405.

53. Gao, Y., K. Peng, and S. Mitragotri, *Covalently Crosslinked hydrogels via step-growth reactions: crosslinking chemistries, polymers, and clinical impact.* Advanced Materials, 2021. **33**(25): p. 2006362.

54. Wu, S., J. Liang, Y. Shi, M. Huang, X. Bi, Z. Wang, and J. Jin, *Design of interchain hydrogen bond in polyimide membrane for improved gas selectivity and membrane stability.* Journal of Membrane Science, 2021. **618**: p. 118659.

55. Ramly, N., N. Aini, N. Sahli, S. Aminuddin, M. Yahya, and A. Ali, *Dielectric behaviour of UV-crosslinked sulfonated poly (ether ether ketone) with methyl cellulose (SPEEK-MC) as proton exchange membrane.* International Journal of Hydrogen Energy, 2017. **42**(14): p. 9284-9292.

56. Teruel-Juanes, R., B. Pascual-Jose, C. del Río, O. García, and A. Ribes-Greus, *Dielectric analysis of photocrosslinked and post-sulfonated styrene-ethylene-butylene-styrene block copolymer based membranes.* Reactive and Functional Polymers, 2020. **155**: p. 104715.

57. Meng, N., F. Lian, and G. Cui, *Macromolecular design of lithium conductive polymer as electrolyte for solid-state lithium batteries.* Small, 2021. **17**(3): p. 2005762.

58. Kumari, M., H.S. Sodaye, D. Sen, and R.C. Bindal, *Properties and morphology studies of proton exchange membranes based on cross-linked sulfonated poly (ether ether ketone) for electrochemical application: effect of cross-linker chain length.* Solid State Ionics, 2018. **316**: p. 75-84.

59. Ajitha, A. and S. Thomas, *Introduction: Polymer blends, thermodynamics, miscibility, phase separation, and compatibilization*, in *Compatibilization of polymer blends*. 2020, Elsevier. p. 1-29.

60. Liang, J., J. Ge, K. Wu, Q. Zhang, J. Wang, and Z. Ye, *Sulfonated polyaryletherketone with pendant benzimidazole groups for proton exchange membranes.* Journal of Membrane Science, 2020. **597**: p. 117626.

61. Simari, C., C.L. Vecchio, V. Baglio, and I. Nicotera, *Sulfonated polyethersulfone/polyetheretherketone blend as high performing and cost-effective electrolyte membrane for direct methanol fuel cells.* Renewable Energy, 2020. **159**: p. 336-345.

62. Raja, K., M. Raja Pugalenthi, and M. Ramesh Prabhu, *Investigation on the sulfonated poly (ether ether ketone)/poly (amide‐imide)/barium cerate‐based nanocomposite membrane for proton exchange membrane fuel cells.* International Journal of Energy Research, 2021. **45**(6): p. 8564-8576.

63. Li, C., Z. Yang, X. Liu, Y. Zhang, J. Dong, Q. Zhang, and H. Cheng, *Enhanced performance of sulfonated poly (ether ether ketone) membranes by blending fully aromatic polyamide for practical application in direct methanol fuel cells (DMFCs).* international journal of hydrogen energy, 2017. **42**(47): p. 28567-28577.

64. Haragirimana, A., P.B. Ingabire, Y. Liu, N. Li, Z. Hu, and S. Chen, *An effective strategy to enhance the performance of the proton exchange membranes based on sulfonated poly (ether ether ketone) s.* International Journal of Hydrogen Energy, 2020. **45**(16): p. 10017-10029.

65. Shang, Z., R. Wycisk, and P. Pintauro, *Electrospun composite proton-exchange and anion-exchange membranes for fuel cells.* Energies, 2021. **14**(20): p. 6709.

66. Qian, X., M. Ostwal, A. Asatekin, G.M. Geise, Z.P. Smith, W.A. Phillip, R.P. Lively, and J.R. McCutcheon, *A critical review and commentary on recent progress of additive manufacturing and its impact on membrane technology.* Journal of Membrane Science, 2022. **645**: p. 120041.

67. Nayak, J.K., U. Shankar, and K. Samal, *Fabrication and development of SPEEK/PVdF-HFP/SiO2 proton exchange membrane for microbial fuel cell application.* Chemical Engineering Journal Advances, 2023. **14**: p. 100459.

68. Çalı, A., A. Şahin, and A. Irfan, *Experimental Investigation of boron phosphate Incorporated speek/pvdf blend membrane for proton exchange membrane fuel cells.* International Journal of Hydrogen Energy, 2022. **47**(95): p. 40476-40490.

69. Wang, D. and C.J. Cornelius, *Ionomer thermodynamic interrelationships associated with wettability, surface energy, swelling, and water transport.* European Polymer Journal, 2016. **85**: p. 126-138.

70. Liu, Q., X. Li, S. Zhang, Z. Wang, Y. Chen, S. Zhou, C. Wang, K. Wu, J. Liu, and Q. Mao, *Novel sulfonated N-heterocyclic poly (aryl ether ketone ketone) s*

*with pendant phenyl groups for proton exchange membrane performing enhanced oxidative stability and excellent fuel cell properties.* Journal of Membrane Science, 2022. **641**: p. 119926.

71. Zhao, G., L. Shi, M. Zhang, B. Cheng, G. Yang, and X. Zhuang, *Self-assembly of metal-organic framework onto nanofibrous mats to enhance proton conductivity for proton exchange membrane.* International Journal of Hydrogen Energy, 2021. **46**(73): p. 36415-36423.
72. da Trindade, L., L. Zanchet, R. Dreon, J. Souza, M. Assis, E. Longo, E. Martini, A. Chiquito, and F. Pontes, *Microwave-assisted solvothermal preparation of Zr-BDC for modification of proton exchange membranes made of SPEEK/PBI blends.* Journal of Materials Science, 2020. **55**: p. 14938-14952.
73. Daud, S.N.S.S., M.M. Norddin, J. Jaafar, R. Sudirman, M. Othman, and A. Ismail, *Highly sulfonated poly (ether ether ketone) blend with hydrophobic polyether sulfone as an alternative electrolyte for proton exchange membrane fuel cell.* Arabian Journal for Science and Engineering, 2021. **46**: p. 6189-6205.
74. Wei, P., Y. Sui, X. Li, Q. Liu, B. Zhu, C. Cong, X. Meng, and Q. Zhou, *Sandwich-structure PI/SPEEK/PI proton exchange membrane developed for achieving the high durability on excellent proton conductivity and stability.* Journal of Membrane Science, 2022. **644**: p. 120116.
75. Chu, F., X. Chu, T. Lv, Z. Chen, Y. Ren, S. Zhang, N. Yuan, B. Lin, and J. Ding, *Amphoteric membranes based on sulfonated polyether ether ketone and imidazolium‐functionalized polyphenylene oxide for vanadium redox flow battery applications.* ChemElectroChem, 2019. **6**(19): p. 5041-5050.
76. Yang, X., H. Zhu, F. Jiang, and X. Zhou, *Notably enhanced proton conductivity by thermally-induced phase-separation transition of Nafion/Poly (vinylidene fluoride) blend membranes.* Journal of Power Sources, 2020. **473**: p. 228586.
77. Liu, G., W.-C. Tsen, S.-C. Jang, F. Hu, F. Zhong, H. Liu, G. Wang, S. Wen, G. Zheng, and C. Gong, *Mechanically robust and highly methanol-resistant sulfonated poly (ether ether ketone)/poly (vinylidene fluoride) nanofiber composite membranes for direct methanol fuel cells.* Journal of Membrane Science, 2019. **591**: p. 117321.
78. Chamakh, M. and A.I. Ayesh, *Production and investigation of flexible nanofibers of sPEEK/PVP loaded with RuO2 nanoparticles.* Materials & Design, 2021. **204**: p. 109678.

79. Purnama, H., M. Mujiburohman, M. Hakim, and N. Hidayati. *Preparation and Characterisation of Composite Sulfonated Polyether Ether Ketone for Direct Methanol Fuel Cells*. in *Journal of Physics: Conference Series*. 2019. IOP Publishing.

80. Abu-Thabit, N.Y., S.A. Ali, S.J. Zaidi, and K. Mezghani, *Novel sulfonated poly (ether ether ketone)/phosphonated polysulfone polymer blends for proton conducting membranes.* Journal of Materials Research, 2012. **27**(15): p. 1958-1968.

81. Sultan, A., J.K. Adewole, A. Al-Ahmed, M. Nazal, and S.J. Zaidi, *Preparation and performance evaluation of speek/polyaniline composite membrane for direct methanol fuel cell.* International Polymer Processing, 2017. **32**(1): p. 41-49.

82. Han, M., G. Zhang, M. Li, S. Wang, Z. Liu, H. Li, Y. Zhang, D. Xu, J. Wang, and J. Ni, *Sulfonated poly (ether ether ketone)/polybenzimidazole oligomer/epoxy resin composite membranes in situ polymerization for direct methanol fuel cell usages.* Journal of Power Sources, 2011. **196**(23): p. 9916-9923.

83. Hidayati, N., T. Harmoko, M. Mujiburohman, and H. Purnama. *Characterization of sPEEK/chitosan membrane for the direct methanol fuel cell*. in *AIP Conference Proceedings*. 2019. AIP Publishing.

84. Sun, X., S.C. Simonsen, T. Norby, and A. Chatzitakis, *Composite membranes for high temperature PEM fuel cells and electrolysers: a critical review.* Membranes, 2019. **9**(7): p. 83.

85. Liu, G., W.-C. Tsen, S.-C. Jang, F. Hu, F. Zhong, B. Zhang, J. Wang, H. Liu, G. Wang, and S. Wen, *Composite membranes from quaternized chitosan reinforced with surface-functionalized PVDF electrospun nanofibers for alkaline direct methanol fuel cells.* Journal of Membrane Science, 2020. **611**: p. 118242.

86. Li, Z., Z. Guan, C. Wang, B. Quan, and L. Zhao, *Addition of modified hollow mesoporous organosilica in anhydrous SPEEK/IL composite membrane enhances its proton conductivity.* Journal of Membrane Science, 2021. **620**: p. 118897.

87. Sivasubramanian, G., K. Hariharasubramanian, P. Deivanayagam, and J. Ramaswamy, *High-performance SPEEK/SWCNT/fly ash polymer electrolyte nanocomposite membranes for fuel cell applications.* Polymer Journal, 2017. **49**(10): p. 703-709.

88. Gahlot, S. and V. Kulshrestha, *Dramatic improvement in water retention and proton conductivity in electrically aligned functionalized CNT/SPEEK nanohybrid PEM.* ACS Applied Materials & Interfaces, 2015. **7**(1): p. 264-272.
89. Di, Y., W. Yang, X. Li, Z. Zhao, M. Wang, and J. Dai, *Preparation and characterization of continuous carbon nanofiber-supported SPEEK composite membranes for fuel cell application.* RSC Advances, 2014. **4**(94): p. 52001-52007.
90. He, S., Y. Ai, W. Dai, S. Zhai, H. Song, and J. Lin, *Composite membranes anchoring phosphotungstic acid by β-cyclodextrins modified halloysite nanotubes.* Polymer Testing, 2021. **100**: p. 107246.
91. Oh, S., T. Yoshida, G. Kawamura, H. Muto, M. Sakai, and A. Matsuda, *Proton conductivity and fuel cell property of composite electrolyte consisting of Cs-substituted heteropoly acids and sulfonated poly (ether–ether ketone).* Journal of Power Sources, 2010. **195**(18): p. 5822-5828.
92. Peighambardoust, S., S. Rowshanzamir, M. Hosseini, and M. Yazdanpour, *Self-humidifying nanocomposite membranes based on sulfonated poly (ether ether ketone) and heteropolyacid supported Pt catalyst for fuel cells.* International journal of hydrogen energy, 2011. **36**(17): p. 10940-10957.
93. Colicchio, I., F. Wen, H. Keul, U. Simon, and M. Moeller, *Sulfonated poly (ether ether ketone)–silica membranes doped with phosphotungstic acid. Morphology and proton conductivity.* Journal of Membrane Science, 2009. **326**(1): p. 45-57.
94. Doğan, H., T.Y. Inan, E. Unveren, and M. Kaya, *Effect of cesium salt of tungstophosphoric acid (Cs-TPA) on the properties of sulfonated polyether ether ketone (SPEEK) composite membranes for fuel cell applications.* international journal of hydrogen energy, 2010. **35**(15): p. 7784-7795.
95. Das, P., B. Mandal, and S. Gumma, *L-tyrosine grafted palladium graphite oxide and sulfonated poly (ether ether ketone) based novel composite membrane for direct methanol fuel cell.* Chemical Engineering Journal, 2021. **423**: p. 130235.
96. Yogarathinam, L.T., J. Jaafar, A.F. Ismail, P.S. Goh, M.H. Bin Mohamed, M.F. Radzi Hanifah, A. Gangasalam, and J. Peter, *Polyaniline decorated graphene oxide on sulfonated poly (ether ether ketone) membrane for direct methanol fuel cells application.* Polymers for Advanced Technologies, 2022. **33**(1): p. 66-80.

97. Maiti, T.K., P. Dixit, J. Singh, N. Talapatra, M. Ray, and S. Chattopadhyay, *A novel strategy toward the advancement of proton exchange membranes through the incorporation of propylsulfonic acid-functionalized graphene oxide in crosslinked acid-base polymer blends.* International Journal of Hydrogen Energy, 2023. **48**(4): p. 1482-1500.
98. Martina, P., R. Gayathri, M.R. Pugalenthi, G. Cao, C. Liu, and M.R. Prabhu, *Nanosulfonated silica incorporated SPEEK/SPVdF-HFP polymer blend membrane for PEM fuel cell application.* Ionics, 2020. **26**: p. 3447-3458.
99. Meng, X., C. Li, J. Wen, H. Ye, C. Cong, Q. Zhou, and L. Xu, *The effect of amino‐modified mesoporous silica nanospheres on properties of SPEEK/HPW@ Mesoporous Silica Nanoparticles proton exchange membrane.* Journal of the Chinese Chemical Society, 2021. **68**(7): p. 1197-1204.
100. Sahin, A., *The development of Speek/Pva/Teos blend membrane for proton exchange membrane fuel cells.* Electrochimica Acta, 2018. **271**: p. 127-136.
101. Kumar, V., S. GokulaKrishnan, G. Arthanareeswaran, A.F. Ismail, J. Jaafar, D.B. Das, and L.T. Yogarathinam, *Cloisite-and bentonite-based stable nanocomposite membranes for enhancement of direct methanol fuel cell applications.* Polymer Bulletin, 2023: p. 1-19.
102. Gokulakrishnan, S., V. Kumar, G. Arthanareeswaran, A. Ismail, and J. Jaafar, *Thermally stable nanoclay and functionalized graphene oxide integrated SPEEK nanocomposite membranes for direct methanol fuel cell application.* Fuel, 2022. **329**: p. 125407.
103. Charradi, K., Z. Ahmed, P. Aranda, and R. Chtourou, *Silica/montmorillonite nanoarchitectures and layered double hydroxide-SPEEK based composite membranes for fuel cells applications.* Applied Clay Science, 2019. **174**: p. 77-85.
104. Selvakumar, K., S. Rajendran, and M. Ramesh Prabhu, *Influence of barium zirconate on SPEEK-based polymer electrolytes for PEM fuel cell applications.* Ionics, 2019. **25**: p. 2243-2253.
105. Wang, Y., J. You, Z. Cheng, K. Jiang, L. Zhang, W. Cai, Y.-Q. Liu, and S. Li, *A promising Al-CeZrO4/HPW-incorporated SPEEK composite membrane with improved proton conductivity and chemical stability for PEM fuel cells.* High Performance Polymers, 2021. **33**(3): p. 295-308.

106. Gandhimathi, S., H. Krishnan, and D. Paradesi, *Development of proton-exchange polymer nanocomposite membranes for fuel cell applications.* Polymers and Polymer Composites, 2020. **28**(7): p. 492-501.
107. Prathap, M., K. Poonkuzhali, M.M. Berlina, P. Hemalatha, and D. Paradesi, *Synthesis and characterization of sulfonated poly (ether ether ketone)/zinc cobalt oxide composite membranes for fuel cell applications.* High Performance Polymers, 2020. **32**(9): p. 984-991.
108. Zhang, X., H. Ma, T. Pei, R. Zhang, and Y. Liu, *Anchoring HPW by amino-modified MIL-101 (Cr) to improve the properties of SPEEK in proton exchange membranes.* Journal of Applied Polymer Science, 2023: p. e53978.
109. Huang, H., Y. Ma, Z. Jiang, and Z.-J. Jiang, *Spindle-like MOFs-derived porous carbon filled sulfonated poly (ether ether ketone): A high performance proton exchange membrane for direct methanol fuel cells.* Journal of Membrane Science, 2021. **636**: p. 119585.
110. Sun, L., S. Qu, X. Lv, L. Ding, J. Duan, and W. Wang, *Sulfonated Poly Ether Ether Ketone Membranes Reinforced by Metal–Organic Frameworks/Ionic Liquids.* ACS Applied Polymer Materials, 2023. **5**(12): p. 10081-10090.
111. Aparna, M., P. Hemalatha, D. Paradesi, and D.A. Raj, *Design and development of copper trimesic acid anchored sPEEK/polyimide composite membranes for fuel cell applications.* ChemistrySelect, 2023. **8**(14): p. e202204584.
112. Sun, H., B. Tang, and P. Wu, *Two-dimensional zeolitic imidazolate framework/carbon nanotube hybrid networks modified proton exchange membranes for improving transport properties.* ACS applied materials & interfaces, 2017. **9**(40): p. 35075-35085.
113. Barjola, A., J.L. Reyes-Rodríguez, O. Solorza-Feria, E. Giménez, and V. Compan, *Novel SPEEK-ZIF-67 proton exchange nanocomposite membrane for PEMFC application at intermediate temperatures.* Industrial & Engineering Chemistry Research, 2021. **60**(25): p. 9107-9118.
114. Taufiq Musa, M., N. Shaari, and S.K. Kamarudin, *Carbon nanotube, graphene oxide and montmorillonite as conductive fillers in polymer electrolyte membrane for fuel cell: an overview.* International Journal of Energy Research, 2021. **45**(2): p. 1309-1346.
115. Gupta, N., S.M. Gupta, and S. Sharma, *Carbon nanotubes: Synthesis, properties and engineering applications.* Carbon Letters, 2019. **29**: p. 419-447.

116. Nqakala, N.C., *Construction of an enzyme-free electrochemical sensor based on Ag-Fe2O3/POM/RGO novel nanocomposite for hydrogen peroxide detection.* 2018.
117. Li, N., J. Liu, J.J. Liu, L.Z. Dong, S.L. Li, B.X. Dong, Y.H. Kan, and Y.Q. Lan, *Self‐Assembly of a Phosphate‐Centered Polyoxo‐Titanium Cluster: Discovery of the Heteroatom Keggin Family.* Angewandte Chemie International Edition, 2019. **58**(48): p. 17260-17264.
118. Weinstock, I.A., R.E. Schreiber, and R. Neumann, *Dioxygen in Polyoxometalate Mediated Reactions.* Chemical reviews, 2017. **118 5**: p. 2680-2717.
119. Ponomareva, O., O. Matveeva, A. Nikiforov, I. Dobryakova, I. Kasyanov, A. Shkuropatov, and I. Ivanova, *Synthesis of butadiene from Formaldehyde and Propylene on Cesium Salts of Silicotungstic heteropoly Acid.* Petroleum Chemistry, 2021. **61**(8): p. 916-924.
120. Sánchez-Velandia, J.E., H.G. Baldoví, A.Y. Sidorenko, J.A. Becerra, and F. Martínez, *Synthesis of heterocycles compounds from condensation of limonene with aldehydes using heteropolyacids supported on metal oxides.* Molecular Catalysis, 2022. **528**: p. 112511.
121. Shaari, N., N.F. Raduwan, Y.N. Yusoff, N.A.M. Harun, and N.F.H.N. Zaiman, *Membrane and catalyst in direct methanol fuel cell and direct borohydride fuel cell application*, in *Renewable Energy Production and Distribution Volume 2*. 2023, Elsevier. p. 409-458.
122. Mao, H., X. Li, F. Xu, Z. Xiao, W. Zhang, and T. Meng, *Vapour-phase selective O-methylation of catechol with methanol over metal phosphate catalysts.* Catalysts, 2021. **11**(5): p. 531.
123. Ryu, G.Y., H. Jae, K.J. Kim, H. Kim, S. Lee, Y. Jeon, D. Roh, and W.S. Chi, *Hollow Heteropoly Acid-Functionalized ZIF Composite Membrane for Proton Exchange Membrane Fuel Cells.* ACS Applied Energy Materials, 2023. **6**(8): p. 4283-4296.
124. Zhang, Y., H. Zhang, C. Bi, and X. Zhu, *An inorganic/organic self-humidifying composite membranes for proton exchange membrane fuel cell application.* Electrochimica Acta, 2008. **53**(12): p. 4096-4103.
125. Ghosh, A., *Synthesis of Graphene: Theory and Application*, in *Constraint Decision-Making Systems in Engineering*. 2023, IGI Global. p. 219-238.

126. Esrafili Dizaji, L., *Synthesis of new nano metal-organic frameworks with urea and thiourea ligands and investigation of their application in sensing, catalysis and removal of hazardous materials*. 2022, University of Antwerp.

127. Collomb, D., P. Li, and S. Bending, *Frontiers of graphene-based Hall-effect sensors.* Journal of Physics: Condensed Matter, 2021. **33**(24): p. 243002.

128. Guo, W., M. Zhang, Z. Xue, P.K. Chu, Y. Mei, Z. Tian, and Z. Di, *Extremely High Intrinsic Carrier Mobility and Quantum Hall Effect Of Single Crystalline Graphene Grown on Ge (110).* Advanced Materials Interfaces, 2023. **10**(23): p. 2300482.

129. Mbayachi, V.B., E. Ndayiragije, T. Sammani, S. Taj, and E.R. Mbuta, *Graphene synthesis, characterization and its applications: A review.* Results in Chemistry, 2021. **3**: p. 100163.

130. Sun, J., D. Han, M.M. Mohideen, S. Li, C. Wang, P. Hu, and Y. Liu, *Constructing vertical proton transport channels in proton exchange membranes of fuel cells.* International Journal of Hydrogen Energy, 2023.

131. Guo, Z., J. Chen, J.J. Byun, R. Cai, M. Perez-Page, M. Sahoo, Z. Ji, S.J. Haigh, and S.M. Holmes, *High-performance polymer electrolyte membranes incorporated with 2D silica nanosheets in high-temperature proton exchange membrane fuel cells.* Journal of Energy Chemistry, 2022. **64**: p. 323-334.

132. Porozhnyy, M., S. Shkirskaya, D.Y. Butylskii, V. Dotsenko, E.Y. Safronova, A. Yaroslavtsev, S. Deabate, P. Huguet, and V. Nikonenko, *Physicochemical and electrochemical characterization of Nafion-type membranes with embedded silica nanoparticles: Effect of functionalization.* Electrochimica Acta, 2021. **370**: p. 137689.

133. Mohamednour, A.E.E., N.A.H.M. Nordin, M.R. Bilad, S.N.A. Shafie, S.M. Hizam, and N.I.M. Nawi, *Quantifying the impact of silica hydrophilicity and loading on membrane surface properties through response surface methodology.* Journal of Materials Science, 2023. **58**(35): p. 13974-13993.

134. Pal, N. and M. Agarwal, *Advances in materials process and separation mechanism of the membrane towards hydrogen separation.* International Journal of Hydrogen Energy, 2021. **46**(53): p. 27062-27087.

135. Morariu, S. and M. Teodorescu, *Laponite®–A versatile component in hybrid materials for biomedical applications.* Mem Sci Sect Romanian Acad, 2020. **43**: p. 141-155.

136. Mohapi, M., J.S. Sefadi, M.J. Mochane, S.I. Magagula, and K. Lebelo, *Effect of LDHs and other clays on polymer composite in adsorptive removal of contaminants: a review.* Crystals, 2020. **10**(11): p. 957.
137. Dor, M., Y. Levi-Kalisman, R.J. Day-Stirrat, Y. Mishael, and S. Emmanuel, *Assembly of clay mineral platelets, tactoids, and aggregates: Effect of mineral structure and solution salinity.* Journal of colloid and interface science, 2020. **566**: p. 163-170.
138. Chen, M., C. Zhao, F. Sun, J. Fan, H. Li, and H. Wang, *Research progress of catalyst layer and interlayer interface structures in membrane electrode assembly (MEA) for proton exchange membrane fuel cell (PEMFC) system.* ETransportation, 2020. **5**: p. 100075.
139. Abyzov, A., *Aluminum oxide and alumina ceramics (review). Part 1. Properties of Al 2 O 3 and commercial production of dispersed Al 2 O 3.* Refractories and industrial ceramics, 2019. **60**: p. 24-32.
140. Liu, F., P. Dong, W. Lu, and K. Sun, *On formation of AlOC bonds at aluminum/polyamide joint interface.* Applied Surface Science, 2019. **466**: p. 202-209.
141. Kamal, A., M. Ashmawy, A.M. Algazzar, and A.H. Elsheikh, *Fabrication techniques of polymeric nanocomposites: A comprehensive review.* Proceedings of the Institution of Mechanical Engineers, Part C: Journal of Mechanical Engineering Science, 2022. **236**(9): p. 4843-4861.
142. Unnikrishnan, V., O. Zabihi, M. Ahmadi, Q. Li, P. Blanchard, A. Kiziltas, and M. Naebe, *Metal–organic framework structure–property relationships for high-performance multifunctional polymer nanocomposite applications.* Journal of Materials Chemistry A, 2021. **9**(8): p. 4348-4378.
143. Yang, S., V.V. Karve, A. Justin, I. Kochetygov, J. Espin, M. Asgari, O. Trukhina, D.T. Sun, L. Peng, and W.L. Queen, *Enhancing MOF performance through the introduction of polymer guests.* Coordination Chemistry Reviews, 2021. **427**: p. 213525.
144. Nabipour, H., X. Wang, L. Song, and Y. Hu, *Metal-organic frameworks for flame retardant polymers application: A critical review.* Composites Part A: Applied Science and Manufacturing, 2020. **139**: p. 106113.
145. Jayabal, R., *Towards a carbon-free society: innovations in green energy for a sustainable future.* Results in Engineering, 2024: p. 103121.

146. Qazi, U.Y., *Future of hydrogen as an alternative fuel for next-generation industrial applications; challenges and expected opportunities.* Energies, 2022. **15**(13): p. 4741.

147. Awan, T.I., S. Afsheen, and A. Mushtaq, *Carbon-Free Energy—Free Energy Supply*, in *Influence of Noble Metal Nanoparticles in Sustainable Energy Technologies*. 2025, Springer. p. 19-47.

148. Aminudin, M., S. Kamarudin, B. Lim, E. Majilan, M. Masdar, and N. Shaari, *An overview: Current progress on hydrogen fuel cell vehicles.* International Journal of Hydrogen Energy, 2023. **48**(11): p. 4371-4388.

149. Hwang, J., K. Maharjan, and H. Cho, *A review of hydrogen utilization in power generation and transportation sectors: Achievements and future challenges.* International journal of hydrogen energy, 2023. **48**(74): p. 28629-28648.

150. Bhandari, R. and N. Adhikari, *A comprehensive review on the role of hydrogen in renewable energy systems.* International Journal of Hydrogen Energy, 2024. **82**: p. 923-951.

151. Filippov, S.P. and A.B. Yaroslavtsev, *Hydrogen energy: Development prospects and materials.* Russian Chemical Reviews, 2021. **90**(6): p. 627.

152. Li, H., X. Qin, X.-G. Zhang, K. Jiang, and W.-B. Cai, *Boron-doped platinum-group metals in electrocatalysis: a perspective.* ACS Catalysis, 2022. **12**(20): p. 12750-12764.

153. Li, J., Y. Xu, C. Wang, Z. Wu, Y. Shiraishi, and Y. Du, *Interfacial engineering of platinum group metals electrocatalysts for advanced electrocatalysis.* Surfaces and Interfaces, 2023. **42**: p. 103360.

154. Shah, A.H., Z. Zhang, Z. Huang, S. Wang, G. Zhong, C. Wan, A.N. Alexandrova, Y. Huang, and X. Duan, *The role of alkali metal cations and platinum-surface hydroxyl in the alkaline hydrogen evolution reaction.* Nature Catalysis, 2022. **5**(10): p. 923-933.

155. Gao, G., G. Zhu, X. Chen, Z. Sun, and A. Cabot, *Optimizing Pt-based alloy electrocatalysts for improved hydrogen evolution performance in alkaline electrolytes: a comprehensive review.* ACS nano, 2023. **17**(21): p. 20804-20824.

156. Tan, H., B. Tang, Y. Lu, Q. Ji, L. Lv, H. Duan, N. Li, Y. Wang, S. Feng, and Z. Li, *Engineering a local acid-like environment in alkaline medium for efficient hydrogen evolution reaction.* Nature Communications, 2022. **13**(1): p. 2024.

157. Ferriday, T.B., P.H. Middleton, and M.L. Kolhe, *Review of the hydrogen evolution reaction—A basic approach.* Energies, 2021. **14**(24): p. 8535.

158. Hanslin, S.Ø., H. Jónsson, and J. Akola, *Is the doped MoS 2 basal plane an efficient hydrogen evolution catalyst? Calculations of voltage-dependent activation energy.* Physical Chemistry Chemical Physics, 2023. **25**(22): p. 15162-15172.

159. Mua, Y. and T. Quickenden, *Power conversion efficiency, electrode separation, and overpotential in the ferricyanide/ferrocyanide thermogalvanic cell.* Journal of The Electrochemical Society, 1996. **143**(8): p. 2558.

160. Angulo, A., P. van der Linde, H. Gardeniers, M. Modestino, and D.F. Rivas, *Influence of bubbles on the energy conversion efficiency of electrochemical reactors.* Joule, 2020. **4**(3): p. 555-579.

161. Zhang, Y., X. Zheng, X. Guo, J. Zhang, A. Yuan, Y. Du, and F. Gao, *Design of modified MOFs electrocatalysts for water splitting: High current density operation and long-term stability.* Applied Catalysis B: Environmental, 2023. **336**: p. 122891.

162. Zhu, E., M. Wu, H. Xu, B. Peng, Z. Liu, Y. Huang, and Y. Li, *Stability of Platinum-Group-Metal-Based Electrocatalysts in Proton Exchange Membrane Fuel Cells.* Advanced Functional Materials, 2022. **32**(30): p. 2203883.

163. Bernard, P., P. Stelmachowski, P. Broś, W. Makowski, and A. Kotarba, *Demonstration of the influence of specific surface area on reaction rate in heterogeneous catalysis.* Journal of chemical education, 2021. **98**(3): p. 935-940.

164. Danish, M.S.S., *Exploring metal oxides for the hydrogen evolution reaction (HER) in the field of nanotechnology.* RSC Sustainability, 2023. **1**(9): p. 2180-2196.

165. Yue, M., H. Lambert, E. Pahon, R. Roche, S. Jemei, and D. Hissel, *Hydrogen energy systems: A critical review of technologies, applications, trends and challenges.* Renewable and Sustainable Energy Reviews, 2021. **146**: p. 111180.

166. Zhang, P., S. Hong, N. Song, Z. Han, F. Ge, G. Dai, H. Dong, and C. Li, *Alloy as advanced catalysts for electrocatalysis: From materials design to applications.* Chinese Chemical Letters, 2024. **35**(6): p. 109073.

167. Jin, D., F. Qiao, H. Chu, and Y. Xie, *Progress in electrocatalytic hydrogen evolution of transition metal alloys: synthesis, structure, and mechanism analysis.* Nanoscale, 2023. **15**(16): p. 7202-7226.
168. Gebremariam, G.K., A.Z. Jovanović, A.S. Dobrota, N.V. Skorodumova, and I.A. Pašti, *Hydrogen Evolution Volcano (es)—From Acidic to Neutral and Alkaline Solutions.* Catalysts, 2022. **12**(12): p. 1541.
169. Sanchis-Gual, R., A. Seijas-Da Silva, M. Coronado-Puchau, T.F. Otero, G. Abellán, and E. Coronado, *Improving the onset potential and Tafel slope determination of earth-abundant water oxidation electrocatalysts.* Electrochimica Acta, 2021. **388**: p. 138613.
170. Ahmad, A., A. Nairan, Z. Feng, R. Zheng, Y. Bai, U. Khan, and J. Gao, *Unlocking the potential of high entropy alloys in electrochemical water splitting: a review.* Small, 2024. **20**(29): p. 2311929.
171. Ibn Shamsah, S.M., *Earth-abundant electrocatalysts for water splitting: current and future directions.* Catalysts, 2021. **11**(4): p. 429.
172. Tian, N., Z.-Y. Zhou, and S.-G. Sun, *Platinum metal catalysts of high-index surfaces: from single-crystal planes to electrochemically shape-controlled nanoparticles.* The Journal of Physical Chemistry C, 2008. **112**(50): p. 19801-19817.
173. Wang, C., Q. Zhang, B. Yan, B. You, J. Zheng, L. Feng, C. Zhang, S. Jiang, W. Chen, and S. He, *Facet engineering of advanced electrocatalysts toward hydrogen/oxygen evolution reactions.* Nano-micro letters, 2023. **15**(1): p. 52.
174. Cui, Z., W. Jiao, Z. Huang, G. Chen, B. Zhang, Y. Han, and W. Huang, *Design and synthesis of noble metal‐based alloy electrocatalysts and their application in hydrogen evolution reaction.* Small, 2023. **19**(35): p. 2301465.
175. Xu, Y., X. Zhang, Y. Liu, R. Wang, Y. Yang, and J. Chen, *A critical review of research progress for metal alloy materials in hydrogen evolution and oxygen evolution reaction.* Environmental Science and Pollution Research, 2023. **30**(5): p. 11302-11320.
176. Li, Q., X. Zhang, S. Dong, Y. Li, H. Zhao, H. Xie, Z. Wang, and C. Zhou, *Effects of doping and modulation on hydrogen evolution reaction of Pt@ MoS2 single-atom catalysts: a first-principles study.* Molecular Catalysis, 2023. **549**: p. 113485.

177. Chen, J., G. Qian, H. Zhang, S. Feng, Y. Mo, L. Luo, and S. Yin, *PtCo@ PtSn heterojunction with high stability/activity for pH-universal H2 evolution.* Advanced Functional Materials, 2022. **32**(5): p. 2107597.

178. Xie, L., Q. Liu, X. Shi, A.M. Asiri, Y. Luo, and X. Sun, *Superior alkaline hydrogen evolution electrocatalysis enabled by an ultrafine PtNi nanoparticle-decorated Ni nanoarray with ultralow Pt loading.* Inorganic Chemistry Frontiers, 2018. **5**(6): p. 1365-1369.

179. Cai, L., H. Bai, C.w. Kao, K. Jiang, H. Pan, Y.R. Lu, and Y. Tan, *Platinum–Ruthenium Dual-Atomic Sites Dispersed in Nanoporous Ni0. 85Se Enabling Ampere-Level Current Density Hydrogen Production.* Small, 2024. **20**(26): p. 2311178.

180. Chen, Z., W. Wei, and B.-J. Ni, *Cost-effective catalysts for renewable hydrogen production via electrochemical water splitting: Recent advances.* Current Opinion in Green and Sustainable Chemistry, 2021. **27**: p. 100398.

181. Liu, Y., Q. Wang, J. Zhang, J. Ding, Y. Cheng, T. Wang, J. Li, F. Hu, H.B. Yang, and B. Liu, *Recent advances in carbon-supported noble-metal electrocatalysts for hydrogen evolution reaction: syntheses, structures, and properties.* Advanced Energy Materials, 2022. **12**(28): p. 2200928.

182. Kim, H.J., H.Y. Kim, J. Joo, S.H. Joo, J.S. Lim, J. Lee, H. Huang, M. Shao, J. Hu, and J.Y. Kim, *Recent advances in non-precious group metal-based catalysts for water electrolysis and beyond.* Journal of Materials Chemistry A, 2022. **10**(1): p. 50-88.

183. Kibsgaard, J., C. Tsai, K. Chan, J.D. Benck, J.K. Nørskov, F. Abild-Pedersen, and T.F. Jaramillo, *Designing an improved transition metal phosphide catalyst for hydrogen evolution using experimental and theoretical trends.* Energy & Environmental Science, 2015. **8**(10): p. 3022-3029.

184. Bai, H., D. Chen, Q. Ma, R. Qin, H. Xu, Y. Zhao, J. Chen, and S. Mu, *Atom doping engineering of transition metal phosphides for hydrogen evolution reactions.* Electrochemical Energy Reviews, 2022. **5**(Suppl 2): p. 24.

185. Shah, S.S.A., N.A. Khan, M. Imran, M. Rashid, M.K. Tufail, A.u. Rehman, G. Balkourani, M. Sohail, T. Najam, and P. Tsiakaras, *Recent advances in transition metal tellurides (TMTs) and phosphides (TMPs) for hydrogen evolution electrocatalysis.* Membranes, 2023. **13**(1): p. 113.

186. Long, X., G. Li, Z. Wang, H. Zhu, T. Zhang, S. Xiao, W. Guo, and S. Yang, *Metallic iron–nickel sulfide ultrathin nanosheets as a highly active electrocatalyst for hydrogen evolution reaction in acidic media.* Journal of the American Chemical Society, 2015. **137**(37): p. 11900-11903.
187. Wang, H., D. Kong, P. Johanes, J.J. Cha, G. Zheng, K. Yan, N. Liu, and Y. Cui, *MoSe2 and WSe2 nanofilms with vertically aligned molecular layers on curved and rough surfaces.* Nano letters, 2013. **13**(7): p. 3426-3433.
188. Xiong, K., L. Li, L. Zhang, W. Ding, L. Peng, Y. Wang, S. Chen, S. Tan, and Z. Wei, *Ni-doped Mo 2 C nanowires supported on Ni foam as a binder-free electrode for enhancing the hydrogen evolution performance.* Journal of Materials Chemistry A, 2015. **3**(5): p. 1863-1867.
189. Wu, H., X. Lu, G. Zheng, and G.W. Ho, *Topotactic engineering of ultrathin 2D nonlayered nickel selenides for full water electrolysis.* Advanced Energy Materials, 2018. **8**(14): p. 1702704.
190. Xiang, Y., K. Xiong, L. Yu, H. Zhang, J. Chen, and M. Xia, *Tuning of crystal phase of nickel telluride nanosheets to construct superior electrocatalyst for hydrogen evolution.* Journal of Alloys and Compounds, 2022. **891**: p. 161955.
191. Gupta, S., R. Fernandes, R. Patel, M. Spreitzer, and N. Patel, *A review of cobalt-based catalysts for sustainable energy and environmental applications.* Applied Catalysis A: General, 2023. **661**: p. 119254.
192. Wang, D.-Y., M. Gong, H.-L. Chou, C.-J. Pan, H.-A. Chen, Y. Wu, M.-C. Lin, M. Guan, J. Yang, C.-W. Chen, Y.-L. Wang, B.-J. Hwang, C.-C. Chen, and H. Dai, *Highly Active and Stable Hybrid Catalyst of Cobalt-Doped FeS2 Nanosheets–Carbon Nanotubes for Hydrogen Evolution Reaction.* Journal of the American Chemical Society, 2015. **137**(4): p. 1587-1592.
193. Xu, X., W. Zhong, M. Chen, L. Zhang, G. Liu, and Y. Du, *Nanostructural Co–MoS2/NiCoS supported on reduced graphene oxide as a high activity electrocatalyst for hydrogen evolution in alkaline media.* International Journal of Hydrogen Energy, 2021. **46**(12): p. 8567-8577.
194. Zhang, J., L. Chen, Y. Fan, C. Zhao, W. Dai, L. Yang, L. Zhou, J. Zou, and X. Luo, *Unraveling the high catalytic activity of single atom Mo-doped TiO2 toward NH3-SCR: Synergetic roles of Mo as acid sites and oxygen vacancies as oxidation sites.* Chemical Engineering Journal, 2023. **465**: p. 142759.

195. Luo, X., Q. Zhou, S. Du, J. Li, L. Zhang, K. Lin, H. Li, B. Chen, T. Wu, and D. Chen, *One-dimensional porous hybrid structure of Mo2C-CoP encapsulated in N-doped carbon derived from MOF: an efficient electrocatalyst for hydrogen evolution reaction over the entire pH range.* ACS Applied Materials & Interfaces, 2018. **10**(49): p. 42335-42347.

196. Huang, C., L. Yu, W. Zhang, Q. Xiao, J. Zhou, Y. Zhang, P. An, J. Zhang, and Y. Yu, *N-doped Ni-Mo based sulfides for high-efficiency and stable hydrogen evolution reaction.* Applied Catalysis B: Environmental, 2020. **276**: p. 119137.

197. Kibsgaard, J. and T.F. Jaramillo, *Molybdenum phosphosulfide: an active, acid-stable, earth-abundant catalyst for the hydrogen evolution reaction.* Angewandte Chemie International Edition, 2014. **53**(52): p. 14433-14437.

198. Wang, X., Y. Zhang, J. Wu, Z. Zhang, Q. Liao, Z. Kang, and Y. Zhang, *Single-atom engineering to ignite 2D transition metal dichalcogenide based catalysis: Fundamentals, progress, and beyond.* Chemical Reviews, 2021. **122**(1): p. 1273-1348.

199. Zhang, B., C. Li, J. Hu, D. Peng, K. Huang, J. Wu, Z. Chen, and Y. Huang, *Cobalt tungsten phosphide with tunable W-doping as highly efficient electrocatalysts for hydrogen evolution reaction.* Nano Research, 2021. **14**: p. 4073-4078.

200. Li, F., C. Wang, X. Han, X. Feng, Y. Qu, J. Liu, W. Chen, L. Zhao, X. Song, and H. Zhu, *Confinement effect of mesopores: in situ synthesis of cationic tungsten-vacancies for a highly ordered mesoporous tungsten phosphide electrocatalyst.* ACS Applied Materials & Interfaces, 2020. **12**(20): p. 22741-22750.

201. Fu, Q., J. Han, X. Wang, P. Xu, T. Yao, J. Zhong, W. Zhong, S. Liu, T. Gao, and Z. Zhang, *2D transition metal dichalcogenides: design, modulation, and challenges in electrocatalysis.* Advanced Materials, 2021. **33**(6): p. 1907818.

202. Sukanya, R., D.C. da Silva Alves, and C.B. Breslin, *Recent developments in the applications of 2D transition metal dichalcogenides as electrocatalysts in the generation of hydrogen for renewable energy conversion.* Journal of The Electrochemical Society, 2022. **169**(6): p. 064504.

203. Huo, J., Y. Dou, C. Wu, H. Liu, S. Dou, and D. Yuan, *Defect Engineering of Metal-Based Atomically Thin Materials for Catalyzing Small-Molecule Conversion Reactions.* Advanced Materials, 2025. **37**(7): p. 2416483.

204. Rezaie, A.A., E. Lee, D. Luong, J.A. Yapo, and B.P. Fokwa, *Abundant active sites on the basal plane and edges of layered van der Waals Fe3GeTe2 for highly efficient hydrogen evolution.* ACS Materials Letters, 2021. **3**(4): p. 313-319.

205. Van Nguyen, T., M. Tekalgne, T.P. Nguyen, Q. Van Le, S.H. Ahn, and S.Y. Kim, *Electrocatalysts based on MoS2 and WS2 for hydrogen evolution reaction: An overview.* Battery Energy, 2023. **2**(3): p. 20220057.

206. Yang, F., X. Huang, C. Su, E.H. Song, B.X. Liu, and B.B. Xiao, *2D Transition Metal Chalcogenides (TMDs) for Electrocatalytic Hydrogen Evolution Reaction: A Review.* ChemPhysChem, 2024. **25**(23): p. e202400640.

207. Zhao, L., Y. Song, Z. Xie, K. Velez, Q. Liu, and Q. An, *Atomic‐Level Engineering of Transition Metal Dichalcogenides for Enhanced Hydrogen Evolution Reaction.* Small Methods, 2025: p. 2500223.

208. Lei, Y., S. Pakhira, K. Fujisawa, X. Wang, O.O. Iyiola, N.s. Perea López, A. Laura Elías, L. Pulickal Rajukumar, C. Zhou, and B. Kabius, *Low-temperature synthesis of heterostructures of transition metal dichalcogenide alloys (W x Mo1–x S2) and graphene with superior catalytic performance for hydrogen evolution.* ACS nano, 2017. **11**(5): p. 5103-5112.

209. Mondal, A. and A. Vomiero, *2D transition metal dichalcogenides‐based electrocatalysts for hydrogen evolution reaction.* Advanced Functional Materials, 2022. **32**(52): p. 2208994.

210. Gebremariam, G.K., A.Z. Jovanović, and I.A. Pašti, *The effect of electrolytes on the kinetics of the hydrogen evolution reaction.* Hydrogen, 2023. **4**(4): p. 776-806.

211. Zhang, R.Z., L.L. Lu, Z.H. Chen, X. Zhang, B.Y. Wu, W. Shi, and P. Cheng, *Bimetallic Cage‐Based Metal–Organic Frameworks for Electrochemical Hydrogen Evolution Reaction with Enhanced Activity.* Chemistry–A European Journal, 2022. **28**(28): p. e202200401.

212. Cheng, W., H. Zhang, D. Luan, and X.W. Lou, *Exposing unsaturated Cu1-O2 sites in nanoscale Cu-MOF for efficient electrocatalytic hydrogen evolution.* Science advances, 2021. **7**(18): p. eabg2580.

213. Zhu, Y., Q. Lin, Y. Zhong, H.A. Tahini, Z. Shao, and H. Wang, *Metal oxide-based materials as an emerging family of hydrogen evolution electrocatalysts.* Energy & Environmental Science, 2020. **13**(10): p. 3361-3392.

214. Tahir, A., F. Arshad, T.u. Haq, I. Hussain, S.Z. Hussain, and H.u. Rehman, *Roles of metal oxide nanostructure-based substrates in sustainable electrochemical water splitting: Recent development and future perspective.* ACS Applied Nano Materials, 2023. **6**(3): p. 1631-1647.

215. Das, C., N. Sinha, and P. Roy, *Transition metal non‐oxides as electrocatalysts: advantages and challenges.* Small, 2022. **18**(28): p. 2202033.

216. Israr, M., M. Humayun, M.H. Suliman, M. Abdinejad, T. Rasheed, A. Helal, I. Khan, M. Bououdina, C. Wang, and M. Usman, *Multi-metallic electrocatalysts as emerging class of materials: opportunities and challenges in the synthesis, characterization, and applications.* Catalysis Reviews, 2024: p. 1-61.

217. Yang, W., X. Wang, S. Song, and H. Zhang, *Syntheses and applications of noble-metal-free CeO2-based mixed-oxide nanocatalysts.* Chem, 2019. **5**(7): p. 1743-1774.

218. Wei, X., Y. Zhang, H. He, D. Gao, J. Hu, H. Peng, L. Peng, S. Xiao, and P. Xiao, *Carbon-incorporated NiO/Co 3 O 4 concave surface microcubes derived from a MOF precursor for overall water splitting.* Chemical Communications, 2019. **55**(46): p. 6515-6518.

219. Peera, S.G. and S.W. Kim, *Rare earth Ce/CeO2 electrocatalysts: role of high electronic spin state of Ce and Ce3+/Ce4+ redox couple on oxygen reduction reaction.* Nanomaterials, 2025. **15**(8): p. 600.

220. Bezkrovnyi, O., M. Szymczak, L. Marciniak, V. Seminko, P. Kraszkiewicz, M. Małecka, M. Pawlyta, M. Vorochta, and I. Matolínová, *Advances and Limitations of the Eu3+ Luminescent Probe for Monitoring Ce4+/Ce3+ Transitions in Ceria.* The Journal of Physical Chemistry C, 2025.

221. Zhang, Y., W. Liao, and G. Zhang, *A general strategy for constructing transition metal Oxide/CeO2 heterostructure with oxygen vacancies toward hydrogen evolution reaction and oxygen evolution reaction.* Journal of Power Sources, 2021. **512**: p. 230514.

222. Singh, K.P., C.-H. Shin, H.-Y. Lee, F. Razmjooei, A. Sinhamahapatra, J. Kang, and J.-S. Yu, *TiO2/ZrO2 nanoparticle composites for electrochemical hydrogen evolution.* ACS Applied Nano Materials, 2020. **3**(4): p. 3634-3645.

223. Munawar, T., S. Fatima, F. Iqbal, A. Bashir, M. Rafaqat, Z. Tu, L. Shen, S.A. Khan, M. Koc, and C.-F. Yan, *Enhanced electrochemical performance of ZrTe-Mn2O3 nanocomposite electrocatalyst for HER and OER in alkaline medium.* Fuel, 2025. **381**: p. 133197.

224. Groß, A., *Reversible vs standard hydrogen electrode scale in interfacial electrochemistry from a theoretician's atomistic point of view.* The Journal of Physical Chemistry C, 2022. **126**(28): p. 11439-11446.

225. An, Z., R. Jia, Q. Li, D. Zhang, X. Du, W. Li, and T. Shi, *Safety of LiFePO4/Graphite Li-ion pouch batteries under simulated external short-circuit (high rate) conditions.* Journal of Power Sources, 2025. **629**: p. 236038.

226. Komsiyska, L., T. Buchberger, S. Diehl, M. Ehrensberger, C. Hanzl, C. Hartmann, M. Hölzle, J. Kleiner, M. Lewerenz, and B. Liebhart, *Critical review of intelligent battery systems: Challenges, implementation, and potential for electric vehicles.* Energies, 2021. **14**(18): p. 5989.

227. Edgington, J., A. Deberghes, and L.C. Seitz, *Glassy carbon substrate oxidation effects on electrode stability for oxygen evolution reaction catalysis stability benchmarking.* ACS Applied Energy Materials, 2022. **5**(10): p. 12206-12218.

228. Wachs, I.E., *Number of surface sites and turnover frequencies for oxide catalysts.* Journal of Catalysis, 2022. **405**: p. 462-472.

229. Zaman, N., T. Noor, and N. Iqbal, *Recent advances in the metal–organic framework-based electrocatalysts for the hydrogen evolution reaction in water splitting: a review.* RSC advances, 2021. **11**(36): p. 21904-21925.

230. Rafiee, M., D.J. Abrams, L. Cardinale, Z. Goss, A. Romero-Arenas, and S.S. Stahl, *Cyclic voltammetry and chronoamperometry: mechanistic tools for organic electrosynthesis.* Chemical Society Reviews, 2024. **53**(2): p. 566-585.

231. Sun, X., X. Zhang, K. Wang, Y. An, X. Zhang, C. Li, and Y. Ma, *Determination strategy of stable electrochemical operating voltage window for practical lithium-ion capacitors.* Electrochimica Acta, 2022. **428**: p. 140972.

# CHAPTER 3: EXPERIMENTAL

## 3. Instrumentations and methods

This chapter is an overview of various instrumentation techniques, such as Fourier transform infrared (FTIR), Raman, Thermogravimetric analysis (TGA), Brunauer-Emmet-Teller (BET), X-ray diffraction (XRD) spectroscopy, X-ray photoelectron spectroscopy (XPS), ultraviolet-visible (UV-vis) spectrometer, photoluminescence (PL), scanning electron microscopy (SEM) and Transmission electron microscopy (TEM) used in characterising all synthesized samples. The overview encompasses a brief detailed discussion on the theoretical aspects, working principles and instrumentation infrastructures. The materials and methods associated with different studies are described in the respective following chapters.

## 3.1. Fourier transform infrared spectroscopy (FTIR)

In analytical infrared-based studies, absorption or reflection of electromagnetic radiation should be between 1-1000 mm. The infrared (IR) region of the electromagnetic spectrum is generally subdivided into near IR (500 – 4000 cm$^{-1}$), mid IR (4000– 400 cm$^{-1}$) and far IR (400–50 cm$^{-1}$). The mid-IR is most commonly employed for laboratory investigations since it covers the vibrational transitions. The FTIR spectroscopy is a crucial instrumental tool for determining the chemical structure of a compound through the functional group associated with that particular chemical structure. This tool provides absorption information measurements of various infrared frequencies presented in the form of spectrum.

### 3.1.1 Working principle of FTIR

Fig. 3.1 illustrates a typical working principle of an FTIR instrument. In a typical working FTIR, the sample is mounted in a sample holder in the path of IR radiation. The Infrared beam enters the ATR crystal and becomes reflected through the crystal to the sample interface. The molecules of the sample are excited to a higher energy state after absorbing IR energy from a polychromatic IR radiation source that passes through the sample. The beam reflectance creates a momentary wave that is altered in the region of the IR spectrum where the specimen absorbs energy. The attenuated energy of the specimen then passes back to the IR beam after one or several reflections, which then exits the attenuated crystal and gets directed to the IR detector. The absorbed IR energy characterizes the molecular structure or chemical bonding of the sample material. The complete IR spectrum of a sample can then be obtained over a wide range of frequencies. Different electronic structures resulting from the different atomic group symmetry governs the provision of the unique absorption patterns of every material.

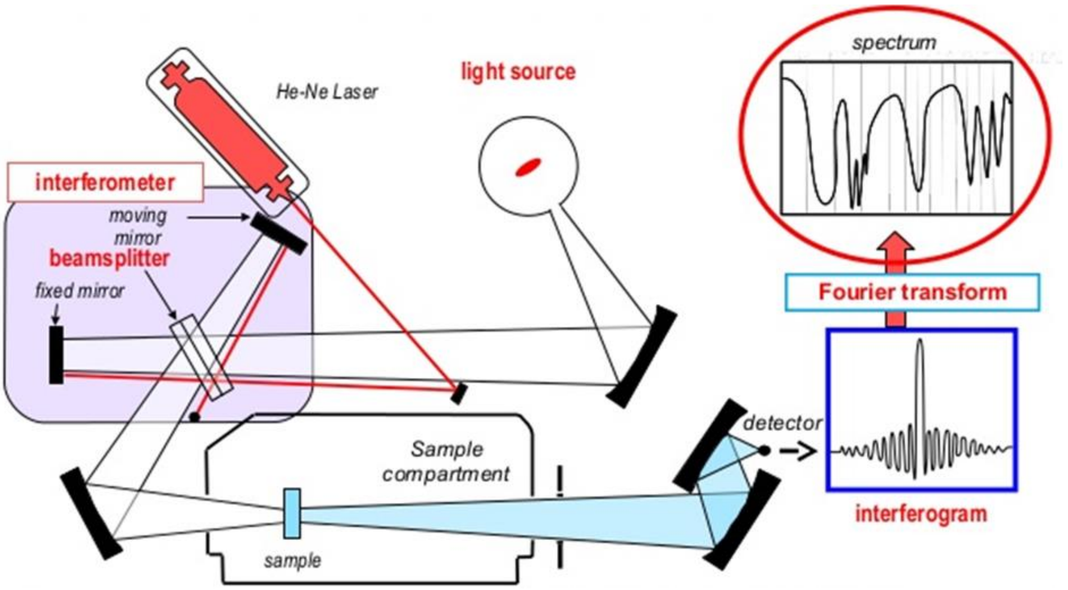

**Fig. 3. 1:** *Schematic diagram of Bruker Vertex 70 FTIR working principle.*

### 3.1.2 FTIR instrumentation

Fourier transform spectrometers is one of the infrared instrument categories (FTIR) which contains a single beam optical assembly with an interferometer component (often of Michelson type) located between the source and the sample. The spectrometry was developed in order to overcome the limitations encountered with dispersive instruments such as the slow scanning process. Employing an interferometer optical device allowed the reduction of time element per sample measurement from minutes to few seconds. Most interferometers use a beam splitter to divide the incoming infrared beam into two optical beams. One beam reflects off on a flat mirror in a fixed position while the other reflects off on a flat mirror in a manner that allows the mirror to move a short distance away from the beam splitter. The two beams reflecting off from their respective mirrors are recombined when they meet at the beam splitter. The resulting signal is called interferogram.

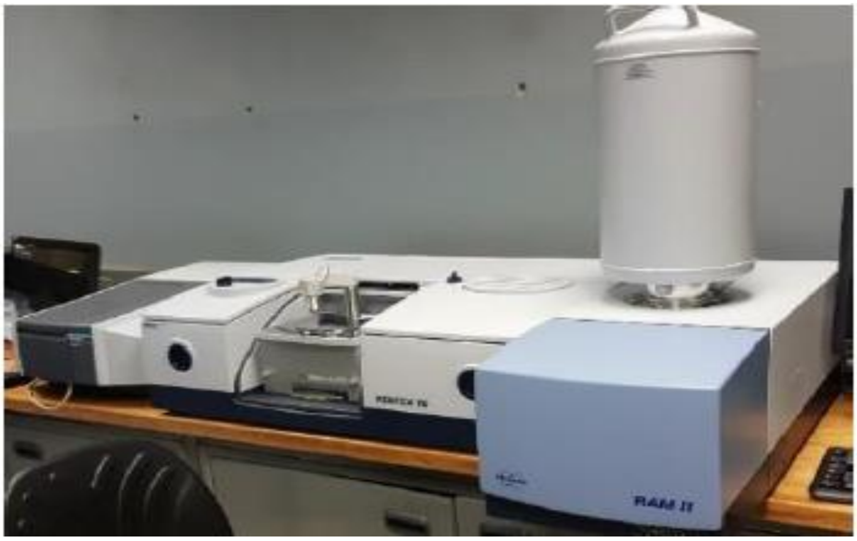

**Fig. 3. 2:** Bruker Vertex 70 FTIR spectroscopy.

The signal has information about every infrared frequency which comes from the source thus allows frequencies to be measured simultaneously. “Decoding” of interferogram signal is attained mathematically via Fourier transformation technique in order to make identification of measured frequencies. Bruker Vertex 70 FTIR spectrometer, in Fig. 3.2, was used to record sample spectra, for this study.

## 3.2. Raman spectroscopy

Raman spectroscopy is a versatile non-destructive light scattering technique that can be used qualitatively and quantitatively, to probe the molecular vibrations of a sample. The technique is based on the frequency of a small fraction of a scattered radiation called Raman effect. The Raman effect where the scattered photons have an energy or wavelength that is either greater or smaller than that of the incident radiation light, is said to be inelastic. Only molecular object whose major dimension is less than 1-1.5 wavelengths will scatter light, while others will diffusely reflect it. The selection of the laser is critical not only for the lateral resolution but also for any broad fluorescence background influencing prominent Raman bands. The commonly used solid-state laser emits at 785 nm. However, the Raman scattering is approximately five times less intense than a 532 nm excitation source.

### 3.2.1 Working principle of Raman spectroscopy

Fig. 3.3 illustrate a typical working principle of Raman spectroscopy. The sample is irradiated with a monochromatic laser beam that interact with sample molecule to initiate the Raman light scattering. During Raman scattering process, the photon of the laser radiation interacts with characteristic vibrational modes of the molecules due to polarizability. The shift causes the photon to either loss or gain of energy and provide information on the vibration, rotational and other low frequency transitions in molecules. Detection of scattered light is presented as spectrum.

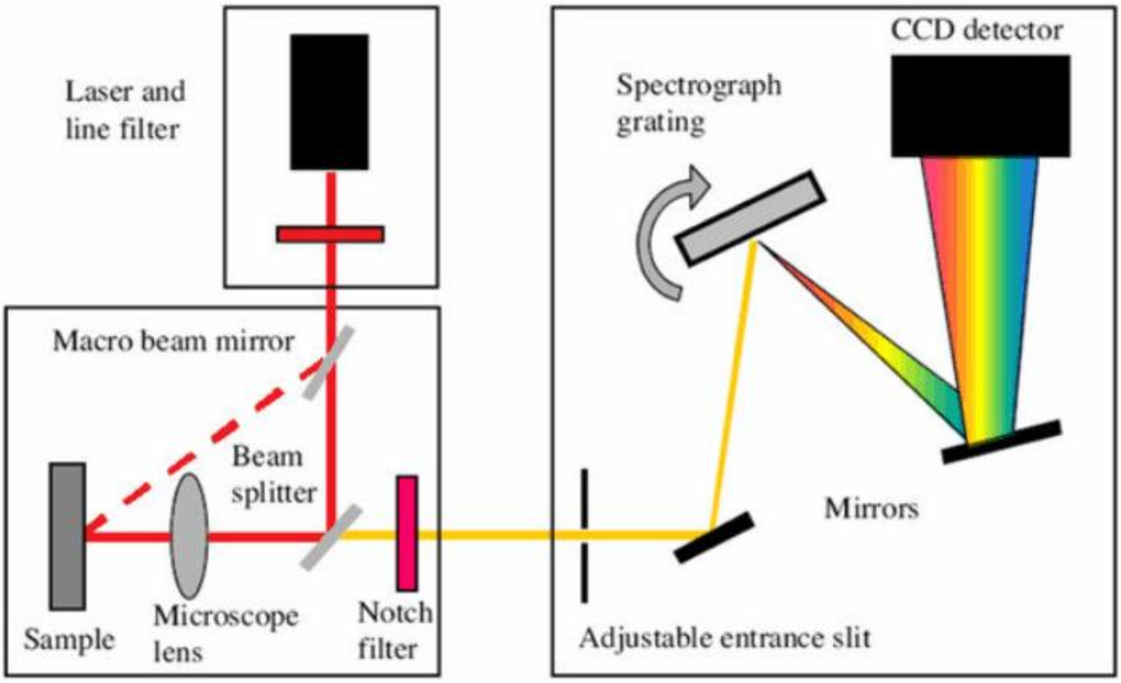

**Fig. 3. 3:** Schematic diagram of working principle of Raman spectroscopy [1].

Spectrum obtained comprises of number of peaks, which are indicative of particular chemical bonds and their vibrations. Raman spectroscopy technique can be used to examine the solid, liquid and gaseous samples.

### 3.2.2 Raman instrumentation

Raman spectrophotometers can be dispersive or non-dispersive. Dispersive instrument use prism or grating while the non-dispersive spectrophotometer uses interferometer, such as Michelson interferometer as in FTIR spectrophotometer. The Raman spectra cover the range of 4000–10 $cm^{-1}$, depending on the spectrophotometers design and optical components. Fig. 3.4 illustrate a typical WITech Alpha300 Raman spectroscopic instrument.

**Fig. 3. 4:** Raman spectroscopy analyzer.

The instrument consists of light source, sample cell (or glass), beam filters, grating monochromators, optical lens, photomultiplier tubes and detectors. The WITech Alpha300 Raman spectroscopy (Germany) was used for this study to obtain spectral analysis, with argon ion ($Ar^+$) laser light of wavelength (l) = 532 /514 nm at room temperature.

## 3.3. Thermogravimetric analyzer (TGA)

Thermogravimetric analyzer (TGA) is an analytical tool frequently used to measure the change on a sample mass as a function of temperature over time, under a controlled temperature programmed. It provides an information for the measure of the structural decomposition where a mass loss is recorded during heating process and predicts the thermal stability of the material. TGA instrument can detect and quantify the presence of bulk water or hygroscopic water within the sample. It also provides the thermal stability information at which the material may start to decompose and how many different stages or steps are involved during degradation.

### 3.3.1 Working principle of TGA

The instrument comprises of a sample holder connected to precision balance that is located inside a furnace, a sensor detector to measure the sample parameters and temperature, an enclosure to control the experimental parameter, and a computer for electronic collection and processing of data. Aluminium or platinum pan is used to hold the sample. The sample is then heated in an electronic furnace at a preferred heating rate, *i.e.*, 5 °C or 10 °C min$^{-1}$. Platinum pan is usually employed for sample analysis required at extremely high temperatures. The sample analysis may be performed under various pressures (such as constant pressure, high pressure, or high vacuum) and atmospheres (such as but not limited to vacuum, oxidising or reducing gases, corrosive gases, ambient air, or inert gas). The sample weight changes from the TGA measurements are quantified and plotted against temperature to obtain the thermal curve called thermogram. Thermogram curve provide the extent of the thermal stability of the sample.

### 3.3.3 TGA instrument

In this study, a Perkin-Elmer Pyris 1 thermogravimetric analyser (TGA) was used as shown in Fig.3.5. The thermal degradation of the samples was evaluated from 30 to 900 °C at a heating rate of 10 °C min$^{-1}$ under nitrogen atmosphere with 20 ml min$^{-1}$. The sample masses were ~10 mg.

**Fig. 3. 5:** Perkin Elmer Pyris 1 TGA spectroscopy analyzer.

## 3.4. Surface area analysis

Evaluation of surface area of a sample, especially in a powder form, is an important physical property of a solid phase chemical that impact its utility and quality. The commonly applied technique for surface area measurement is a Brunauer-Emmet-Teller (BET).

### 3.4.1 Working principle of BET

BET measures surface area based on physical adsorption of gas or vapour on a surface of a solid sample and the analysis provide the specific surface area of a sample. The amount of adsorbate (gas) corresponding to a monomolecular layer on the surface measured as a function of relative pressure can be calculated. The analysis provides the specific surface area of the sample. Measuring the pressure of the gas above the sample as a function of the volume of the gas into the chamber using the micromeritics gas adsorption analyser, provides an adsorption isotherm. Surface area of the material and specific surface area ($S_{BET}$) can be calculated using BET equations **3.1** and **3.2**, respectively as follows:

$$\frac{1}{V\left[\left(\frac{Po}{P}\right)-1\right]} = \frac{C-1}{VmC} \text{ x} \left(\frac{P}{Po}\right) + \frac{1}{VmC} \qquad \textbf{(3.1)}$$

P= equilibrium pressure of the adsorbate $P_o$ = saturation pressure of the adsorbate at the temperature of adsorption, n = amount of gas adsorbed (in volume units), $n_m$ = volume of the gas required to form a monolayer, c= BET constant.

$$S_{BET} = 0.269\ n_m\ s_m \qquad \textbf{(3.2)}$$

$s_m$= area that one adsorbed molecule will occupy in a complete monolayer.

### 3.4.2 BET instrumentation

Brunauer, Emmett, Teller adsorption technique applying nitrogen ($N_2$) isotherm under vacuum, was used to determine the surface area of prepared samples. Micromeritics TriStar II 3020 BET instrument was used for analysis in this study. Fig. 3.6 illustrate a micromeritics TriStar II 3020 instrument.

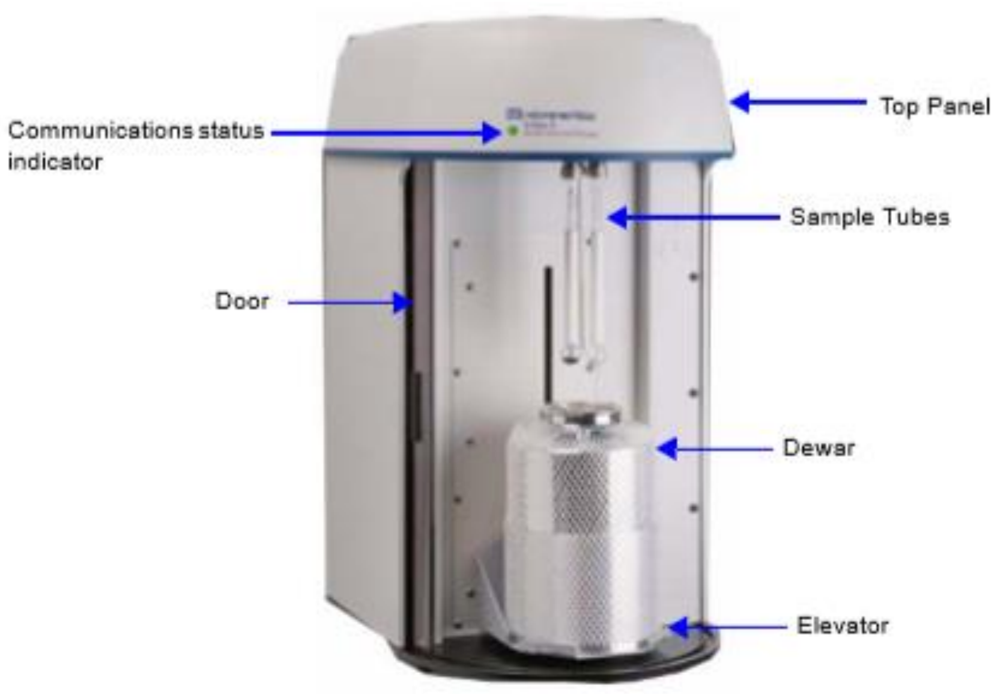

**Fig. 3. 6:** Micromeritics Trista II 3020 analyzer

## 3.5. X-ray diffraction spectroscopy (XRD)

X-ray diffraction is a versatile, non-destructive technique that depicts detailed information about the chemical composition and crystallographic structure of natural and man-made samples. The technique allows to determine whether a sample to be analysed has crystalline or amorphous nature. X-ray powder diffraction technique is unique in that it is capable of providing qualitative and quantitative information about compounds present in a solid sample. The constituent particles: atoms, ions or molecules; in a crystalline solid are arranged in a regular order.

### 3.5.1 Working principle of XRD

For analytical diffraction studies, a finely grounded homogeneous powder is placed in a thin-walled glass. XRD is based on constructive interference of monochromatic X-rays from a crystalline sample. When the crystals of a powdered solid are randomly orientated, then some of the crystals in the powder will be in the correct horizontal orientation with respect to the X-ray source, for all sets of planes ($h\ k\ l$), in order to satisfy Bragg's law for angle $q$. At least few of the mineral grains in a powder will diffract X-ray beam for each of the planes ($h\ k\ l$) during a scan through the angles.

The focused x-rays generated from a cathode tube is filtered to produce a monochromatic radiation, and a collimated beam is directed towards the sample. When the focused beam interacts with atomic planes causes the beam to go through modification stages such as transmission , absorption, refraction, scattering and diffraction, to provide a peak intensity when conditions satisfy Bragg’s law, given by equation (**3.3**):

$$2d\ \mathrm{Sin}q = nl \qquad \textbf{(3.3)}$$

$d$ =spacing between the planes in the atomic lattice, $q$ = angle between the incident ray and the scattering planes, $n$ = an integer, $l$ = wavelength of the incident wave. The correlation between the wavelength of electromagnetic radiation to the diffraction angle and the lattice spacing in a crystalline sample is described by this equation (**3.3**). The sample in X-ray diffractometer rotates at an angle q and the X-ray detector rotates at an angle of 2q in order to collect the diffracted X-rays and record the intensity of the reflected X-rays. Characteristic of the sample diffraction pattern is obtained by plotting the angular position (2q) and intensities of the diffracted peaks of radiation. Fig. 3.7 illustrate a working principle of XRD spectroscopy.

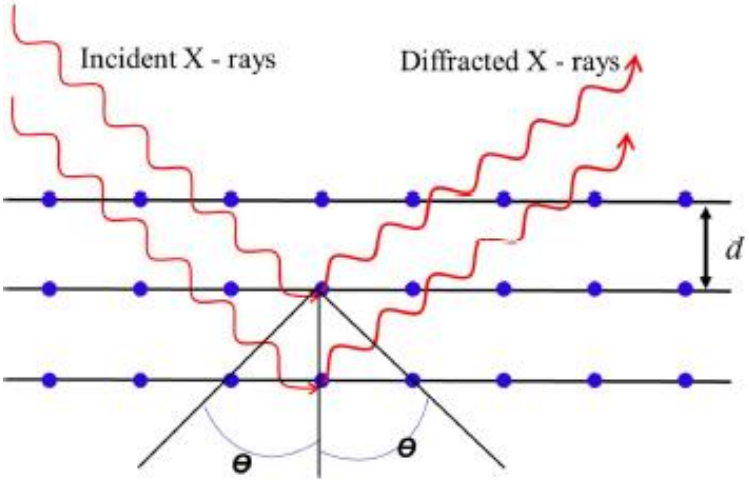

**Fig. 3. 7:** Schematic diagram of X-ray diffractometer working principle.

### 3.5.2 Powder X-Ray Diffraction (XRD)

Generally, a typical X-ray diffractometer consists of radiation source, a monochromator to select the wavelength, slits for adjustment of the beam shape, a sample and a detector. The goniometer is used for fine adjustment of the positions of a sample and the detector. The common component of the X-ray source includes $K_\alpha$ and $K_\beta$. while the specific wavelengths are characteristics of the target materials such as tungsten (W), rhodium (Rh), molybdenum (Mo), chromium (Cr), copper (Cu), or cobalt amongst others.

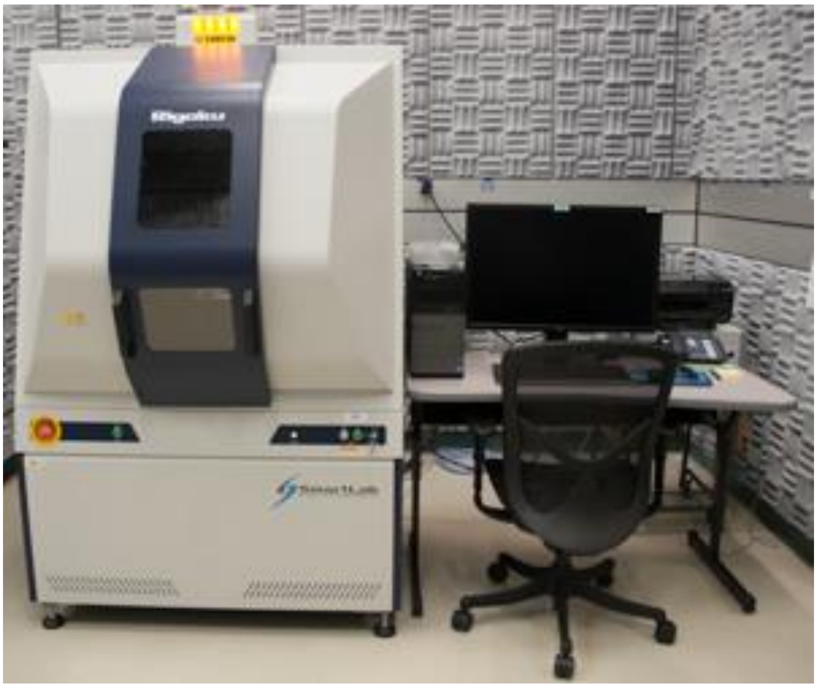

**Fig. 3. 8:** Rigaku SmartLab 9KW X-ray diffraction instrument.

Filters and monochromators are used to absorb the unsolicited emissions with wavelength $K_\beta$ while allowing $K_\alpha$ (desired wavelength) to pass through. Copper has a characteristic wavelength for $K_\alpha$ radiation of 1.5418 Å and has been frequently used as X-ray radiation source. The diffracted beam in every possible 2q from a sample after radiation can be detected through a movable detector (for example, Geiger counter) that is connected to the signal recorder. In this study, XRD sample spectra were recorded using Rigaku SmartLab X-ray diffractometer (Japan) with monochromatic Cu-Ka radiation source (l = 1.54 Å), 45 kV and 200 mA. The 2q scanning range of 5-90° was used. Fig. 3.8 illustrates the Rigaku SmartLab XRD analyser.

## 3.6 Ultraviolet-visible (UV-vis) spectrophotometer

UV-visible is an analytical instrument used for both qualitative and quantitative analysis of a sample. The absorption spectroscopy employs electromagnetic radiations to provide information regarding the adsorption of ultraviolet or visible radiation of different substance in the visible or ultraviolet region, mainly in 190-900 nm. Optical properties of materials can be studied with the help of UV-vis spectra.

### 3.6.1 Working principle of UV-vis spectrophotometer

Absorption of radiation energy ($E = hv$, **E** is energy in joules, $h$ is Planck's constant of $6.62 \times 10^{-34}$ J s and $v$ *is* frequency in Hertz) at a wavelength by various inorganic metals or ions, exhibit absorption in the visible or ultraviolet region of the electromagnetic radiation that effect the electronic transition within the structure. Qualitative information regarding the electronic structure of the sample is determined by the wavelength at which maximum adsorption occurs. Intensity of the light passing through the sample ($I$) and compared with light intensity before passing through the sample ($I_0$) is measured by UV-vis spectrometer at defined wavelength using the formula (**3.4**):

$$A = \log_{10} (I/I_0), \qquad \textbf{(3.4)}$$

A is the absorbance at a defined wavelength. Quantitative information of the sample relate to the concentration of the absorbing species in the solution, is determined using the Lambert-Beer law as given in equation (**3.5**):

$$A = \varepsilon.\ c.\ L \qquad \textbf{(3.5)}$$

ε = molar absorption coefficient, c = concentration of the analyte species in the solution, L=path length of the light in the sample.

### 3.6.2 UV-vis instrumentation

Generally, UV-vis spectrometer consists of five components that includes the source, monochromator, sample holder (cuvette or glass slides in case of powder sample analysis), detector and signal processor. Deuterium discharge lamp is the usual light source for UV measurements while tungsten-halogen lamp serves as the light source for visible and near-infrared (NIR) measurements. The instruments swap the lamps automatically when scanning between the UV and visible region. Light from lamp source passes through the slits then enters the monochromator. Monochromatic light passes through several sets of mirrors that resulted in splitting of a beam into two halves where one gave rise to reference beam and the other is referred to as sample beam since it is directed towards the sample and passes through the sample.

**Fig. 3. 9:** Perkin-Elmer UV-vis instrument.

Sample and the reference are kept in transparent quartz sample holders. Fig. 3.9 illustrate a typical working UV-vis spectrometer. In this work Perkin-Elmer UV-Lambda 6505 was used to characterize the optical properties of the synthesised powdered materials.

## 3.7. Scanning electron microscopy SEM

The detailed knowledge of the physical nature and chemical composition of the surfaces of solids on a submicrometer scale is important for investigation of surface morphology of the sample. SEM is a non-destructive technique; thus, the sample volume is not affected generated X-rays from the sample’s interaction with electron and same sample can be used repeatedly.

### 3.7.1 Working principle of SEM

To perform an electron microprobe analysis and obtain an electron microscopic image the following procedural steps must occur repeatedly; (1) the surface of a solid sample is brushed in a raster pattern with a finely focused beam of electrons in a straight line, (2) beam is returned to its starting position, and (3) shifted downwards by a standard increment.

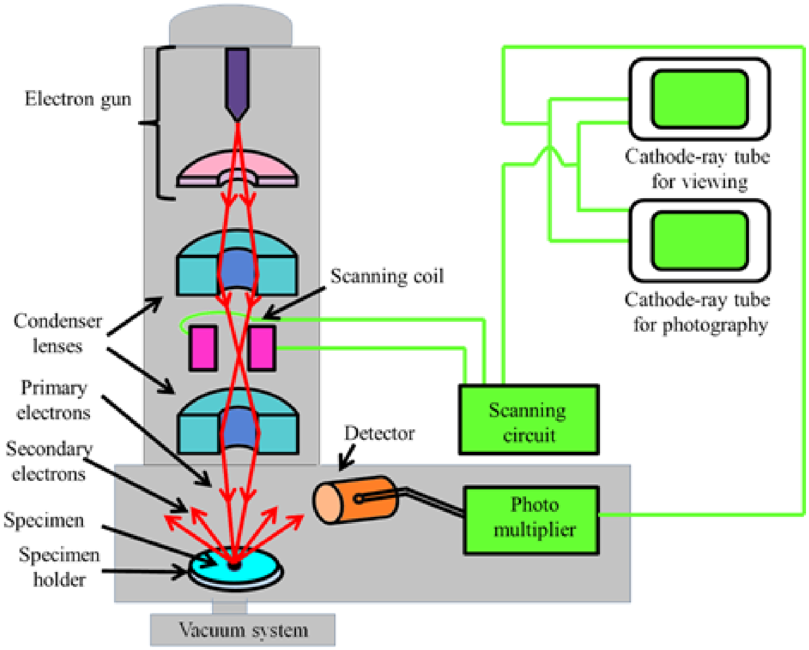

**Fig. 3. 10:** Schematic representation of SEM instrument.

Several types of signals are produced from the surface after being scanned with energetic beam of electrons, as injected into the system by means of electron gun. External morphology, chemical composition and crystallographic structure of the material are determined by these signals. The signals include backscattered and secondary electrons (serve as basis of SEM), auger electrons, X-ray fluorescence (used in electron microprobe analysis) and other photons of various energies. The microscope chamber must be used under vacuum to prevent electron and gas molecule collision that my lead to diminishing of microscope resolution, while low kV primary electron is essential to avoid beam penetration into the sample necessary. The schematic representation of a working principle of SEM is shown on Fig. 3.10.

Typical essential components of a SEM include electron source (gun), electron lenses, a sample stage, detectors for all signals of interest, display data output devices. High energy electrons generated by a field emission source in a high vacuum condition are accelerated by a field gradient, allowing the passing through of electromagnetic set of lenses, focussing onto the sample. Small quantity of a natural of synthesised sample is sprinkled on a metal stump containing a double-sided carbon tape and the excess sample is removed by gently blowing it away with a duster spray. Structural morphology and compositions of samples were obtained using Field emission scanning electron microscopy (JOEL JSM-610 Plus) attached to the energy dispersed X-ray spectrometer (EDS), shown in Fig. 3.11. The samples for SEM analysis were first dried at ambient temperatures prior to being carbon coated as preparatory step for analysis.

**Fig. 3. 11:** FE-SEM JSM 610 Plus instrument

## 3.8. Transmission electron microscopy (TEM)

Transmission electron microscope is essential technique to analyse the atomic and molecular arrangement of a sample at an atomic scale. The technique allows to study the size, shape and the internal structure of nanoparticles.

### 3.8.1 Working principle of TEM

TEM working principle is like that of SEM and allows provision of higher resolution images using high energy electron beam (~60-3000 kV). Fig. 3.12 illustrate the schematic diagram of a TEM instrument. The high energy electron beam is ejected from electron gun fitted with tungsten filament cathode as electron source and focussed through series of electromagnetic lenses. Ejected electron beam passes through the sample, get transmitted after interacting with the sample. Electron beam emerged from the sample carries the information about the fine structure of a sample that is transformed into an image and can be observed on fluorescent screen. Generally, TEM image resolution is in the range of few nanometres. The resolution may be restricted by spherical deviation, however that drawback can be overcome by high resolution transmission electron microscopy (HR-TEM) by producing images of resolution below 0.5 angstrom (Å).

### 3.8.2 TEM instrumentation

TEM instrument consists of an electron emission source, electromagnetic lens system, sample holder, and imaging system. The system permits only electrons within small energy range to pass through to have the electrons of the beam with a well-defined energy. The transmitted beam replicates the pattern on the sample and get projected onto a phosphor screen. Microstructural images of all research samples were observed using JEOL field emission electron microscope (JEM-2100F) analyzer at an accelerating voltage of 200 kV. Sample preparation began by dispersing the sample in alcohol, sonicated, and then drop casted on a carbon coated copper (Cu) grid.

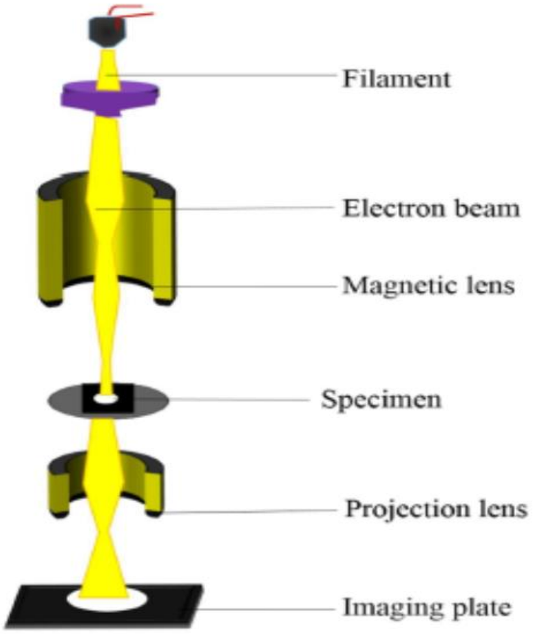

**Fig. 3. 12:** Schematic diagram of TEM microscopy.

## 3.9. Electrochemical studies

Cyclic voltammetry (CV) and Electrochemical impedance spectroscopy (EIS) studies were performed within a potential window of -0.3 and +0.70 V and at $1 \times 10^5$ Hz to 0.1 Hz frequency with the applied potential of 0.24 V *using* a three-electrode cell (TEC) connected to a Metrohm Autolab Potentiostat (PGSTAT30) equipped with Nova software version 2.1. The TEC consists of platinum wire, Ag/AgCl (3M KCl) and as-synthesized materials on graphite electrode as counter, reference and working electrode respectively.

## 3.10. The membrane properties

### 3.10.1. Proton conductivity measurement

Proton conductivities of the composite membranes were measured by AC impedance spectroscopy using an electrochemical workstation (Autolab PGSTAT302N, Switzerland) in the frequency range of 1 MHz to 100 Hz with an amplitude of 5 mV. Prior to testing, all membranes were hydrated by immersion in deionized water for 24 h at room temperature. A sample of the pre-hydrated membrane was wrapped around graphite electrode, then the tip of the covered electrode was immersed in H2SO4 0.5M during proton conductivity measurement. The proton conductivity (σ) was calculated as follows:

$$\sigma = \frac{\mathrm{l}}{\mathrm{RA}} \qquad \textbf{(3.6)}$$

where L, refers to the thickness of the membrane (2.16 cm), R= resistance of the membrane (Ω) and A= cross-sectional area ($cm^2$).

### 3.10.2 Ion Exchange Capacity

The ion exchange capacity provides information on the density of ionizable functional groups present in the membrane matrix, which are responsible for the charged nature of the membrane and thus membrane conductivity [2]. IEC is a measure of the number of counter ions exchangeable in SPEEK. IEC is defined as the milliequivalents of $H^+$ per weight of the dry polymer. The prepared SPEEK membranes were stored in 1 M HCl for 24 hours to bring the sample into complete SPEEK-$H^+$ form. Membranes were then rinsed in DI water and equilibrated in 1 M NaCl solutions for 24 hours to completely exchange the cations and achieve SPEEK-$Na^+$ form. The ion exchange capacity was measured using the back-titration method as described in several previous papers [3-5]. The NaCl solution was back titrated with 0.01 M NaOH using phenolphthalein as an indicator to determine the cations exchanged. The IEC was calculated as the ratio of total charge by dry weight of the membrane samples.

$$\mathrm{IEC} = \frac{C_{\mathrm{NaOH}} V_{\mathrm{NaOH}}}{m_{\mathrm{dry}}} \quad \textbf{(3.7)}$$

Where, $C_{NaOH}$ is the concentration of the sodium hydroxide solution used, $V_{NaOH}$ is the volume of NaOH solution consumed in the titration and $m_{dry}$ is the dry weight of the membrane.

### 3.10.3 Oxidative stability

The oxidative stability of SPEEK and SPEEK/SZr:$SiO_2$ composite membranes was studied using Fenton's test. Fenton's reagent was prepared by producing a solution with 3 vol% of hydrogen peroxide and 3 ppm of $F^{2+}$ ions. The weight of the dried membrane was measured before immersing it into the Fenton's reagent at different temperatures. The membranes were constantly weighed (every 10 minutes) and the change in dried weight of the membrane was used to evaluate its degradation oxidative stability as shown in Equation (3.8).

$$\text{Oxidative stability (\%)} = \frac{W_{\mathrm{dry}}}{W_{\mathrm{initial}}} \times 100 \quad \textbf{(3.8)}$$

where: $W_{dry}$ is the dry weight of the membrane after Fenton’s test (g) and $W_{initial}$ is the initial dry weight of the membrane (g).

### 3.10.4 Water uptake and dimensional swelling

Water uptake and dimensional swelling/swelling ratio were measured in the temperature range 25–80 °C. For the water uptake measurement, a membrane was first equilibrated in deionized water at the target temperature for 8 hours and weighted immediately after the removal of surface water (Wwet). The membrane was then vacuum dried for approximately 2 hours at 60 °C so that it reached a constant weight (Wdry). The water uptake (WU) of the membrane was calculated as:

$$\mathrm{WU} = \frac{(\mathrm{W_{wet}} - \mathrm{W_{dry}})}{\mathrm{W_{dry}}} \times 100 \qquad \textbf{(3.9)}$$

The measurement of membrane dimensional swelling proceeded similarly. Firstly, the membrane was cut into a strip with predetermined dimensions (2cm in length and 1 cm in width) and equilibrated in water at the target temperature for 8 h to obtain the wet length (Lwet). The sample was then dried in vacuum at 60 °C to yield the dry length (Ldry). The extent of water swelling (SR) of the membrane was calculated as:

$$\mathrm{SR} = \frac{(\mathrm{L_{wet}} - \mathrm{L_{dry}})}{\mathrm{L_{dry}}} \times 100 \qquad \textbf{(3.10)}$$

## 3.11. Preparation of MEA and evaluation of single-cell performance

The performance of the resulting membrane was evaluated in a PEMFC single cell. The MEA preparation method was adapted from techniques utilized by Wu et al. [6] and Moreira et al. [7] with some modifications.The electrode and gas diffusion layer (GDL) were created using a brushing method. The palladium catalyst (Pd/C, 10%) was mixed with isopropanol and deionized (DI) water in a volumetric ratio of 6:4 (catalyst to solution) to prepare the ink slurries. Next, a 5 wt.% SPEEK solution was used as a binder at a ratio of 6:2 (catalyst to SPEEK solution) and sonicated for 40 minutes. The GDL was prepared by brushing the slurry onto carbon paper with a palladium loading of 0.2 mg. The coated materials were then dried at 60 °C under vacuum for 5 hours. Single cell experiments were performed by measuring the voltage–current density curves, placing the MEA in a commercial fuel cell hardware. Hydrogen and oxygen gas were fed to the anode and the cathode, respectively. A voltage of 0.6 V was applied to the cell for 5 minutes prior to each polarization curve in order to activate the electrocatalysts

## 3.12. References

1. Broadbent, B., J. Tseng, R. Kast, T. Noh, M. Brusatori, S.N. Kalkanis, and G.W. Auner, *Shining light on neurosurgery diagnostics using Raman spectroscopy.* Journal of neuro-oncology, 2016. **130**: p. 1-9.
2. Zuo, P., Z. Xu, Q. Zhu, J. Ran, L. Ge, X. Ge, L. Wu, Z. Yang, and T. Xu, *Ion exchange membranes: constructing and tuning ion transport channels.* Advanced Functional Materials, 2022. **32**(52): p. 2207366.
3. Yee, R.S., K. Zhang, and B.P. Ladewig, *The effects of sulfonated poly (ether ether ketone) ion exchange preparation conditions on membrane properties.* Membranes, 2013. **3**(3): p. 182-195.
4. Sgreccia, E., C. Rogalska, F.S. Gallardo Gonzalez, P. Prosposito, L. Burratti, P. Knauth, and M.L. Di Vona, *Heavy metal decontamination by ion exchange polymers for water purification: counterintuitive cation removal by an anion exchange polymer.* Journal of Materials Science, 2024. **59**(7): p. 2776-2787.
5. Li, H., X. Ren, J. Dong, X. Che, R. Liu, and J. Yang, *Anion exchange membranes based on sulfonated poly (ether ether ketone) crosslinked methylpyrrolidinium functionalized poly (vinyl benzyl chloride) with high chemical stability.* Journal of The Electrochemical Society, 2019. **166**(15): p. F1134.
6. Wu, X., J. Benziger, and G. He, *Comparison of Pt and Pd catalysts for hydrogen pump separation from reformate.* Journal of Power Sources, 2012. **218**: p. 424-434.
7. Moreira, J., P. Del Angel, A. Ocampo, P. Sebastian, J. Montoya, and R. Castellanos, *Synthesis, characterization and application of a Pd/Vulcan and Pd/C catalyst in a PEM fuel cell.* International Journal of Hydrogen Energy, 2004. **29**(9): p. 915-920.

## CHAPTER 4: HYDROGEN EVOLUTION ON GRAPHITE/SULFATED POLYETHER ETHER KETONE (SPEEK) SURFACE USING ZIRCONIUM OXIDE-STABILIZED CERIUM OXIDE NANOCOMPOSITES

Published research paper: Hydrogen evolution on graphite/sulfonated polyether ether ketone (SPEEK) surface using zirconium oxide-stabilized cerium oxide nanocomposites. *Journal of Power Sources*, *629*, p.235975.

### 4.1. Introduction

The extensive exploitation of fossil fuel resources has serious consequences for carbon emissions, leading to unpredictable and catastrophic natural events caused by climate change, such as flooding, unusual tornadoes, wildfires, and extreme temperature fluctuations [1-3]. In 2022, approximately 72% of global greenhouse gas emissions were attributed to $CO_2$, which is the primary contributor to global warming [4]. As global warming and its consequences continue to worsen over time, there is growing concern about the lack of assurance that most countries will achieve zero carbon emissions anytime soon. As a result, there has been an increasing call to intensify efforts in alternative energy use over the past few years [5]. In response to this urgent issue, significant attention is now being directed toward exploring hydrogen as an alternative fuel source [6-8].

Hydrogen offers the advantage of being a relatively cost-effective and environmentally friendly energy source, producing only water as its combustion byproduct. Additionally, the production process for hydrogen features improved energy efficiency and cost-effectiveness, making it a viable option for large-scale industrial use [9]. However, the transition from pilot-scale to large-scale hydrogen production has encountered numerous practical challenges related to performance and maintenance issues. Furthermore, the use of platinum, the metal commonly regarded as the gold standard in catalysis, is limited due to the scarcity of its raw materials and the high costs associated with processing these resources. As a result, significant efforts are currently underway to identify non-platinum alternatives. While many alternative materials have been studied so far [10-15], very few investigations have focused on the use of polymeric membranes within catalytic compositions. Polymers are unique materials that can help address the durability limitations of current electrodes. By incorporating polymers through composting or surface coverage, they can enhance the functionality of electrodes by providing benefits such as ion binding, ion exchange, increased conductivity, sensing capabilities, energy storage, and protection against corrosion. For example, Garcia-Raminez et al. [16] used $Cu_{0·9}Zn_{0·1}Al_2O_4$ powders along with a polymeric blend membrane to effectively generate hydrogen in an aqueous medium. They highlighted the role of a blended polymeric composition—comprising cellulose acetate, nanocrystalline cellulose, and polyvinyl alcohol—as a viable catalytic support for hydrogen production. Despite their potential, many of these alternative materials still fall short of achieving the desired performance levels. Therefore, significant efforts are focused on identifying non-precious metal (NPM) catalysts that can demonstrate ideal performance characteristics.

Ceria and zirconia, which are semiconductive materials with excellent catalytic properties, have been extensively studied for their potential industrial applications [17]. Cerium oxide ($CeO_2$) is a stable rare earth oxide, known as a good electron acceptor, and it boasts excellent biocompatibility with minimal toxicity. Additionally, it is inexpensive and environmentally friendly. However, ceria is recognized for its poor thermal stability and susceptibility to photo-corrosion. Despite these challenges, incorporating zirconium into the ceria lattice has been shown to enhance these properties.

To produce mixed oxides of cerium and zirconium, various strategies have been developed, including solid-state reactions, milling, citrate methods, wet impregnation, sol-gel processes, and precipitation. Chemical reactions typically yield more homogeneous materials. The catalytic efficiency of these oxides is influenced by several factors, such as the Ce/Zr ratio, morphology, particle size, catalyst homogeneity, and the crystallographic nature of the phases formed. These characteristics can be improved based on the chosen preparation method [18-20]. Cerium-zirconium-based oxides with different Ce/Zr ratios exhibit distinct physicochemical properties. For instance, Eaimsumang et al. found that the catalytic activity of CexZr1-x$O_2$ for CO oxidation decreases as the Ce/Zr ratio increases [21]. Additionally, Zhang et al. [22] observed that while zirconium-rich ceria-zirconia solid solutions are more thermally stable than cerium-rich samples, they are still prone to transitioning from a cubic to a tetragonal phase. Despite the significance of thermal behavior in industrial applications, the thermal characteristics of ceria-zirconia-based oxides with varying Ce/Zr ratios have attracted relatively little attention in the literature.

## 4.2 Materials and methods

Cerium (III) nitrate hexahydrate ($Ce(NO_3)_3.6H_2O$), sodium hydroxide pellets (NaOH, 98% purity), Zirconium acetate ($Zr_6O_4(OH)_4(O_2CCH_3)_{12}$, dimethylformamide (DMF), potassium ferricyanide, and potassium ferrocyanide were purchased from Sigma-Aldrich (South Africa).

### 4.2.1 Synthesis of $CeO_2$-$ZrO_2$ nanocomposites

The ceria-zirconia binary oxide nanoparticles were synthesized using a coprecipitation method. Cerium nitrate hexahydrate and zirconium acetate were mixed in various molar ratios of $CeO_2$ to $ZrO_2$: 1:1, 1:2, 2:1, 1:0, and 0:1, corresponding to 4:4, 4:2, 2:4, 4:0, and 0:4 g/g, respectively. In the experiment, a calculated amount of cerium nitrate hexahydrate and zirconium acetate ($Zr_6O_4(OH)_4(O_2CCH_3)_{12}$), along with 10 g of sodium hydroxide (the precipitating agent), were added to 100 mL of deionized water. The mixture was stirred magnetically until the materials were fully dissolved. The resulting precipitates were then centrifuged, washed multiple times with distilled water, and dried at 100 °C for 24 hours. The dried samples were subsequently calcined at 600 °C for 2 hours. The final products were designated as $CeO_2$:$ZrO_2$ (1:1), $CeO_2$:$ZrO_2$ (1:2), $CeO_2$:$ZrO_2$ (2:1), $CeO_2$, and $ZrO_2$.

### 4.2.2 Working electrode fabrication

8 mg of each catalyst were applied to the surface of graphite, which was coated with a drop of sulfonated polyether ether ketone (SPEEK) previously dissolved in dimethylformamide (DMF) (0.27 g in 9.4 mL, followed by 5 minutes of sonication). The mixture was then dried in an oven at 80°C for 4 minutes. The SPEEK solution had a slightly viscous consistency, allowing for membrane formation in the presence of moist air or water. For stability and comparison experiments, the SPEEK-Ce: Zr mixture was simply dipped in water (using the phase inversion method) and used directly, as the membrane had already formed on the graphite electrode substrate (see Fig. 4S1 in the Supplementary Materials).

### 4.2.3 Material Characterization

The morphologies of $CeO_2$:$ZrO_2$ samples were examined using transmission electron microscopy (TEM) Joel JEM-2100 model. Thermal properties were investigated using a PerkinElmer thermogravimetric analyser (TGA) in air and nitrogen flow at a heating rate of 10 °C/min from 35 °C to 900 °C. Diffraction patterns were obtained through Rigaku SmartLab X-ray diffractometer (XRD) with Cu-Kα radiation source operated at 30 kV and a current of 200 mA with a scanning rate of 0.026 °/sec from 5° to 90°. Cyclic voltammetry (CV) and Electrochemical impedance spectroscopy (EIS) studies were performed within a potential window of -0.3 and +0.70 V and at $1 \times 10^5$ Hz to 0.1 Hz frequency with the applied potential of 0.24 V *using* a three-electrode cell (TEC) connected to a Metrohm Autolab Potentiostat (PGSTAT30) equipped with Nova software version 2.1. The TEC consists of platinum wire, Ag/AgCl (3M KCl) and as-synthesized materials on a graphite electrode as counter, reference, and working electrode, respectively. The electrochemical electrolyte solution temperature was at 20.3 $^0$C except for the comparative experiment, in which the experiment was run at 25 $^0$C. The hydrogen was generated in 0.5 M $H_2SO_4$ at a pH of 0.00. The current density was estimated by dividing the output current by the geometrical area of the graphite electrode. The overpotential was calculated by subtracting the open circuit potential from the applied potential. The potential of the Ag/AgCl electrode was converted to RHE using the relation Eq (4.1'):

$E_{RHE} = E_{applied}$ ( vs Ag/AgCl) + 0.059pH +0.197……………………………(4.1').

## 4.3. Results and discussion

### 4.3.1 Material characterization

The results X-ray diffraction patterns of the as-synthesized materials are presented in Fig. 4.1a. The characteristic cubic face-centred fluorite structure of ceria was confirmed at a 2θ value of 28.62°, 33.34°, 47.66°, 56.34°, 59.24°, and 69.46°, corresponding to the (111), (200), (220), (311), (222), and (400) planes, respectively (JCPDS card number 34-394). In contrast, the tetragonal phase of zirconia ($ZrO_2$), identified by the (101), (110), (112), and (211) planes, was observed at 2θ values of 30.36°, 35.17°, 50.40°, and 60.15° (JCPDS card number 80-2155). Additionally, a monoclinic phase was detected at 2θ values of 24.58° and 42.17° (JCPDS card number 7-3430). The XRD patterns for the hybrid materials, $CeO_2$:$ZrO_2$ in ratios of 1:1, 1:2, and 2:1, exhibited cubic phases resembling those of ceria. The observed peak shifts towards higher 2θ values indicate the presence of $Zr^{4+}$ in the hybrid material, confirming the successful preparation of the composite [23].

.

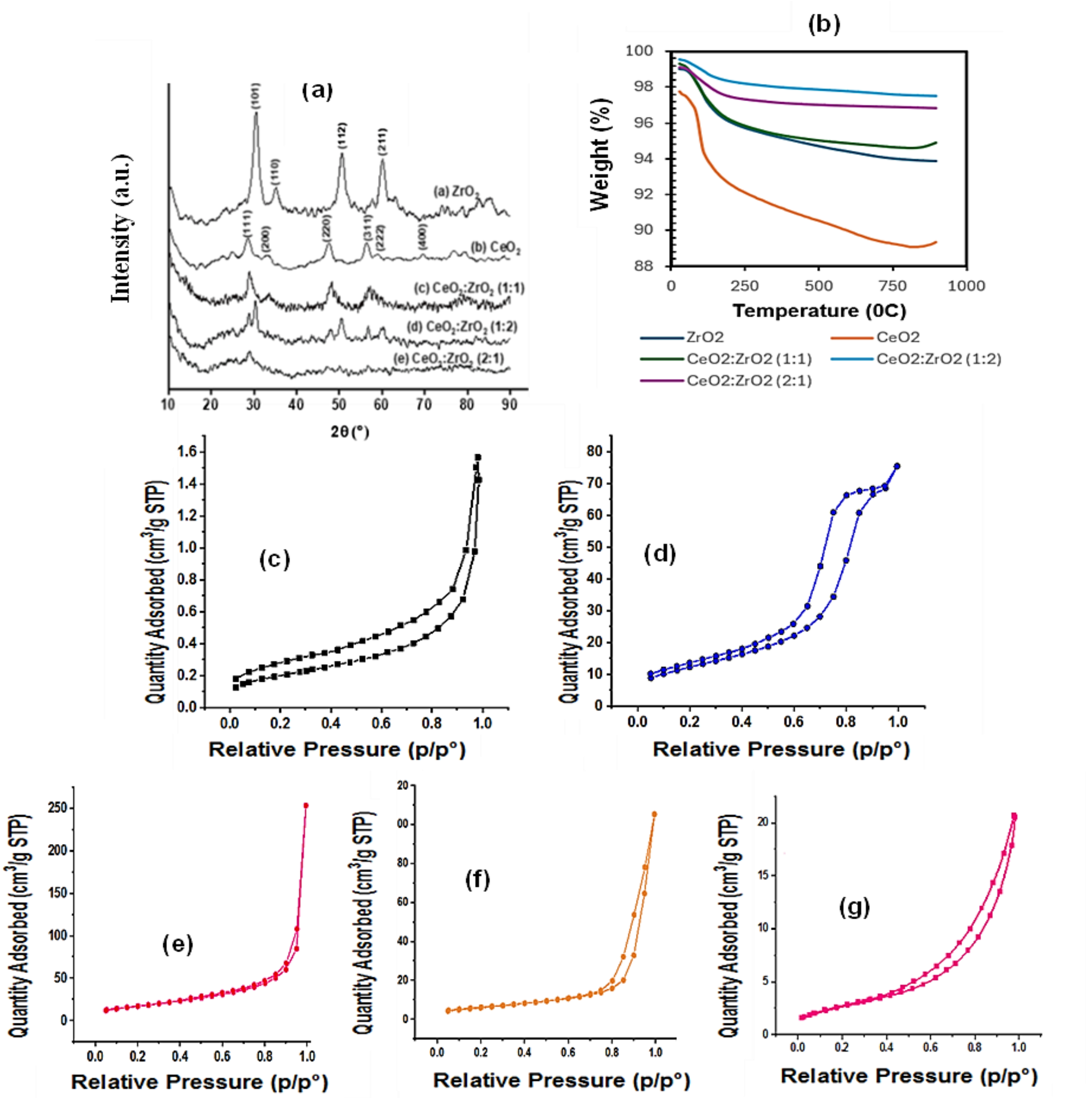

**Fig. 4. 1:** Crystallinity, thermal and surface area characterizations of the as-synthesized materials. (a) XRD;(b) TGA; (c-g) $N_2$ adsorption and desorption.

The thermogravimetric analysis (TGA) results for the ceria and zirconia electrocatalysts are shown in Fig. 4.1b. The thermograms reveal two stages of thermal degradation for each sample. The initial weight loss around 100 °C is attributed to the release of water trapped within the material. The subsequent weight loss, occurring from 100 to 900 °C, represents the actual weight loss of the catalysts. The thermograms indicate that the samples were stable, as there was minimal oxide decomposition. The total weight loss for the $ZrO_2$, $CeO_2$, $CeO_2$:$ZrO_2$ (1:1), $CeO_2$:$ZrO_2$ (1:2), and $CeO_2$:$ZrO_2$ (2:1) samples was recorded as 3%, 7%, 4%, 5%, and 2%, respectively.

### 4.3.2 Surface area, morphology and elemental composition

The results of the $N_2$ adsorption and desorption BET surface area analyses of the as-synthesized materials are shown in Fig. 4.1c-d and Table 4.1. As indicated in these figures and the table, the $CeO_2$:$ZrO_2$ (1:1) composition demonstrated superior characteristics compared to all other tested materials, exhibiting a higher specific surface area and smaller pore size. Additionally, all materials showed similar pore volume characteristics, suggesting that the addition of $ZrO_2$ to the ceria structure did not significantly impact the overall pore volume.

However, it was observed that increasing the amounts of either $CeO_2$ or $ZrO_2$ resulted in a decrease in surface area compared to pure $CeO_2$. Specifically, higher $ZrO_2$ content led to a reduction in both pore volume and pore size, while increasing $CeO_2$ content similarly decreased pore volume and pore size relative to $CeO_2$ alone. Consequently, it is reasonable to expect that the $CeO_2$:$ZrO_2$ (1:1) mixture would exhibit better catalytic performance than the other materials tested.

**Table 4. 1:** BET, Pore Volume and Pore size of $CeO_2$, $ZrO_2$ and $CeO_2$:$ZrO_2$ oxide at different $CeO_2$ and $ZrO_2$ loading.

| **Sample** | **Surface Area ($m^2/g$)** | **Pore Volume ($cm^3/g$)** | **Pore size (nm)** |
|---|---|---|---|
| **$CeO_2$** | 52.37 | 0.11 | 1.93 |
| **$ZrO_2$** | 44.75 | 0.10 | 4.78 |
| **$CeO_2$:$ZrO_2$ (1:1)** | 63.41 | 0.12 | 1.71 |
| **$CeO_2$:$ZrO_2$ (1:2)** | 14.99 | 0.10 | 1.75 |
| **$CeO_2$:$ZrO_2$ (2:1)** | 48.75 | 0.11 | 2.81 |

Fig. 4.2a-l presents the results from the TEM and SEM analyses. As illustrated in Figures 4.2a-h, all materials displayed a mixture of spherical and rod-like morphological structures with highly crystalline properties. Notably, the $CeO_2$ and $ZrO_2$ in a 1:1 ratio exhibited a greater presence of rod-like structures compared to ceria, ceria-zirconia in a 1:2 ratio, and ceria-zirconia in a 2:1 ratio. Additionally, as the zirconium (Zr) content increased, a higher number of spherical structures were observed. The predominant rod-like characteristics of $CeO_2$:$ZrO_2$ (1:1) may provide a

competitive advantage over the other materials due to its three-dimensional configuration. Figures 4.2i-l show the SEM analyses of the synthesized materials, specifically $CeO_2$ and $CeO_2$:$ZrO_2$ (1:1).

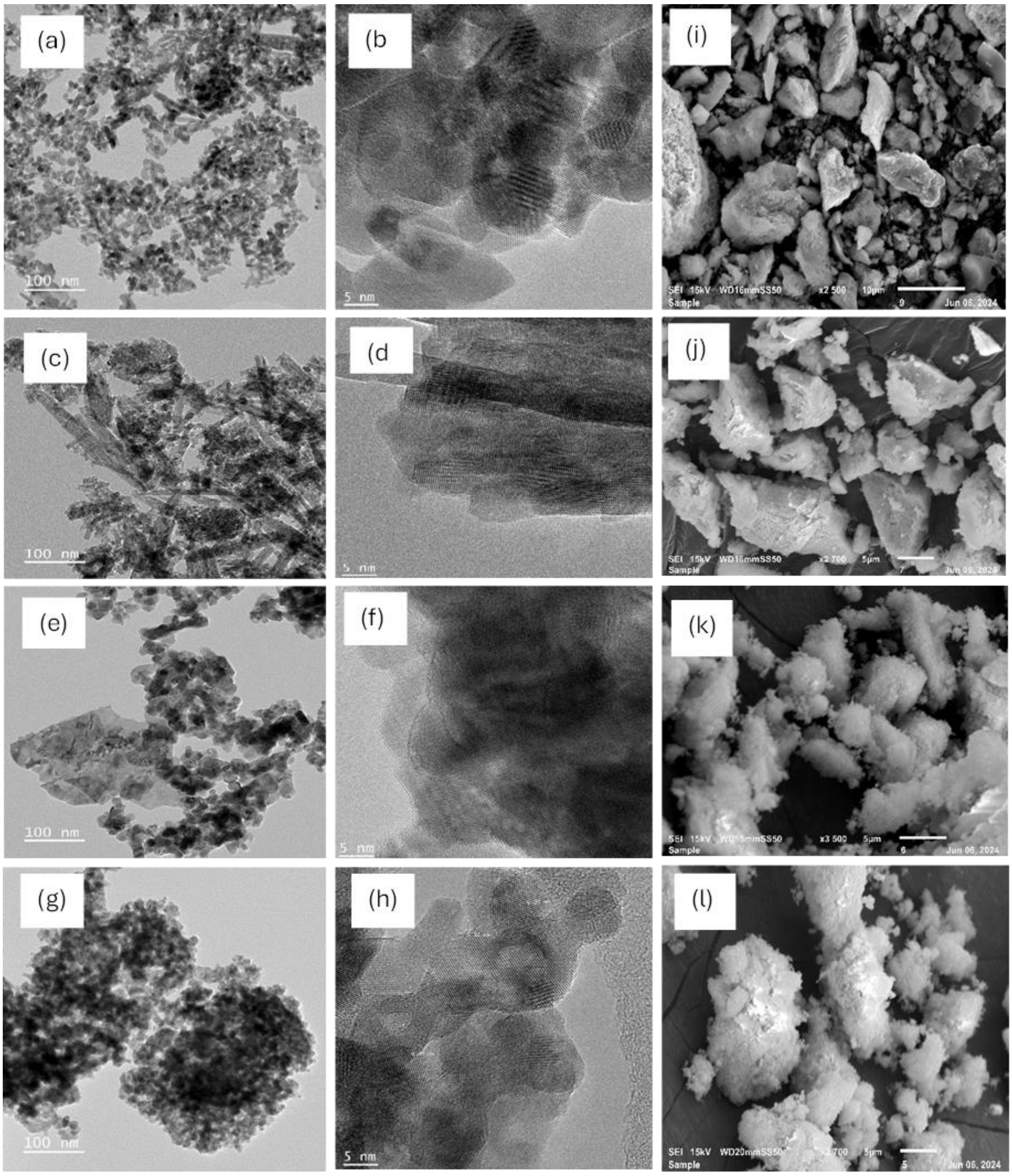

***Fig.4.2***: Transmission electronic nanographs (TEM) and scanning electron micrographs (SEM) of the as-synthesized nanocomposites.TEM: (a,b) $CeO_2$ ; (c,d) $CeO_2$:$ZrO_2$ (1:1);(e,f) ) $CeO_2$:$ZrO_2$ (1:2);(g,h) ) $CeO_2$:$ZrO_2$ (2:1); SEM: (I,j) $CeO_2$; (k,l) $CeO_2$:$ZrO_2$ (1:1).

As depicted in Figures 4.2i-j, the pristine $CeO_2$ displayed a semi-spherical morphology with a compact appearance. In contrast, with the addition of $ZrO_2$, a sheet-like structure became evident on the surface of the hybrid material. This sheet may act as an active site for hydrogen adsorption and desorption during the hydrogen evolution reaction (HER) process. Furthermore, the entire material seemed less compact than that of pristine $CeO_2$, which could further improve proton penetration and increase the production of hydrogen molecules.

### 4.3.2 Electrochemical surface area (ECSA) and turnover frequency (TOF)

As shown in Eqs. (4.2-4.3), the ECSA is an effective tool for assessing electrocatalyst efficiency. The capacitance plot is a useful graph for predicting ECSA, which is used to calculate TOF.

$$\mathrm{ECSA} = S_{cdl} \times A_{Geo}/C_s \qquad \textbf{(4.2)}$$

$$\mathrm{TOF} = j_{(ECSA)} / n_e \,.\, n_{cat.}\, F \qquad \textbf{(4.3)}$$

Where $S_{cdl}$ = slope of the plot of average difference in current density of the anode and cathode ((▲$j_{(a-c)}$ / 2) vs. scan rate of a capacitance plot, where a = anode, c = cathode and $C_s$ = specific capacitance (assumingly = 20 $\mu Fcm^{-2}$ ), $n_e$ = number of electron required to produce 1 mol of hydrogen molecule ($H_2$), i.e. 2 as shown in Eq. (4.4), $n_{cat}$ = number of mole of the catalyst on the support's surface and F = Faraday's constant (96485 C $mol^{-1}$).

$$2H^{+}\,(aq) + 2e- \longrightarrow H_2\,(g) \qquad \textbf{(4.4)}$$

As shown in Table 2, the capacitance and ECSA values decreased after adding all catalysts in a variable manner relative to the supporting material.

**Table 4. 2:** Capacitance and ECSA values of various electrocatalysts.

| **Materials** | **Capacitance (μF)** | **ECSA ($cm^2$)** |
|---|---|---|
| Graphite | 80 | 7,04 |
| Graphite + SPEEK* | 70 | 6,16 |
| Graphite + SPEEK + CeO2 | 60 | 5,28 |
| graphite+SPEEK-CeO2-Zro2 (1:1) | 50 | 4,4 |
| graphite+SPEEK-CeO2-Zro2 (1:2) | 50 | 4,4 |
| graphite+SPEEK-CeO2-Zro2 (2:1) | 60 | 5,28 |

*SPEEK = sulfonated poly (ether ether ketone) as a binder

From Table 4.2, it can be deduced that the modification of the supporting graphites with SPEEK resulted in approximately a 12.50% decrease in both capacitance and ECSA (Electrochemical Surface Area) values. In contrast, blending SPEEK with $CeO_2$ before applying it to the surface of the graphites led to a more significant reduction, with capacitance and ECSA values decreasing by 16.67% and 14.29%, respectively. Furthermore, modifying the Graphite/SPEEK surface with a 1:1 ratio of $CeO_2$ to $ZrO_2$ caused an additional decrease in capacitance and ECSA values of about 16.67%.

Interestingly, increasing the amount of $ZrO_2$ in the surface matrix did not affect the capacitance or ECSA values. However, an increase in $CeO_2$ resulted in a change in capacitance and ECSA values from 50 to 60 and from 4.4 to 5.28, representing an increase of approximately 16.67%. While excess $ZrO_2$ did not enhance the ECSA value, a moderate amount contributed to an improvement in the HER (Hydrogen Evolution Reaction) current, as illustrated in Figures 4.3a-c.

In Fig. 4.3a-b, adding $ZrO_2$ to the $CeO_2$ framework (1:1) boosted the currents from 3 x $10^{-5}$ to 2.3 x $10^{-5}$ A (capacitance) and 4.7 to 6.1 mA/$cm^2$ (faradaic), resulting to a TOF transition from 5.2 X $10^{-4}$ to 1.1 x $10^{-2}$ $cm^2$ $s^{-1}$. Furthermore, as the $ZrO_2$ content increased, the current and TOF decreased dramatically, consistent with the data shown in Table 4.2. Similarly, as demonstrated in Fig. 4.3b-c, increasing the $CeO_2$ content significantly decreased the current, demonstrating that $CeO_2$-$ZrO_2$ (1:1) is the material with the best catalytic properties.

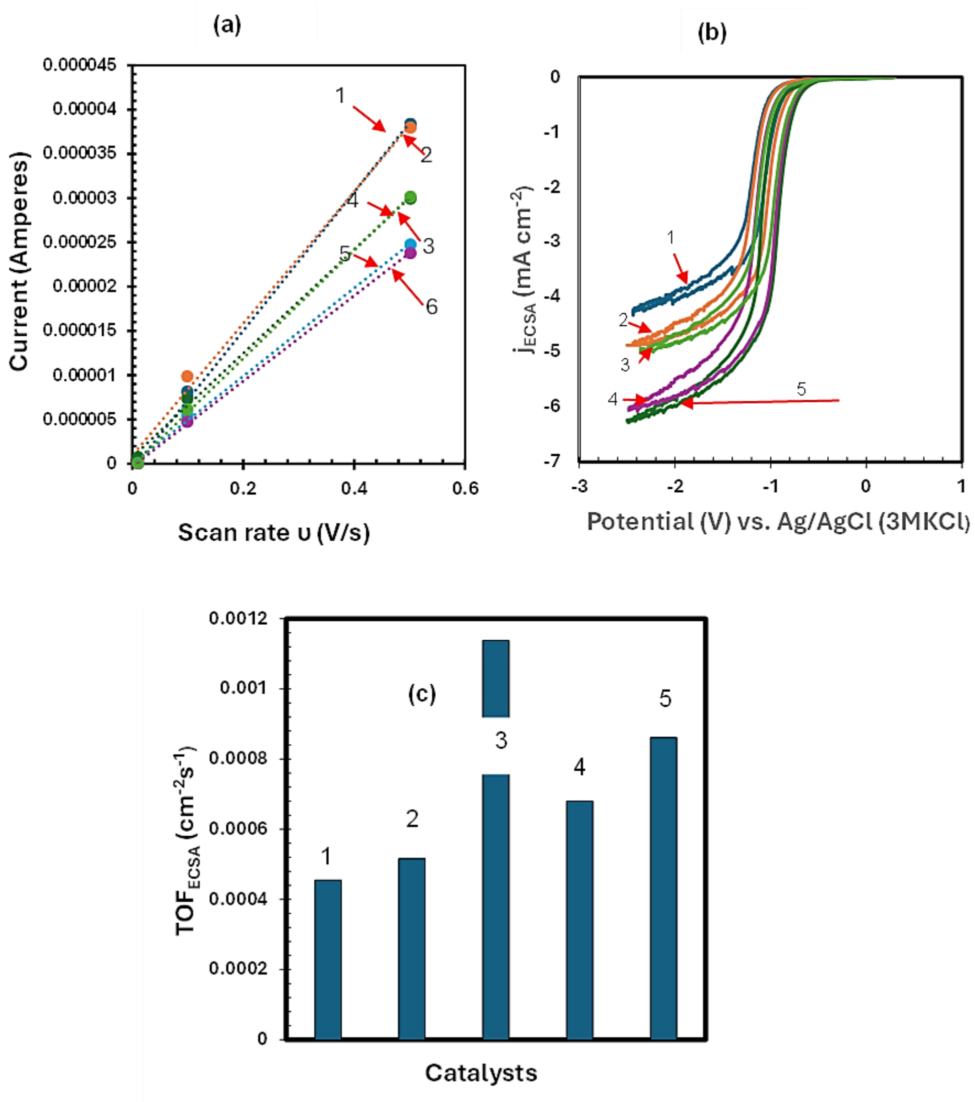

**Fig. 4. 3:** ECSA and TOF estimations. (a) Capacitance plots at 0.4V (1 = Graphite, 2 = Graphite-SPEEK, 3 = Graphite-SPEEK-$CeO_2$, 4 = Graphite-SPEEK-$CeO_2$-$ZrO_2$ (2:1), 5 = Graphite-SPEEK-$CeO_2$-$ZrO_2$ (1:2), 6 = Graphite-SPEEK-$CeO_2$-$ZrO_2$ (1:1); (b) $CV_{ECSA}$ plot (1 = Graphite-SPEEK, 2 = Graphite-SPEEK-$CeO_2$, 3 = Graphite-SPEEK-$CeO_2$-$ZrO_2$ (2:1), 4 = Graphite-SPEEK-$CeO_2$-$ZrO_2$ (1:2), 5 = Graphite-SPEEK-$CeO_2$-$ZrO_2$ (1:1); (c) TOF (1 = Graphite-SPEEK, 2 = Graphite-SPEEK-$CeO_2$, 3 = Graphite-SPEEK-$CeO_2$-$ZrO_2$ (1:1), 4 = Graphite-SPEEK-$CeO_2$-$ZrO_2$ (1:2), 5 = Graphite-SPEEK-$CeO_2$-$ZrO_2$ (2:1)

### 4.3.4 Role of SPEEK

SPEEK is a proton exchange membrane (PEM) material commonly used in PEM fuel cell assemblies. In this study, SPEEK was utilized for two main purposes. First, it served to strongly bond ceria-zirconia particles to the supporting graphite, while also protecting the underlying electrode from corrosion. As illustrated in Fig. 4.4a-b, modifying the surface of the graphite with SPEEK resulted in an $E_{corrosion}$ overpotential ($E_{corr}$) of approximately -0.33 V. However, after binding with ceria and zirconia composites, the $E_{corr}$ value became more positive, from -0.33 V to -0.29 V for all SPEEK-$CeO_2$ systems without $ZrO_2$, except for graphite-SPEEK-$CeO_2$-$ZrO_2$ (1:2) and graphite-SPEEK-$CeO_2$-$ZrO_2$ (2:1) and from -0.33 V to -0.28 V for the graphite-SPEEK-$CeO_2$-$ZrO_2$ (1:2) system. This suggests that addition $ZrO_2$ caused a more tendency for the catalyst to be less prone to corrosion (see Table 4.3).

**Table 4. 3:** Corrosion potentials for graphite-SPEEK electrochemical catalysts

| **Catalyst** | **$E_{corr}$ (V)** |
|---|---|
| Graphite/SPEEK | -0.33 |
| Graphite/SPEEK/$CeO_2$ | -0.29 |
| Graphite/SPEEK/CeZr 1:1 | -0.29 |
| Graphite/SPEEK/CeZr 1:2 | -0.28 |
| Graphite/SPEEK/CeZr 2:1 | -0.29 |

The geometric current density measured approximately -44 mA $cm^{-2}$ for graphite and Graphite/SPEEK, while for the Graphite + SPEEK + Ce:Zr (1:1) configurations, it was -43 mA $cm^{-2}$ for Layer 1 and -42 mA $cm^{-2}$ for Layer 2 (see Fig. 4.4c). Therefore, no significant change was observed when the surface of graphite/SPEEK was coated once or twice with the nanocomposite. As illustrated in Fig. 4.4d, the onset potential for graphite was -0.05 V, whereas for the Graphite/SPEEK and Graphite + SPEEK + Ce:Zr composites, it was -0.07 V. This indicates that modifying the surface of graphite with SPEEK and SPEEK-Ceria-Zirconia composites resulted in a shift of approximately 0.02 V in the applied potential. The results from the EIS Nyquist plots and the circuit fitting data for the optimal performing electrode (Graphite + SPEEK + Ce:Zr (1:1), Layer 2) are presented in Fig. 4.5 and Table 4.4.

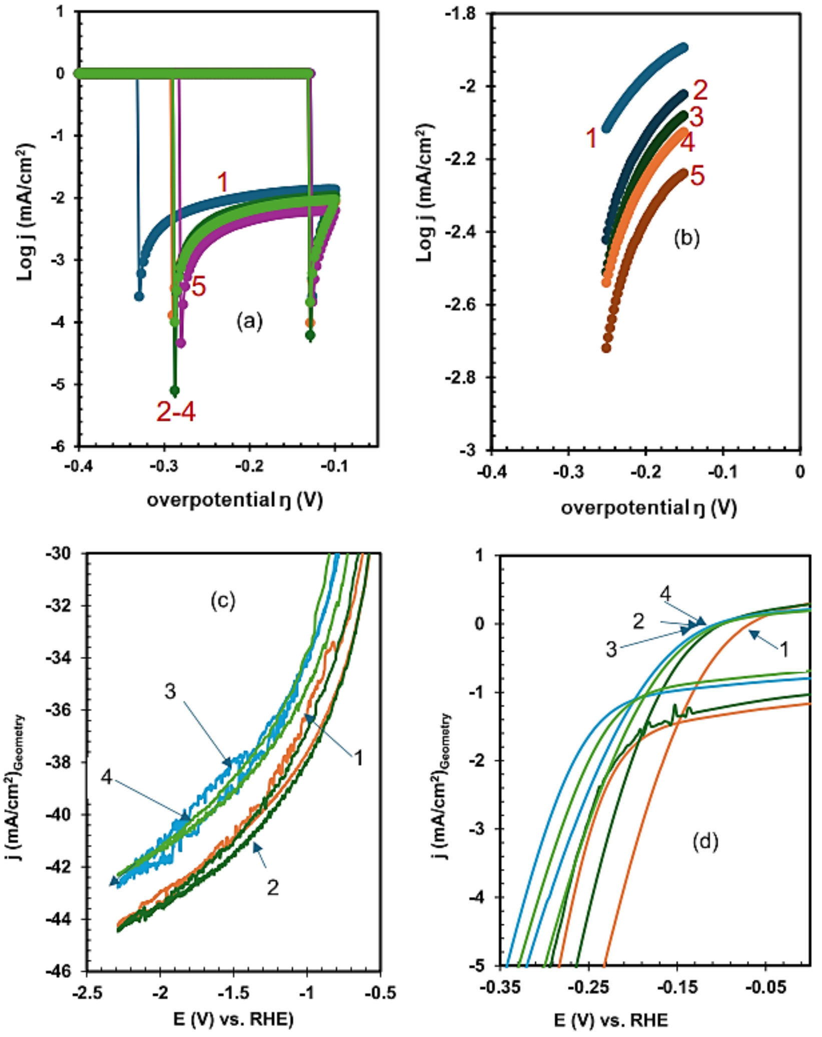

**Fig. 4. 4:** Polarization plots. (a) Corrosion plots: 1 = Graphite + SPEEK, 2 = Graphite + SPEEK + $CeO_2$, 3 = Graphite + SPEEK + CeZr (1:1), 4 = Graphite + SPEEK + CeZr (2:1), 5 = Graphite + SPEEK + CeZr (1: 2) (b) Enlargement of the Tafel region in (a); (c) Hydrogen evolution (Graphite + SPEEK + CeZr (1:1): 1 = Graphite, 2 = Graphite + SPEEK, 3 = Graphite + SPEEK + CeZr (1:1) (Layer 1), 4 = Graphite + SPEEK + CeZr (1:1) (Layer 2); (d) Onset potentials identification (Graphite + SPEEK + CeZr (1:1)). OCP = 0.4 V.

.

As shown, there was no significant difference in the performance of the electrode's surface when coated once (Layer 1) compared to twice (Layer 2).

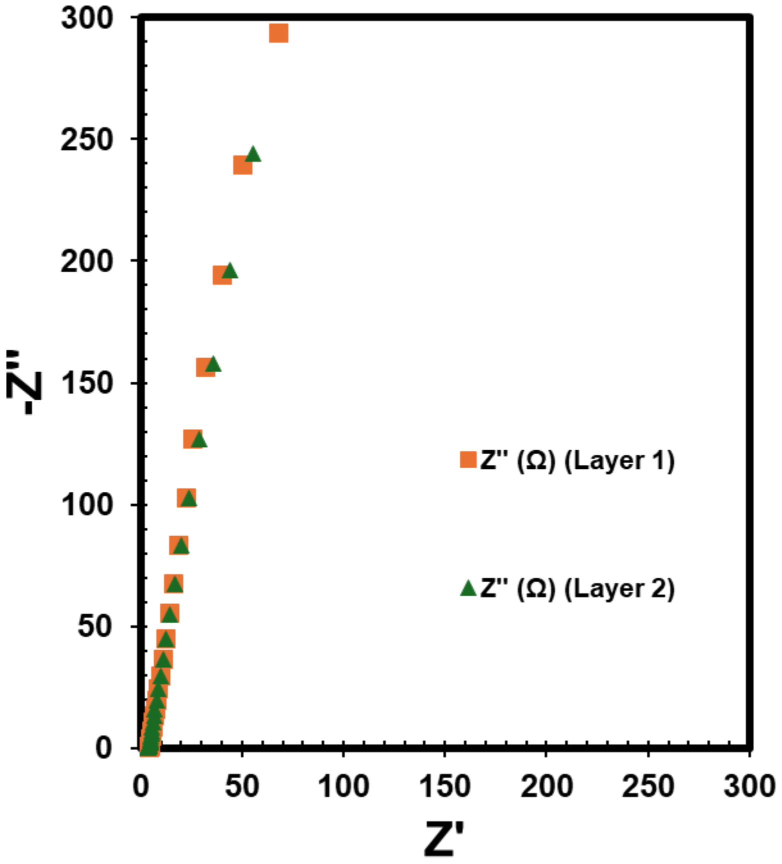

**Fig. 4. 5:** Nyquist plots of the Graphite + SPEEK + CeZr (1:1) electrode.

**Table 4. 4:** Circuit fitting data of Graphite + SPEEK + CeZr (1:1) nanocomposite electrode.

| Material | Rp kΩ | Rs Ω |
|---|---|---|
| **Graphite/SPEEK/CeZr 1:1 (Layer 1 = 1 mm)** | 3.54 | 4.44 |
| **Graphite/SPEEK/CeZr 1:1 (Layer 2 = 2 mm)** | 7.14 | 4.27 |

### 4.3.5. Cell voltage and current behavior

The results of the chronoamperometric and chronopotentiometric analyses at various applied potentials and a current of 0.001 A are presented in Figures 4.6a and 4.6b, respectively. As shown in Figure 4.6a, all current readings remained stable over time. Additionally, the current signals were correlated with an increase in solution temperature at higher applied voltages. However, at a lower applied voltage of -1.0 V (vs. Ag/AgCl with a 3M KCl reference electrode), there was a slight decrease in temperature from 20.6 °C to 20.3 °C.

This increase in temperature at higher voltages was attributed to the rapid formation of hydrogen gas bubbles at the electrode's surface, which created vigorous bubbling in the solution and led to an exothermic effect. In contrast, the slight drop and subsequent stabilization of the temperature at -1.0 V were likely due to less vigorous bubbling of hydrogen molecules at the electrode's surface. The experiment was conducted at room temperature and under normal atmospheric pressure, meaning that the pressure remained constant even as the temperature gradually increased.

As shown in Fig. 4.7, the results from the chronoamperometric (CA) analysis indicated that the rate of hydrogen production increased over time as the electrode interaction continued. The current measured during the CA is directly proportional to the volume of hydrogen produced. According to Charles's Law, the increase in volume results in a temperature rise, while the pressure remains constant at approximately 1 atmosphere. Furthermore, an increase in the rate of gas bubbling correlates with an increased rate of $H_2$ production, again supporting Charles's Law.

**(a)**

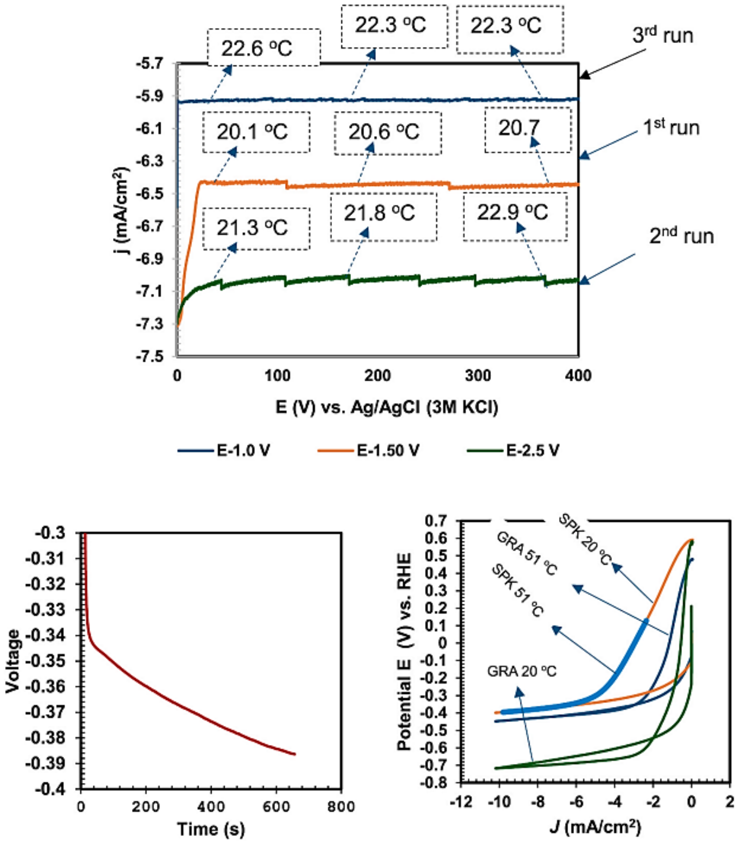

**Fig. 4. 6:** Current and voltage stability test. (a) Chronoamperometry at -1.0 to -2.5 V; (b) Chronopotentiometry at 0.001 A; (c) J-V curve at different temperatures. GRA = Graphite; SPK =SPEEK/$CeO_2$-$ZrO_2$.

As shown in Fig. 4.6b, the voltage generation rate using the Graphite/SPEEK-ceria-zirconia nanocomposite electrode was approximately 5 x $10^{-5}$ V/s at an applied current of 1 mA. Additionally, the J-V curves illustrating the cell's performance at 20°C and 51°C are presented in Fig. 4.6c. The results indicate that coating the graphite with SPEEK/$CeO_2$-$ZrO_2$ improved the overpotential by 44.44% at 20°C and 11.11% at 51°C. Notably, there was no change in the voltage after applying the SPEEK/CeO2-$ZrO_2$ coating at both temperatures, highlighting the protective nature of the SPEEK nanocomposites.

Fig. 4.7a-b display the hydrogen production rate over time. The data reveals that the hydrogen production rate increases over time at a rate of 9.6111 x $10^{-5}$ A/s, with a rate constant of 8.35 x 10-5 $s^{-1}$. When compared to conventional electrocatalysts such as platinum (Pt) and palladium (Pd), as illustrated in Fig. 4.7c, the as-synthesized material combined with SPEEK on the graphite surface demonstrated competitive performance in terms of current generation (-0.38 A for SPEEK/$CeO_2$:$ZrO_2$) on graphite vs. -0.39 A for Pt). However, it did show a slightly higher onset potential (-0.75 V for SPEEK/$CeO_2$:$ZrO_2$ on graphite vs. -0.40 V for Pt).

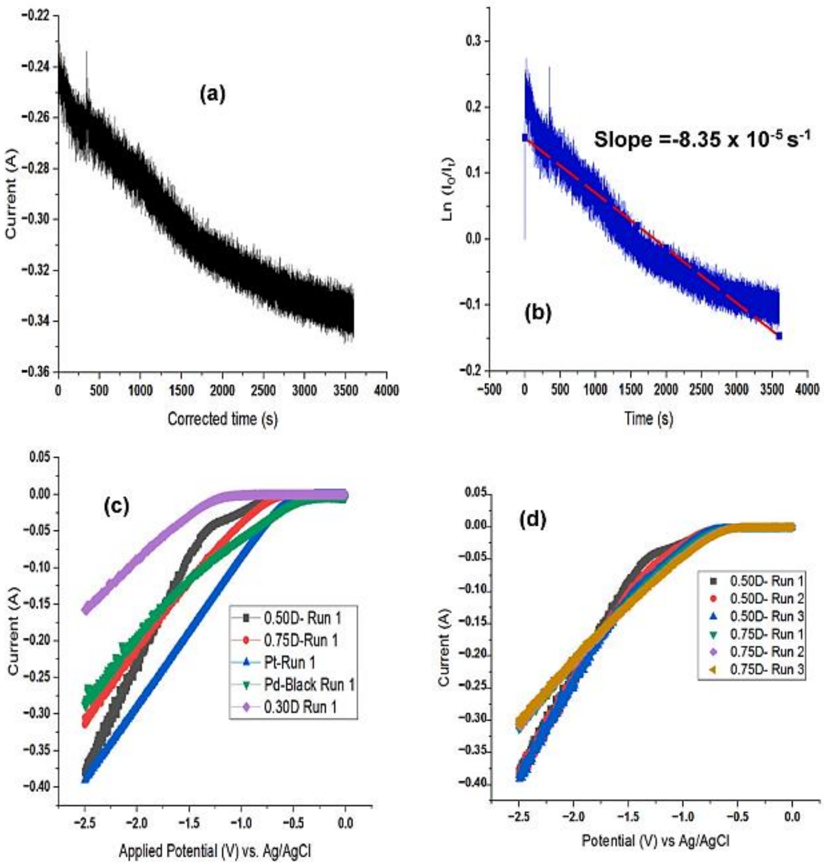

**Fig. 4. 7:** Chronoamperometric rate and linear sweep voltammetric (LSV) studies. (a) Increase of current with time; (b) First order kinetic plot; (c) Comparative voltammograms with other electrocatalysts; (d) LSV stability studies. 0.3D, 0.5D, 0.75D = Graphite with variable diameter of 0.3, 0.5 and 0.75 cm.

Remarkably, the as-synthesized material produced a higher current than palladium black (-0.38 A for the as-synthesized material vs. -0.29 A for Pd), as depicted in Fig. 4.7c. This figure also suggests the potential of the as-synthesized material for large-scale hydrogen production, as evidenced by the increase in current with the increase in electrode diameter (comparing 0.30D vs. 0.5D, or 0.75D, where D is the diameter in cm).As illustrated in Fig. 4.7c, electrocatalysts with larger electrode diameters (0.5D or 0.75D) produced more current than those with lower diameters (0.3D). The modest decrease in current relative to 0.75D graphite from 0.5D was caused by variations in manufacturing conditions (0.5D (Gamry), 0.7D (obtained from a dry cell battery) (Fig. 4S2, Supplementary Material). Fig. 4.7d depicts the findings of current stability measured using linear scan voltammetry. Despite using two different graphite sources (0.5D (Gamry) and 0.7D (obtained from a dry cell battery), the current remained steady (Fig. 4.7d).

### 4.3.6 SPEEK and hydrogen production mechanism

Sulfonated polyether ether ketone (SPEEK) is a powerful proton exchange membrane that was applied to the surface of graphite to effectively bind semiconductor nanoparticles. It was previously noted that coating the graphite surface with SPEEK did not significantly alter the current. However, as shown in Fig. 4.5b, the hydrogen evolution reaction (HER) current increased on the graphite-SPEEK surface with the introduction of electrocatalysts, observed in the order of $CeO_2$ < $CeO_2$:$ZrO_2$ (2:1) < $CeO_2$:$ZrO_2$ (1:2) < $CeO_2$:$ZrO_2$ (1:1). Notably, the $CeO_2$:$ZrO_2$ (1:1) formulation outperformed all other tested electrocatalysts. This superior performance of the $CeO_2$:$ZrO_2$ (1:1) nanocomposite can be attributed to its enhanced crystallinity, BET surface area, particle and pore sizes, and electrochemically active surface area (ECSA) values. The binding mechanism of SPEEK involves complexation between its sulfonic acid groups and the cerium and zirconium ions within the nanocomposite matrix. The formation of the membrane further strengthens this interaction through the nonsolvent phase inversion process, which occurs during the immersion of the mixture in water (the nonsolvent medium) (see Fig. 4S1, Supplementary Material).

According to the Volmer-Tafel mechanism, hydrogen production happens in three stages: protons are reduced to hydrogen atoms, which then adsorb onto the catalyst surface as H*. Subsequently, two H* atoms combine on the surface to form a hydrogen gas molecule ($H_2$), which eventually desorbs from the surface [24, 25]. In this study, hydrogen bubbles were observed growing on and detaching from the catalyst's surface. Therefore, it is reasonable to conclude that the HER mechanism mediated by $CeO_2$:$ZrO_2$ (1:1) on the graphite surface followed the Tafel-Volmer mechanism.

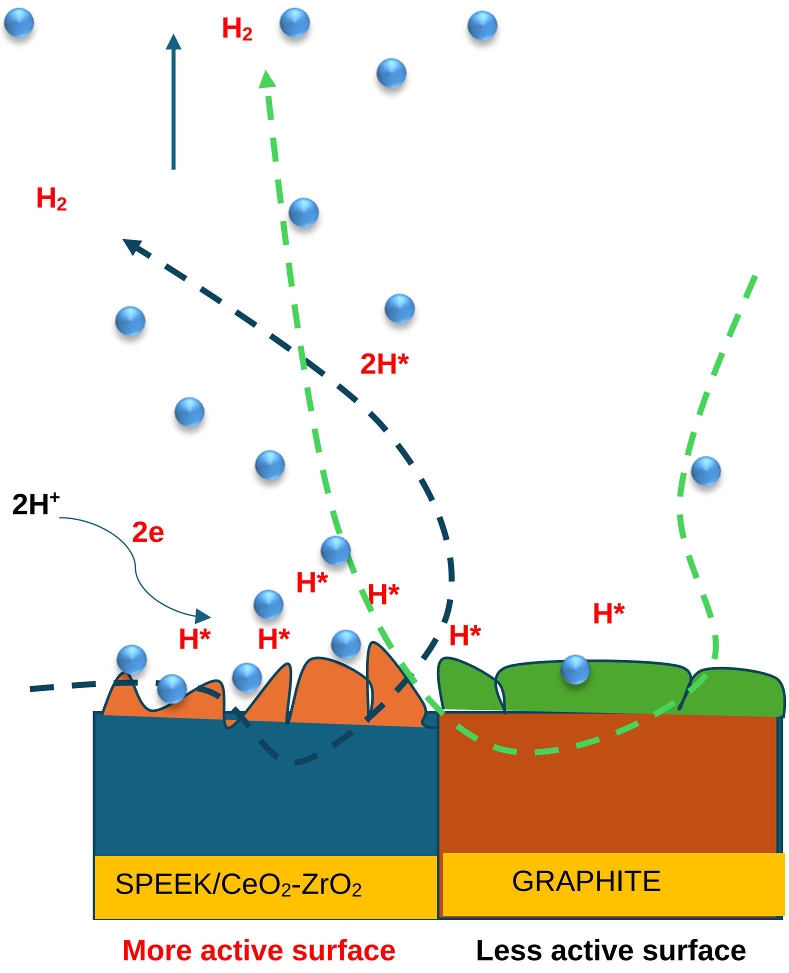

**Scheme 4.1.** Proposed HER mechanism by $CeO_2$:$ZrO_2$ electrocatalysts overpotential at 10 mA/cm$^2$ than most of the previously reported catalysts.

Table 4.5 compares the current work to various previous works described in the literature. As demonstrated in Table 4.5, the present material outperformed all previously reported materials in terms of current density, indicating the significant potential of combining SPEEK/$CeO_2$:$ZrO_2$ on a graphite surface to generate hydrogen gas from aqueous sulphuric acid. Table 4.5 and Fig. 4S2 (Supplementary Material) reveal that the SPEEK/$CeO_2$:$ZrO_2$ graphite electrode has a current density of up to 2000 mA/cm$^2$.

**Table 4. 5:** Comparison between present work and works reported in the literature.

| **Material** | **Current density (mA/cm$^2$)** **Geometrical** | **Reference** |
|---|---|---|
| PtRu/CC$_{1500}$ | 175.7 | [24] |
| PtNi/Pt DNPs | 250 | [25] |
| MoSe 2-ts | 86.7 | [26] |
| $Sr_2RuO_4$ | 1000 | [27] |
| CoMoSx | 500 | [28] |
| Ru-$NiSe_2$ | 1000 | [29] |
| Co−P | 500 | [30] |
| CoOx−$RuO_2$/NF | 1500 | [31] |
| $Mo_2C$-$Mo_2N$@CNWs/D | 1000 | [32] |
| Graphite-SPEEK@CeZr | 2000 | This work |

## 4.4. Conclusion

SPEEK in combination with zirconium oxide-stabilized cerium oxide, was used as an effective electrode on a graphite surface to generate hydrogen in an acidic medium. Among the materials tested, the $CeO_2$:$ZrO_2$ (1:1) showed the highest efficiency, outperforming palladium black. When compared to platinum, it produced a nearly equivalent current, indicating its strong potential as a cost-effective alternative to this more expensive standard electrode. The enhanced current efficiency is attributed to its superior morphology, which features a mix of spherical, rod, and sheet-like structures, as well as its impressive surface area with a BET of 63.41 m$^2$/g, ECSA of 4.4 cm$^2$, and a pore size of 1.71 nm. The optimal material achieved a hydrogen production current rate of approximately -9.61 x $10^{-5}$ A/s, with a first-order kinetic rate constant of 8.35 x $10^{-5}$ $s^{-1}$. Additionally, a current density of 2000 mA/cm$^2$ was recorded for the synthesized electrocatalyst on a 0.5 cm diameter graphite electrode, which is a remarkably high value compared to previous work reported in the literature. In this study, SPEEK acted as both a binder and a complexing ligand for the inorganic components, securing them firmly to the electrode surface to prevent detachment during the experiments. This research highlights the benefits of using SPEEK as a nanoparticle binder on graphite electrodes for hydrogen gas generation. It is recommended that future evaluations consider SPEEK as a binder for semiconducting materials currently employed for hydrogen gas generation on various conventional electrode materials.

## 4.5 Reference

1. Adebiyi, F.M., *Air quality and management in petroleum refining industry: A review.* Environmental Chemistry and Ecotoxicology, 2022. **4**: p. 89-96.
2. Islam, A., S.H. Teo, C.H. Ng, Y.H. Taufiq-Yap, S.Y.T. Choong, and M.R. Awual, *Progress in recent sustainable materials for greenhouse gas (NOx and SOx) emission mitigation.* Progress in Materials Science, 2023. **132**: p. 101033.
3. Islam, A., A. Malek, S.H. Teo, H.M. Marwani, M.M. Rahman, A.M. Asiri, M.A.R. Khan, Y.H. Taufiq-Yap, and M.R. Awual, *Smart materials for $CO_2$ conversion into renewable fuels and emission reduction.* Sustainable Materials and Technologies, 2023. **37**: p. e00636.
4. Karakurt, I., B.D. Avci, and G. Aydin, *Leveraging the trend analysis for modeling of the greenhouse gas emissions associated with coal combustion.* Environmental Science and Pollution Research, 2024. **31**(39): p. 52448-52472.
5. Raihan, A., L.C. Voumik, G. Zimon, B. Sadowska, M. Rashid, and S. Akter, *Prioritising sustainability: how economic growth, energy use, forest area, and globalization impact on greenhouse gas emissions and load capacity in Poland?* International Journal of Sustainable Energy, 2024. **43**(1): p. 2361410.
6. Wen, Y., Z. Zhang, H. Zhu, K. Xu, Y. Zhao, L. Ma, and H. Yan, *Preparation of Ni nanocone/Grid electrodes by laser-electrodeposition combined process as an efficient and stable electrocatalyst for hydrogen evolution reaction.* International Journal of Hydrogen Energy, 2024. **89**: p. 518-530.
7. Fu, Y., F. Wang, C. Qing, Y. Zhang, M. Li, X. Cao, S. Gong, L. Luo, and Z. Li, *Atomically L12 ordered (PtHf) x (NiTi) 100-x/CNT as bifunctional catalysts for hydrogen evolution reaction and methanol oxidation reaction with high activity and durability.* Chemical Engineering Journal, 2024. **498**: p. 155800.
8. Islam, A., S.H. Teo, M.T. Islam, E. Ahamed, M.S. Islam, A.G. Alsultan, H.M. Marwani, M.M. Rahman, A.M. Asiri, and Y.H. Taufiq-Yap, *Boosting biodiesel production over silicon heterojunction with visible light irradiation.* Energy Conversion and Management, 2023. **292**: p. 117435.

9. Islam, A., S.H. Teo, M.R. Awual, and Y.H. Taufiq-Yap, *Improving the hydrogen production from water over MgO promoted Ni–Si/CNTs photocatalyst.* Journal of Cleaner Production, 2019. **238**: p. 117887.

10. Feng, A., M. Yang, Z. Zhang, H. Xia, W. Jin, B. Shen, Y. Hu, and Q. Li, *Electrocatalytic hydrogen evolution coupled with dye hydrogenation reactions for sustainable wastewater treatment using transition-metal (Fe, Co, Ni, Cu) nanoparticles with ZnO nanowire supports.* Chemical Engineering Journal, 2024. **496**: p. 153751.

11. Jiang, J., Y. Zhou, J.-l. Zhang, K. Gao, J. Pan, and P. Dong, *Accelerating the charge separation from the Schottky junction effect of Pd-loaded Al: $SrTiO_3$ for highly efficient photocatalytic hydrogen evolution.* International Journal of Hydrogen Energy, 2024. **82**: p. 646-654.

12. García-Ramírez, P., L. Diaz-Torres, S. Castañeda-Palafox, M. Villagómez-Mora, E. Ávalos-Marrón, and R.L. González, *Photocatalytic hydrogen evolution on tubular shape cellulose acetate/crystalline nanocellulose/polyvinyl alcohol membranes with embedded nanocrystalline catalysts.* International Journal of Hydrogen Energy, 2024. **79**: p. 943-951.

13. Yang, J., H. Chen, P. Bai, J. Xie, H. Wang, K. Jiang, and C. Yang, *Modulating the electronic structure of macroporous $SrTiO_3$ through cobalt doping for enhance photocatalytic hydrogen evolution.* International Journal of Hydrogen Energy, 2024. **80**: p. 104-114.

14. Orak, C. and A. Yüksel, *Comparison of photocatalytic performances of solar-driven hybrid catalysts for hydrogen energy evolution from 1, 8–Diazabicyclo [5.4. 0] undec-7-ene (DBU) solution.* International Journal of Hydrogen Energy, 2022. **47**(14): p. 8841-8857.

15. Gadge, S.S., Y.A. Sethi, M. Shinde, R. Chauhan, C. Ramana, M. Ashokkumar, and S.W. Gosavi, *Catalysing a sustainable future: Harnessing solar energy with novel $Co_3O_4$@ $VO_2$ nanocomposites for enhanced photocatalytic hydrogen generation and dye degradation.* International Journal of Hydrogen Energy, 2024. **67**: p. 200-215.

16. Liu, J., Z. Zhao, C. Xu, and J. Liu, *Structure, synthesis, and catalytic properties of nanosize cerium-zirconium-based solid solutions in environmental catalysis.* Chinese Journal of Catalysis, 2019. **40**(10): p. 1438-1487.

17. Majumder, S., *Synthesis methods of nanomaterials for visible light photocatalysis*, in *Nanostructured Materials for Visible Light Photocatalysis*. 2022, Elsevier. p. 47-113.
18. Zhou, Y., *Controllable design, synthesis and characterization of nanostructured rare earth metal oxides.* Physical Sciences Reviews, 2020. **5**(3): p. 20180084.
19. Eaimsumang, S., S. Wongkasemjit, S. Pongstabodee, S.M. Smith, S. Ratanawilai, N. Chollacoop, and A. Luengnaruemitchai, *Effect of synthesis time on morphology of CeO2 nanoparticles and Au/CeO2 and their activity in oxidative steam reforming of methanol.* Journal of Rare Earths, 2019. **37**(8): p. 819-828.
20. Zhang, G., Z. Zhao, J. Xu, J. Zheng, J. Liu, G. Jiang, A. Duan, and H. He, *Comparative study on the preparation, characterization and catalytic performances of 3DOM Ce-based materials for the combustion of diesel soot.* Applied Catalysis B: Environmental, 2011. **107**(3-4): p. 302-315.
21. Stawowy, M., R. Ciesielski, T. Maniecki, K. Matus, R. Łużny, J. Trawczynski, J. Silvestre-Albero, and A. Łamacz, *CO2 hydrogenation to methanol over Ce and Zr containing UiO-66 and Cu/UiO-66.* Catalysts, 2019. **10**(1): p. 39.
22. Li, Y., L.A. Zhang, Y. Qin, F. Chu, Y. Kong, Y. Tao, Y. Li, Y. Bu, D. Ding, and M. Liu, *Crystallinity dependence of ruthenium nanocatalyst toward hydrogen evolution reaction.* Acs Catalysis, 2018. **8**(7): p. 5714-5720.
23. Lin, J.-W., C.-A. Liao, B.-H. Chen, X. Cai, and P.-T. Chen, *Understanding mechanism conversion in hydrogen evolution reaction on PtSe2: Role of layer number explored by density functional theory.* International Journal of Hydrogen Energy, 2024. **69**: p. 1129-1136.
24. Li, L., G. Zhang, B. Wang, T. Yang, and S. Yang, *Electrochemical formation of PtRu bimetallic nanoparticles for highly efficient and pH-universal hydrogen evolution reaction.* Journal of Materials Chemistry A, 2020. **8**(4): p. 2090-2098.
25. Li, L., S. Wang, L. Xiong, B. Wang, G. Yang, and S. Yang, *Surface-engineered mesoporous Pt nanodendrites with Ni dopant for highly enhanced catalytic performance in hydrogen evolution reaction.* Journal of Materials Chemistry A, 2019. **7**(20): p. 12800-12807.
26. Basu, M., *2D Thin Sheet Heterostructures of $MoS_2$ on $MoSe_2$ as Efficient Electrocatalyst for Hydrogen Evolution Reaction in Wide pH Range.* 2020.

27. Zhang, Y., K.E. Arpino, Q. Yang, N. Kikugawa, D.A. Sokolov, C.W. Hicks, J. Liu, C. Felser, and G. Li, *Observation of a robust and active catalyst for hydrogen evolution under high current densities.* Nature Communications, 2022. **13**(1): p. 7784.

28. Wen, X. and J. Guan, *Recent progress on MOF-derived electrocatalysts for hydrogen evolution reaction.* Applied Materials Today, 2019. **16**: p. 146-168.

29. Bai, Y., H. Zhang, X. Lu, L. Wang, Y. Zou, J. Miao, M. Qiao, Y. Tang, and D. Zhu, *Self-supported Ru-incorporated NiSe2 for ampere-level current density hydrogen evolution.* Chemistry–A European Journal, 2023. **29**(28): p. e202300205.

30. Li, Y., B. Wei, Z. Yu, O. Bondarchuk, A. Araujo, I. Amorim, N. Zhang, J. Xu, I.C. Neves, and L. Liu, *Bifunctional porous cobalt phosphide foam for high-current-density alkaline water electrolysis with 4000-h long stability.* ACS Sustainable Chemistry & Engineering, 2020. **8**(27): p. 10193-10200.

31. Yu, T., Q. Xu, G. Qian, J. Chen, H. Zhang, L. Luo, and S. Yin, *Amorphous CoO x-decorated crystalline $RuO_2$ nanosheets as bifunctional catalysts for boosting overall water splitting at large current density.* ACS Sustainable Chemistry & Engineering, 2020. **8**(47): p. 17520-17526.

32. Zhai, Z., C. Zhang, B. Chen, L. Liu, H. Song, B. Yang, Z. Zheng, J. Li, X. Jiang, and N. Huang, *A Highly Active Porous $Mo_2C$-$Mo_2N$ Heterostructure on Carbon Nanowalls/Diamond for a High-Current Hydrogen Evolution Reaction.* Nanomaterials, 2024. **14**(3): p. 243.

## 4.6 Appendix A. Supplementary Material.

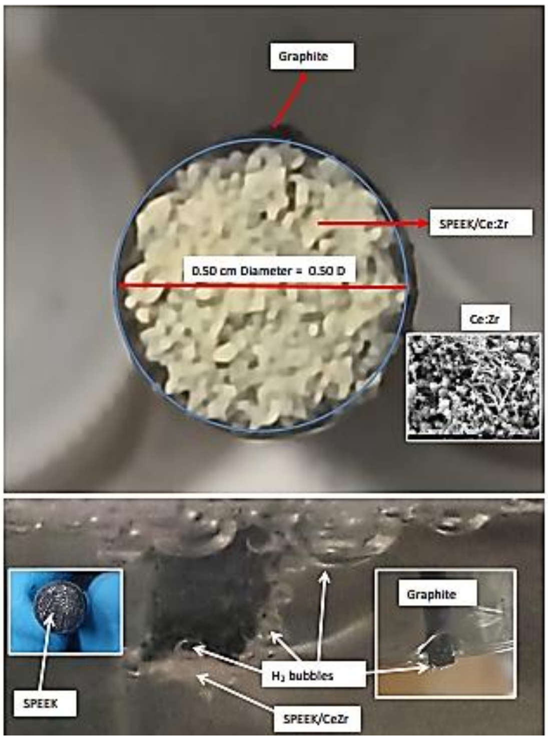

**Fig. 4S1:** Digital images of electrodes. (a) SPEEK/Ce:Zr after hydrogen generation; (b) Phase

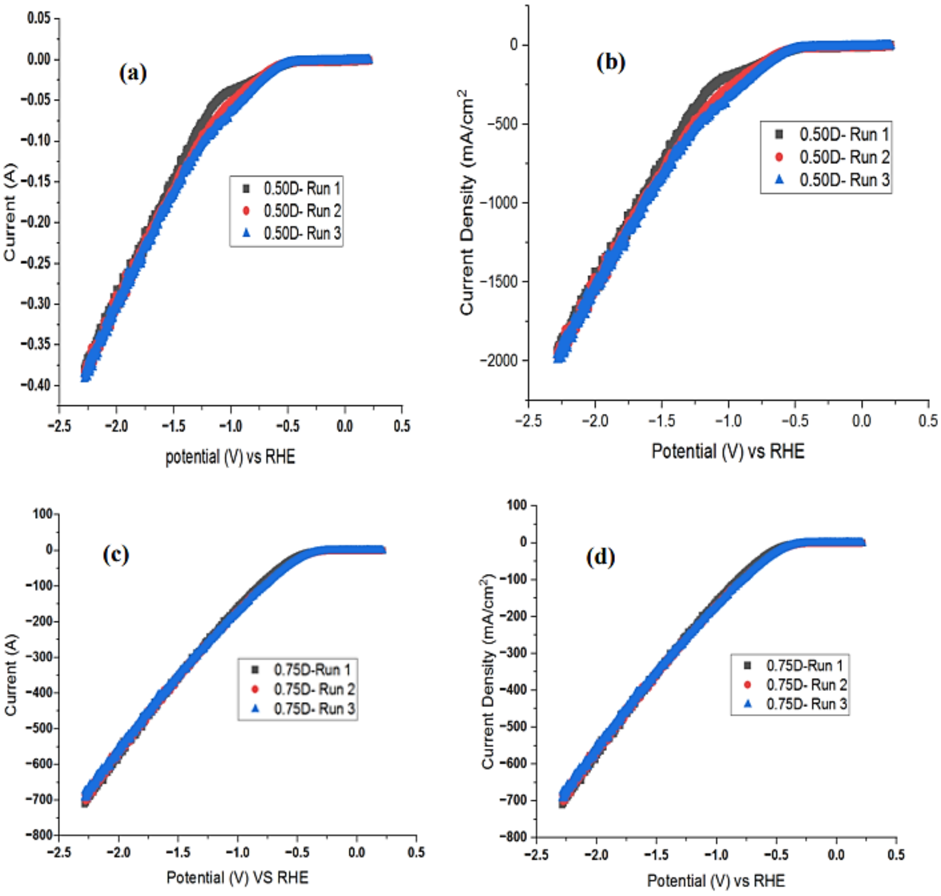

**Fig. 4S2:** LSV plot of current/current density vs Potential (V) vs RHE. (a- b) SPEEK/Ce:Zr on 0.5 cm diameter graphite (Gamry); after hydrogen generation; (c-d) SPEEK/Ce:Zr on 0.75 cm diameter graphite (from a dry cell battery).

# CHAPTER 5: HYDROGEN EVOLUTION REACTION BY SULFATED ZIRCONIUM OXIDE NANOPARTICLES

## 5.1. Introduction

The combustion of hydrocarbon-based fuels releases a substantial amount of carbon dioxide (a greenhouse gas) into the atmosphere, contributing to global warming. It is now clear that this significantly impacts the world’s climate conditions [1]. As a result, developing alternative energy sources, particularly non-carbon-based fuel, is critical and, thus, an attractive area of research globally. As one of the alternative fuels currently being considered, hydrogen has proven to be a fascinating energy source. Hydrogen, the universe's most abundant element, has long been known for its energy potential. It is a versatile fuel that may be utilized in a variety of applications, including heating, manufacturing, power generation, and transportation [2, 3]. One of the primary benefits of hydrogen is its ability to generate electricity without producing greenhouse gases or other hazardous pollutants when used as fuel for fuel cells or combustion engines [4]. This makes hydrogen an intriguing choice for accomplishing decarbonisation and dealing with climate change challenges. Several processes can be used to produce hydrogen, including reforming, electrolysis, and the autothermal procedure [5]. Hydrogen produced by reforming and autothermal technologies demands high temperatures and contributes significantly to environmental pollution [6]. On the other hand, hydrogen produced through electrolysis is an environmentally beneficial method, making electrolysis a desirable and promising process [7].

The hydrogen evolution reaction (HER), one of the half-reactions in the process of electrocatalytic water splitting, has received a lot of attention in the last few decades, leading to the discovery and design of several active catalysts [8-10]. Extensive research reveals that catalysts with high intrinsic performance have a large surface area and promote faster electron transfer. This means that increasing these properties should be a major goal while designing and preparing these catalysts. Catalyst fabrication methods can be customized to the aforementioned features based on their internal impacts and extrinsic assistance [11]. The fabrication strategy of intrinsic or extrinsic influences seldom affects the structural or electrical performance of catalytic materials independently but improves both together. For example, nano-structuring impact and narrow size distribution are effective in increasing both interfacial area (due to structural impact) and the number of catalytically active sites that are inherently exposed (electronic impact), increasing electrocatalytic effectiveness [12].

The catalytic properties of metal oxide surfaces are commonly discussed in terms of acid-base properties. Some reactions require acidic sites, whereas others occur at basic sites. Many oxides employed as industrial catalysts are multicomponent materials [13]. It has been discovered that the acid characteristics of mixed metal oxides can be altered by using different metal oxide ingredients at varying concentrations and modifying the sample treatment. Thus, it appears that by carefully selecting the aforementioned variables, mixed oxides can be used to create new catalysts with the appropriate acid characteristics [14, 15].

Zirconia catalyst is an amphoteric oxide with a monoclinic structure at ambient temperature [16], which transforms reversibly to tetragonal [17] and ultimately cubic (distorted fluorite) at higher temperatures [18]. The sulfation treatment of $ZrO_2$ transforms the material into a large surface area and highly acidic tetragonal sulfated structure. Furthermore, dopants such as $SiO_2$ might alter the characteristics of $SZrO_2$-based catalysts by slowing surface area loss and structural modifications that ordinarily occur during heat exposure [19]. Because oxygen vacancies are not expected to form in $SiO_2$-$ZrO_2$ catalytic systems, the observed thermal stability is driven by silica inhibiting the development of $ZrO_2$ particles [20, 21].

In this work, sulphated zirconia ($SZrO_2$) and SZr: $SiO_2$ mixed oxides at varying ratios were synthesized, characterized and explored for use as suitable catalysts for hydrogen evolution reaction (HER). The optimal catalysts were adsorbed onto a graphite electrode’s surface by a drop-dry method and used to generate hydrogen gas under acidic conditions. The kinetics, bubble behaviour as well as mechanism of interaction were comprehensively explored and described.

## 5.2. Materials and methods

### 5.2.1 Materials

Zirconium oxychloride hydrate and tetraethoxysilane (TEOS) were obtained from Sigma Aldrich. Ammonium sulphate, ammonia hydroxide (30-33%), and ethanol were purchased from Merck. All the chemicals were used without further purification. Millipore ultrapure water (18.2 MΩ.cm) was used for all aqueous preparations.

### 5.2.2 Synthesis of $SiO_2$

Silica ($SiO_2$) materials were synthesized by the Stöber method using tetraethyl orthosilicate (TEOS) as a silica source [22]. In a typical procedure, a certain amount of ethanol, deionized (DI) water, and ammonia were stirred together. The TEOS was added dropwise into the mixture to form a turbid suspension. The resultant mixture was stirred for 6 hours, and then placed in a sonicating bath for 10 minutes at room temperature. The colloidal suspension was centrifuged and washed several times with ethanol until the pH dropped to 7 (sonicating for 5 minutes between washes to avoid agglomeration). The material was then dried overnight at 70 °C and subsequently calcined at 600 °C for 2 hours.

### 5.2.3 Synthesis of sulfated zirconia (SZr) nanoparticles

$ZrO_2$ nanoparticles were synthesized by precipitation technique, with starting components being ammonia ($NH_3$) and zirconium oxychloride hydrate ($ZrOCl_2.8H_2O$) [138]. The precipitation of zirconium hydroxide ($Zr(OH)_4$) was achieved by adding an aqueous ($NH_3$) solution dropwise to an aqueous solution of 0.2M $ZrOCl_2.8H_2O$ at room temperature while rapidly stirring until the necessary pH of 10 was reached. The precipitate was centrifuged and washed with deionized water until the chlorine ions ($Cl^-$) were undetectable by the silver nitrate ($AgNO_3$) test, on the suspension [$Zr(OH)_4$]. The suspension was dried in an oven overnight at 80 $^oC$. Then dried material and ammonium sulfate were ground for 10 minutes and placed for 18 hours at room temperature to produce sulfated zirconia (SZr). The resulting solid was then calcined at 600 $^oC$ for 2 hours, and then further ground to an ultra-fine powder using a mortar and pestle.

### 5.2.4 Synthesis of SZr: $SiO_2$ powder

Varied amounts of silica and sulfated Zirconia powder were suspended in 60 ml ethanol solution and stirred for 15 minutes, then ultrasonicated in a bath for 1 hour. After sonication, the sulphated zirconium-silica (SZr: $SiO_2$) material was collected by centrifugation, washed several times in ethanol then dried overnight at 70 °C, and subsequently calcined at 550 °C for 5 hours.

### 5.2.5 Material Characterization

The morphologies of SZr and SZr: $SiO_2$ metal oxides were examined using scanning electron microscopy (SEM) JEOL JMS-7800F model coupled with electron dispersive spectroscopy (EDS) Oxford Aztec 350 X-Max80. To investigate the changes in chemical bond structures and identification of functional groups, Bruker Vertex 70 Fourier-transform infrared spectroscopy (FTIR) was used. The FT-IR spectra were recorded within a wavenumber window of 400–4000 $cm^{-1}$. Diffraction patterns were obtained through Rigaku SmartLab X-ray diffractometer (XRD) with a Cu-Kα radiation source operated at 30 kV and a current of 200 mA with a scanning rate of 0.026 °/sec from 5° to 90°. Cyclic voltammetry (CV) and Electrochemical impedance spectroscopy (EIS) studies were performed within a potential window of -0.05 and +0.70 V and at $1 \times 10^5$ Hz to 0.1 Hz frequency with an open circuit potential (OCP) of 0.24 V *using* a three-electrode cell (TEC) connected to a Metrohm Autolab Potentiostat (PGSTAT30) equipped with a Nova software version 2.1. The TEC consists of platinum wire, Ag/AgCl (3M KCl) and as-synthesized materials on a graphite substrate as counter, reference and working electrodes, respectively.

## 5.3. Results and discussion

### 5.3.1 XRD and FTIR characterizations

The X-ray diffraction patterns of SZr and SZr: $SiO_2$ mixed oxides are shown in Fig. 5.1a. As shown in Fig.1a, the XRD pattern of SZr exhibits intense peaks at 2θ = 17.36°, 23.99°,28.05°, 31.33°, 33.98°,40.95°, 45.28°, 48.65°, 55.42°, 59.73°, 65.59° and 74.88° attributed to the monoclinic mineral baddeleyite phase of zirconia corresponding to (100), (011), (-111), (111), (002), (102), (-202), (-212), (122), (-302), (-231) and (140) planes (JCPDS card number 70-7359), respectively. In addition, the pattern of SZr shows other peaks at 2θ = 29.95°, 34.96° and 49.73°, which are related to the monoclinic phase corresponding to (101), (110) and (112) planes (JCPDS card number 5-4252).

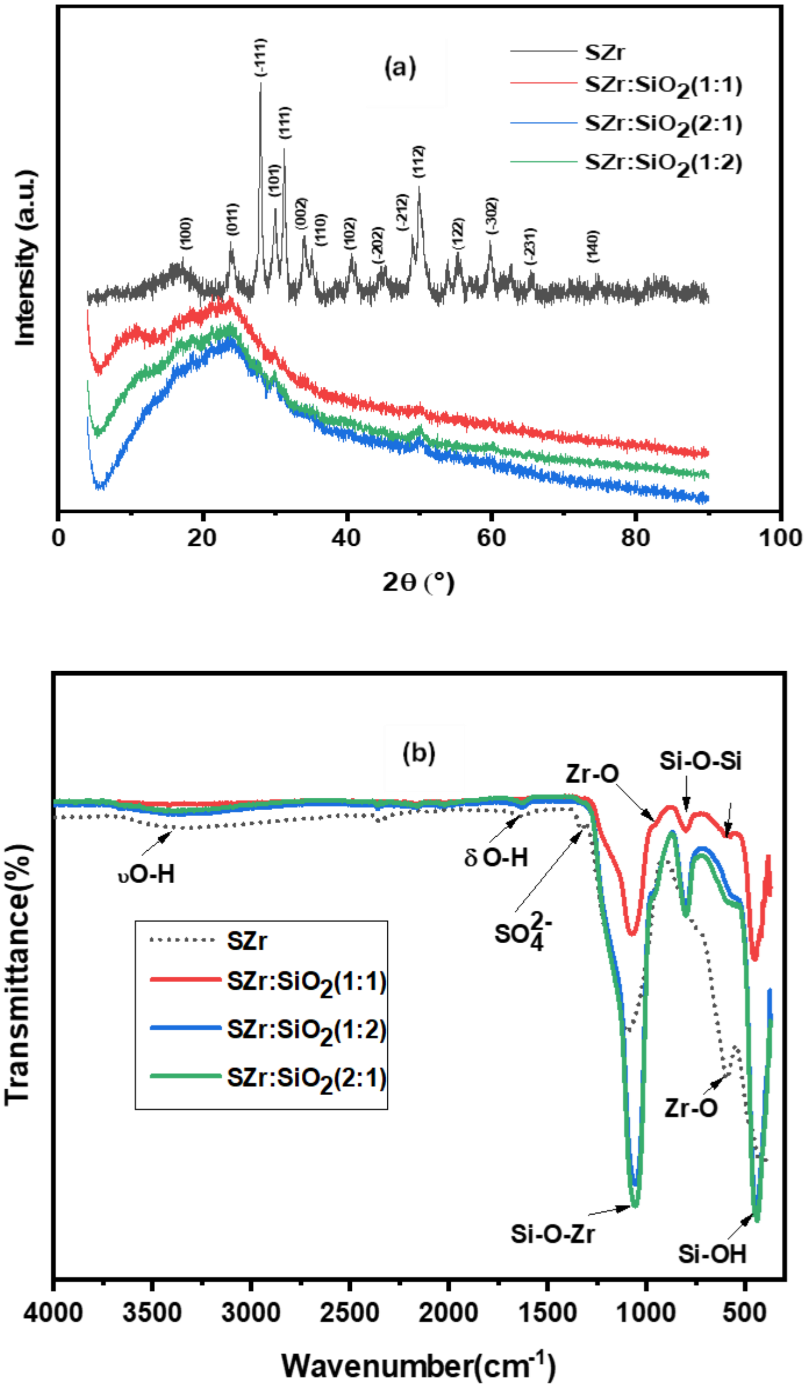

***Fig. 5. 1***: Crystallinity and functional group characterizations. (a) XRD patterns; (b) FTIR.

These results suggest that both monoclinic and tetragonal phases coexisted in this sample. The characteristic broad peak of amorphous silica in the 2θ range of 20° - 30º was observed in all mixed metal oxides. The XRD patterns of the SZr: $SiO_2$ (1:1

through 2:1) samples were found to be amorphous as no distinct diffraction lines were observed, which signifies that zirconia is distributed uniformly within the structure with little to no phase separation.

The IR spectra of all samples displayed absorption bands within 3386–3405 $cm^{-1}$ and at 1620 $cm^{-1}$, corresponding to O-H stretching and bending modes of water molecules, respectively (Fig. 5.1b). A small band situated at 1342 $cm^{-1}$ for SZr was also observed, representing the sulfate group's coordinated molecular water [24]. All SZr: $SiO_2$ samples showed the silanol Si-OH bond at around 451-445 $cm^{-1}$ and the asymmetric stretching vibration for Si-O-Si at 808 $cm^{-1}$. When SZr was fully incorporated into the $SiO_2$ material, it was expected that the silanol groups of the $SiO_2$ spheres should be modified [25]. The band at 1056 $cm^{-1}$ underwent a shift at 1091 $cm^{-1}$ caused by the Si-O-Zr formation, and the degree of the band shift depends on the number of Si-O-Zr bonds, in line with the increment in zirconium precursor concentration [26]. The appearance of absorption bands around 820 $cm^{-1}$ associated with a Zr-O stretching vibration signal was found readily displayed in SZr: $SiO_2$ (1:1), SZr: $SiO_2$ (1:2), and SZr: $SiO_2$ (2:1). The infrared vibration peaks at 451 and 445 $cm^{-1}$ were ascribed to the characteristic vibration of tetragonal zirconia (Zr-O) clusters in agreement with the XRD results.

### 5.3.2 SEM analysis

The SEM and elemental mapping analysis were carried out to study the morphology of the prepared samples. The SZr image showed that the sample contained rod/bar-like nanoparticles that had undergone agglomeration (Fig. 5.2a). The $SiO_2$ image (Fig. 5.2b) showed that the sample was made up of agglomerated small spherical-like particles. Fig. 5.2c-d shows the SEM image of composite SZr: $SiO_2$ material prepared at a ratio of 1:1 with insert magnification (Fig. 5.2d′). It was observed that the morphology of the $SiO_2$ underwent a change from agglomerated spherical-like particles to a multilayered-like material after being loaded with SZr particles. Furthermore, it was observed as well that the degree of agglomeration of SZr particles was drastically reduced when loaded on the surface of silica material, suggesting that the SZr particles might be evenly dispersed on the surface of $SiO_2$. When the preparation ratio of the composite material was adjusted to 1:2 (SZr: $SiO_2$), the material displayed bigger pore defects (Fig. 5.2e-f).

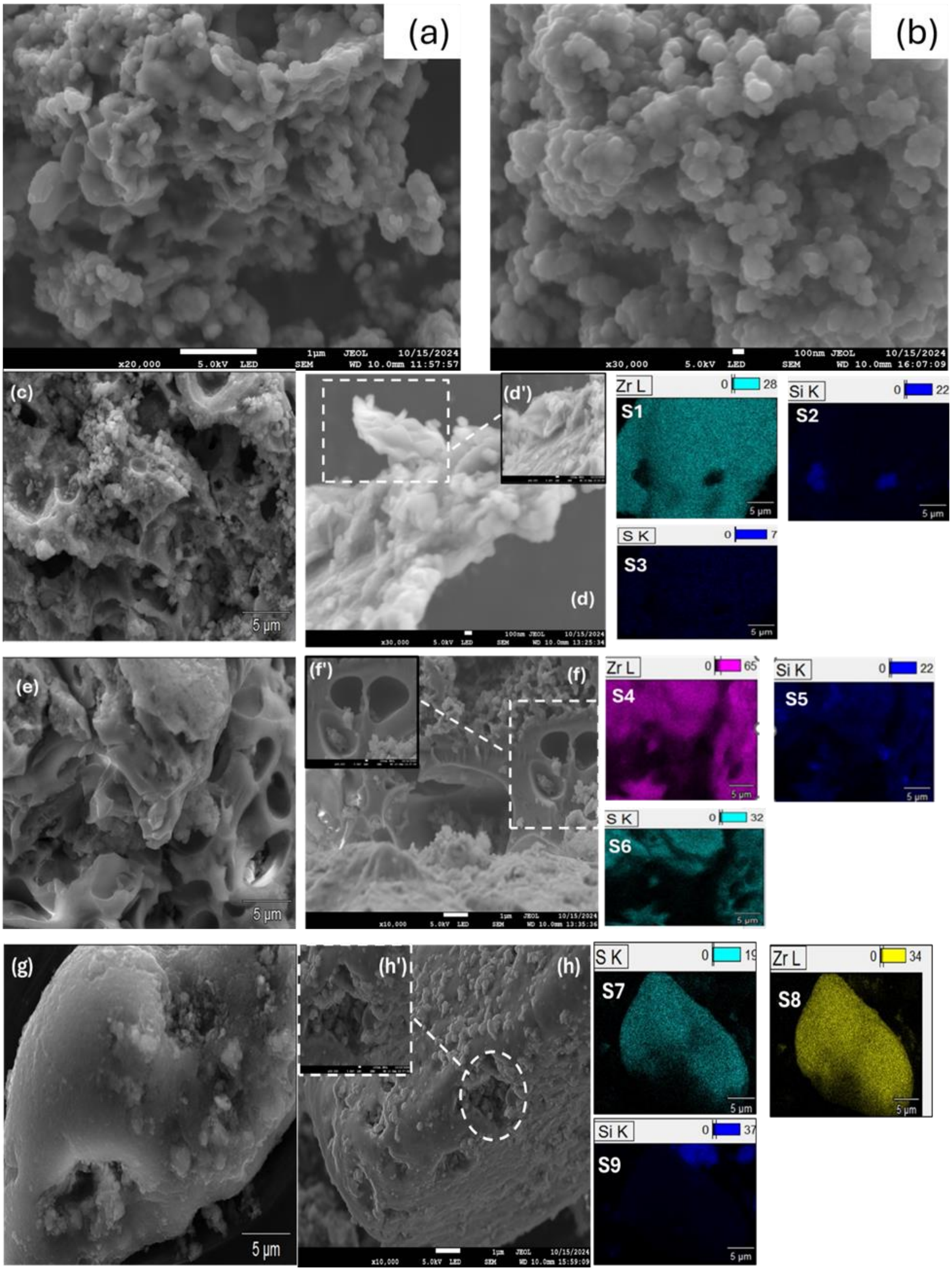

**Fig. 5. 2:** SEM images of the as-synthesized materials. (a-b) SZr and $SiO_2$, respectively; (c-d) SZr: $SiO_2$ (1:1); (e-f) SZr: $SiO_2$ (1:2); (g-h) SZr: $SiO_2$ (2:1), with insert magnification (d′,f′,h′) and elemental mapping (S1-S9).

When the preparation ratio was adjusted to a ratio of 2:1 (SZr: $SiO_2$), the SEM imaging showed material with reduced pore defects (Fig. 5.2g-h).

The elemental mappings of the materials are shown in Fig 5.2 (S1-S3), which further confirmed the even distribution of SZr on $SiO_2$ for all tested materials. The instrumentation confirms the successful preparation of the composite materials by identifying the presence of S, Zr, and Si as compositional elements in the as-synthesized materials.

### 5.3.3 Electrochemical characterizations

Cyclic voltametric analyses alongside the Randles-Sevcik plots were used to evaluate the redox properties of the as-synthesized electrocatalysts in the presence of the ferrocyanide redox probe (Fig. 5.3a-j). As shown in Fig. 5.3a-j, all materials favoured the diffusion-controlled process. Also, the electrocatalysts improved the oxidation process of the graphite support. In addition, it is worth noting that increasing the amount of SZr improved the cathodic interactions than increasing the amount of $SiO_2$ in the composites. Thus, among the tested electrocatalysts, SZr: $SiO_2$ (2:1) exhibited the highest redox activity relative to oxidizing Fe(II) to Fe(III) system and vice versa, having $R^2$ of 0.99855 and 0.98203 for both anodic (oxidation) and cathodic (reduction) reactions.

The results of the Nyquist plots and Bode analyses are shown in Fig. 5.4a-b. Fig. 5.4c shows the circuit representation of the EIS analyses. As shown in Fig. 5.4a-b, in the high-frequency region (1000-10000 Hz), the semicircle and phase angle decreased in the following order: GE-SZr: $SiO_2$ (2:1) > GE-SZr: $SiO_2$ (1:1) > GE-SZr: $SiO_2$ (1:2) > GE-SZr > GE revealing the superiority of the SZr: $SiO_2$ (2:1) compared to other tested materials in terms of better charge transfer effectiveness relative to the redox probe couple (Fe(II/Fe(III) (Table 5.1). The reversibility of an electron exchange process on an electroactive surface can be determined using the value corresponding to the difference between the anodic and cathodic peaks ($\Delta$Ep), with a value of 57 mV representing a reversible charge transfer process at 25 $^0$C for a one-electron exchange process [27, 28]. The extent of deviation from this value at this temperature suggests a quasi-reversible (smaller deviation) or irreversible electron exchange process. As shown in Table 1, the values of $\Delta$Ep for the as-synthesized materials were not too far from 57 mV (0.057 V), implying their characteristics to be quasi-reversible [27-29]

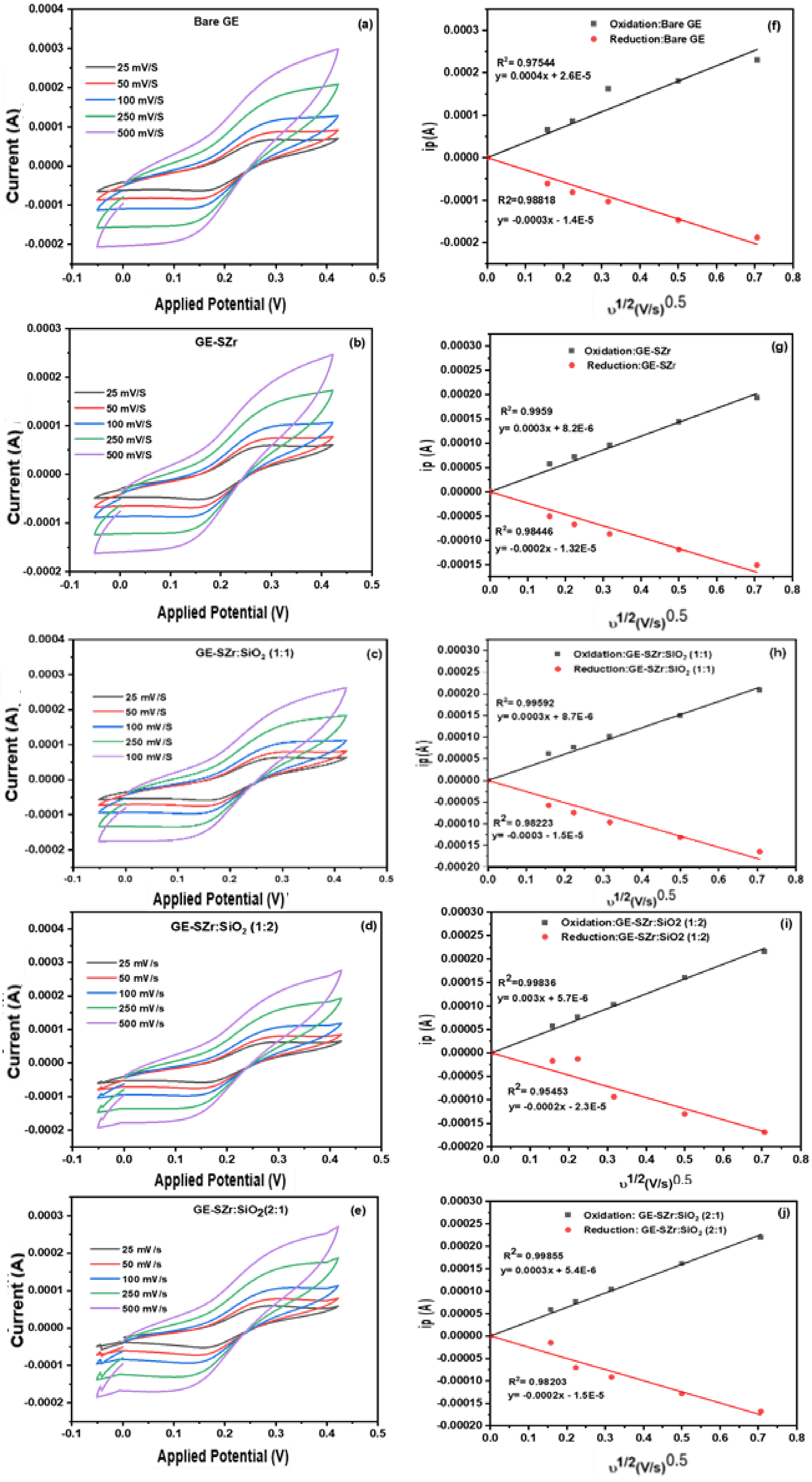
Bare GE
(a)
25 mV/S
50 mV/S
100 mV/S
250 mV/S
500 mV/S
Current (A)
Applied Potential (V)
Oxidation:Bare GE
Reduction:Bare GE
(f)
R² = 0.97544
y= 0.0004x + 2.6E-5
R2=0.98818
y= -0.0003x - 1.4E-5
ip (A)
υ1/2(V/s)0.5
GE-SZr
(b)
Oxidation:GE-SZr
Reduction:GE-SZr
(g)
R² = 0.9959
y= 0.0003x + 8.2E-6
R²= 0.98446
y= -0.0002x - 1.32E-5
GE-SZr:SiO2 (1:1)
(c)
25 mV/S
50 mV/S
100 mV/S
250 mV/S
100 mV/S
Oxidation:GE-SZr:SiO2 (1:1)
Reduction:GE-SZr:SiO2 (1:1)
(h)
R²= 0.99592
y= 0.0003x + 8.7E-6
R²= 0.98223
y= -0.0003 - 1.5E-5
GE-SZr:SiO2 (1:2)
(d)
25 mV/s
50 mV/s
100 mV/s
250 mV/s
500 mV/s
Oxidation:GE-SZr:SiO2 (1:2)
Reduction:GE-SZr:SiO2 (1:2)
(i)
R²=0.99836
y= 0.003x + 5.7E-6
R²= 0.95453
y= -0.0002x - 2.3E-5
GE-SZr:SiO2(2:1)
(e)
25 mV/s
50 mV/s
100 mV/s
250 mV/s
500 mV/s
Oxidation: GE-SZr:SiO2 (2:1)
Reduction: GE-SZr:SiO2 (2:1)
(j)
R²= 0.99855
y= 0.0003x + 5.4E-6
R²= 0.98203
y= -0.0002x - 1.5E-5

**Fig. 5. 3:** Voltammograms of the as-synthesized electrocatalysts with Randles-Sevcik plots. (a) Graphite Electrode (GE); (b) GE-SZr; (c) SZr: $SiO_2$ (1:1); (d) SZr: $SiO_2$ (1:2); (e) SZr: $SiO_2$ (2:1); (f-j) Randles-Sevcik plots of GE, GE-SZr, GE-SZr: $SiO_2$ (1:1), GE-SZr: $SiO_2$ (1:2) and GE-SZr: $SiO_2$ (2:1) respectively. Redox probe: $[Fe(CN)_6]^{3/-4-}$ Scan rates: 25–500 mV/s.

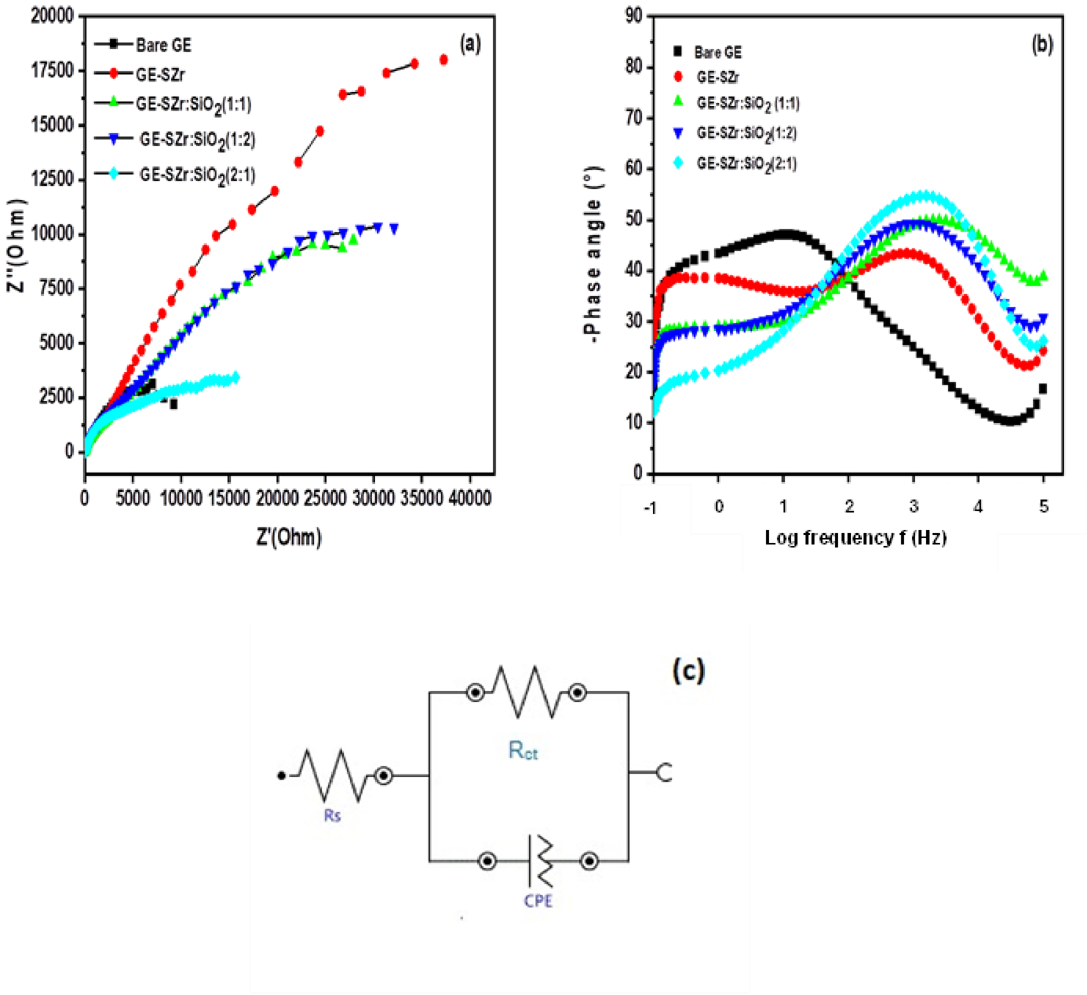

**Fig. 5. 4:** EIS analyses. (a) Nyquist plots; (b) Bode plot. Electrolyte: 0.1 M KCl containing $[Fe(CN)_6]^{3-/4-}$ ; (c) Randles fitting circuit model (Table 5.1).

**Table 5. 1:** Summary of CV and EIS data in 1 mM [Fe $(CN)_6]^{3-/4-}$

| Electrode | Rct (kΩ) | Rs (kΩ) | Phase angle Deg. | ∆Ep (V) |
|---|---|---|---|---|
| Bare GE | 12.1 | 29.9 | 48.13 | 0.1602 |
| GE-SZr | 101 | -23.7 | 43.45 | 0.1929 |
| GE-SZr:$SiO_2$ (1:1) | 59.5 | -37.9 | 49.83 | 0.1762 |
| GE-SZr:$SiO_2$ (1:2) | 77.8 | 206 | 49.63 | 0.1636 |
| GE-SZr:$SiO_2$ (2:1) | 4.42 | 35.7 | 55.16 | 0.1588 |

### 5.3.4 ECSA and Tafel polarization.

The results of the ECSA and Tafel polarization of the as-synthesized materials are shown in Fig. 5.5a-d and Table 5.2. The ECSA was estimated using the Eq (4.2). As shown in Fig. 5.5a and Table 5.2, the capacitance and thus the ECSA values of the bare electrode (GE) did not change after modification of the surface with the as synthesized electrocatalysts except for SZr which reduced the value by a 100 unit. Also, the corrosion potential remains the same as that of the bare electrode for all tested materials except for GE-SZr and GE-SZr: $SiO_2$ (2:1) which increased the values from -0,2389 to -0,2413 and -0,2438 V respectively. These results shows that all the tested electrode materials were less prone to corrosion since their corrosion potentials lied slightly in the negative potential window. However, GE/SZrSi (2:1) showed higher tendency to corrosion than GE, GE/SZr, GE/SZrSi (1:1) or GE/SZrSi (Table 5.2). These facts were further supported by the Tafel slopes of the tested electrocatalysts. In terms of the Tafel slopes, the lower the values, the faster is the reaction rate occurring at either the anode or cathode to cause a change in the potential. Thus, materials corrode easily and faster at lower Tafel slopes. As shown in Table 5.2, the GE/SZrSi (2:1) exhibited the least Tafel slope value (111.37) while the bare electrode GE showed the highest. This makes GE the material with the slowest corrosion rate while GE/SZrSi (2:1) exhibits the fastest corrosion speed.

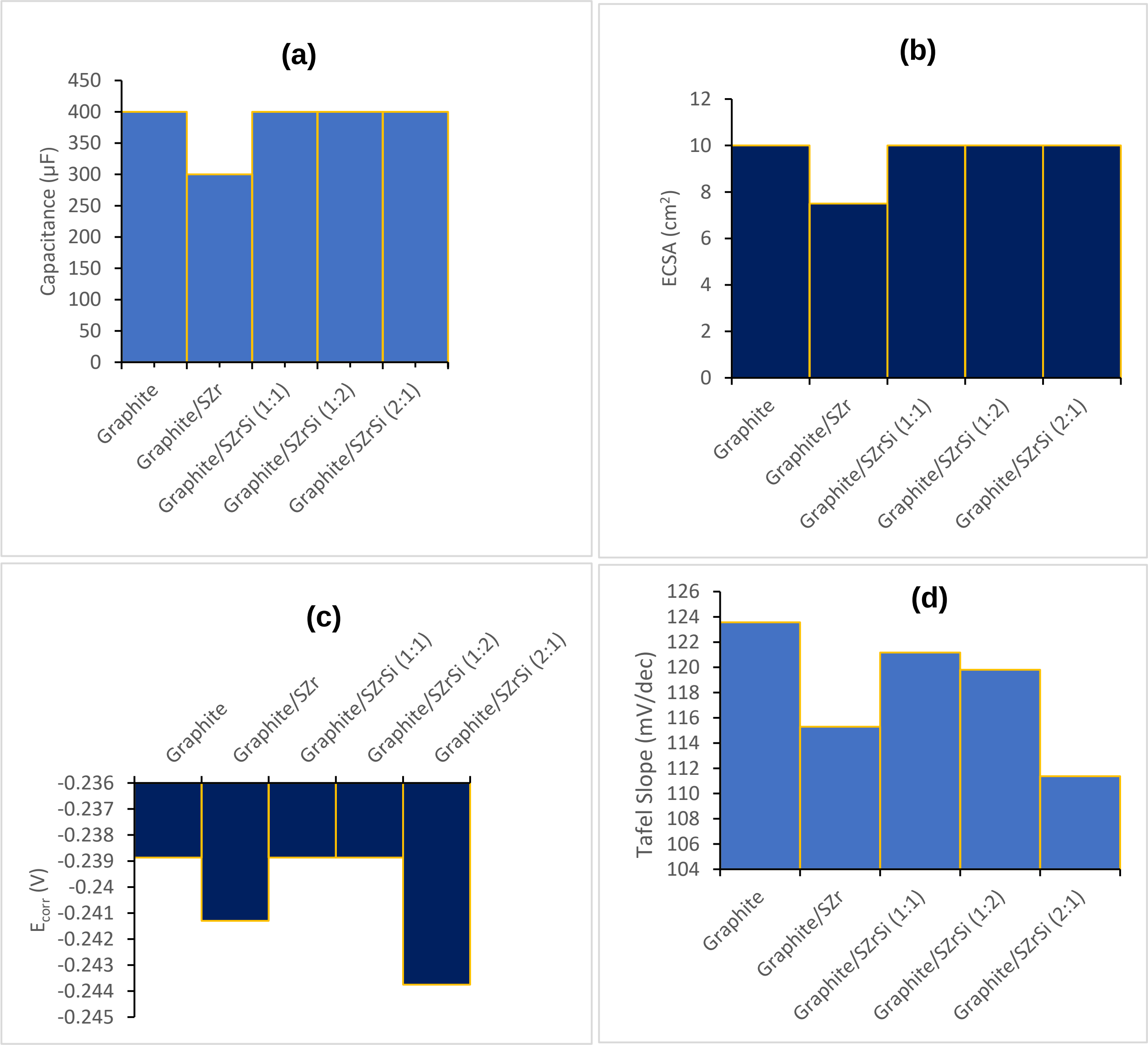

**Fig.5.5:** Polarization properties of the as-synthesized materials. (a) Capacitance values; (b) ECSA; (c) Corrosion potentials; (d) Tafel slopes.

**Table 5. 2: ECSA and Tafel polarization**

| Catalyst | Cdl (µF)[a] | ECSA ($cm^2$) | $E_{corr}$ (V) | Slope log A vs n | Tafel Slope (mV/dec) |
|---|---|---|---|---|---|
| GE | 400 | 10 | -0,2389 | 8,093 | 123,56 |
| GE-SZr | 300 | 7,5 | -0,2413 | 8,673 | 115,30 |
| GE-SZr:$SiO_2$ (1:1) | 400 | 10 | -0,2389 | 8,252 | 121,18 |
| GE/SZr:$SiO_2$ (1:2) | 400 | 10 | -0,2389 | 8,346 | 119,81 |
| GE/SZr:$SiO_2$ (2:1) | 400 | 10 | -0,2438 | 8,979 | 111,37 |

### 5.3.4 Hydrogen Production, mechanism and Turnover frequency.

The synthesized materials were investigated for HER activity in an acidic medium. The electrochemical hydrogen evolution reaction was carried out using linear scan voltammetry (LSV) in 0.33 M $H_2SO_4$ at a scan rate of 10 mV/s in a potential range between -2.3 and 0.25 V (vs. RHE). Fig. 5.5a shows a comparison of HER activity of Graphite-SPEEK/SZr and Graphite-SPEEK/SZr: $SiO_2$ mixed oxides with that of bare graphite electrode. The HER current density values of 880, 126, 1482 and 1442 mA/cm$^2$ at -2.3 V were observed for catalysts SZr, SZr:$SiO_2$ (1:1), SZr:$SiO_2$ (1:2), and SZr: $SiO_2$ (2:1), with onset potentials of -0.69, -2.2, -0.61, -0.66 V, respectively. The current density of the bare GE and Graphite/SPEEK was 1740 and 1159 mA/cm$^2$. The higher HER activity Graphite-SPEEK/SZr:$SiO_2$ (1:2) followed by Graphite-SPEEK/SZr: $SiO_2$ (2:1) metal oxides can be attributed to the strong interaction between the surface functional group SiO-H and $H^+$ ion Eq. (5.1-5.3) Scheme 1.

$$\text{Si-OH}_{(s)} + H^+_{(aq)} \longrightarrow (\text{SiO}^+(H_{(aq)})\text{-H})_{(s)} \qquad \textbf{(5.1)}$$

$$(\text{SiO}^+(H_{(aq)})\text{-H})_{(s)} + e^- \longrightarrow (\text{SiO}^+(H_{(ads)})\text{-H})_{(s)} \qquad \textbf{(5.2)}$$

$$2(\text{SiO}^+(H_{(ads)})\text{-H})_{(s)} \longrightarrow 2\text{SiO-H}_{(s)} + \uparrow H_{2(g)}\ \text{(Bubble)} \qquad \textbf{(5.3)}$$

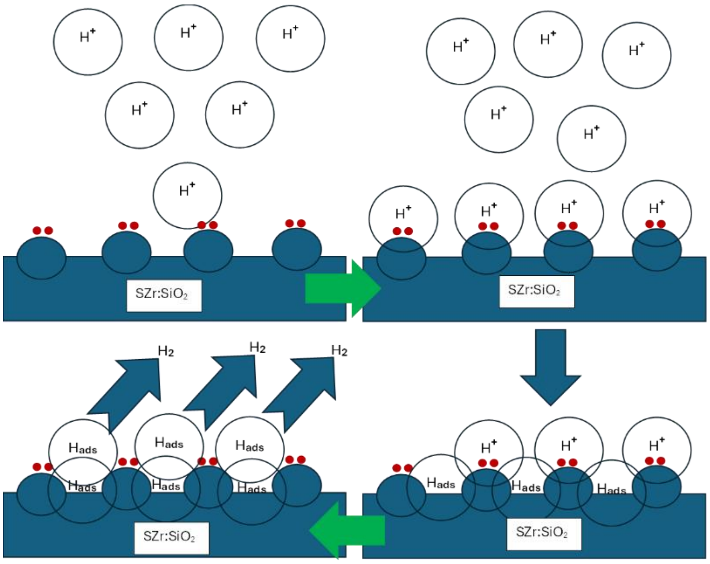

**Scheme 5.1:** Proposed mechanism of hydrogen evolution on Szr:$SiO_2$.

According to Eq. (5.1-5.3) Scheme 5.1, the silanol group (Fig. 5.1b) on the as-synthesized materials attracted a proton from the aqueous stream via covalent donation forming a protonated species Eq. (5.1). The protonated silanol system then interacted with an electron under the reducing electrode environment to generate an atom of surface adsorbed hydrogen Eq. (5.2). Afterwards, combination of two surface adsorbed H atoms formed the hydrogen gas, the bubble of which detached from the silanol surface Eq. (5.3).

In order to establish the stability of the current produced by the material, chronoamperometric experiments at a controlled potential were carried out. Fig. 5.5b shows the chronoamperometric profiles measured at room temperature in 0.3333 M $H_2SO_4$ at an applied potential of − 2.5 V. As shown in Fig. 5.5b, the 1:2 composite material showed the highest stability among all tested materials. This stability property may be related to the presence of excess $SiO_2$ on the surface of the material Eq. (5.1-5.3).

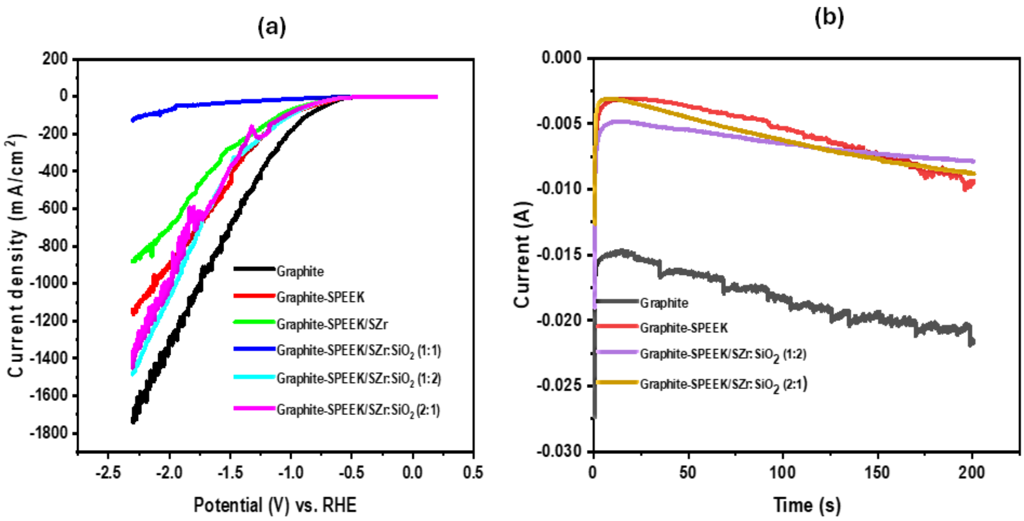

**Fig. 5.6:** HER outputs of the as synthesized electrocatalysts. (a) LSV plots vs. RHE; (b) Chronoamperometry plots at -2.5 V (vs Ag/AgCl (3M KCl)). Electrolyte solution: 0.33 M $H_2SO_4$.

Turnover frequency (TOF) measures the catalytic activity of a catalyst, defined by the number of substrate molecules that are converted to the product per active site of the catalyst per unit time. It helps in assessing how effective a catalyst is by showing the efficiency of its active sites in propelling a reaction. The values of the estimated TOF of the tested electrocatalysts are shown in Table 5.3. as shown in Table 5.3, the order of increasing TOF for all tested electrocatalysts is GE < GE/SZr <GE/SZr:$SiO_2$ (2:1) < GE/SZr:$SiO_2$ (1:2) < GE/SZr:$SiO_2$ (1:1), making the GE/SZr:$SiO_2$ (1:1) the best material for the hydrogen generation in terms of TOF at -0.55 V vs RHE. The TOF data was obtained from LSV results shown in Fig. 5.7 in conjunction with the ECSA data in Table 5.3 and Eq. (4.3).

**Table 5. 3:** Turnover frequency data of the as-synthesized materials.

| Catalyst | ECSA | $J_{ECSA}$ at -0.55 V ($A/cm^2$) | TOF= $J_{ECSA}/2n_{cat}F$ ($cm^{-2}s^{-1}$) | TOF ($s^{-1}$) |
|---|---|---|---|---|
| GE | 10 | -0,725 | -0,0045 | -0,0451 |
| GE/SZr | 7,5 | -0,600 | -0,0719 | -0,5392 |
| GE/SZr:$SiO_2$ 1:1 | 10 | -1,700 | -0,2566 | -2,5662 |
| GE/SZr:$SiO_2$ 1:2 | 10 | -1,275 | -0,2322 | -2,3216 |
| GE/SZr:$SiO_2$ 2:1 | 10 | -0,550 | -0,1455 | -1,4551 |

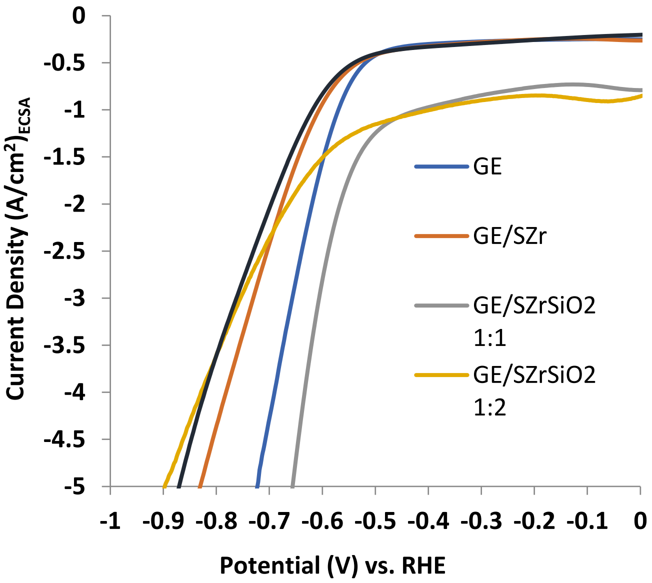

**Fig. 5. 7:** Polarization curves of the tested HER electrocatalysts.

Table 5.4 shows the comparison between the hydrogen production current density data value of the present work and some work reported in the literature. As shown in Table 5.4, the present material exhibits better HER activity than the reported works.

**Table 5.4**: Comparative HER activity data with some reported literature works.

| Material | Current density vs. RHE ($mA/cm^2$) | Ref. |
|---|---|---|
| Ni-Ce-Pr-Ho/NF | -50 | [30] |
| Biochar | -100 | [31] |
| nPdNFs | -50 | [32] |
| VN/Co@GNC | > -200* | [33] |
| Copper-N-$SiO_2$ | -60 | [34] |
| MoS2@AB | -550 | [35] |
| GE/SZr:$SiO_2$ (1:1) | -1700 | Present work |
| GE/SZr:$SiO_2$ (1:2) | -1275 | Present work |

*Slightly.

## 5.4. Conclusion

This research investigates SZr:$SiO_2$ mixed oxides as alternatives to platinum catalysts for the hydrogen evolution reaction (HER). The modified graphite (GE) electrodes, particularly the GE/SZr:$SiO_2$ (1:1) and GE/SZr:$SiO_2$ (1:2), respectively demonstrated exceptional performance with a hydrogen evolution current density of -1.70 and -1.28 $A/cm^2$ at -0.55 V vs. RHE based on ECSA dimension. These high performances were attributed to the easy exchange of electron between their surfaces and aqueous hydrogen ions and availability of numerous active sites on their surfaces. The research significantly advances the development of effective electrocatalysts for energy conversion devices in acidic environments and highlights the potential of non-platinum alternatives in sustainable energy applications.

## 5.5. References

1. Dhamodaran, G., G.S. Esakkimuthu, T. Palani, and A. Sundaraganesan, *Reducing gasoline engine emissions using novel bio-based oxygenates: a review.* Emergent materials, 2023. **6**(5): p. 1393-1413.
2. Badea, N.I., *Hydrogen as energy sources—Basic concepts.* Energies, 2021. **14**(18): p. 5783.
3. McCay, M.H. and S. Shafiee, *Hydrogen: An energy carrier*, in *Future energy*. 2020, Elsevier. p. 475-493.
4. Ishaq, H., I. Dincer, and C. Crawford, *A review on hydrogen production and utilization: Challenges and opportunities.* International Journal of Hydrogen Energy, 2022. **47**(62): p. 26238-26264.
5. Minutillo, M., A. Perna, and A. Sorce, *Green hydrogen production plants via biogas steam and autothermal reforming processes: energy and exergy analyses.* Applied Energy, 2020. **277**: p. 115452.
6. Song, H., Y. Liu, H. Bian, M. Shen, and X. Lin, *Energy, environment, and economic analyses on a novel hydrogen production method by electrified steam methane reforming with renewable energy accommodation.* Energy Conversion and Management, 2022. **258**: p. 115513.
7. Wang, T., X. Cao, and L. Jiao, *PEM water electrolysis for hydrogen production: fundamentals, advances, and prospects.* Carbon Neutrality, 2022. **1**(1): p. 21.
8. Liu, F., C. Shi, X. Guo, Z. He, L. Pan, Z.F. Huang, X. Zhang, and J.J. Zou, *Rational design of better hydrogen evolution electrocatalysts for water splitting: a review.* Advanced Science, 2022. **9**(18): p. 2200307.
9. Gong, Y., J. Yao, P. Wang, Z. Li, H. Zhou, and C. Xu, *Perspective of hydrogen energy and recent progress in electrocatalytic water splitting.* Chinese Journal of Chemical Engineering, 2022. **43**: p. 282-296.
10. Xu, Y., X. Zhang, Y. Liu, R. Wang, Y. Yang, and J. Chen, *A critical review of research progress for metal alloy materials in hydrogen evolution and oxygen evolution reaction.* Environmental Science and Pollution Research, 2023. **30**(5): p. 11302-11320.

11. Rahamathulla, N. and A.P. Murthy, *Advanced heterostructures as bifunctional electrocatalysts for overall water splitting-a review.* Journal of Energy Storage, 2023. **73**: p. 109127.
12. Yu, J., X. Du, H. Liu, C. Qiu, R. Yu, S. Li, J. Ren, and S. Yang, *Mini review on active sites in Ce-based electrocatalysts for alkaline water splitting.* Energy & Fuels, 2021. **35**(23): p. 19000-19011.
13. Bosica, G. and R. Abdilla, *Recent advances in multicomponent reactions catalysed under operationally heterogeneous conditions.* Catalysts, 2022. **12**(7): p. 725.
14. Qumar, U., J.Z. Hassan, R.A. Bhatti, A. Raza, G. Nazir, W. Nabgan, and M. Ikram, *Photocatalysis vs adsorption by metal oxide nanoparticles.* Journal of Materials Science & Technology, 2022. **131**: p. 122-166.
15. Marikutsa, A., M. Rumyantseva, E.A. Konstantinova, and A. Gaskov, *The key role of active sites in the development of selective metal oxide sensor materials.* Sensors, 2021. **21**(7): p. 2554.
16. Wen, Y., C. Zhou, L. Yu, Q. Zhang, W. He, and Q. Liu, *Preparation of nanometer zirconia by hydrothermal method: Influence of temperature and mechanism.* Solid State Sciences, 2023. **142**: p. 107237.
17. Asgerov, E.B., A.I. Beskrovnyy, N.V. Doroshkevich, C. Mita, D.M. Mardare, D. Chicea, M.D. Lazar, A.A. Tatarinova, S.I. Lyubchyk, and S.B. Lyubchyk, *Reversible martensitic phase transition in Yttrium-Stabilized $ZrO_2$ nanopowders by adsorption of water.* Nanomaterials, 2022. **12**(3): p. 435.
18. Cissé, C. and M.A. Zaeem, *A phase-field model for non-isothermal phase transformation and plasticity in polycrystalline yttria-stabilized tetragonal zirconia.* Acta Materialia, 2020. **191**: p. 111-123.
19. EL-Desouki, D.S., A.H. Ibrahim, S.M. Abdelazim, N.A. Aboul-Gheit, and D.R. Abdel-Hafizar, *The optimum conditions for methanol conversion to dimethyl ether over modified sulfated zirconia catalysts prepared by different methods.* Journal of Fuel Chemistry and Technology, 2021. **49**(1): p. 63-71.
20. Shearer, A., M. Montazerian, B. Deng, J.J. Sly, and J.C. Mauro, *Zirconia-containing glass-ceramics: From nucleating agent to primary crystalline phase.* International Journal of Ceramic Engineering & Science, 2024. **6**(2): p. e10200.

21. Zhang, M., Y. Hu, H. Wang, H. Li, X. Han, Y. Zeng, and C.C. Xu, *A review of bio-oil upgrading by catalytic hydrotreatment: Advances, challenges, and prospects.* Molecular Catalysis, 2021. **504**: p. 111438.
22. Kaur, H., S. Chaudhary, H. Kaur, M. Chaudhary, and K.C. Jena, *Hydrolysis and condensation of tetraethyl orthosilicate at the air–aqueous interface: implications for silica nanoparticle formation.* ACS applied nano materials, 2021. **5**(1): p. 411-422.
23. Sadr, S., A.E. Langroudi, A. Nejaei, A. Rabiee, and N. Mansouri, *Arsenic and lead removal from water by nano-photocatalytic systems (a review).* Anthropogenic Pollution, 2021. **5**(1): p. 72-80.
24. Cao, J., D. Zhang, Y. Yue, R. Chanajaree, S. Wang, J. Han, X. Zhang, J. Qin, and Y. Huang, *Regulating solvation structure to stabilize zinc anode by fastening the free water molecules with an inorganic colloidal electrolyte.* Nano Energy, 2022. **93**: p. 106839.
25. Maderuelo-Solera, R., S. Richter, C.P. Jiménez-Gómez, C. García-Sancho, F.J. García-Mateos, J.M. Rosas, R. Moreno-Tost, J.A. Cecilia, and P. Maireles-Torres, *Porous $SiO_2$ nanospheres modified with $ZrO_2$ and their use in one-pot catalytic processes to obtain value-added chemicals from furfural.* Industrial & Engineering Chemistry Research, 2021. **60**(51): p. 18791-18805.
26. Bhaskar, S., E.W. Awin, K.H. Kumar, A. Lale, S. Bernard, and R. Kumar, *Design of nanoscaled heterojunctions in precursor-derived t-$ZrO_2$/SiOC (N) nanocomposites: Transgressing the boundaries of catalytic activity from UV to visible light.* Scientific reports, 2020. **10**(1): p. 430.
27. Elgrishi, N., K.J. Rountree, B.D. McCarthy, E.S. Rountree, T.T. Eisenhart, and J.L. Dempsey, *A practical beginner's guide to cyclic voltammetry.* Journal of chemical education, 2018. **95**(2): p. 197-206.
28. Fakayode, O.J., R.L. Mohlala, R. Ratshiedana, B.M. May, E.E. Ebenso, U. Feleni, and T.T. Nkambule, *Electrocatalytic oxidation of pyrrole on a quasi-reversible silver nanodumbbell particle surface for supramolecular porphyrin production.* ChemistryOpen, 2024. **13**(7): p. e202300212.
29. Li, M., S.A. Odom, A.R. Pancoast, L.A. Robertson, T.P. Vaid, G. Agarwal, H.A. Doan, Y. Wang, T.M. Suduwella, and S.R. Bheemireddy, *Experimental protocols for studying organic non-aqueous redox flow batteries*. 2021, ACS Publications.

30. Liu, W., W. Tan, H. He, Y. Peng, Y. Chen, and Y. Yang, *One–step electrodeposition of Ni–Ce–Pr–Ho/NF as an efficient electrocatalyst for hydrogen evolution reaction in alkaline medium.* Energy, 2022. **250**: p. 123831.
31. Ying, Z., Y. Du, X. Gu, X. Yu, X. Zheng, B. Dou, and G. Cui, *Biochar-assisted water electrolysis for energy-saving hydrogen production: Evolution of corn straw-based biochar structure and its enhanced effect on Cr (VI) removal.* Energy, 2024. **305**: p. 132277.
32. Raj, S.K., K.B. Patel, V. Sharma, D.N. Srivastava, and V. Kulshrestha, *Nanopalladium-anchored MXene Nanoflowers for boosting Electrocatalytic hydrogen evolution reaction.* Energy & Fuels, 2023. **37**(21): p. 16856-16865.
33. Feng, L.-L., D.-M. Li, Q.-Q. Liu, C.-L. Fu, H.-Y. Yin, L. Feng, Y.-H. Li, H. Chen, and X.-X. Zou, *Ultrasmall VN/Co heterostructure with optimized N active sites anchored in N-doped graphitic nanocarbons for boosting hydrogen evolution.* Advanced Sensor and Energy Materials, 2022. **1**(3): p. 100027.
34. Khdary, N.H., M.A. Ghanem, M.E. Abdelsalam, D.N. Khdary, and N.H. Alotaibi, *Copper-N-$SiO_2$ nanoparticles catalyst for hydrogen evolution reaction.* international journal of hydrogen energy, 2019. **44**(41): p. 22926-22935.
35. Guo, L., Q. Liu, Y. Liu, Z. Chen, Y. Jiang, H. Jin, T. Zhou, J. Yang, and Y. Liu, *Self-supported tremella-like MoS2-AB particles on nickel foam as bifunctional electrocatalysts for overall water splitting.* Nano Energy, 2022. **92**: p. 106707.

# CHAPTER 6: ACIDIC WATER SPLITTING OF CERIUM-SILICA MIXED OXIDES FOR SUSTAINABLE ELECTROCATALYTIC HYDROGEN PRODUCTION.

## 6.1. Introduction

Over the last few decades, energy demand has skyrocketed due to increases in population, automobiles, and energy-based devices, resulting in massive use of fossil fuels [1]. The development of alternative fuels has been strongly encouraged by environmental pollution and the "greenhouse effect" caused by conventional energy sources. As an alternative to fossil fuels, hydrogen is currently seen as a clean and renewable energy source [2]. Hydrogen generation from alkaline water electrolysis is a key component of various emerging clean-energy technologies such as thermochemical water splitting, electrolysis, and photoelectrolysis [3-5]. However, the fundamental issue with electrolytic hydrogen is its low energy conversion efficiency and high energy consumption. From an electrochemical standpoint, the energy conversion efficiency of electrolytic hydrogen can be improved by selecting a suitable cathode material with high inherent catalytic activity for the hydrogen evolution process (HER) and/or increasing the electrode's active surface area [4, 6, 7].

Platinum group metals, such as Pt and Ru, are well-known as top HER catalysts, but their scarcity and high cost now prevent their widespread use [8, 9]. To address the issue, extensive research on the HER is being conducted to develop new electrode materials that will minimize both the cathodic overpotential and the cost. It is critical to address the aforementioned energy crisis by utilizing low-cost, earth-abundant electrocatalysts. Many non-precious metals, including transition metal-based compounds and metal-free carbonaceous materials, have been employed in both HER and oxygen evolution reaction (OER) processes [10]. Furthermore, diverse TiOx, MoOx, $Fe_2O_3$, WOx, and rare earth metal oxides such as $CeO_2$, $La_2O_3$, and so on have been used in both half-reactions, greatly improving the catalytic activity towards the OER and HER processes [11].

Cerium oxide ($CeO_2$) is particularly important among rare earth metal oxides due to its favourable features such as low toxicity and good chemical stability. It has also been used in a variety of applications, including fuel cells, photocatalysts, polishing materials, and sensors [12]. Cerium's unique redox properties and high oxygen storage/release capacity via the $Ce^{4+/}Ce^{3+}$ pair play an important role in these applications [13, 14]. Pure $CeO_2$ has poor thermal stability [15]. Thus, at high temperatures, ceria's high oxygen mobility and catalytic activity are dramatically reduced. One viable strategy to overcome this difficulty is to use thermally stable inert supports, which provide $CeO_2$ with the requisite thermal stability while preserving its unique properties [[16, 18]. In this regard, silica ($SiO_2$) is one of the most popular supports due to its good chemical inertness, thermal stability, large specific surface area, and inexpensive cost [19]. Thus, $SiO_2$ can increase the dispersion and catalytic activity of most deposited active oxides [20, 21]. In fact, mixed oxides ceria-silica have increased surface oxygen mobility compared to ceria alone; the greater surface area of $SiO_2$ materials also allows for better active species dispersion on ceria support, resulting in higher catalytic performance [22, 23].

This study introduces cerium-silica ($CeO_2$:$SiO_2$) composites as an efficient electrocatalyst for HER. The electrocatalysts were synthesized by hydrothermal method. Cerium remarkably improved the electrochemical characteristics of pure silica so that $CeO_2$:$SiO_2$ composites can notably enhance the HER performance in terms of activity, stability, and durability. Thus, this study provides a comprehensive insight into the development of efficient electrocatalysts for HER and could inspire future works to introduce novel materials for HER electrocatalysis.

## 6.2. Materials and methods

### 6.2.1. Chemicals

Cerium (III) nitrate hexahydrate, Tetraethyl orthosilicate (TEOS), Ethanol, Sodium hydroxide (NaOH), Potassium hydroxide (KOH), Potassium chloride (KCl), Potassium ferricyanide, ammonia hydroxide (30-33%), ethanol (all Merck). All the chemicals were used without further purification.

### 6.2.2. Silica nanoparticle synthesis

Silica oxide ($SiO_2$) material was synthesized by the Stöber method using tetraethyl orthosilicate (TEOS) as a silica source [24]. In a typical procedure, a certain amount of ethanol, deionized (DI) water, and ammonia was stirred together. The TEOS was added dropwise into the mixture to form a turbid suspension. The resultant mixture was stirred for 6 hours, then placed in a sonicating bath for 10 minutes at room temperature. The colloidal suspension was centrifuged and washed several times with ethanol until the pH drops to 7 (sonicating for 5 minutes between washes to avoid agglomeration). The material was then dried overnight at 70 °C, and subsequently calcined at 600 °C for 2 hours.

### 6.2.3. $CeO_2$:$SiO_2$ composite synthesis

$CeO_2$:$SiO_2$ composite catalysts were synthesized by hydrothermal method. Varying amounts of $SiO_2$ were dispersed in Cerium (III) nitrate hexahydrate ($Ce(NO_3)_3.6H_2O$) solution in order to make ratios of (1:1,1:2 and 2:1), was stirred at 60 °C for 2 hours. Then a known amount of NaOH solution was carefully added to the mixture and stirred for 3 hours. The resultant mixture was then transferred into an autoclave and kept in a vacuum oven at 150 °C for 16 hours. Finally, the obtained $CeO_2$:$SiO_2$ material was continuously washed by deionized water followed by ethanol then dried overnight at 80 °.

### 6.2.4 Modification and fabrication of electrode

Recycled AA battery graphite electrode (GE) surface of thickness 3 mm was polished with alumina slurry of particle size 0.05 µm by nylon polishing cloth, later washing with double distilled water 3-4 times. Afterward polished PGE surface was sonicated approximately for 5 minutes in ethanol and washed 3-4 times with water finally to clean impurities preceding to fabrication [25]. A given amount of the catalyst (4 mg each) ($SiO_2$ and $CeO_2$:$SiO_2$ powders) was added to 1 drop of a SPEEK/DMSO viscous solution, followed by stirring with the head of a graphite rod electrode (GE) to make a paste. The latter was then cast onto the surface of the GE successively with the aid of a spatula, followed drying in the air for 30 seconds and dipping in deionized water for 1 minute.

### 6.2.5. Characterization techniques

Fourier Transform Infrared Spectroscopy (FTIR) spectra was recorded from 4000 cm to 400 cm-1 range by Bruker Vertex 70 for functional group analysis. UV-visible spectra were adopted from 200 nm to 800 nm range for optical study by using Shimadzu UV-3600i plus spectrophotometer. X-ray Diffraction (XRD) spectral analysis was performed on Rigaku SmartLab with Cu-Kα radiation source operated at 30 kV and a current of 200 mA with a scanning rate of 0.026 °/sec from 5° to 90°. The surface morphology of synthesized materials was studied by Scanning Electron Microscopy (SEM) with Joel JMS-7800F coupled with Energy Dispersive Spectroscopy (EDS) elemental mapping Oxford Aztec 350 X-Max80. Thermal properties were investigated using Perkin Elmer thermogravimetric analyser (TGA) in air and nitrogen flow at a heating rate of 10 °C/min from 35 °C to 900 °C. The specific surface area and porosity of silica sample were determined using Brunauer, Emmett, Teller (BET) adsorption technique on micromeritics Tristar II plus analyzer at 77 K (-196 °C) on dried silica samples that have been degassed at 90 °C for an hour and then further at 250 °C for 4 h under vacuum. Cyclic voltammetry (CV) and Electrochemical impedance spectroscopy (EIS) studies were performed within a potential window of -0.3 and +0.70 V and at $1\times10^5$ Hz to 0.1 Hz frequency with the applied potential of 0.24 V *using* a three-electrode cell (TEC) connected to a Metrohm Autolab Potentiostat (PGSTAT30) equipped with Nova software version 2.1. The TEC consists of platinum wire, Ag/AgCl (3M KCl) and as-synthesized materials on graphite electrode as counter, reference and working electrode, respectively.

## 6.3. Results and discussion

### 6.3.1. FTIR analysis

FTIR study of $SiO_2$ and $CeO_2$: $SiO_2$ materials in the 4000 $cm^{-1}$ to 400 $cm^{-1}$ range are represented by Fig. 6.1. The peaks at 665 $cm^{-1}$ signify characteristic $CeO_2$ vibrations [26]. The peaks at 1060, 795, and 442 $cm^{-1}$ are attributed to stretching and bending vibrations of Si–O–Si bonds [27-29], indicating the condensation of silanols to Si–O–Si bonds and the formation of the silica network. The peak at 946 $cm^{-1}$ represents the Si-O-Ce vibrational band [30]. The presence of $CeO_2$ is further confirmed by the peaks at around 410 $cm^{-1}$ which are attributed to Ce–O bonds [31]. The displacement and increased intensity of characteristic bands specify the chemical change due to $CeO_2$ and $SiO_2$ NPs coupling in $CeO_2$:$SiO_2$ composites formation [32]. Further, the absorption peak at 2343 $cm^{-1}$ and 3122 $cm^{-1}$ indicates O-H bending vibrations in $SiO_2$ and $CeO_2$: $SiO_2$ nanoparticles, due to the reabsorption of water molecules on the material surface [25].

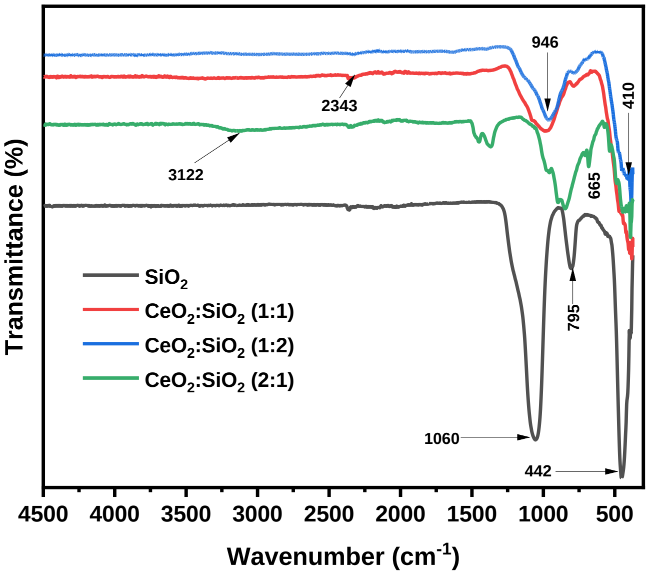

**Fig. 6.1:** FTIR spectra of $SiO_2$ and $CeO_2$:$SiO_2$ mixed oxides.

### 6.3.2. TGA analysis

Fig. 6.2 depicts the thermogravimetric analysis (TGA) curves of pure $SiO_2$ and $CeO_2$: $SiO_2$ composite powders. The $SiO_2$ curve shows one stage of weight loss at roughly 97 °C due to the removal of water. It is consistent with silica hydrophilic properties, which are caused by the Si-OH groups that are still present on its surface. The sol-gel-prepared $SiO_2$ has around 10% water content [33]. Then, no weight loss occurred and 99.4% of the total weight remains. It shows the high thermal stability of the pure $SiO_2$ up to 900 °C. As can be further noted from this figure, the $CeO_2$: $SiO_2$ samples exhibit one major and three minor weight loss peaks. The major low-temperature peak in the range of 35–100 °C is primarily due to the loss of no dissociative adsorbed water as well as water held on the surface by hydrogen bonding. The second weight loss peak in the range of 156–230 °C could result from combustion/oxidation of the remaining organic matter. A further loss of water occurs around 277–450 °C due to dehydroxylation of the surface [34]. Additionally, during the synthesis, polyhydrous cerium oxide Ce(OH)x (4−x) $yH_2O$ may have been produced. The breakdown of hydrous cerium oxide typically occurs at temperatures ranging from 250 to 300 °C. As a result, the small weight loss in the TG profile is most likely caused by both surface dehydroxylation and hydrous cerium oxide breakdown. The weight loss peak between 600-721 °C could be due to water loss from the composite's micropores.

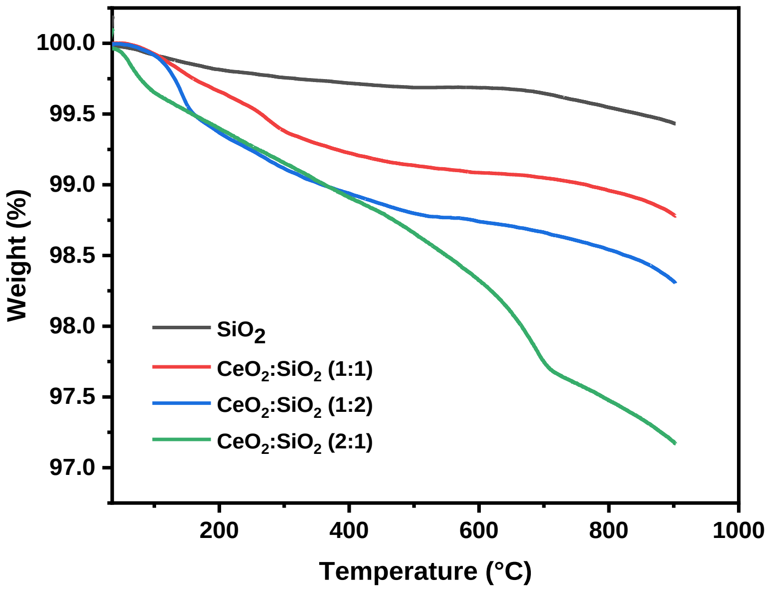

**Fig. 6. 2:** TGA analysis of $SiO_2$ and $CeO_2$:$SiO_2$ mixed oxides

### 6.3.3. UV-vis analysis

Fig.6.3(a-d) illustrates UV-vis absorption spectra of $SiO_2$ nanoparticles and $CeO_2$: $SiO_2$ composites at varying ratios, respectively. The absorbance peak of $SiO_2$ nanoparticles lies between 200-400 nm in the UV region [37]. While for $CeO_2$: $SiO_2$ (1:1), $CeO_2$: $SiO_2$ (1:2), and $CeO_2$: $SiO_2$ composites the absorbance peaks are in the visible light region at 700, 592, and 543 nm, respectively with higher absorbance in comparison to $SiO_2$ NPs. $CeO_2$: $SiO_2$ composites' red shift in the absorption band indicated the formation of charge transfer complexes (CTCs) [25]. Optical energy band gap by using Davis and Mott equation of direct transition $((\alpha h\nu)^2=B(h\nu - Eg))$, here $\alpha$ denotes the coefficient of absorption, $Eg$ denotes band gap and $B$ is a constant value is represented by Tauc's plot in Fig.3 (e-h) [35]. The band energy values for $SiO_2$ NPs, $CeO_2$: $SiO_2$ (1:1), $CeO_2$: $SiO_2$ (1:2), and $CeO_2$: $SiO_2$ composites are found to be 3.36 eV, 3.25 eV and 3.61 eV and 2.03 eV, respectively. The decrease in band gap value for composites could be due to the reflection propensity of $SiO_2$ compositing with $CeO_2$ by producing localized energy states and overlapping with the band system, indicating the development of charge transfer complexes [36].

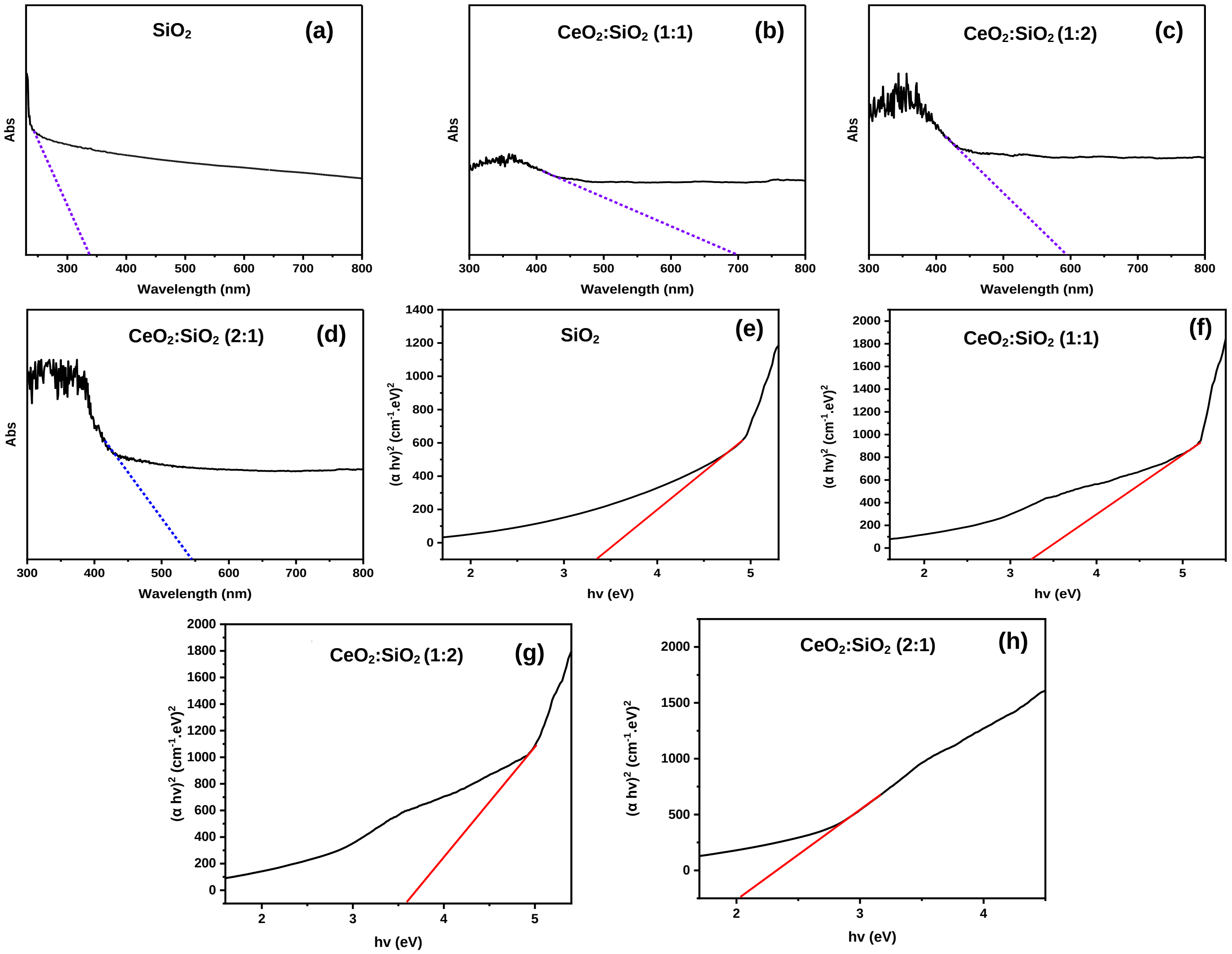

***Fig. 6. 3**:* (a-d) UV-vis absorbance spectra's and (e-h) Tauc plots of $SiO_2$ and Ce:$SiO_2$ composites.

### 6.3.4. XRD analysis

Fig. 6.4 shows the XRD patterns of $SiO_2$, and Ce:$SiO_2$ composite particles. The XRD pattern of SiO2 reveals a large peak around 24.5˚, indicating the amorphous nature or minimal crystallite size of particles [37]. In the XRD plot of Ce:$SiO_2$ composite, the peaks at $2\theta$ values of 28.71˚, 33.05˚, 47.34˚, 56.65˚, 58.99˚and 69.22˚ represent (111), (200), (220), (311), (222) and (400) plane. This result indicates that the $CeO_2$ in Ce: $SiO_2$ composite particles is in a cubic fluorite structure. The peak at 77.26˚ is the (220) phase of $SiO_2$ [38].

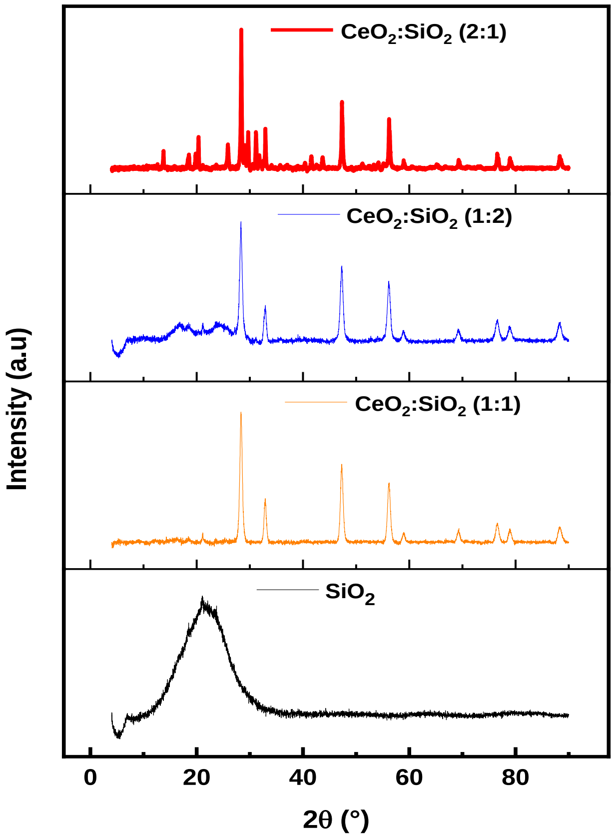

**Fig. 6.4:** XRD spectra of $SiO_2$ and Ce:$SiO_2$ composites at varying $CeO_2$ and $SiO_2$ loading.

### 6.3.5. SEM analysis

SEM micrographs of $SiO_2$ and $CeO_2$:$SiO_2$ composites and their elemental mapping and EDS spectra are shown in Fig. 6.5 (a-d) and Fig. 6.5 (S1 &S2), respectively. $SiO_2$ exposed regular spherical-shaped morphology (Fig. 5a). SEM image of $CeO_2$:$SiO_2$ (1:1) displays agglomerated regular spherical structures with silica covered by certain symmetrical-shaped $CeO_2$ nanoparticles during nanosphere formation (Fig. 6.5b).$CeO_2$:$SiO_2$ (1:2) image shows that the agglomerated spheres of $CeO_2$ have formed irregular platelets with $SiO_2$ particles nested on the surface of the platelets (Fig. 6.5c). The $CeO_2$:$SiO_2$ (2:1) sample features the morphology of an agglomerated cube-like structure where sharp corners and a smooth surface are seen (Fig. 5d). Fig. 5(S1 and S2) represents the mapping and EDS spectrum of $SiO_2$ and $CeO_2$:$SiO_2$ composites. The mapping images and EDS peaks confirm the presence of Si, Ce, and O elements in the material.

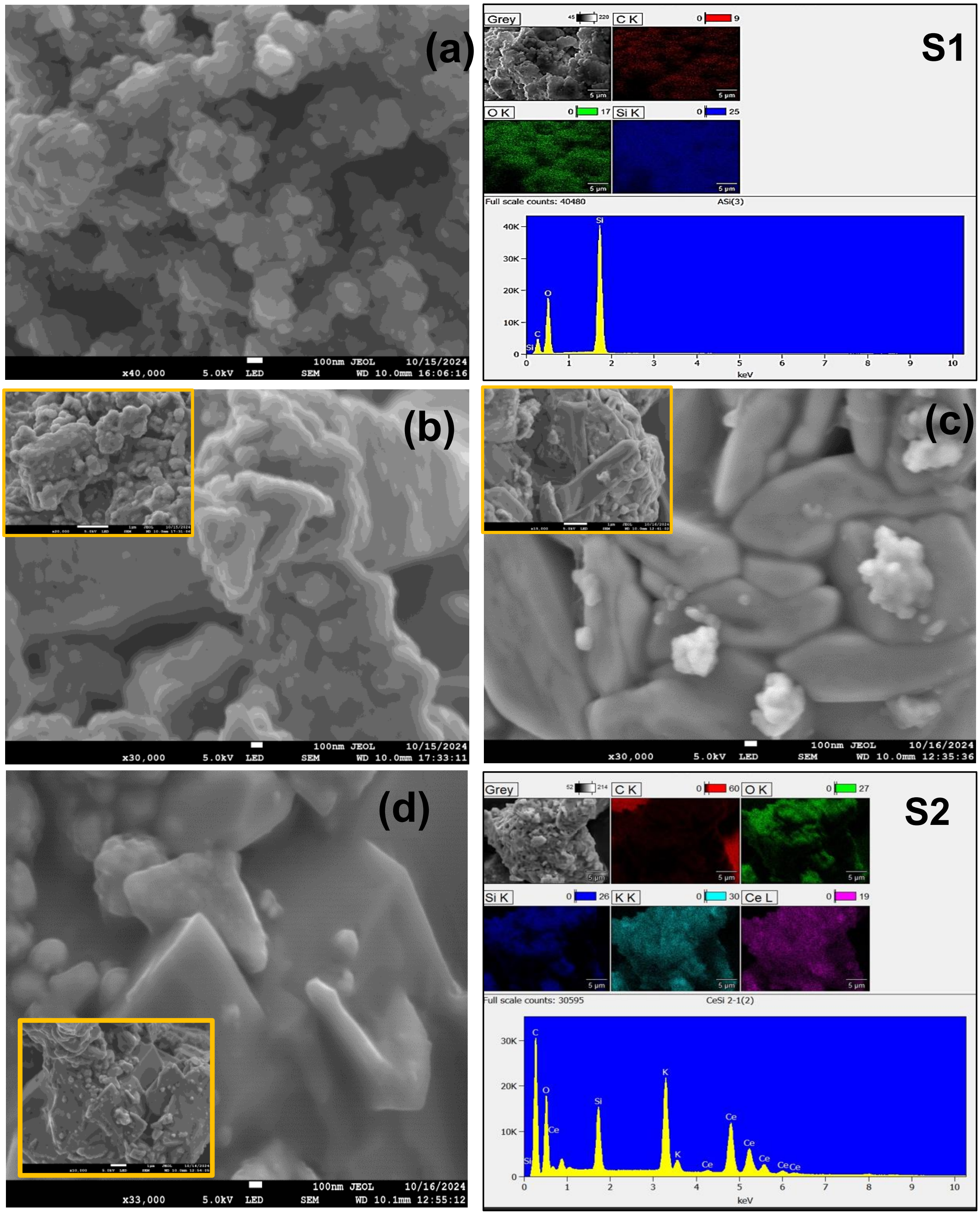

**Fig. 6.5:** SEM images of (a) $SiO_2$, (b-d) $CeO_2$:$SiO_2$ composites at varying $CeO_2$:$SiO_2$ ratios, (S1-S2) mapping overlays and EDS spectra of $SiO_2$ and $CeO_2$:$SiO_2$.

### 6.3.6. Nitrogen adsorption-desorption studies

$N_2$ adsorption/desorption isotherm curve of synthesised $SiO_2$ and $CeO_2$:$SiO_2$ mixed oxides are shown in Fig 6.7. It is observed that all samples were classified as type IV isotherm with H3 hysteresis loop characteristic of mesoporous material. The textural properties of the prepared $SiO_2$ and $CeO_2$:$SiO_2$ metal oxides are summarised in Table 6.1. The specific surface area of the $CeO_2$:$SiO_2$ (1:2) sample is greater than that of $CeO_2$:$SiO_2$ (1:1) and $CeO_2$:$SiO_2$ (2:1), as silica is a recognized surface area stabilizer. The efficiency of foreign cations ($Si^{4+}$) enhances the specific surface area and could be connected to differences in the rate of crystal formation. This variation is determined by the kind and concentration of foreign cations in the system [39]. Furthermore, the BET surface area is clearly inversely proportional to the pore diameter, suggesting that the surface area of samples of $SiO_2$ and $CeO_2$:$SiO_2$ metal oxides increases as the pore size decreases.

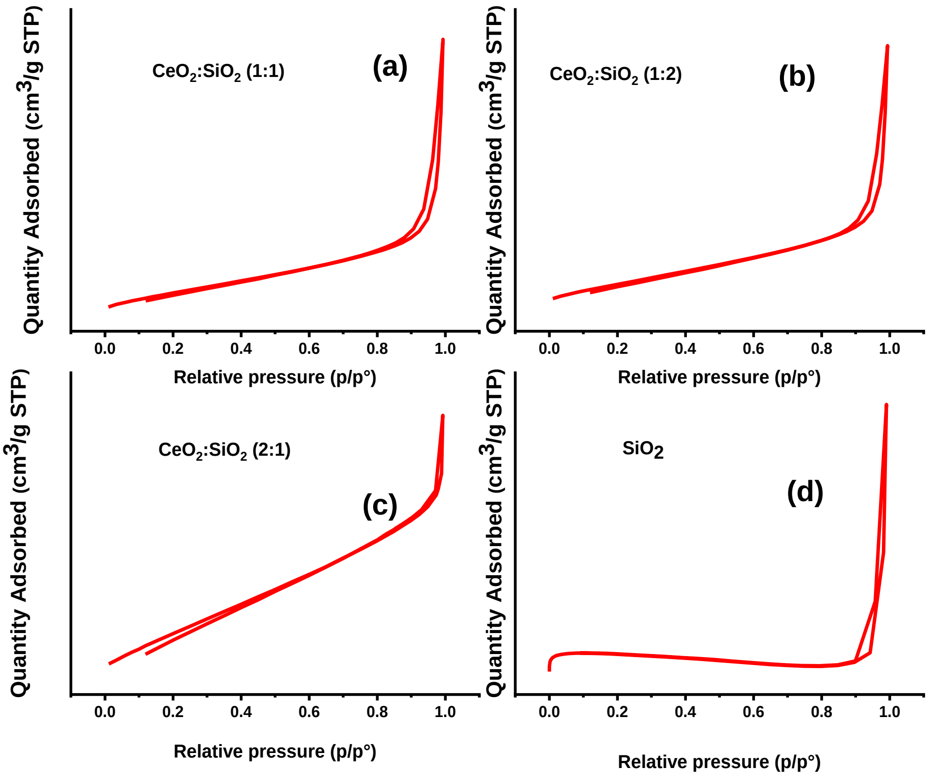

**Fig. 6.6:** $N_2$ adsorption-desorption isotherms of (a-c) $CeO_2$:$SiO_2$ mixed oxides, and (d) $SiO_2$.

**Table 6.1:** Summary of textural properties of the prepared $SiO_2$ and $CeO_2$:$SiO_2$ metal oxides

| *Sample* | *Surface Area ($m^2$/g)* | *Pore Volume ($cm^3$/g)* | *Pore diameter (nm)* |
|---|---|---|---|
| *$SiO_2$* | 161.12 | 0.009 | 2.7 |
| *$CeO_2$:$SiO_2$ (1:1)* | 139.91 | 0.003 | 4.27 |
| *$CeO_2$:$SiO_2$ (1:2)* | 193.17 | 0.004 | 4.17 |
| *$CeO_2$:$SiO_2$ (2:1)* | 96.12 | 0.0019 | 4.06 |

## 6.4. ECSA and Tafel polarization.

The results of the ECSA and Tafel polarization of the as-synthesized materials are shown in Fig. 6. 7a-d and Table 6.2. The ECSA was estimated using the equation 4.2. As shown in Fig. 6.7 and Table 6.2, the capacitance and thus the ECSA values of the tested materials increases from that of the bare electrode from 30 to 40, 80 and 100 µF and 0.75 to 1.0, 2.0 and 2.5 $cm^2$ for graphite electrode GE/$CeO_2$:$SiO_2$ (1:1), GE/$CeO_2$:$SiO_2$ (2:1) and GE/$CeO_2$:$SiO_2$ (1:2) respectively.

In terms of the corrosion potential, the bare (GE) as well as GE/$CeO_2$:$SiO_2$ (1:1) exhibited least tendency to corrode compare to GE/$CeO_2$:$SiO_2$ (1:2) or GE/$CeO_2$:$SiO_2$ (2:1), the order being GE/$CeO_2$:$SiO_2$ (1:1) < GE < GE/$CeO_2$:$SiO_2$ (1:2) = GE/$CeO_2$:$SiO_2$ (2:1), indicating the superiority of the $CeO_2$:$SiO_2$ (1:1) over $CeO_2$:$SiO_2$ (1:2) and $CeO_2$:$SiO_2$ (2:1) electrocatalysts counterparts in terms of tendency to be prone to corrosion. Moreover, further insights of these results were seen through analyzing the Tafel slopes of the tested electrocatalysts. The lower the Tafel slope the slower is the corrosion rate of the material. As shown in Fig. 6. 7d and Table 6.2, the GE/$CeO_2$:$SiO_2$ (1:2) showed the lowest Tafel slope potential, making it the slowest among the tested materials in terms of corrosion rate. The order of increasing Tafel slopes is 402,61 < 696,23 < 742,61 < 858,74 for GE/$CeO_2$:$SiO_2$ (1:2), GE/$CeO_2$:$SiO_2$ (1:1), GE and GE/$CeO_2$:$SiO_2$ (2:1) respectively.

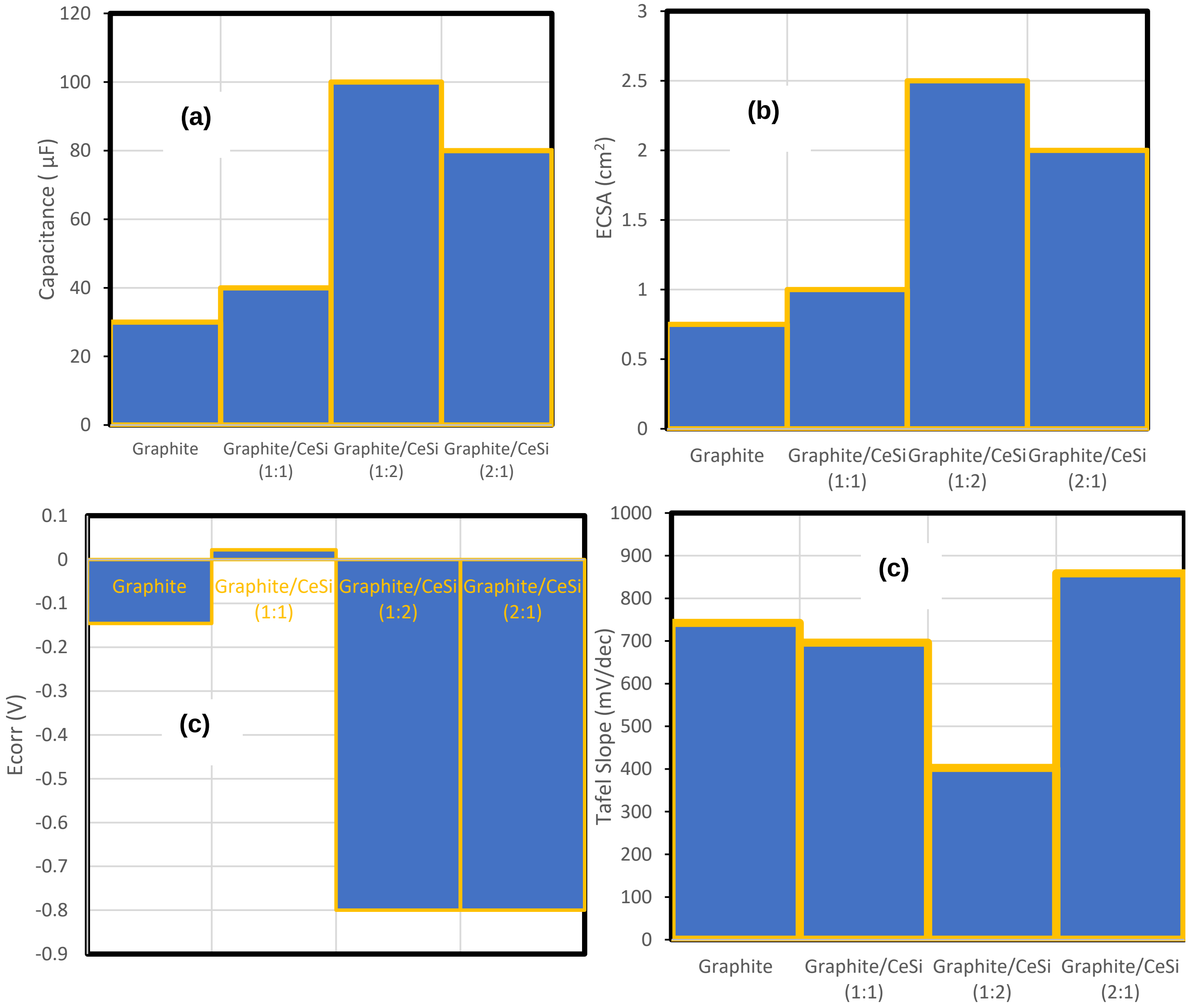

**Fig. 6.7:** Polarization properties of the as-synthesized materials. (a) Capacitance values; (b) ECSA; (c) Corrosion potentials; (d) Tafel slopes.

**Table 6. 2:** ECSA and Tafel polarization

| Catalyst | CdL **(µF)**[a] | ECSA ($cm^2$) | $E_{corr}$ (V) | Slope log A vs n | Tafel Slope (mV/dec) |
|---|---|---|---|---|---|
| GE | 30 | 0,75 | -0,15 | 1,3466 | 742,61 |
| GE/$CeO_2$:$SiO_2$ (1:1) | 40 | 1.0 | 0,02 | 1,4363 | 696,23 |
| GE/$CeO_2$:$SiO_2$ (1:2) | 100 | 2,5 | -0,80 | 2,4838 | 402,61 |
| GE/$CeO_2$:$SiO_2$ (2:1) | 80 | 2.0 | -0,80 | 1,1645 | 858,74 |

[a]Capacitance.

## 6.5. Hydrogen evolution reaction measurements

HER performance (LSV) and chronoamperometry of the supporting bare electrode (graphite or GE) and GE/$CeO_2$:$SiO_2$ mixed oxides catalysts are shown in Fig 6.8(a-c). A three-electrode system was used to measure the HER performance of catalysts in an acidic medium of 0.5 M $H_2SO_4$ electrolyte. The $CeO_2$:$SiO_2$ mixed oxides were tested by loading the catalysts on a graphite electrode (GE) using SPEEK as a binder. As shown in Fig. 6.8a, adding $CeO_2$:$SiO_2$ metal oxide catalyst (2:1) improved the GE catalytic activity by 20 current density units while reduction by 10 and 20 current density units were observed for GE/$CeO_2$:$SiO_2$ (1:1) and GE/$CeO_2$:$SiO_2$ (1:2) respectively. Thus, GE/$CeO_2$:$SiO_2$ (2:1) showed the highest HER catalytic activity followed by GE/$CeO_2$:$SiO_2$ (1:1) then GE/$CeO_2$:$SiO_2$ (1:2) based on geometrical current density at -0.4 V vs RHE. However, extending the applied potential to -2.1 V increased the current density while the graphite took the lead, followed by GE/$CeO_2$:$SiO_2$ (1:2), GE/$CeO_2$:$SiO_2$ (2:1) and then GE/$CeO_2$:$SiO_2$ (1:1) (Fig. 6.8b). The change in the production pattern of the electrocatalysts at higher applied potential may be as a result of the robustness of the inherent material composition to withstand the high energy input caused by the high overpotential.

Another important consideration for any long-term practical application of electrocatalysts is stability. Fig.6.8c shows the HER stability (chronoamperometry) testing of the electrocatalysts in an acidic medium of 0.5 M $H_2SO_4$ at − 2.1 V applied potential.

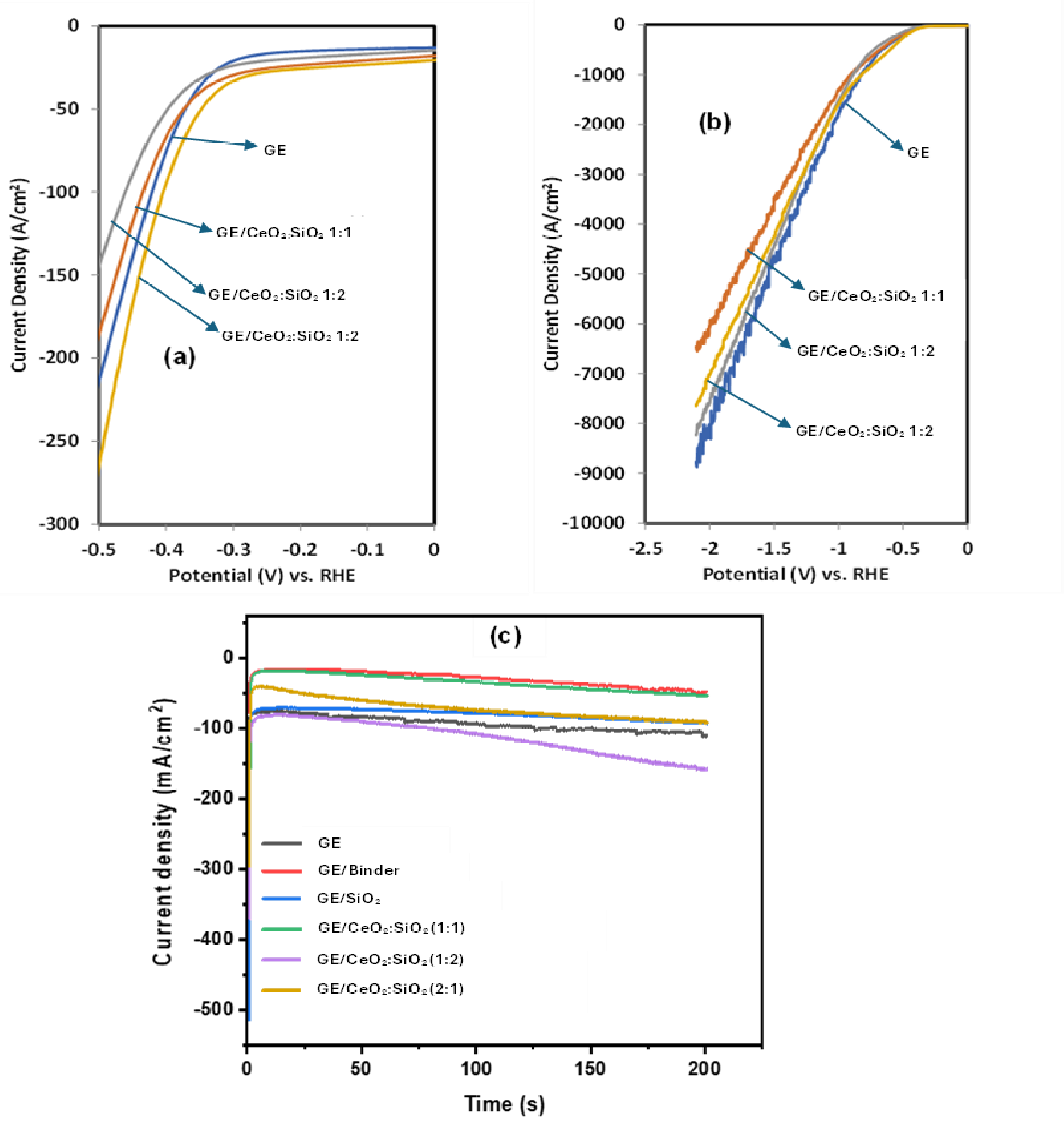

**Fig. 6.8:**HER activity and stability of electrocatalysts. (a) LSV (electrode geometry = 0.50 cm diameter), potential window of 0-(-0.50 V) vs. RHE; (b) LSV (electrode

geometry = 0.50 cm diameter), potential window of 0-(-2.1 V) vs. RHE ; (c) Chronoamperometry stability test of the electrocatalysts at -2.1 V (electrode geometry = 0.30 cm diameter).

As revealed in Fig. 6.8c, GE/$CeO_2$: $SiO_2$ (2:1) mixed oxides showed excellent HER current stability than its counterparts (GE/$CeO_2$:$SiO_2$ (1:2) and GE/$CeO_2$: $SiO_2$ (1:1)) after 100 s.

Turnover frequency (TOF) is the number of substrate molecules that are converted to the product per active site of the catalyst per unit time. It helps in defining how effective a catalyst is by showing the efficiency of its active sites in driving a reaction to product formation. The values of the estimated TOF of the tested electrocatalysts based on ECSA are shown in Table 6.3. As shown in Table 6.3, the order of increasing TOF for all tested electrocatalysts is GE < GE/$CeO_2$:$SiO_2$ (1:1) < GE/$CeO_2$:$SiO_2$ (1:2) < GE/$CeO_2$:$SiO_2$ (2:1), making the GE/$CeO_2$:$SiO_2$ (2:1) the best material for the hydrogen generation in terms of TOF at -0.50 V vs. RHE, supporting the previously discussed stability results (Fig. 6.8c). The TOF data is obtained from LSV results shown in Fig. 6.9a in conjunction with the ECSA data in Table 6.3 and Eq. (4.3).

**Table 6.3:**Turnover frequency data of the as-synthesized materials

| Catalyst | ECSA ($cm^{-2}$) | $J_{ECSA}$ at -0.5 V ($A/cm^{-2}$) | $TOF_{ECSA} = J_{ECSA}/2n_{cat}F$ ($cm^{-2}s^{-1}$) | TOF ($s^{-1}$) |
|---|---|---|---|---|
| GE | 0,75 | -5,65 | -0,0351 | -0,0264 |
| GE/$CeO_2$:$SiO_2$ 1:1 | 1 | -5,90 | -0,7466 | -0,7466 |
| GE/$CeO_2$:$SiO_2$ 1:2 | 2,5 | -1,90 | -0,2996 | -0,7490 |

| | | | | |
|---|---|---|---|---|
| GE/$CeO_2$:$SiO_2$ 2:1 | 2 | -3,30 | -0,7119 | -1,4239 |

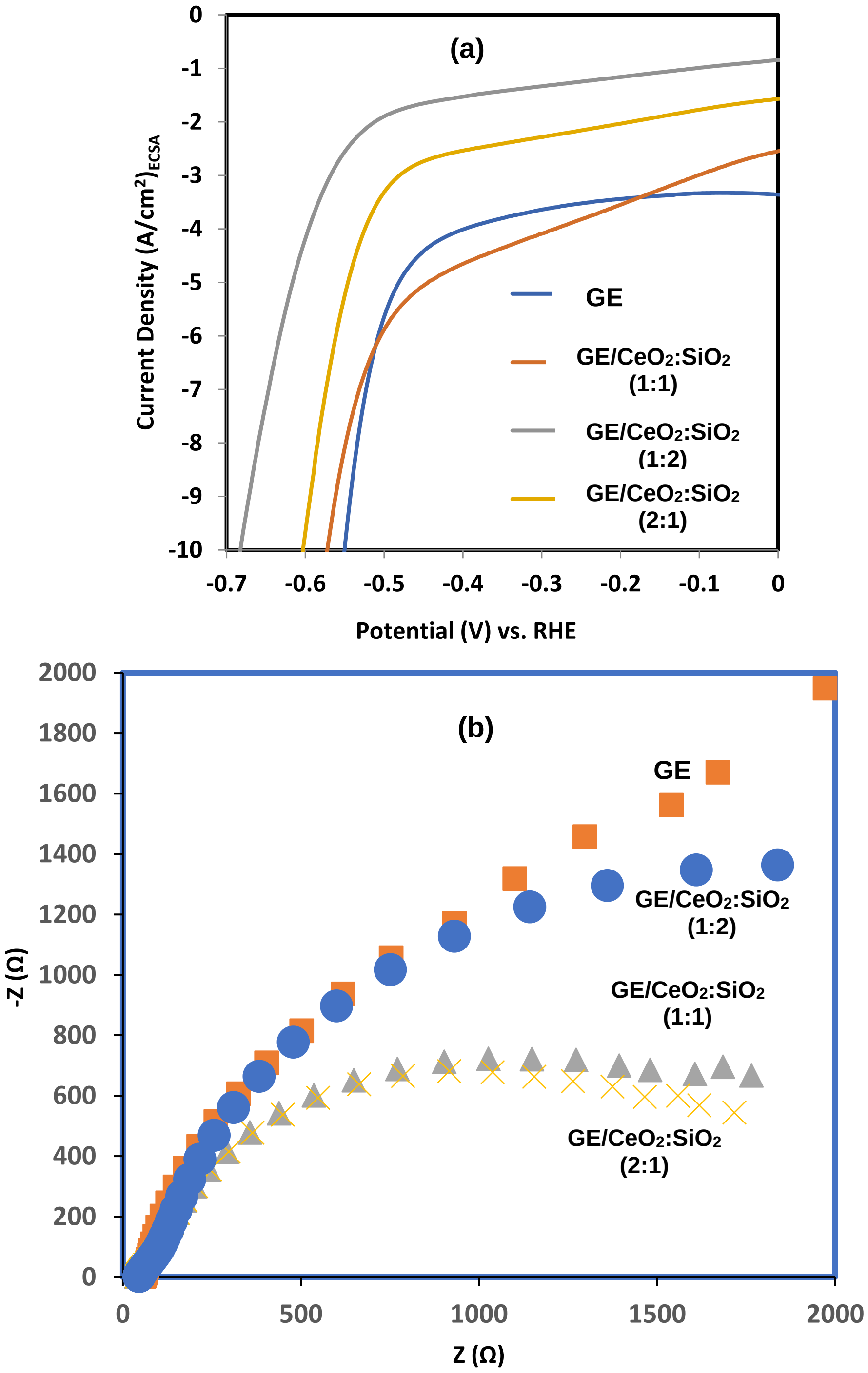

**Fig. 6.9:** Polarization curve and Nyquist plots of the tested HER electroctalysts (a) LSV plots; (b) Nyquist plots.

The results of the Nyquist plots of the tested electrocatalysts are shown in Fig. 6.9b. As shown in Fig. 6.9b, GE/$CeO_2$:$SiO_2$ 2:1 exhibited the smallest semi-circle, making it the best material for electron exchange among the tested electrocatalysts. This further supports why this material has the best TOF values compared to its counterparts.

Table 6.4 shows the comparison between the hydrogen production current density data value of the present work and some work previously reported in the literature. As shown in Table 6.4, the present material exhibits better HER activity than the reported works.

**Table 6.4:** Comparative HER activity data with some reported literature works.

| Material | Current density (A /$cm^2$) | Reference |
|---|---|---|
| HC-$MoS_2$/$Mo_2C$ | -1 | [40] |
| $Mo_2C$/MoC/CNT | -1.5 | [41] |
| h-NiMoFe | -1 | [42] |
| NC@NiNPs | -0.01 | [43] |
| Ni/NiO@$MoO_{3-x}$ | -0.2 | [44] |
| Ni/$Ni_xS_y$-PNF | -0.5 | [45] |
| $CeO_2$:$SiO_2$ (2:1) | -3,3 | This work |

## 6.6. Conclusion

Ce:$SiO_2$ electrocatalysts of varying ratio (1:1, 1:2 and 2:1) were successfully synthesized by hydrothermal method. Compared with other tested materials, $CeO_2$:$SiO_2$ (2:1) catalyst exhibited excellent electrocatalytic activity toward HER with a TOF value of -1,4239 $s^{-1}$ in an acidic medium. This high performance was attributed to the easy exchange of electron between the electrocatalyst's surface and aqueous hydrogen ions and availability of numerous active sites on the material's surface. The electrocatalyst also showed excellent stability compared to other tested materials. The excellent performance of the $CeO_2$:$SiO_2$ (2:1) catalyst in acidic media makes it a potential candidate for HER applications in the near future.

## 6.7. Reference

1. Zahoor, A., F. Mehr, G. Mao, Y. Yu, and A. Sápi, *The carbon neutrality feasibility of worldwide and in China's transportation sector by E-car and renewable energy sources before 2060.* Journal of Energy Storage, 2023. **61**: p. 106696.
2. Sharma, M., V. Tyagi, R. Kouser, K. Kumari, K. Chopra, and R. Kothari, *Green Hydrogen and Climatic Change: Current Status and Future Outlook*, in *Green Hydrogen Economy for Environmental Sustainability. Volume 2: Applications, Challenges, and Policies*. 2024, ACS Publications. p. 31-54.
3. Qureshi, F., M. Yusuf, M.A. Khan, H. Ibrahim, B.C. Ekeoma, H. Kamyab, M.M. Rahman, A.K. Nadda, and S. Chelliapan, *A State-of-The-Art Review on the Latest trends in Hydrogen production, storage, and transportation techniques.* Fuel, 2023. **340**: p. 127574.
4. Benghanem, M., A. Mellit, H. Almohamadi, S. Haddad, N. Chettibi, A.M. Alanazi, D. Dasalla, and A. Alzahrani, *Hydrogen production methods based on solar and wind energy: a review.* Energies, 2023. **16**(2): p. 757.
5. Bhandari, R. and N. Adhikari, *A comprehensive review on the role of hydrogen in renewable energy systems.* International Journal of Hydrogen Energy, 2024. **82**: p. 923-951.
6. Arsad, A., M. Hannan, A.Q. Al-Shetwi, R. Begum, M. Hossain, P.J. Ker, and T.I. Mahlia, *Hydrogen electrolyser technologies and their modelling for sustainable energy production: A comprehensive review and suggestions.* International Journal of Hydrogen Energy, 2023. **48**(72): p. 27841-27871.
7. Rampai, M., C. Mtshali, N. Seroka, and L. Khotseng, *Hydrogen production, storage, and transportation: recent advances.* RSC advances, 2024. **14**(10): p. 6699-6718.
8. Li, Y., L. Zhou, and S. Guo, *Noble metal-free electrocatalytic materials for water splitting in alkaline electrolyte.* EnergyChem, 2021. **3**(2): p. 100053.
9. Du, N., C. Roy, R. Peach, M. Turnbull, S. Thiele, and C. Bock, *Anion-exchange membrane water electrolyzers.* Chemical reviews, 2022. **122**(13): p. 11830-11895.

10. Aralekallu, S., K.S. Lokesh, and V. Singh, *Advanced bifunctional catalysts for energy production by electrolysis of earth-abundant water.* Fuel, 2024. **357**: p. 129753.
11. Ikram, M., A. Raza, J.Z. Hassan, A.A. Rafi, A. Rafiq, S. Altaf, and A. Ashfaq, *Rational Design and Advance Applications of Transition Metal Oxides'.* Transition Metal Compounds: Synthesis, Properties, and Application, 2021. **3**.
12. Ishfaq, M., T. Kousar, H. Somaily, S. Mubeen, E. Potrich, N.M. Panduro-Tenazoa, M.A. Salam, S.R. Ejaz, and M. Aadil, *Synergistic effect of binary metal doping and nanotechnology to boost the light-harvesting properties of rare earth metal oxide.* Ceramics International, 2023. **49**(1): p. 745-754.
13. Putla, S.B., M. Kamali, B. Swapna, B.M. Reddy, and P. Sudarsanam, *Review of Shape-Controlled CeO2 Nanocatalysts for Purification of Auto-Exhaust Pollutants.* ACS Applied Nano Materials, 2024. **7**(7): p. 6749-6771.
14. Venâncio, S.A. and P.E.V. de Miranda, *Ni-Free SOFC Anode Material with Thermal and Redox Stabilities for the Direct Utilization of Ethanol.* Catalysts, 2023. **13**(1): p. 134.
15. Zheng, J., Z. Wang, Z. Chen, and S. Zuo, *Mechanism of CeO2 synthesized by thermal decomposition of Ce-MOF and its performance of benzene catalytic combustion.* Journal of Rare Earths, 2021. **39**(7): p. 790-796.
16. Datye, A.K. and M. Votsmeier, *Opportunities and challenges in the development of advanced materials for emission control catalysts.* Nature Materials, 2021. **20**(8): p. 1049-1059.
17. Li, G., Y. Gou, J. Qiao, W. Sun, Z. Wang, and K. Sun, *Recent progress of tubular solid oxide fuel cell: From materials to applications.* Journal of power sources, 2020. **477**: p. 228693.
18. Das, S., A. Kundu, T. Kuila, and N.C. Murmu, *Recent advancements on designing transition metal-based carbon-supported single atom catalysts for oxygen electrocatalysis: Miles to go for sustainable Zn-air batteries.* Energy Storage Materials, 2023: p. 102890.
19. Wu, T., Q. Ke, M. Lu, P. Pan, Y. Zhou, Z. Gu, G. Cui, and H. Lu, *Recent advances in carbon-silica composites: preparation, properties, and applications.* Catalysts, 2022. **12**(5): p. 573.

20. Han, K., W. Yu, L. Xu, Z. Deng, H. Yu, and F. Wang, *Reducing carbon deposition and enhancing reaction stability by ceria for methane dry reforming over Ni@ SiO2@ CeO2 catalyst.* Fuel, 2021. **291**: p. 120182.
21. Meng, Z. and Z. Wang, *The effect of different promoters (La2O3, CeO2, and ZrO2) on the catalytic activity of the modified vermiculite-based bimetallic NiCu/EXVTM-SiO2 catalyst in methane dry reforming.* ACS omega, 2021. **6**(44): p. 29651-29658.
22. Nguyen, Q.B., N.C. Pham, T.H.C. Nguyen, T.D. Doan, T.L. Duong, N.N. Pham, V.N.M. Nguyen, and N.N. Dao, *Porous nonhierarchical CeO2-SiO2 nanocomposites for improving the ultraviolet resistance capacity of polyurethane coatings.* Materials Research Express, 2021. **8**(5): p. 056405.
23. Kaplin, I.Y., E.S. Lokteva, E.V. Golubina, and V.V. Lunin, *Template synthesis of porous ceria-based catalysts for environmental application.* Molecules, 2020. **25**(18): p. 4242.
24. Zhang, Y., J. Lu, L. Zhang, T. Fu, J. Zhang, X. Zhu, X. Gao, D. He, Y. Luo, and D.D. Dionysiou, *Investigation into the catalytic roles of oxygen vacancies during gaseous styrene degradation process via CeO2 catalysts with four different morphologies.* Applied Catalysis B: Environmental, 2022. **309**: p. 121249.
25. Tessema, B., G. Gonfa, S.M. Hailegiorgis, and S.V. Prabhu, *Characteristic investigations on bio-silica gel prepared from teff (eragrostis tef) straw: effect of calcination time.* Materials Research Express, 2023. **10**(11): p. 115102.
26. Li, B., J. Han, D. Wei, H. Ji, T. Yao, H. Wang, J. Han, and Y. Zhang, *A molecular dynamics simulation study on the recovery performance of aged asphalt binder by waste vegetable oil rejuvenators.* Journal of Cleaner Production, 2024. **442**: p. 140796.
27. Caldas, B.S., C.S. Nunes, M.R. Panice, D.B. Scariot, C.V. Nakamura, and E.C. Muniz, *Manufacturing micro/nano chitosan/chondroitin sulfate curcumin-loaded hydrogel in ionic liquid: A new biomaterial effective against cancer cells.* International journal of biological macromolecules, 2021. **180**: p. 88-96.
28. Liang, J., W. Chen, G. Liao, J. Wang, X. Wei, Y. Tang, X. Li, and L. Li, *Facile regulation of Lewis sites and 3D mesoporous channel within Ce-SBA-15 for catalytic ozonation of clofibric acid.* Journal of Environmental Chemical Engineering, 2022. **10**(6): p. 109017.

29. Wang, H., H. Zhu, Y. Zhang, and J. Pu, *Highly active Ni/CeO2 for the steam reforming of acetic acid using CTAB as surfactant template.* International Journal of Hydrogen Energy, 2022. **47**(64): p. 27493-27507.
30. Asaithambi, S., P. Sakthivel, M. Karuppaiah, R. Yuvakkumar, K. Balamurugan, T. Ahamad, M.M. Khan, G. Ramalingam, M.K. Mohammed, and G. Ravi, *Preparation of Fe-SnO2@ CeO2 nanocomposite electrode for asymmetric supercapacitor device performance analysis.* Journal of Energy Storage, 2021. **36**: p. 102402.
31. Yadav, M., M. Dhanda, R. Arora, S. Ahlawat, G. Singh, K. Nehra, and S. Lata, *Dual applicability of ceria and silica nanospheres (CeO2@ SiO2 NSs) assembled with pencil graphite electrode to sense ascorbic acid, extended with their antibacterial property.* Materials Science and Engineering: B, 2023. **297**: p. 116719.
32. Ślosarczyk, A., I. Klapiszewska, and Ł. Klapiszewski, *Influence of nanosilica and binary oxide systems on the selected physical and mechanical properties of cement composites.* Physicochemical Problems of Mineral Processing, 2022. **58**.
33. Angelopoulos, P.M., N. Manic, B. Jankovic, and M. Taxiarchou, *Thermal decomposition of volcanic glass (rhyolite): Kinetic deconvolution of dehydration and dehydroxylation process.* Thermochimica Acta, 2022. **707**: p. 179082.
34. Klein, J., L. Kampermann, B. Mockenhaupt, M. Behrens, J. Strunk, and G. Bacher, *Limitations of the Tauc plot method.* Advanced Functional Materials, 2023. **33**(47): p. 2304523.
35. Bonyad-Shekalgourabi, S.-M. and Z. Shariatinia, *Hexagonal mesoporous silica/perovskite oxides composites as unique scattering layers in photoelectrodes of high performance dye-sensitized photovoltaics.* International Journal of Hydrogen Energy, 2024. **51**: p. 1397-1412.
36. Pornea, A.M. and H. Kim, *Design and synthesis of SiO2/TiO2/PDA functionalized phase change microcapsules for efficient solar-driven energy storage.* Energy Conversion and Management, 2021. **232**: p. 113801.
37. Yadav, M., M. Dhanda, S. Ahlawat, D.G. Singh, K. Nehra, and S. Lata, *Simultaneous Investigation of Ceria and Silica Nanospheres (Ceo2@ Sio2 Nss) Assembled with Pencil Graphite Electrode for Amperometric Sensing of Ascorbic Acid and Antibacterial Performance.* Available at SSRN 4180244.

38. Reddy, B.M., A. Khan, Y. Yamada, T. Kobayashi, S. Loridant, and J.-C. Volta, *Structural characterization of* $CeO_2$*−* $MO_2$ *(M= Si4+, Ti4+, and Zr4+) mixed oxides by Raman spectroscopy, X-ray photoelectron spectroscopy, and other techniques.* The Journal of Physical Chemistry B, 2003. **107**(41): p. 11475-11484.

39. Espinoza, E.M., J.A. Clark, J. Soliman, J.B. Derr, M. Morales, and V.I. Vullev, *Practical aspects of cyclic voltammetry: how to estimate reduction potentials when irreversibility prevails.* Journal of The Electrochemical Society, 2019. **166**(5): p. H3175-H3187.

40. *Zhang, C., Luo, Y., Tan, J., Yu, Q., Yang, F., Zhang, Z., Yang, L., Cheng, H.M. and Liu, B., 2020. High-throughput production of cheap mineral-based two-dimensional electrocatalysts for high-current-density hydrogen evolution. Nature communications,* ***11****(1), p.3724*.

41. *Li, C., Wang, Z., Liu, M., Wang, E., Wang, B., Xu, L., Jiang, K., Fan, S., Sun, Y., Li, J. and Liu, K., 2022. Ultrafast self-heating synthesis of robust heterogeneous nanocarbides for high current density hydrogen evolution reaction. Nature Communications, 13(1), p.3338.*

42. *Luo, Y., Zhang, Z., Yang, F., Li, J., Liu, Z., Ren, W., Zhang, S. and Liu, B., 2021. Stabilized hydroxide-mediated nickel-based electrocatalysts for high-current-density hydrogen evolution in alkaline media. Energy & Environmental Science,* ***14****(8), pp.4610-4619.*

43. *Tang, Y., Liu, F., Liu, W., Mo, S., Li, X., Yang, D., Liu, Y. and Bao, S.J., 2023. Multifunctional carbon-armored Ni electrocatalyst for hydrogen evolution under high current density in alkaline electrolyte solution. Applied Catalysis B: Environmental, 321, p.122081.*

44. *Zhang, J.Y., Liang, J., Mei, B., Lan, K., Zu, L., Zhao, T., Ma, Y., Chen, Y., Lv, Z., Yang, Y. and Yu, C., 2022. Synthesis of Ni/NiO@ MoO3− x composite nanoarrays for high current density hydrogen evolution reaction. Advanced Energy Materials,* ***12****(22), p.2200001*.

45. *Zhong, B., Wan, S., Kuang, P., Cheng, B., Yu, L. and Yu, J., 2024. Crystalline/amorphous Ni/NixSy supported on hierarchical porous nickel foam*

*for high-current-density hydrogen evolution. Applied Catalysis B: Environmental,* ***340****, p.123195*.

## A: The proton conductivity and mechanical properties of SPEEK-Ce: Zr nanocomposite membrane

### 7.1. Introduction

Fuel cells in particular, proton exchange membrane fuel cells, or PEMFCs have become a popular new way to generate electricity in recent years because of its high energy generation efficiency, environmental friendliness, and adaptability for portable and transportation applications [1, 2]. The fundamental component in PEMFC is the proton exchange membrane or polymer electrolyte membrane (PEM), via which protons are continually transferred from the anode to the cathode [3]. The most widely used commercial proton exchange membranes (PEM) at the moment are perfluorinated sulfonic acid membranes (PFSA), such as Nafion, because of their great proton conductivity and relative stability [4]. Because of its rapid water intake, superior proton conductivity ($10^{-2}$ S/cm$^{1}$), and chemical/thermal stability, Nafion is a well-known hydrous PEM [5, 6]. However, the inertness of fluorocarbon chains appears to limit the chemical alteration that can be made to improve performance. Due to their high mechanical, thermal, and chemical stability as well as their processability, a number of alternative PEMs have been proposed recently, particularly aromatic polymers like sulfonated polyether ether ketone (SPEEK), sulfonated poly(arylene ether), and sulfonated poly(sulfone) [7].

SPEEK is one of the most promising non-fluorinated aromatic polymers for commercial proton exchange membrane fuel cell (PEMFC) applications. Its adequate proton conductivity, superior thermal stability, and reduced cost are the reasons for this. As a result, over the past 20 years, a great deal of study has been done and many discoveries have been published. The primary chain of SPEEK is made up of benzene rings, to which $SO_3H$ is directly bonded. In general, SPEEK's chemical structure is more stable than Nafion's [8]. Various additives, including zeolite [9], zirconium oxide [10], aluminium oxide [11], and heteropolyacids [12], were typically incorporated into the SPEEK matrix to enhance its performance such as proton conductivity, reduction of methanol permeability, improvement of mechanical strength.

One of the most important performance metrics that needs to be significantly enhanced is the proton conductivity of membranes. Nowadays, inorganic compounds such as zirconite/$TiO_2$ [13] and PVdFHFP–tin oxide [14], are frequently added to the polymer matrix in order to improve the conductivity of membranes. Wang et al. prepared Al-$CeZrO_4$/HPW incorporated SPEEK composite membrane, and the fuel cell performance of the synthesized membranes exhibited excellent power density of 1.01 $Wcm^{-2}$ which is great fuel cell performance [15]. Gashoul et al. [16] concentrated on employing zirconia nanoparticles to enhance the electrochemical characteristics of proton exchange membranes based on SPEEK. Furthermore, due to their extreme acidity and distinctive structure, heteropoly acids (HPAs), including phosphotungstic acid (HPW), are thought to be among the most effective proton conductors. Li et al. [17] had studied  Schiff-base networks (SNWs) for the conductivity improvement and found that the proton conductivity of SPEEK/S-SNW-15 composite membranes was improved to 115.53 mS/cm at 80 °C and 100% RH. Meng et al. [18] prepared novel composite membranes based on the SPEEK/ HPW/K-r-$SiO_2$. The incorporation of HPW/K-r-$SiO_2$ additive  improved  both the proton conductivity and dimensional stability of the composite membranes.

In this study, the incorporation of both $CeO_2$ and $ZrO_2$ into the SPEEK membrane resulted in improved mechanical strength, proton conductivity, and chemical stability. The effects of adding $CeO_2$:$ZrO_2$ nanoparticles on membrane performance were analyzed using techniques such as Fourier Transform Infrared (FTIR) spectroscopy, Scanning Electron Microscopy (SEM), and Thermogravimetric Analysis (TGA). We also investigated the ion exchange capacity (IEC), water uptake, proton conductivity, and tensile strength of the membranes. One of the advantages of the developed composite membrane is the more uniform distribution of the inorganic substances ($CeO_2$:$ZrO_2$) within the polymeric SPEEK matrix, which minimised agglomeration. This uniformity contributes to enhanced proton conductivity, chemical stability, and mechanical strength. Such composite membranes are anticipated to be effective polymer electrolyte membranes for fuel cells operating in high-temperature and low-humidity environments.

## 7.2. Experimental

### 7.2.1. Materials

Poly (ether ether ketone) powder, cerium (III) nitrate hexahydrate ($Ce(NO_3)_36H_2O$), concentrated sulfuric acid ($H_2SO_4$, 98%), zirconium acetate ($Zr_6O_4(OH)_4(O_2CCH_3)_{12}$, Dimethyl sulfoxide (DMSO), and sodium hydroxide pellets were all purchased from Sigma. All the materials were of analytical grade and used as received. In addition, the deionized water (DI) produced from our lab was also used throughout the experiments.

### 7.2.2. Synthesis of cerium-zirconia nanoparticles ($CeO_2$:$ZrO_2$)

The ceria–zirconia binary oxide nanoparticles were synthesized by the coprecipitation method. Cerium nitrate and zirconium acetate were mixed according to the molar ratios of $CeO_2$:$ZrO_2$ = 1:1, 1:2, 2:1,1:0 and 0:1. Experimentally, a calculated amount of ($Ce(NO_3)_3{\cdot}6H_2O$), ($Zr_6O_4(OH)_4(O_2CCH_3)_{12}$ and Sodium hydroxide (precipitating agent) were added in 100 mL of deionized water to fully dissolve the materials under magnetic stirring. The obtained precipitates were centrifuged and washed several times with distilled water and dried at 100 °C for 24 hours. The dried samples were then calcined at 600 °C for 2 hours.

### 7.2.3. Preparation of nanocomposite membranes

SPEEK-based composite membranes containing varying amounts of $CeO_2$:$ZrO_2$ were prepared by solution casting. A standard process involved dissolving 1g of PEEK powder in 15mL of DMSO and stirring until all of the SPEEK had been dissolved and a clear solution had formed. $CeO_2$:$ZrO_2$ powder was gradually added to the beaker of SPEEK solution, and the mixture was stirred to ensure the powder was evenly distributed throughout. After that, the mixture was poured into a casting tray, dried at 80 °C overnight. After that, the tray was submerged in DI water to facilitate the polymer's easy removal. The polymer was further dried under vacuum for two hours at 80 °C to eliminate the solvent. After drying, the thicknesses of the nanocomposite membranes were measured with a digital micrometre (0.18 mm). Each thickness was measured in the average of 3-7 readings at different positions of the membrane and was repeated twice on each membrane to obtain the average value.

### 7.2.4. Characterization of SPEEK-$CeO_2$:$ZrO_2$ membranes

#### 7.2.4.1. Thermal gravimetric analysis (TGA), Scanning electron microscopy (SEM) and Fourier-transform infrared spectroscopy (FTIR)

The thermal properties and the characteristics of the samples were studied by thermal gravimetric analysis (TGA) under nitrogen flow. TGA data was obtained using TGA instrument (PerkinElmer) over nitrogen and at a heating rate of 10° C/min from 35° C to 900° C. The surface morphologies of all the membranes were studied using Scanning electron microscopy (SEM). Fourier-transform infrared spectroscopy (FTIR) was employed to investigate the changes in the chemical structure of the membrane.

#### 7.2.4.2. Tensile test

A uniaxial testing device was used to record the nanocomposite membranes' uniaxial mechanical characteristics. Before testing, the samples' length and width were measured with a ruler and noted. The membrane samples' testing area measured 2 mm by 7 mm. A CellScale Ustretch device was used to assess the tensile strength of SPEEK and SPEEK-$CeO_2$:$ZrO_2$ composite membranes at 25 °C with actuator speeds of 10 mm/s, 20 mm/s, 30 mm/s, 40 mm/s.

#### 7.2.4.3. Water uptake (WU) and swelling ratio (SR)

We investigated water uptake (WU) and dimensions swelling/swelling ratio (SR) at temperatures ranging from 25 to 80 °C. To assess water uptake, a membrane was equilibrated with deionized water at the appropriate temperature for 8 hours before being weighed immediately after surface water removal. The membrane was vacuum dried for 2 hours at 60°C to achieve a consistent weight ($W_{dry}$). The water uptake (WU) of the membrane was computed as follows:

$$\mathrm{WU} = \frac{(\mathrm{W_{wet}} - \mathrm{W_{dry}})}{\mathrm{W_{dry}}} \times 100 \qquad \textbf{(7.1)}$$

The measurement of membrane dimensional swelling proceeded similarly. Firstly, the membrane was cut into a strip with predetermined dimensions (2cm in length and 1 cm in width) and equilibrated in water at the target temperature for 8 hours to obtain the wet length (Lwet). The sample was then dried in vacuum at 60 °C to yield the dry length (Ldry). The extent of water swelling (SR) of the membrane was calculated as:

$$\mathrm{SR} = \frac{(\mathrm{L_{wet}} - \mathrm{L_{dry}})}{\mathrm{L_{dry}}} \times 100 \tag{7.2}$$

### 7.2.4.4. Ion exchange capacity (IEC)

Ion exchange capacity (IEC) of SPEEK and SPEEK-$CeO_2$:$ZrO_2$ composite membrane were determined by titration method:

$$\mathrm{IEC} = \frac{\mathrm{C_{NaOH} V_{NaOH}}}{\mathrm{m_{dry}}} \tag{7.3}$$

Where $V_{NaOH}$ is the titrated volume of sodium hydroxide (NaOH) and $m_{dry}$ is the weight of the dry membranes.

### 7.2.4.5. Oxidative stability

The oxidative stability of SPEEK and SPEEK-$CeO_2$:$ZrO_2$ composite membranes was investigated using Fenton's test. Fenton's reagent was prepared by creating a solution containing 3 vol% hydrogen peroxide and 3 ppm of $Fe^{2+}$ ions. The weight of each dried membrane was measured before immersing it in the Fenton's reagent at various temperatures. The membranes were weighed at regular intervals of 10 minutes, and the change in weight was used to assess the oxidative stability of the membranes, as indicated in Eq. (7.4).

$$\text{Oxidative stability } (\%) = \frac{\mathrm{W_{dry}}}{\mathrm{W_{initial}}} \times 100 \tag{7.4}$$

where: $W_{dry}$ is the dry weight of the membrane after Fenton’s test (g) and $W_{initial}$ is the initial dry weight of the membrane (g).

### 7.2.4.6. Proton Conductivity measurement

Proton conductivities of the composite membranes were measured by AC impedance spectroscopy using an electrochemical workstation (Autolab PGSTAT302N, Switzerland) in the frequency range of 1 MHz to 100 Hz with an amplitude of 5 mV. Prior to testing, all membranes were hydrated by immersion in deionized water for 24 hours at room temperature. A sample of the pre-hydrated membrane was wrapped around a graphite electrode, then the tip of the covered electrode was immersed in $H_2SO_4$ 0.5M during proton conductivity measurement. The proton conductivity (σ) was calculated as follows:

$$\sigma = \frac{l}{RA} \tag{7.5}$$

where L, refers to the thickness of the membrane (2.16 cm), R=the resistance of the membrane (Ω) and A=cross-sectional area ($cm^2$).

## 7.3. Results and discussion

### 7.3.1. Fourier Transform Infrared (FTIR) analysis

$CeO_2$:$ZrO_2$ nanoparticles were successfully incorporated within the SPEEK matrix, and the structural combination was confirmed by FTIR spectroscopy as indicated in Fig 7.1. Fig. 7.1 shows the spectra of SPEEK and SPEEK-$CeO_2$:$ZrO_2$ composite membranes in the range of 400-4000 $cm^{-1}$. The band at 3378 $cm^{-1}$ shows the O-H stretching vibration corresponding to physically adsorbed water. It was observed that the $ZrO_2$ and $CeO_2$ bands at 771 $cm^{-1}$ and 504 $cm^{-1}$ correspond to stretching peaks of Zr–O and Ce-O, respectively [19]. As observed on the spectra, the peaks of source C-H, and C=O from the polymer matrix chain were found at wavenumbers 1299 and 1598 $cm^{-1}$, respectively. Additionally, both the symmetric and asymmetric stretching bands of S=O and O=S=O were observed at 1026 and 1083 $cm^{-1}$ for SPEEK, and these peaks are the characteristic peaks of SPEEK.

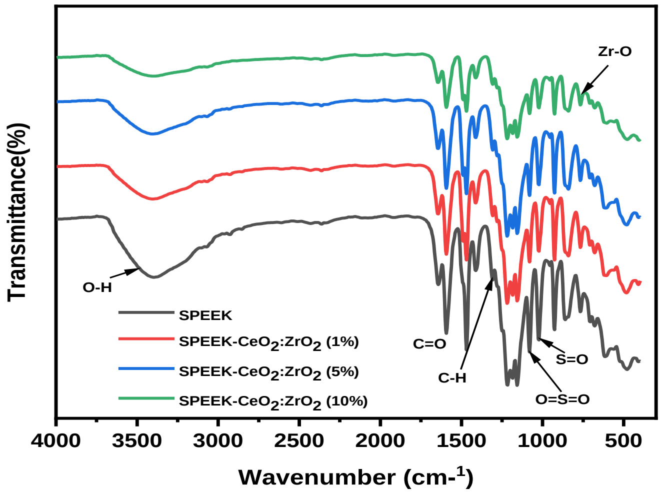

**Fig. 7.1:** FTIR spectra of SPEEK and SPEEK-$CeO_2$:$ZrO_2$ composite membranes at different filler loading.

### 7.3.2. Scanning electron microscopy (SEM)

The polymers' surface morphology was examined using field emission SEM (FE-SEM) analysis. Fig. 7. 2(a–d) depicts image of pure SPEEK, SPEEK-$CeO_2$:$ZrO_2$ (1%), SPEEK-$CeO_2$:$ZrO_2$ (5%), and SPEEK-$CeO_2$:$ZrO_2$ (10%) composite membranes. In contrast, the SEM images of the polymer nanocomposites, presented in Fig. 7.2(b-d), clearly reveal that the $CeO_2$:$ZrO_2$ nanoparticles are distributed on the surfaces of the polymeric membranes due to the introduction of these nanofillers. This incorporation allows the nanocomposite membranes to retain water molecules, thereby enhancing proton conductivity [20].

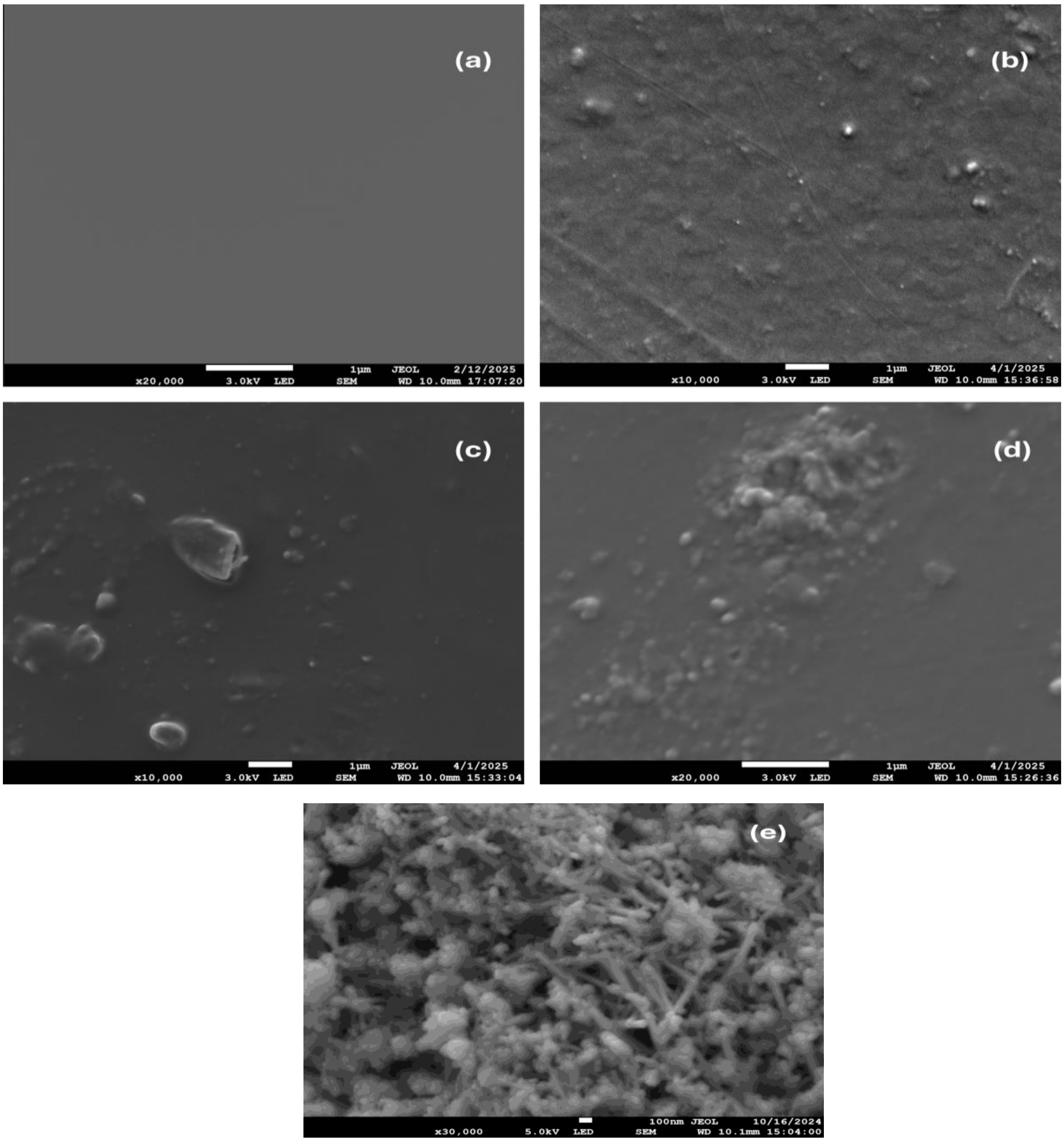

**Fig. 7. 2:** (a) SEM micrograph of (a) SPEEK membrane, (b) SPEEK/ $CeO_2$:$ZrO_2$ (1%), (c) SPEEK-$CeO_2$:$ZrO_2$ (5%), (d) SPEEK-$CeO_2$:$ZrO_2$ (10%) composite membranes and (e) $CeO_2$:$ZrO_2$ nanoparticles (100 nm)

### 7.3.3. Thermo-gravimetric analysis (TGA)

The thermal behaviour of the prepared nanocomposite membranes was examined using Thermogravimetric Analysis (TGA). As shown in Fig. 7.3, the TGA curve exhibited three distinct stages of weight loss over the temperature range studied. The first stage, occurring between 35 °C and 150 °C, resulted in a weight loss of 8 wt.%. This loss was attributed to the evaporation of adsorbed moisture and residual solvents [21]. The second stage, occurring between 250 °C and 410 °C, involved the decomposition of sulfonic acid groups in SPEEK. The final stage, associated with the decomposition of the polymer backbone, occurred at approximately 560 °C.

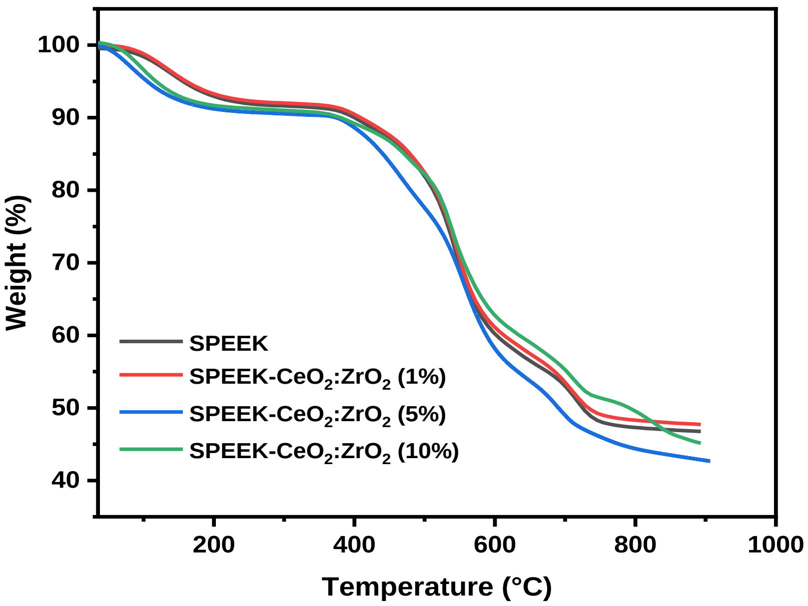

**Fig. 7.3:** TGA curves of SPEEK and SPEEK-$CeO_2$:$ZrO_2$ composite membranes.

Notably, the SPEEK-$CeO_2$:$ZrO_2$ nanocomposite membrane exhibited lower weight loss compared to SPEEK alone. Additionally, the motion of the polymer chains was restricted in the nanocomposite membranes, leading to a slightly elevated onset temperature for thermal degradation [22]. This observation indicates an improvement in the thermal stability of the nanocomposite membranes. These results confirm the role of $CeO_2$:$ZrO_2$ nanoparticles in enhancing the thermal stability of SPEEK membranes, aligning with our expectations.

### 7.3.4. Tensile test

Fig.7.4 (a-d) illustrates the stress-strain curves of the pristine SPEEK membrane compared to SPEEK-$CeO_2$:$ZrO_2$ composite membranes with varying concentrations of 1%, 5%, and 10% at actuator speeds of 10 mm/s, 20 mm/s, 30 mm/s, and 40 mm/s. All samples exhibited strain when the strain rate was increased to 40 mm/s. The SPEEK-$CeO_2$:$ZrO_2$ composite membranes demonstrated an increase in tensile stress compared to the pristine SPEEK membrane, likely due to the incorporation of $CeO_2$:$ZrO_2$ nanoparticles into the SPEEK matrix.

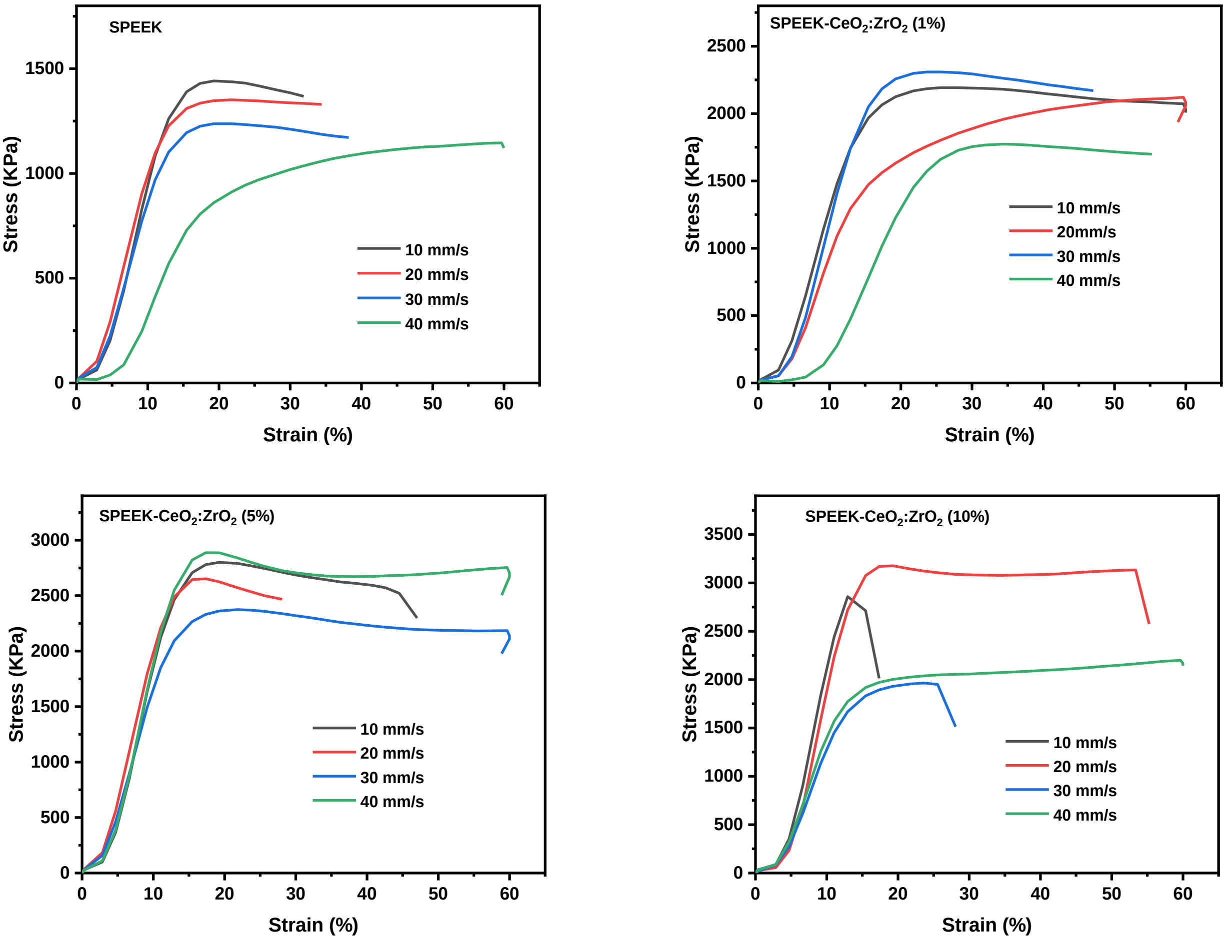

**Fig. 7. 4:** Mechanical tensile tests results of (a) SPEEK, (b) SPEEK-$CeO_2$:$ZrO_2$ (1%), (c) SPEEK-$CeO_2$:$ZrO_2$ (5%) and (d) SPEEK-$CeO_2$:$ZrO_2$ (10%) composite membranes.

Notably, the SPEEK-$CeO_2$:$ZrO_2$ (10%) composite reached the highest tensile stress of 3169 kPa and an elongation of 60% at an actuator speed of 20 mm/s. The SPEEK-$CeO_2$:$ZrO_2$ (1%) and SPEEK-$CeO_2$:$ZrO_2$ (5%) composite membranes also showed impressive tensile strengths of 2298 kPa and 2887 kPa, respectively, both of which are higher than that of the pristine SPEEK.

The results indicate that tensile strength increases with higher filler loading when compared to other composite membranes. Overall, the modification of the SPEEK membrane with $CeO_2$:$ZrO_2$ fillers positively affects its tensile strength, which is advantageous for fuel cell applications [15]. However, the stress-strain behavior of the modified membrane with higher percentages of $CeO_2$:$ZrO_2$ nanoparticles is not compatible with strain rates of 10 mm/s and 30 mm/s, as it reduces elasticity and mechanical properties. This is evident in Fig. 7.4(d), where the membrane exhibits brittleness at these rates. This brittleness may be attributed to the high concentration of $CeO_2$:$ZrO_2$ nanoparticles introduced into the SPEEK matrix, leading to brittle fracture in the modified membrane [22].

### 7.3.5. Oxidative Stability of the membranes

The membranes' oxidative stability was assessed using Fenton's test. The test was carried out at 80 °C for five (5) hours in order to replicate the PEMFC operating condition. Fig. 7.5 below illustrates the oxidative stability of SPEEK and SPEEK-$CeO_2$:$ZrO_2$ composite membranes. SPEEK, SPEEK-$CeO_2$:$ZrO_2$ (1%), SPEEK-$CeO_2$:$ZrO_2$ (5%) and SPEEK-$CeO_2$:$ZrO_2$ (10%) membranes have measured residual weights of 77%, 77.9%, 84.2%, and 88.5%, respectively. Eqns. (7.6) to (7.10) below illustrate how the addition of Fe derivatives catalyzes the production of hydroxyl (HO•) and hydroperoxyl (HOO•) radicals in $H_2O_2$ solution during the oxidative test [23].

$$Fe^{2+} + H_2O_2 \longrightarrow OH^- + HO\bullet + Fe^{3+} \qquad \textbf{(7.6)}$$

$$Fe^{2+} + HO\bullet \longrightarrow OH^- + Fe^{3+} \qquad \textbf{(7.7)}$$

$$H_2O_2 + HO\bullet \longrightarrow HOO\bullet + H_2O \qquad \textbf{(7.8)}$$

$$Fe^{2+} + HOO\bullet \longrightarrow OOH^- + Fe^{3+} \qquad \textbf{(7.9)}$$

$$Fe^{3+} + HOO\bullet \longrightarrow H^+ + O_2 + Fe^{2+} \qquad \textbf{(7.10)}$$

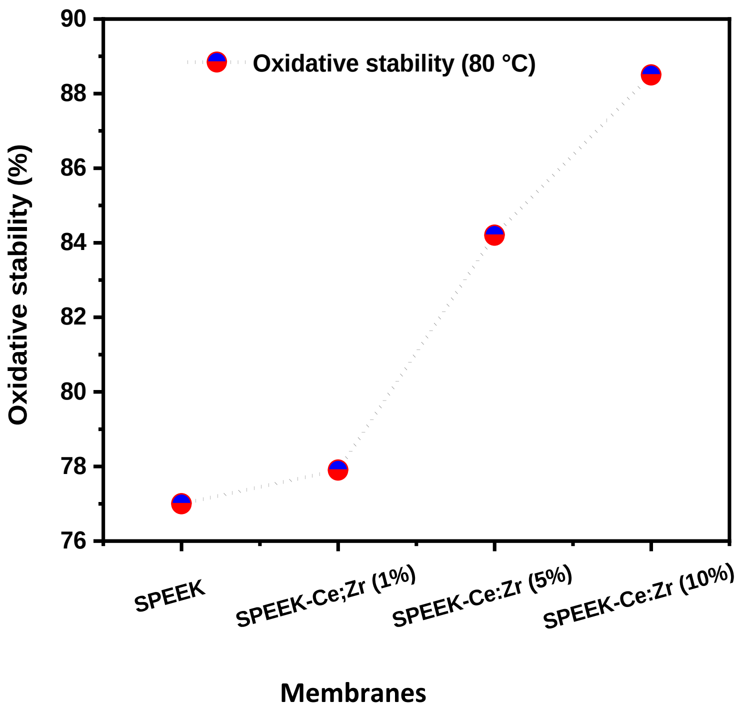

**Fig. 7.5:** Oxidative stability of SPEEK and SPEEK-$CeO_2$:$ZrO_2$ composite membranes at 80 °C.

SPEEK-$CeO_2$:$ZrO_2$ membranes were less damaged by free radicals due to the radical scavenging properties of $CeO_2$ nanoparticles. In contrast, the pristine SPEEK membrane lost 23% of its weight, indicating that sulfonated hydrocarbons are susceptible to free radicals. However, in real-time PEMFC operation, radical production is less intense than in the oxidative test we performed.

### 7.3.6. Water uptake, dimensional swelling ratio, Ion exchange capacity and proton conductivity measurement

Fig. 7.6(a) depicts water uptake by SPEEK and SPEEK-$CeO_2$:$ZrO_2$ composite membranes. The influence of $CeO_2$:$ZrO_2$ nanofiller on water uptake by nanocomposite membranes was observed. Fig. 7.6(a) indicates that the composite membrane has a larger water uptake than the SPEEK membrane. At 80 °C, the SPEEK-$CeO_2$:$ZrO_2$ (10%) composite membrane showed a greater water uptake of 60.3% than the pristine SPEEK membrane (57.2%), which might be due to inorganic fillers inserted across the pores of the swelling membrane to increase SPEEK's hydrophilicity [24]. Incorporating

$CeO_2$:$ZrO_2$ nanoparticles increases water retention within composite membranes, which results in increased proton conductivity due to an increase in the number of exchange sites available per cluster, which is an important parameter for fuel cells to operate at higher temperatures [25]. In general, the water uptake of nanocomposite membranes increases as the $CeO_2$:$ZrO_2$ weight content within the SPEEK membrane matrix increases, which could be due to the hydrophilicity of nanoparticles adsorbed on the membrane's surface to introduce the hydrophilicity of modified membrane surfaces. As seen in Fig. 7.6(a), the dimensional swelling ratio at 25 °C, 40 °C, and 80 °C increases marginally as the weight percentage of $CeO_2$:$ZrO_2$ nanoparticles in the membrane increases. However, a larger dimensional swelling ratio of 34.6% is obtained when the SPEEK-$CeO_2$:$ZrO_2$ (10%) composite membrane is soaked at a higher temperature of 80 °C. This could be because of the water that is absorbed within the membrane matrix.

Table 7.1 shows the ion exchange capacity (IEC) and proton conductivity of SPEEK, SPEEK-$CeO_2$:$ZrO_2$ composite membranes. The composite membranes' proton conductivities at both temperatures were found to be higher than those of pristine SPEEK, as shown in Fig. 7.6(b) and Table 7.1; this could be attributed to inorganic particles within the SPEEK matrix. The results suggest that adding $CeO_2$:$ZrO_2$ nanoparticles into the membrane increases proton conductivity as temperature increases [15, 26]. The data show the same trend as Fig. 7.6(a), which depicts water uptake. Table 7.1 and Fig. 7.6(c) demonstrate that SPEEK-$CeO_2$:$ZrO_2$(1%), SPEEK-$CeO_2$:$ZrO_2$ (5%), and SPEEK-$CeO_2$:$ZrO_2$ (10%) composite membranes had higher IEC values of 2.4 meg/g, 3 meg/g, and 5.1 meg/g, respectively, as compared to 2 meg/g of pristine SPEEK membrane. These could be due to the incorporation of $CeO_2$:$ZrO_2$ nanoparticles, which improved the membrane's acid property and provided a new strong acid site. Fig. 7.6(c) demonstrates that when the wt.% of $CeO_2$:$ZrO_2$ nanoparticles in the membrane increases, so does the IEC of the composite membranes.

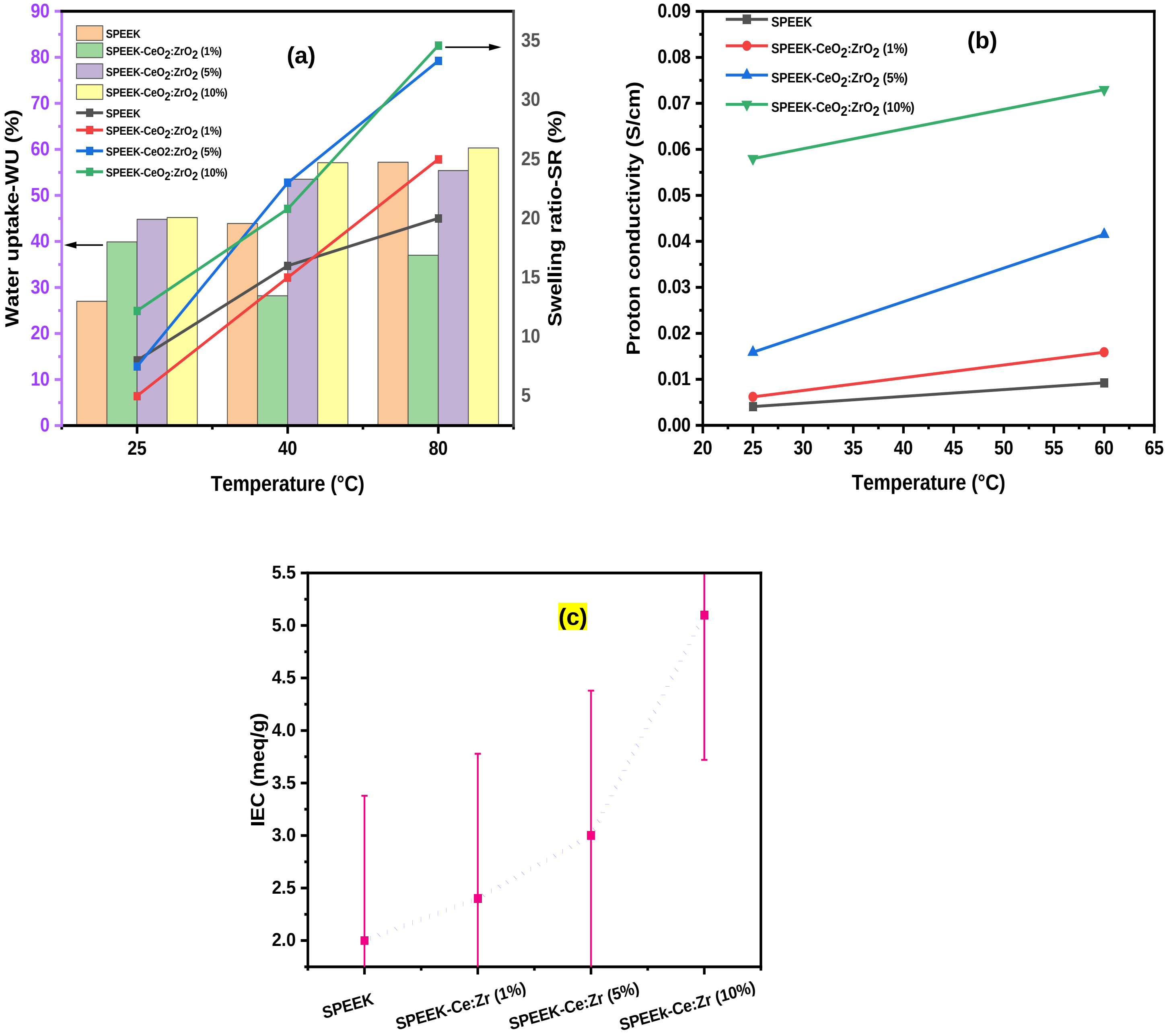

**Fig. 7. 6:** (a) Water uptake and swelling ratio, (b) Ion exchange capacity, and (c) proton conductivity measurement of SPEEK and SPEEK-CeO$_2$:ZrO$_2$ composite membranes**.**

**Table 7.1:** The IEC and proton conductivity of SPEEK and SPEEK-$CeO_2$:$ZrO_2$ composite membranes

| Membranes | Proton conductivity (S/cm) 25 °C | Proton conductivity (S/cm) 60 °C | IEC (meq/g) |
|---|---|---|---|
| SPEEK | 0.00407 | 0.00925 | 2 |
| SPEEK- $CeO_2$:$ZrO_2$ (1%) | 0.0062 | 0.0159 | 2.4 |
| SPEEK -$CeO_2$:$ZrO_2$ (5 %) | 0. 0159 | 0.0415 | 3 |
| SPEEK- $CeO_2$:$ZrO_2$ (10%) | 0.058 | 0.073 | 5.1 |

## 7.4. Conclusion

The SPEEK-$CeO_2$:$ZrO_2$ composite membrane with enhanced proton conductivity was successfully prepared using the recast method. The thermal stability of the composite membrane began to deteriorate at temperatures above 300 °C, which might be attributed to the nature of an inorganic filler that allows them to be use in fuel cells. Nanocomposite membranes outperformed SPEEK membranes at 80 ºC in terms of water uptake, IEC, and swelling ratio. The incorporation of metal oxide elements into the nanocomposite membranes resulted in greater proton conductivity than pristine SPEEK membranes. The improved membrane's greater proton conductivity resistance confirmed its suitability for fuel cells. SEM and FTIR data demonstrate the presence of $CeO_2$:$ZrO_2$ nanoparticles in the SPEEK matrix, which also improves water uptake.

# B: Enhanced Conductivity of Sulfonated Poly (ether ether ketone) membrane by the Incorporation of Cerium-Silica as a Nanofiller for Fuel Cells

## 7.5. Introduction

Fuel cells rely heavily on the solid proton-conducting polymer electrolyte membrane (PEM). An ideal PEM is an electrical insulator, a good proton conductor, and an effective barrier that prevents reactants from crossing the membrane [27]. Nafion, a perfluorinated sulfonic acid membrane, is still employed in modern designs [4, 28]. Its high rate of fuel crossover contributes to the reported low fuel cell efficiency. This has boosted interest in the quest for alternative membrane materials [29]. Polyaryls, such as poly(ether ether ketone) (PEEK), have attracted the most attention because to their excellent engineering features and ease of sulfonation to produce proton conductivity. Compared to Nafion, sulfonated PEEK (SPEEK) exhibits greater resistance to methanol permeability and a lower cost [30]. SPEEK membranes are produced from well-known semicrystalline thermoplastic PEEKs, which have great chemical resistance and good thermomechanical characteristics [31]. However, like Nafion, the proton conductivity of SPEEK membranes is greatly dependent on the amount of humidified water. To ensure optimal electrochemical performance, SPEEK membranes must be produced with a high degree of sulfonation. On the other hand, the high DS (over 60%) leads the SPEEK matrix to absorb a larger amount of water in completely humidified conditions, which might trigger the matrix to swell, reducing the mechanical integrity and chemical stability of the membrane [32, 33]. These limitations of SPEEK membranes can be overcome if PEMFCs are operated at low RH. Nonetheless, only a few studies have examined the performance of SPEEK membranes in PEMFCs working in low humidity environments. Furthermore, the chemical and mechanical integrity of SPEEK membranes can be quickly compromised by the attack of free radicals, which are rapidly produced under anhydrous or low RH PEMFC conditions [34-36].

SPEEK membranes' electrochemical performance, thermomechanical and chemical stability in a low RH PEMFC environment can potentially be improved by boosting their ability to transmit protons in the absence of humidified water molecules and withstand free radical attack. This can be accomplished by incorporating hygroscopic nanofillers ($SiO_2$, sulfonated carbon nanotubes, sulfonated graphene oxide, and $ZrO_2$) for long-term water retention, or by dispersing functionalized nanoparticles (amines, phosphoric acid, and imidazole) containing self-humidified functional moieties into the SPEEK matrix for water-free proton conduction [37]. The latter can be accomplished by using free radical scavengers like $CeO_2$ or $MgO_2$ to reinforce bare SPEEK membranes. For example, Salarizadeh et al. added amine-functionalized titania ($NH_2$-$TiO_2$) nanoparticles to SPEEK membranes and showed that, in addition to boosting total PEMFC production, the functionalized $ATiO_2$ provided an extra hopping channel for proton conduction [38]. Because of the presence of radical scavenging $CeO_2$ nanoparticles, Parnian et al. created SPEEK-ceria ($CeO_2$) nanocomposite membranes for PEMFCs that demonstrated long-term durability [39].

In this study, we investigate how the addition of Ce:$SiO_2$ nanoparticle to SPEEK membranes affects the membranes' ability to absorb water, exchange ions, conduct proton flow, and chemical stability, among other characteristics. SPEEK-Ce:$SiO_2$ material as a proton exchange membrane for PEMFCs has not yet been reported in the literature, and this work is novel in this respect.

## 7.6. Experimental

### 7.6.1. Materials

PEEK powder (450 G) was purchased from Victrex, England. Ce:$SiO_2$ nanoparticles synthesised from our labs. Concentrated sulfuric acid ($H_2SO_4$ , 98% purity), Dimethyl sulfoxide(DMSO), Sodium chloride (NaCl), Hydrochloric acid (HCl), sodium hydroxide pellets (NaOH), and Phenolphthalein were used as received from Sigma Aldrich,USA.

### 7.6.2. Sulfonation of PEEK

The modification of sulfonation aims to enhance the hydrophilic characteristics of polyether ether ketone (PEEK) by introducing a sulfonic acid group ($SO_3H$) into its backbone. In this study, a post-sulfonation process was utilized due to its cost-effectiveness and simplicity. This approach is a primary goal for researchers seeking to develop a cost-effective membrane to replace the currently used Nafion membrane [40]. Although a pre-sulfonation process may prove to be more effective, it was avoided in this case due to its complexity [41]. The sulfonation of PEEK was performed at room temperature by adding 10 grams of dried PEEK to a beaker containing 100 ml of 98% concentrated sulfuric acid. The mixture was stirred mechanically for two hours to achieve the desired degree of sulfonation. During this process, hydrogen atoms in the aromatic groups of PEEKS are replaced by sulfonic acid groups, which enhance proton conductivity.

After the sulfonation reaction, the acidic polymer solution was slowly poured into a beaker containing ice cold water while stirring magnetically, resulting in the precipitation of the polymer. The precipitated polymer was then thoroughly washed with deionized water until the rinsed water reached a pH of 7. The washed samples were separated using vacuum filtration. Finally, the collected polymer was dried in a vacuum oven overnight at 80 °C.

### 7.6.3. Membrane preparation (SPEEK and its modified form)

SPEEK-based composite membranes containing varying amount of $Ceo_2$:$SiO_2$ were prepared by solution casting. In a typical procedure, PEEK powder (1g) was dissolved in DMSO (15 ml) and stirred until all the SPEEK was dissolved to form a clear solution. $SiO_2$ powder was slowly into the beaker containing SPEEK solution which was stirred until the powder was fully dispersed in the solution. The resultant mixture was cast in a glass casting tray and heated to 80 °C overnight. The tray was then immersed under DI water for smooth peeling of polymer from the tray. The solvent in the polymer was removed by further heating at 80 °C under vacuum for 2 hours.

### 7.6.4. Characterization of SPEEK-$Ceo_2$:$SiO_2$ membranes

#### 7.6.4.1. Thermal gravimetric analysis (TGA), Scanning electron microscopy (SEM) and Fourier-transform infrared spectroscopy (FTIR)

FT-IR spectra of the membrane in the wavenumber range of 4000–450$cm^{-1}$ were obtained on a Bruker Fourier transform infrared spectroscopy (FTIR). SEM-Joel scanning electron microscopy (SEM, JMS-6010 Plus) was used to examine the surface morphologies of SPEEK and SPEEK/Ce:$SiO_2$ composite membranes. Thermal properties and characteristics were studied using PerkinElmer thermogravimetric analyser (TGA) under air and nitrogen flow, and operating at a heating rate of 10 °C/min from 35 °C to 900 °C.

#### 7.6.4.2. Tensile test

A uniaxial testing device was used to record the nanocomposite membranes' uniaxial mechanical characteristics. Before testing, the samples' length and width were measured with a ruler and noted. The membrane samples' testing area measured 2 mm by 7 mm. A CellScale Ustretch device was used to assess the tensile strength of SPEEK and SPEEK-$Ceo_2$:$SiO_2$ composite membranes at 25 °C.

### 7.6.4.3. Water uptake (WU) and swelling ratio (SR)

We investigated water uptake (WU) and dimensions swelling/swelling ratio (SR) at temperatures ranging from 25 to 80 ◦C. To assess water uptake, a membrane was equilibrated with deionized water at the appropriate temperature for 8 hours before being weighed immediately after surface water removal. The membrane was vacuum dried for 2 hours at 60°C to achieve a consistent weight ($W_{dry}$). The water uptake (WU) of the membrane was computed as follows:

$$\mathrm{WU} = \frac{(\mathrm{W_{wet}} - \mathrm{W_{dry}})}{\mathrm{W_{dry}}} \times 100 \qquad \textbf{(7.11)}$$

The measurement of membrane dimensional swelling proceeded similarly. Firstly, the membrane was cut into a strip with predetermined dimensions (2cm in length and 1 cm in width) and equilibrated in water at the target temperature for 8 hours to obtain the wet length (Lwet). The sample was then dried in vacuum at 60 °C to yield the dry length (Ldry). The extent of water swelling (SR) of the membrane was calculated as:

$$\mathrm{SR} = \frac{(\mathrm{L_{wet}} - \mathrm{L_{dry}})}{\mathrm{L_{dry}}} \times 100 \qquad \textbf{(7.12)}$$

### 7.6.4.4. Ion exchange capacity (IEC)

Ion exchange capacity (IEC) of SPEEK and SPEEK-$Ceo_2$:$SiO_2$ composite membrane were determined by titration method:

$$\mathrm{IEC} = \frac{\mathrm{C_{NaOH}} \mathrm{V_{NaOH}}}{\mathrm{m_{dry}}} \qquad \textbf{(7.13)}$$

Where $V_{NaOH}$ is the titrated volume of sodium hydroxide (NaOH) and $m_{dry}$ is the weight of the dry membranes.

#### 7.2.4.5. Oxidative stability

The oxidative stability of SPEEK and SPEEK-$CeoO_2$:$SiO_2$ composite membranes was investigated using Fenton's test. Fenton's reagent was prepared by creating a solution containing 3 vol% hydrogen peroxide and 3 ppm of $Fe^{2+}$ ions. The weight of each dried membrane was measured before immersing it in Fenton's reagent at various temperatures. The membranes were weighed at regular intervals of 10 minutes, and the change in weight was used to assess the oxidative stability of the membranes, as indicated in Eqn. (7.14).

$$\text{Oxidative stability } (\%) = \frac{W_{\text{dry}}}{W_{\text{initial}}} \times 100 \qquad \textbf{(7.14)}$$

where: $W_{dry}$ is the dry weight of the membrane after Fenton’s test (g) and $W_{initial}$ is the initial dry weight of the membrane (g).

#### 7.6.4.6. Proton Conductivity measurement

Proton conductivities of the composite membranes were measured by AC impedance spectroscopy using an electrochemical workstation (Autolab PGSTAT302N, Switzerland) in the frequency range of 1 MHz to 100 Hz with an amplitude of 5 mV. Prior to testing, all membranes were hydrated by immersion in deionized water for 24 hours at room temperature. A sample of the pre-hydrated membrane was wrapped around a graphite electrode, then the tip of the covered electrode was immersed in $H_2SO_4$ 0.5M during proton conductivity measurement. The proton conductivity (σ) was calculated as follows:

$$\sigma = \frac{l}{RA} \qquad \textbf{(7.15)}$$

where L, refers to the thickness of the membrane (2.16 cm), R=the resistance of the membrane (Ω) and A=cross-sectional area ($cm^2$).

## 7.7. Results and discussion

### 7.7.1. FTIR analysis

FTIR analysis was successfully employed to examine the sulfuric acid group of the synthesized SPEEK polymer and validate the $CeO_2$:$SiO_2$ filler that was added to the SPEEK. Fig.7.7 shows the FT-IR spectra, which show the O-H vibration associated with the sulfuric acid group and the broad band at about 3409 cm$^{-1}$ in the sulfonation of PEEK polymer. The symmetry of S=O showed absorption peaks at 1080 cm$^{-1}$ and 1026 cm$^{-1}$ in the sulfuric acid group (-$SO_3H$). Carbonyl groups were attributed to the peaks at 1593 cm$^{-1}$ and 1635 cm$^{-1}$ of sulfonated PEEK [42]. The signal at 1469 cm$^{-1}$ corresponds to (-$SO_3H$) [43]. It was a bit difficult to realize the structure changes in the SPEEK and the SPEEK-$CeO_2$:$SiO_2$ membranes, because of the difficulties in identifying sulfuric acid groups that were connected on the surface of $CeO_2$:$SiO_2$ particles.

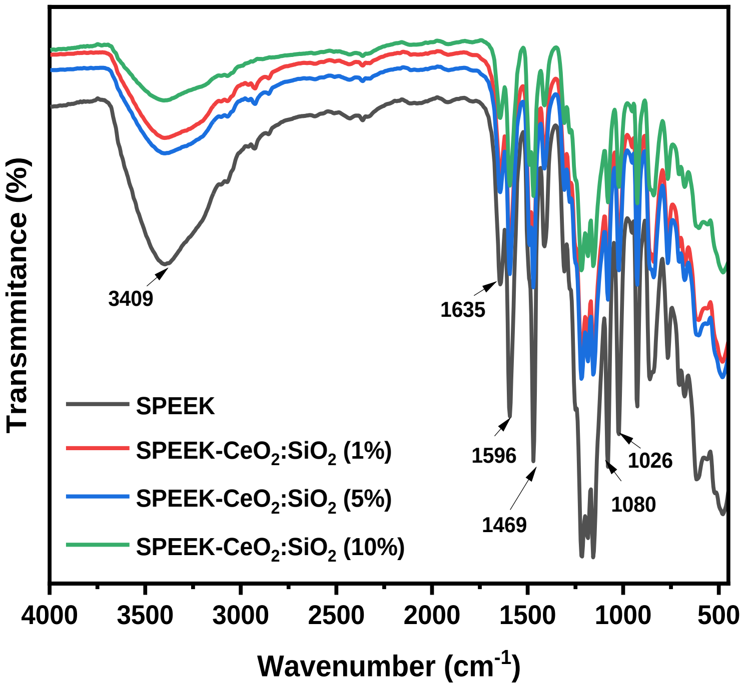

**Fig. 7.7:** FTIR spectra of SPEEK and SPEEK-$CeO_2$:$SiO_2$ composite membranes.

### 7.7.2. TGA analysis

The thermal characteristics of pristine SPEEK and SPEEK-$CeO_2$:$SiO_2$ composite membranes were investigated using TGA; the findings are shown in Fig. 7.8. SPEEK and SPEEK-$CeO_2$:$SiO_2$ composite membranes demonstrated three distinct stages of thermal degradation. The initial weight loss occurred at temperatures ranging from 85°C to 180°C as a result of the breakdown of absorbed water molecules on the membrane surface. Water absorption can be explained by the fact that a polymer having a sulfonic acid group, such as SPEEK, is naturally hydrophilic and absorbs moisture from its surroundings [44]. The majority of the absorbed water molecules are bound rather than free molecules. The second weight loss occurs at temperatures ranging from 300 to 475 °C due to $SO_3H$ group dissociation in membranes [45]. The third weight loss zone occurred at temperatures above 475 °C due to the disintegration of the SPEEK backbone [46]. The addition of $CeO_2$:$SiO_2$ nanoparticles improved the thermal stability of SPEEK-$CeO_2$:$SiO_2$ nanocomposite membranes over pristine SPEEK. This study demonstrated that all membranes have good thermal stability for fuel cell application, with all being thermally stable between 60 and 120 °C of the fuel cell working temperature.

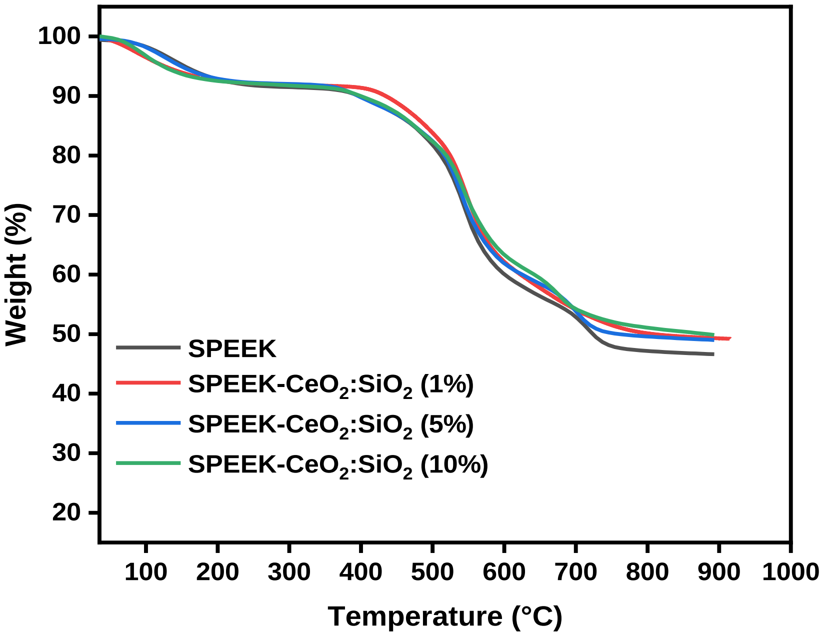

**Fig. 7.8:** Thermograms of SPEEK and SPEEK-Ce:$SiO_2$ composites.

### 7.7.3. SEM analysis

Fig. 7.9 (a–d) shows surface SEM images of SPEEK and SPEEK-$CeO_2$:$SiO_2$ composite membranes. SEM image in Fig. 7.9a shows that the pristine SPEEK membrane was smooth with no cracks or surface damage. In contrast, the surface of the SPEEK-$CeO_2$:$SiO_2$ composite membrane (Fig. 7.9(b-d)) was rough and contained nanoparticles, showing that $CeO_2$:$SiO_2$ nanofillers had been incorporated into the SPEEK matrix.

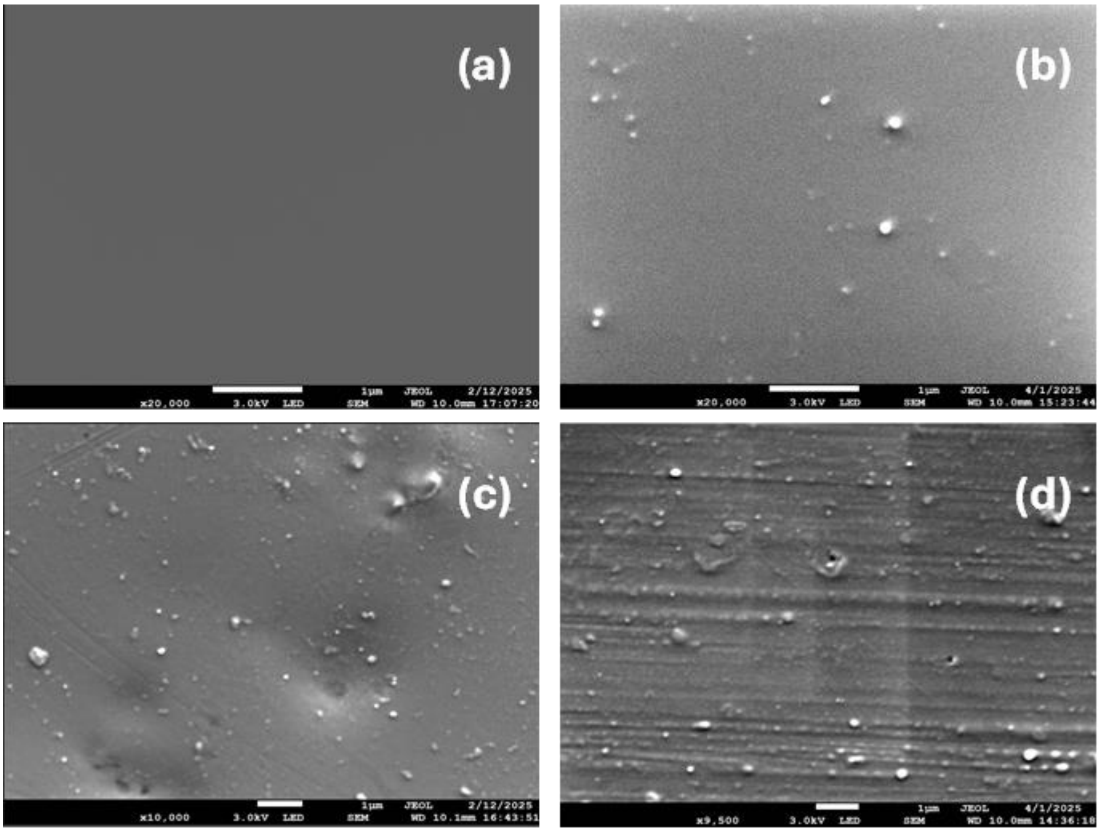

**Fig. 7.9:** SEM images of (a)SPEEK, (b) SPEEK-$CeO_2$:$SiO_2$ (1%), (c) SPEEK-$CeO_2$:$SiO_2$ (5%) and (d) SPEEK-$CeO_2$:$SiO_2$ composite membranes.

### 7.7.4. Water Uptake and Swelling Properties of $CeO_2$:$SiO_2$

The composite membranes' water uptake capacity is a crucial factor for membrane performance toward PEMFC. Proton conductivity, hydrolytic stability, and mechanical stability of PEM are all impacted by water uptake capacity. Fig.7.10 shows the water uptake and swelling ratio values of SPEEK and SPEEK-$CeO_2$:$SiO_2$ composite membranes at room temperature, 40°C and 80 °C. The room temperature water uptake capacities of SPEEK-$CeO_2$:$SiO_2$ membranes containing 1% $CeO_2$:$SiO_2$, 5% $CeO_2$:$SiO_2$, 10% $CeO_2$:$SiO_2$, and pristine SPEEK were found to be 18.67%, 26.12%, 31.00%, and 27.00%, respectively. At 80 °C, the water uptake capacities were recorded as 28.90%, 35.84%, and 42.90% with the order of increasing $CeO_2$:$SiO_2$ amount. The increasing water uptake capacity with increasing $CeO_2$:$SiO_2$ amounts at both temperatures can be explained by the hygroscopic nature of $SiO_2$. It was also observed that the water uptake capacity of membranes increased with the increase in temperature from room temperature to 80°C, and this phenomenon can be explained by the boosting of ionic mobility with increasing temperature.

Membrane swelling is an important characteristic of PEMs since the high swelling leads to membrane failure, eventually leading to the PEMFC system failure [47]. Compared to the bare SPEEK membrane, all composite membranes displayed a low degree of swelling. This behaviour of the SPEEK-$CeO_2$:$SiO_2$ membranes can be attributed to the chemical interactions between the SPEEK matrix and the incorporated $CeO_2$:$SiO_2$. The chemical interaction can restrict the dimensional expansion of composite membranes when hydrated, thereby preventing membrane failure [33].

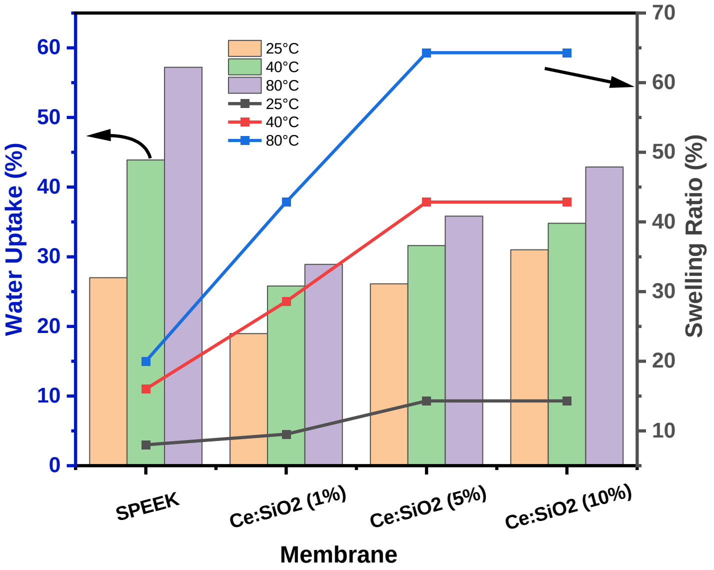

**Fig. 7.10:** Water uptake and swelling ratios of SPEEK and SPEEK-$CeO_2$:$SiO_2$ composite membranes.

### 7.7.5. Oxidative Stability

Another factor that influences the membranes' shelf life and fuel cell efficiency is their oxidative stability. Membranes' oxidative stability indicates their resistance to hydroxyl radicals in fuel cells. These hydroxy radicals can harm the membrane matrix, causing it to become defective. Table 7.3 and Fig. 7.11 show the findings of determining the membranes' oxidative stability by analysing weight loss over time at 80 °C in the Fenton solution. After 3 hours, weight losses for SPEEK-$CeO_2$:$SiO_2$ membranes in Fenton solution range from 78% to 82%. Li et al. [17] observed that the weight loss of the original SPEEK membrane reached as high as 16.23% during oxidative stability testing at 80 °C with 3% $H_2O_2$ and 3 ppm $Fe^{2+.}$ Their results were also compared to membranes doped with silica nano wire (SNW) and it was reported that they could keep a higher residual weight from 87.12 to 90.33%, implying an improvement on oxidative stability. In a separate investigation, Sahin utilized 3% $H_2O_2$ and a Fenton solution containing 4 ppm $Fe^{2+}$. They reported that pristine SPEEK was totally dissolved in Fenton solution after 24 h, pure PVA after 6 h and SPEEK-PVA after 8 h at 68°C [48]. Despite the high temperature and $Fe^{3+}$ concentration, the produced membranes showed excellent oxidative stability. In this study, the membrane containing 5% $CeO_2$:$SiO_2$ had the maximum oxidative stability. This may be because $CeO_2$ has a free radical scavenging effect, which reduces the concentration of OH• and HOO• radicals. This effect further protects the structural integrity of the SPEEK matrix and enhances the antioxidant performance of the composite membranes [49]. However, when the additive is increased over 5% ($CeO_2$:$SiO_2$ 10%), agglomeration is believed to develop, as evidenced by mechanical strength tests, making the membrane more vulnerable than others.

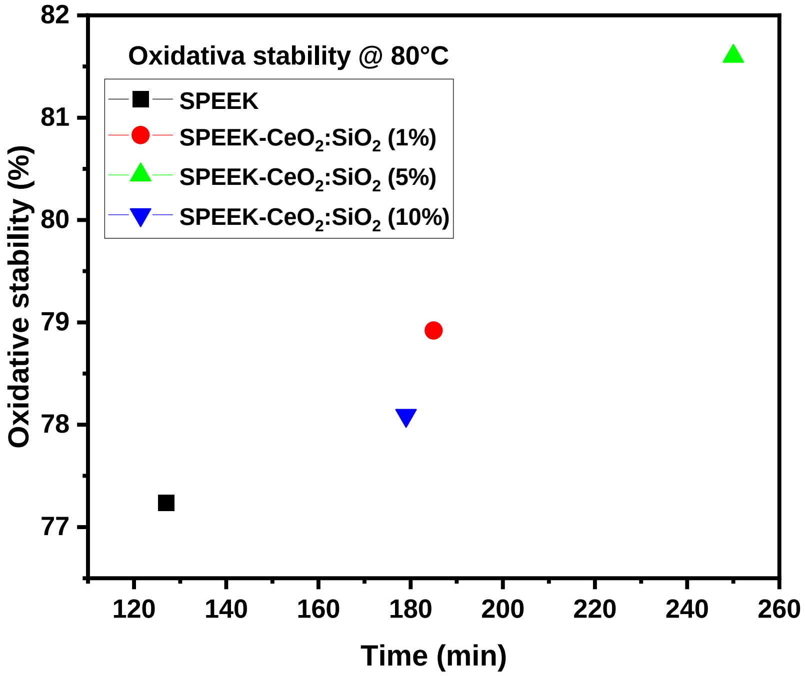

**Fig. 7.11:** Oxidative stability of SPEEK and SPEEK-$CeO_2$:$SiO_2$ composite membranes.

**Table 7.2:** Oxidative stability of SPEEK and SPEEK-$CeO_2$:$SiO_2$ composites at 80°C

| Table 1Sample | Time (min) | Oxidative stability @80°C (%) |
|---|---|---|
| SPEEK | 120 | 77.24 |
| SPEEK-$CeO_2$:$SiO_2$ (1%) | 185 | 78.92 |
| SPEEK-$Ceo_2$:$SiO_2$ (5%) | 250 | 81.6 |
| SPEEK-$Ceo_2$:$SiO_2$ (10%) | 179 | 78.09 |

### 7.7.6. Mechanical stability, IEC and Proton conductivity

The mechanical stability of SPEEK and SPEEK-$CeO_2$:$SiO_2$ composite membranes was evaluated. Young's Modulus, percentage elongation and tensile strength values of the SPEEK and SPEEK-$CeO_2$:$SiO_2$ composite membranes are presented in Table 7.4. Results show that the mechanical stability of the SPEEK membrane can be improved by the addition of $CeO_2$:$SiO_2$. Increase in the tensile strength of the SPEEK composite membrane is ascribed to the nano fillers which act as a reinforcing agent to support the polymeric matrix. Tensile strength of the SPEEK membrane increased from 829.85 kPa to 3144.07 kPa with addition of 5% $CeO_2$:$SiO_2$. Further increase in the $CeO_2$:$SiO_2$ weight percentage to 10% exhibited a decrease in the tensile strength value to 1192.20 kPa. Reason for the decrease in tensile at higher $CeO_2$:$SiO_2$ weight percentage is attributed to the aggregation of the $CeO_2$:$SO_2$ over the SPEEK polymer matrix. Chen et.al reported the similar trend in the tensile strength values with the addition of $CeO_2$:$SiO_2$ nano filler materials [50]. Stress-strain curve for the SPEEK and SPEEK-CeO2:$SiO_2$ composite membranes are presented in Fig. 7.12(a). From this curve it is seen that SPEEK-$CeO_2$:$SiO_2$ composite membrane exhibited a greater yielding up to 5% weight percentage compared to SPEEK membrane. SPEEK-$CeO_2$:$SiO_2$ (1%) membrane showed higher strain value compared to other membranes.

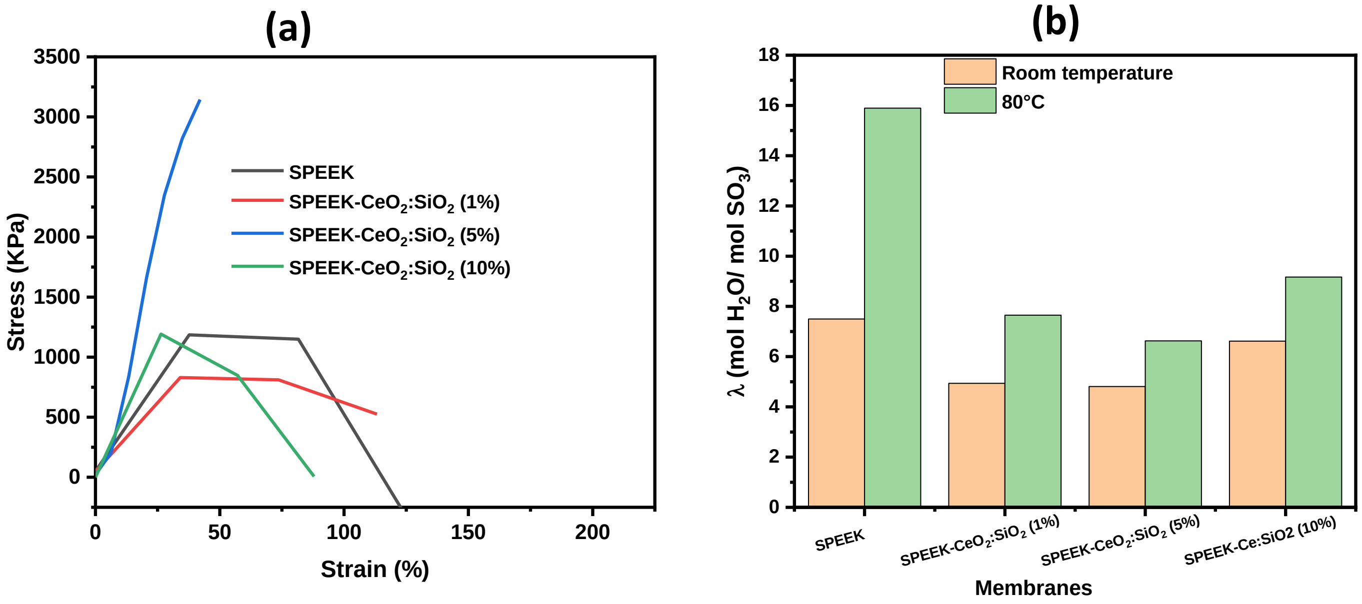

**Fig. 7.12:** (a) Stress-strain curves and (b) hydration degrees of SPEEK and SPEEK-$CeO_2$:$SiO_2$ composite membranes.

IEC, a crucial proton conductivity metric, was used to ascertain if the synthesised polymers contained ion-exchangeable groups. IEC and hydration degrees obtained with the synthesized membranes are given in Table 7.3 and Fig. 7.12(b), respectively. It was determined that the IEC of SPEEK increased with the addition of $CeO_2$: $SiO_2$ filler in the membrane matrix. Moreover, all the synthesized membranes had higher IECs compared to neat SPEEK. According to certain research conducted in the literature with silica sources, the rise in silicon sources in the membrane structure causes a drop in ion exchange groups, which in turn causes a decrease in IEC [51, 52]. However, contrary to this result was noted in this study with the inclusion of $CeO_2$:$SiO_2$ additive membranes. Adding $CeO_2$:$SiO_2$ to sulfonic groups improved membrane IECs. The IEC value for pure SPEEK was 2 meq/g, followed by 2.1 meq/g,3.0 meq/g and 2.6 meq/g for SPEEK-$CeO_2$:$SiO_2$ (1%), SPEEK-$CeO_2$:$SiO_2$ (5%) and SPEEK-$CeO_2$:$SiO_2$ (10%), respectively. The addition of 10% $CeO_2$:$SiO_2$ to the structure causes a decrease in active sulfonic acid groups per unit volume in the membrane matrix. However, the membranes' enhanced absorption capability may have resulted in the development of novel ion exchange groups. Eqn. (7.16) was used to determine the membranes' hydration numbers based on their water absorption capabilities and IEC values.

$$\lambda = \frac{WU \times 10}{IEC \times 18} \tag{7.16}$$

**Table 7. 3:** Mechanical stability, IEC, and Proton conductivity of SPEEK and SPEEK-$CeO_2$:$SiO_2$ composite membranes

| **Sample** | **Young modulus (KPa)** | **Tensile strength (KPa)** | **Elongation at break (%)** | **Proton conductivity (S/cm)** | **IEC ($meq.g^{-1}$)** |
|---|---|---|---|---|---|
| SPEEK | 3.72 | 1185.44 | 81.64 | $4.07 \times 10^{-3}$ | 2 |
| SPEEK-$CeO_2$:$SiO_2$ (1%) | 17.06 | 829.85 | 73.65 | $1.3 \times 10^{-2}$ | 2.1 |
| SPEEK-$CeO_2$:$SiO_2$ (5%) | 61.69 | 3144.07 | - | $3.7 \times 10^{-2}$ | 3 |
| SPEEK-$CeO_2$:$SiO_2$ (10%) | 14.13 | 1192.20 | 57.16 | $2.4 \times 10^{-2}$ | 2.6 |

The degree of hydration is a key factor influencing membrane performance. It is defined as the number of water molecules adsorbed per unit volume of -$SO_3H$ groups. In fuel cells, protons move aided by water molecules, so a higher degree of hydration is expected to enhance proton conductivity within the membrane structure. Among the composite membranes synthesized, the highest degree of hydration at both room temperature and 80°C was achieved with a membrane containing 10% $CeO_2$:$SiO_2$ additive. The hydration values for this membrane are nearly twice as high as those for the 1% $CeO_2$:$SiO_2$ and 5% $CeO_2$:$SiO_2$ membranes under the same conditions. Although the 5% $CeO_2$:$SiO_2$ membranes have more ion-exchangeable groups, it is evident that the degree of hydration plays a crucial role in proton transfer facilitated by water molecules.

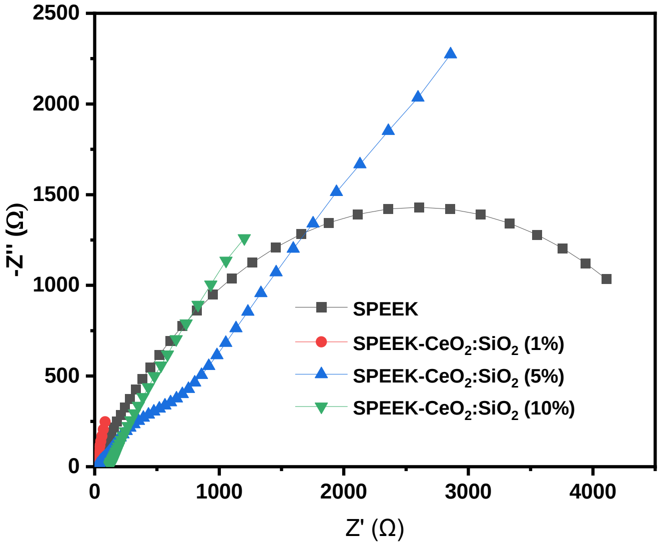

**Fig. 7.13 :** Nyquist plots of SPEEK and SPEEK-$CeO_2$:$SiO_2$ composite membranes.

Proton conductivity results and Nyquist diagrams are presented in Table 7.4 and Fig. 7.13, respectively. Incorporating the $CeO_2$:$SiO_2$ additive into the SPEEK membrane enhances the proton conductivity of the composite membranes. Colloidal silica in $CeO_2$:$SiO_2$ is known for its hygroscopic properties, allowing it to absorb water, which benefits the membrane's proton conductivity [53]. It was observed that the addition of 5% $CeO_2$:$SiO_2$ significantly improved proton conductivity compared to pristine SPEEK, which has a conductivity of 4.07 x $10^{-3}$ S/cm, as well as compared to other composite membranes. This improvement is largely due to the strong interaction between -$SO_3H$ groups and $SiO_2$ in $CeO_2$:$SiO_2$, which creates new proton conduction channels.

## 7.8. Conclusion

SPEEK-$CeO_2$:$SiO_2$ composite membranes with various weight percentages of $CeO_2$:$SiO_2$ were successfully fabricated using a solution casting method. The addition of $CeO_2$:$SiO_2$ nanofiller into the SPEEK matrix led to electrostatic interactions between the polymer matrix and the nanofiller, which effectively prevented the swelling of the membrane when hydrated. The formation of hydrogen bonds and strong electrostatic interactions between the membrane backbone and the nanofiller enhanced the thermal stability and thermomechanical strength of the composite, compared to the pristine SPEEK membrane. The radical scavenging properties of $CeO_2$:$SiO_2$

nanoparticles provided excellent oxidative stability and longer chemical durability for the SPEEK-$CeO_2$:$SiO_2$ (5%) membrane under acidic PEMFC conditions, outperforming the bare SPEEK membrane. This also demonstrated that the development of $CeO_2$ nanoparticles on $SiO_2$ nanoparticles resulted in a membrane with improved radical scavenging ability. The characteristics of SPEEK-$CeO_2$:$SiO_2$ membranes address several shortcomings associated with SPEEK-based membranes, including low mechanical strength and poor thermochemical properties. As a result, the composite membrane developed could be an ideal candidate for use in proton exchange membrane fuel cells (PEMFC) operating under low relative humidity (RH) conditions. This advancement may help avoid the costs associated with installing external humidifiers and the use of commercial Nafion membranes.

**C: Enhanced proton conductivity and oxidative stability of SPEEK-SZr: $SiO_2$ composite membrane for fuel cell application**

## 7.9. Introduction

Proton exchange membrane fuel cells (PEMFCs) are a promising technology in the energy sector due to their high efficiency, zero emissions, high power density, low operating temperatures, and quiet operation [3]. PEMFCs have demonstrated their ability to provide clean and efficient power for both vehicles and stationary applications. In a typical PEMFC, several components are crucial for its operation, including electrocatalysts, the proton exchange membrane, gas diffusion layers, and gas distributors [30, 54]. Among these, the proton exchange membrane plays a critical role and is the focus of extensive research aimed at improving its performance and durability while also reducing costs. Nafion is widely used as the commercial proton exchange membrane in PEMFCs because it has high proton conductivity when fully hydrated, along with good thermal, mechanical, and chemical stability. However, Nafion membranes can experience significant mechanical and chemical degradation due to various mechanisms that occur during fuel cell operation [21, 55]. Consequently, previous studies have concentrated on enhancing the durability of Nafion membranes. Furthermore, the main challenge with Nafion is its high cost and poor performance at elevated temperatures. Consequently, various research groups have been working on developing alternative low-cost proton exchange membranes (PEMs), such as sulfonated hydrocarbon membranes, which offer better thermal stability and reduced reactant gas crossover. However, these alternatives still need improvement in terms of conductivity, as well as chemical and mechanical stability [56-58].

Sulfonated poly(ether ether ketone) (SPEEK) has emerged as a leading candidate for commercial proton exchange membrane fuel cell (PEMFC) applications due to its low cost and adequate ionic conductivity, as well as its thermal, chemical, and mechanical stability [59]. Research efforts have focused on enhancing the proton conductivity and overall performance of SPEEK membranes, yielding promising results. Various additives, including silica, titania, heteropolyacids, and carbon-based materials, have been explored to improve the performance of SPEEK membranes. Additionally, metal oxide nanomaterials are increasingly recognized as effective fillers for fuel cell applications, thanks to their hygroscopic properties and ability to provide proton conductivity at acidic sites. Furthermore, modifications to these nanomaterials have significantly reduced fuel crossover and enhanced both mechanical and thermal properties [60-62].

In addition, modifying certain metal oxides like $ZrO_2$, $TiO_2$, and $Fe_2O_3$ with sulfate produces solid super acids. For instance, sulfated zirconia, which has a Hammett acid strength ($H_0$) of −16.03, exhibits high conductivity ($2.3 \times 10^{-1}$ $S.cm^{-1}$ at temperatures ranging from 105 to 135 °C), excellent thermal stability, relatively low synthesis costs, and low reducibility, making it particularly suitable for use in Proton exchange membrane fuel cells (PEMFCs) [63]. Moreover, the thermal stability of zirconia can be significantly enhanced by incorporating a second metal oxide. Mixed oxides often show increased acidity and higher thermal stability compared to their single oxide counterparts. Research has demonstrated that binary mixed oxides, especially $ZrO_2$-$SiO_2$, have smaller particle sizes than their individual oxide components due to different nucleation processes, resulting in a larger surface area for the nanoparticles [64, 65]. Additionally, the mechanical and thermal strength of this binary oxide makes it an attractive option for improving the physicochemical properties of Sulfonated poly(ether ether ketone) (SPEEK). However, a high loading of nanomaterials in the polymer matrix can lead to nanoparticle agglomeration, which weakens the mechanical properties [66]. Furthermore, excessive substitution can cause significant swelling and impair the membrane's properties.

Despite recognizing the advantages of $ZrO_2$-$SiO_2$, particularly in its sulfated form, there is currently no study addressing the incorporation of sulfated zirconia-silica ($SZr:SiO_2$)

nanoparticles into a SPEEK-based matrix as a prospective alternative for PEMFC applications at moderate temperatures. In this context, we propose the development of a novel, low-cost nanocomposite SPEEK as an alternative to the Nafion membrane, aimed at enhancing chemical and thermal stability as well as increasing proton conductivity.

## 7.10. EXPERIMENTAL

### 7.10.1. Materials

PEEK powder (450 G) was purchased from Victrex, sodium hydroxide (Merck), sulfuric acid (Merck), zirconium acetylacetonate (Merck), N, N-Dimethyl sulfoxide (DMSO) (Merck), methanol (Merck), all materials were obtained and were used as received.

### 7.10.2. Sulfonation of PEEK

Sulfonated PEEK was obtained by the technique that was reported by Somayeh et.al with some modification. 10 g of PEEK was dissolved in 100 ml (98% (wt.%) sulfuric acid in a glass beaker. The obtained reddish-brown solution was transferred to beaker containing ice cold water under slow agitation to stop the sulfonation reaction. Then, the resulted white fibres were washed several times by distilled water to eliminate the excess sulfuric acid and until the rinsed water attain the pH value of 7. Subsequently, the obtained material was dried at 80 °C overnight. Finally, material was cooled and stored in a container.

### 7.10.3. Preparation of SPEEK-SZr: $SiO_2$ nanocomposite membranes

SPEEK-based composite membranes containing varying amounts of SZr:$SiO_2$ were prepared by solution casting. In a typical procedure, PEEK powder (1g) was dissolved in DMSO (15 ml) and stirred until all the SPEEK was dissolved to form a clear solution. SZr:$SiO_2$ powder was slowly into the beaker containing SPEEK solution which was stirred until the powder was fully dispersed in the solution. The resultant mixture was cast in a glass casting tray and heated to 80 °C overnight. The tray was then immersed under DI water for smooth peeling of the polymer from the tray. The solvent was removed by heating at 80 °C under vacuum for 2 hours.

### 7.10.4. Characterization of SPEEK-SZr: $SiO_2$ membranes

#### 7.10.4.1. TGA, SEM and FTIR

FT-IR spectra of the membrane in the wavenumber range of 4000–450cm$^{-1}$ were obtained on a Bruker Fourier transform infrared spectroscopy (FTIR). SEM-Joel scanning electron microscopy (SEM, JMS-6010 Plus) was used to examine the surface morphologies of SPEEK and SPEEK-SZr:$SiO_2$ composite membranes. Thermal properties and characteristics were studied using PerkinElmer thermogravimetric analyser (TGA) under air and nitrogen flow, and operating at a heating rate of 10 °C/min from 35 °C to 900 °C.

#### 7.10.4.2. Tensile test

A uniaxial testing device was used to record the nanocomposite membranes' uniaxial mechanical characteristics. Before testing, the samples' length and width were measured with a ruler and noted. The membrane samples testing area measured 2 mm by 7 mm. A CellScale Ustretch device was used to assess the tensile strength of SPEEK and SPEEK-SZr:$SiO_2$ composite membranes at 25 °C.

#### 7.10.4.3. Water uptake (WU) and swelling ratio (SR)

We investigated water uptake (WU) and dimensions swelling/swelling ratio (SR) at temperatures ranging from 25 to 80 °C. To assess water uptake, a membrane was equilibrated with deionized water at the appropriate temperature for 8 hours before being weighed immediately after surface water removal. The membrane was vacuum dried for 2 hours at 60 °C to achieve a consistent weight ($W_{dry}$). The water uptake (WU) of the membrane was computed as follows:

$$\mathrm{WU} = \frac{(\mathrm{W_{wet}} - \mathrm{W_{dry}})}{\mathrm{W_{dry}}} \times 100 \qquad \textbf{(7.17)}$$

The measurement of membrane dimensional swelling proceeded similarly. Firstly, the membrane was cut into a strip with predetermined dimensions (2cm in length and 1 cm in width) and equilibrated in water at the target temperature for 8 hours to obtain the wet length (Lwet). The sample was then dried in vacuum at 60 °C to yield the dry length (Ldry). The extent of water swelling (SR) of the membrane was calculated as:

$$\mathrm{SR} = \frac{(\mathrm{L_{wet}} - \mathrm{L_{dry}})}{\mathrm{L_{dry}}} \times 100 \qquad \textbf{(7.18)}$$

### 7.10.4.4. Ion exchange capacity (IEC)

Ion exchange capacity (IEC) of SPEEK and SPEEK-SZr:$SiO_2$ composite membrane were determined by titration method:

$$\mathrm{IEC} = \frac{C_{NaOH}V_{NaOH}}{m_{dry}} \qquad \textbf{(7.19)}$$

Where $V_{NaOH}$ is the titrated volume of sodium hydroxide (NaOH) and $m_{dry}$ is the weight of the dry membranes.

### 7.10.4.5. Oxidative stability

The oxidative stability of SPEEK and SPEEK-SZr:$SiO_2$ composite membranes was investigated using Fenton's test. Fenton's reagent was prepared by creating a solution containing 3 vol% hydrogen peroxide and 3 ppm of $Fe^{2+}$ ions. The weight of each dried membrane was measured before immersing it in the Fenton's reagent at various temperatures. The membranes were weighed at regular intervals of 10 minutes, and the change in weight was used to assess the oxidative stability of the membranes, as indicated in Eqn. (7.20).

$$\text{Oxidative stability (\%)} = \frac{W_{dry}}{W_{initial}} \times 100 \qquad \textbf{(7.20)}$$

Where: $W_{dry}$ is the dry weight of the membrane after Fenton’s test (g) and $W_{initia}$l is the initial dry weight of the membrane (g).

### 7.10.4.6. Proton Conductivity measurement

Proton conductivities of the composite membranes were measured by AC impedance spectroscopy using an electrochemical workstation (Autolab PGSTAT302N, Switzerland) in the frequency range of 1 MHz to 100 Hz with an amplitude of 5 mV. Prior to testing, all membranes were hydrated by immersion in deionized water for 24 hours at room temperature. A sample of the pre-hydrated membrane was wrapped around a graphite electrode, then the tip of the covered electrode was immersed in

$H_2SO_4$ 0.5M during proton conductivity measurement. The proton conductivity (σ) was calculated as follows:

$$\sigma = \frac{\mathrm{l}}{\mathrm{RA}} \tag{7.21}$$

where L, refers to the thickness of the membrane (2.16 cm), R=the resistance of the membrane (Ω) and A=cross-sectional area ($cm^2$).

### 7.10.5. Preparation of MEA and evaluation of single-cell performance

The performance of the resulting membrane was evaluated in a PEMFC single cell. The electrode and gas diffusion layer (GDL) were created using a brushing method. The palladium catalyst (Pd/C, 10%) was mixed with isopropanol and deionized (DI) water in a volumetric ratio of 6:4 (catalyst to solution) to prepare the ink slurries. Next, a 5 wt.% SPEEK solution was used as a binder at a ratio of 6:2 (catalyst to SPEEK solution) and sonicated for 40 minutes. The GDL was prepared by brushing the slurry onto carbon paper with a palladium loading of 0.2 mg. The coated materials were then dried at 60 °C under vacuum for 5 hours.

Single cell experiments were performed by measuring the voltage–current density curves, placing the MEA in a commercial fuel cell hardware. Hydrogen and oxygen gas were fed to the anode and the cathode, respectively. A voltage of 0.6 V was applied to the cell for 5 minutes prior to each polarization curve in order to activate the electrocatalysts.

## 7.11. Results and discussion

### 7.11.1. FTIR analysis

The FTIR spectra of the SPEEK and SPEEK/SZr:$SiO_2$ membranes are shown in Fig. 7.14a. By altering charge inconsistencies, the bidentate sulfate group that exhibited the absorption band at 1400 $cm^{-1}$ increased the acidity [67]. The characteristic of S═O in ─$SO_3H$ groups may be shown by the peaks at 1211 and 897 $cm^{-1}$. The interaction of sulfated groups in nanoparticles with sulfonated groups in the polymer matrix results in decreased intensity peaks in this region for the nanocomposite membrane [68]. Furthermore, the signal at 1076 $cm^{-1}$ was linked to the presence of O═S═O in a sulfonated group [69]. As a result, the sulfonation procedure in the PEEK polymer appears to have been completed effectively. The peak at 1639 $cm^{-1}$ confirms the presence of a ─OH bond with the sulfate group on the nanoparticle's surface [70]. The broad peak observed between 3660 and 3116 cm$^{-1}$ suggests the presence of hydroxyl groups in the diblock at one terminal. This indicates the absorption of water due to interaction with the sulfonic group. Additionally, the presence of Si-O and Zr-O bonds is expected to be confirmed by the peaks found between 900 and 400 cm$^{-1}$. Therefore, based on the FTIR results and previous reports, the chemical structure of the $SZr:SiO_2$ nanoparticle can be illustrated in Fig. 7.14b.

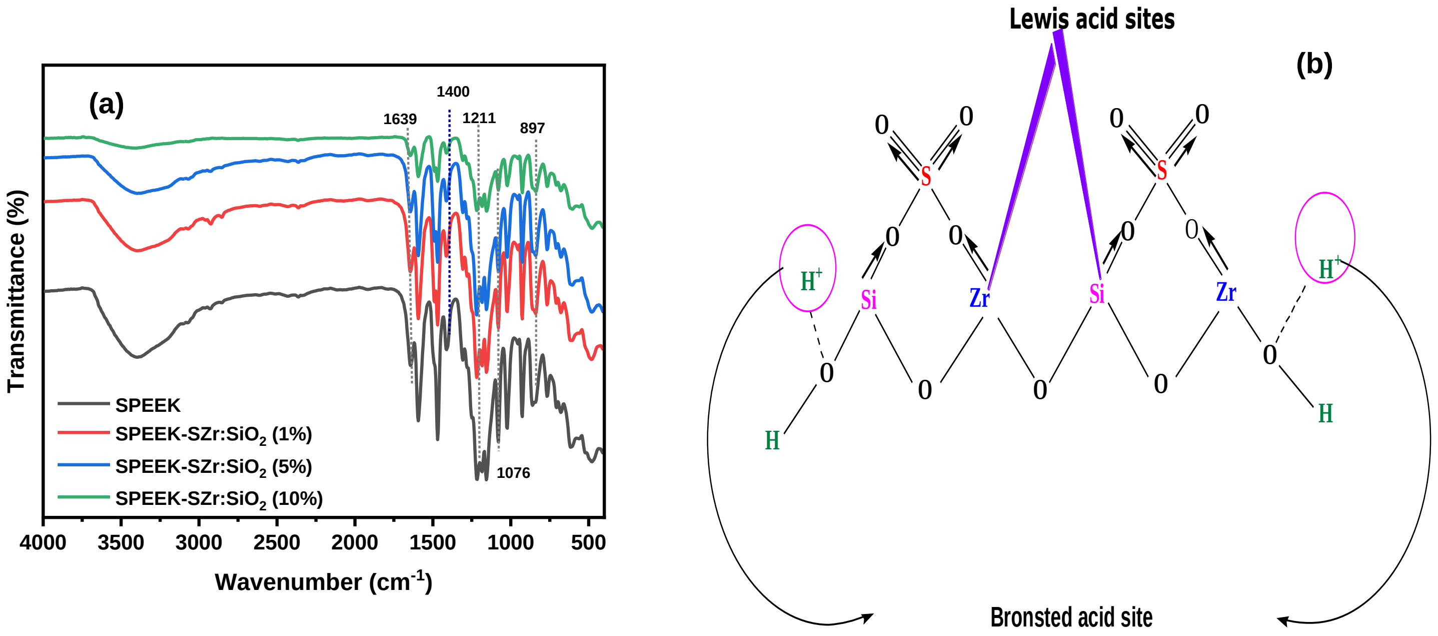

**Fig. 7.14:** (a) FTIR spectra of SPEEK and SPEEK-$SZr:SiO_2$ nanocomposite membranes, (b) proposed chemical structure of the synthesised $SZr:SiO_2$ nanoparticle.

### 7.11.2. TGA analysis

The thermal stability curves for SPEEK and SSPEEK-$SZr:SiO_2$ composite membranes are shown in Fig. 7.15. The thermogravimetric analysis (TGA) curves reveal three distinct regions of weight loss for the membranes. The initial weight loss, which is approximately 5-6% for all samples and occurs below 200 °C, is attributed to the removal of water and solvents. The second phase of weight loss, which takes place up to 400 °C, is due to the decomposition of sulfonic acid groups. Although both membranes contain a relatively similar number of sulfonic acid groups, it was observed that some SPEEK/SZr:$SiO_2$ membranes lose more weight compared to plain SPEEK. This is because the nanocomposite membrane not only loses sulfonic acid groups but also more adsorbed water, owing to the hygroscopic nature of the SZr:$SiO_2$ nanoparticles. Mossayebi et al. [71] reported that the synthesized sulfated zirconia loses its adsorbed water up to 300 °C, while the sulfate groups begin to decompose above 600 °C. The final weight loss, occurring above 400 °C, corresponds to the degradation of the primary polymer chain. As depicted in Fig.7.15, the nanocomposite membrane exhibits less weight loss compared to the plain SPEEK membrane in the last phase of the analysis. This suggests that the formation of hydrogen bonds between the ─OH groups of SZr:$SiO_2$ and the sulfonic acid moieties in the polymer matrix enhances the thermal resistance of the nanocomposite membrane. Similar enhancements in thermal resistance of membranes through the introduction of metal oxides have been reported in earlier reports by other researchers [72, 73].

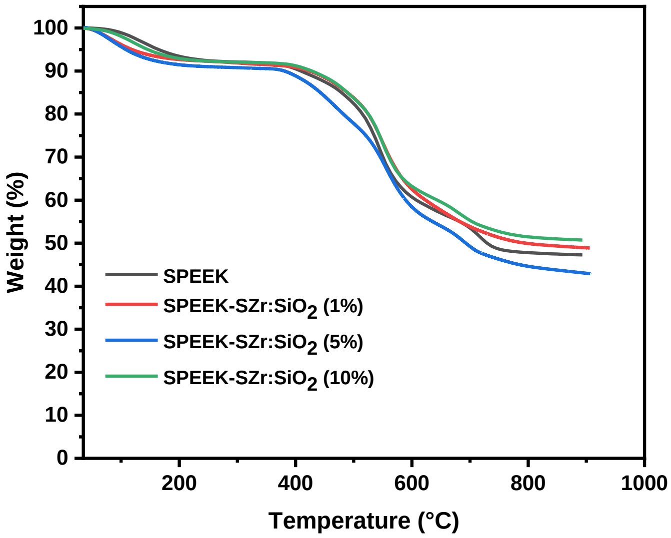

**Fig. 7.15:** Thermal stability curves (TGA) of SPEEK and SPEEK-SZr:$SiO_2$ nanocomposites.

### 7.11.3. SEM analysis

Fig. 7.16 (a-d) shows SEM surface morphologies of neat SPEEK and SPEEK-SZr:$SiO_2$ composite membranes. Fig. 7.16(a) shows the neat SPEEK membrane, which is smooth with no visible cracks. This phenomenon demonstrated that the structure and morphology of the PEMs remained intact before and after the addition of fillers. The SEM image of SPEEK-SZr:$SiO_2$ (1%) and SPEEK-SZr:$SiO_2$ (5%) composite membranes in Fig. 7.16(b-c) shows SZr:$SiO_2$ nanoparticles are well distributed within the membrane matrix with less agglomeration. These results shows that SZr:$SiO_2$ nanoparticles within the membrane are uniform in shape. Fig. 7.16(d) shows the addition of SZr:$SiO_2$ (10%) nanoparticles, which are well distributed within the membrane matrix but with less visible when compared to the lower percentages added in the membrane.

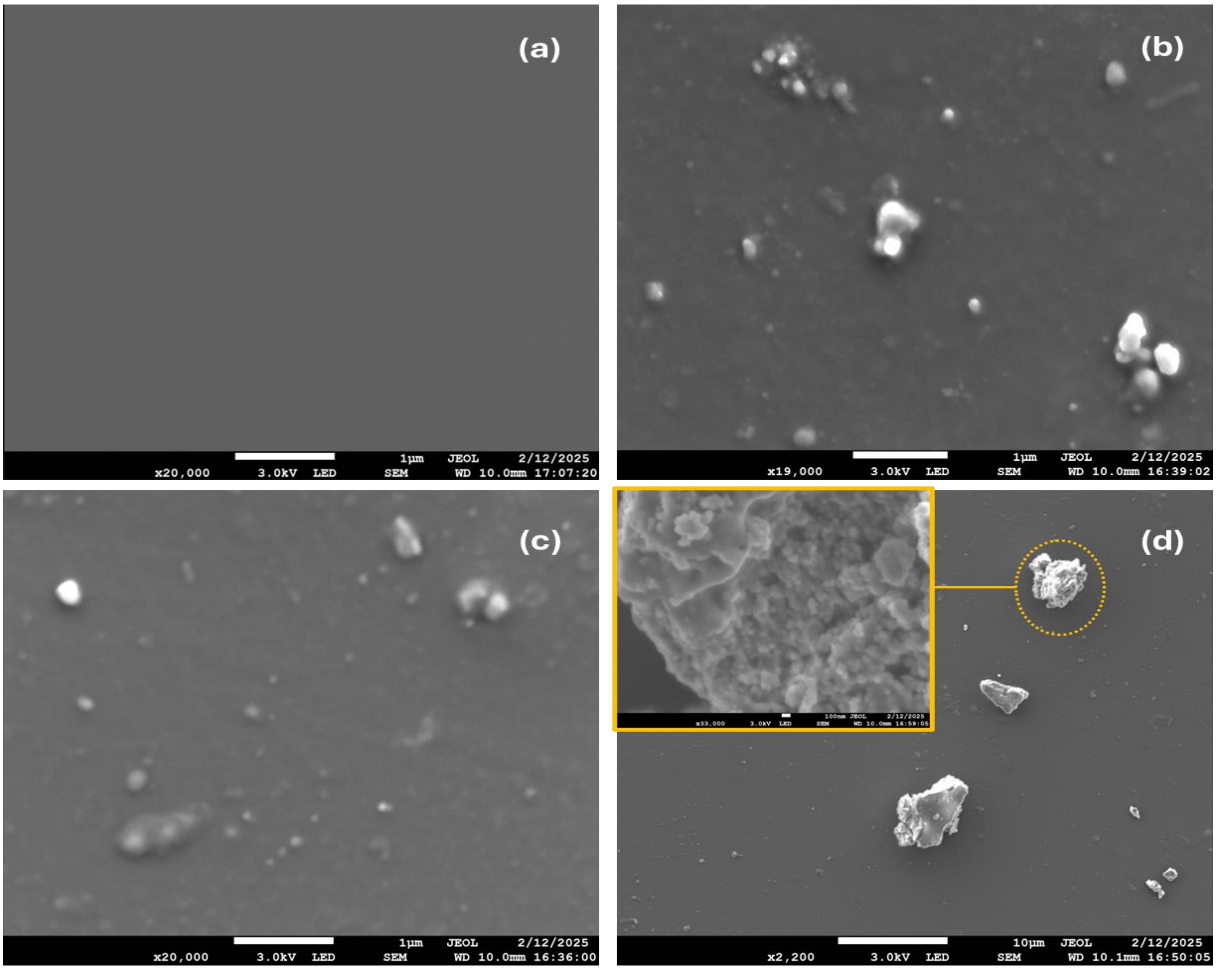

**Fig. 7. 16:** SEM analysis of (a) SPEEK, (b) SPEEK-SZr:$SiO_2$ 1%, (c) SPEEK-SZr:$SiO_2$ 5%, and (d) SPEEK-SZr:$SiO_2$ 10% composite membranes.

### 7.11.4. Mechanical properties

The membrane's mechanical properties were assessed using a tensile test, as shown in Fig. 7.17(a-b) and Table 7.4. As shown in Table 7.5, the tensile strength of the pure membrane was measured at 1185.44 KPa, with a Young's modulus of 30.10 KPa.

After incorporating SZr:$SiO_2$ fillers, both the tensile strength and Young's modulus of the mixed proton exchange membranes (PEMs) significantly improved. The highest values were observed in the membrane with 1% SZr:$SiO_2$, which reached a tensile strength of 2151.29 KPa and a Young's modulus of 49.54 KPa. This enhancement is attributed to the formation of a hydrogen bond network due to the packed –$SO_3H$ groups. Conversely, as the amount of SZr:$SiO_2$ increased, the elongation at break of the composite membrane exhibited a gradual decline. This decrease is likely because SZr:$SiO_2$ is an inorganic filler, which restricts the free movement of the SPEEK backbone and increases the rigidity of the membrane [74]. Furthermore, it can be seen in that the performance metrics for membranes with SZr:$SiO_2$ at 5% and 10% showed a sharp decline, falling below those of the pure SPEEK PEM. This deterioration is attributed to excessive filler content, which leads to aggregation and disrupts the continuity of the polymer microstructure.

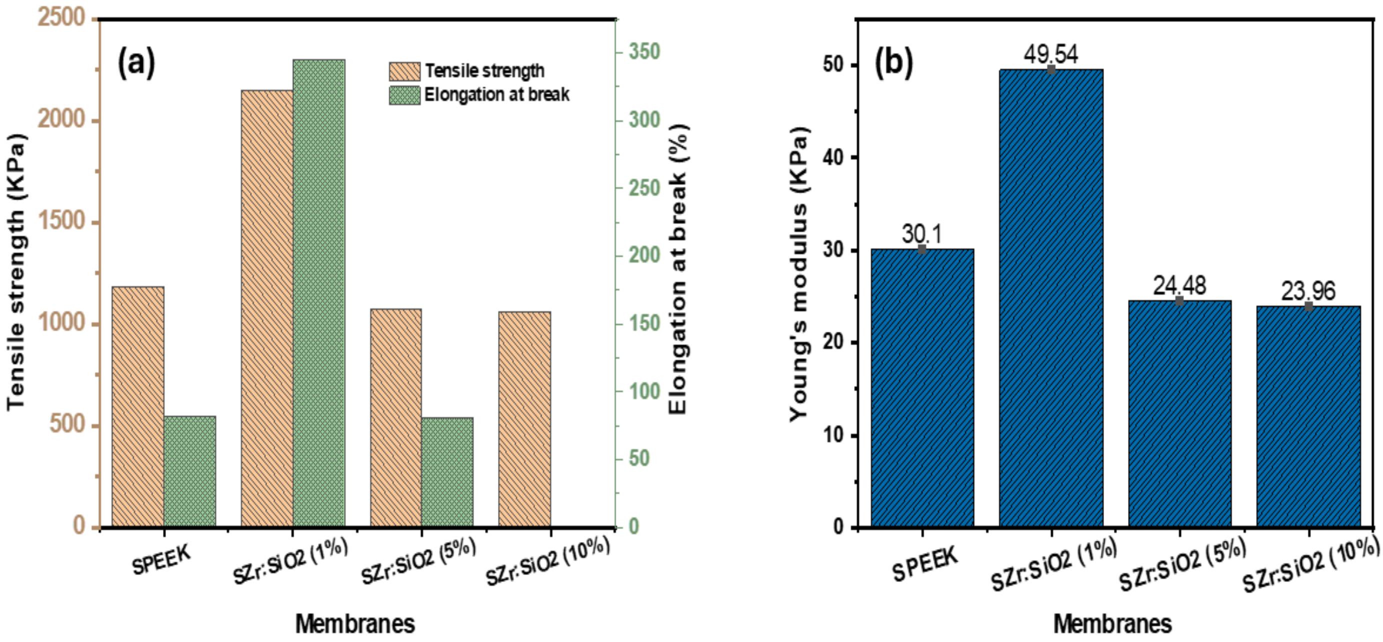

**Fig.7.17:** (a)Tensile strength and (b) Young’s modulus of SPEEK and SPEEK-SZr:$SiO_2$ nanocomposite membranes.

**Table 7.4:** Mechanical properties and IEC of SPEEK and SPEEK-SZr:$SiO_2$ composite membranes

| **Sample** | **Young modulus (kPa)** | **Tensile strength (kPa)** | **Elongation at break (%)** | **IEC (meq/g)** |
|---|---|---|---|---|
| SPEEK | 30.10 | 1185.44 | 81.64 | 2 |
| SPEEK-SZr:$SiO_2$ (1%) | 49.54 | 2151.29 | 345 | 3.1 |
| SPEEK-SZR:$SiO_2$(5%) | 24.48 | 1073.64 | 80.65 | 2.2 |
| SPEEK-SZr:$SiO_2$(10%) | 23.96 | 1063.01 | - | 2.6 |

### 7.11.5. Oxidative stability

During fuel cell operation, proton exchange membranes (PEMs) are susceptible to attacks from hydroxyl (HO·) and perhydroxyl (HOO·) free radicals, which can lead to degradation and breakage of the membrane. The anti-oxidation capacity of the membrane was assessed by measuring the residual mass of the membrane after treatment at 80 °C in Fenton's reagent for 5 hours. As shown in Fig. 7.18, in the redox environment simulated by Fenton's reagent, the SPEEK polymer demonstrated an oxidation stability of 77.24%. The SPEEK membrane began to develop pinholes at the 120-minute mark as free radicals penetrated the polymer matrix, leading to degradation. In contrast, SPEEK-SZr:$SiO_2$ (1%) composite membranes exhibited exceptional antioxidant properties, with a mass retention of 82.87%. This characteristic is crucial for the long-term use of fuel cells. The orderly arrangement of molecules in the composite membrane helps inhibit degradation, allowing it to maintain excellent oxidation stability.

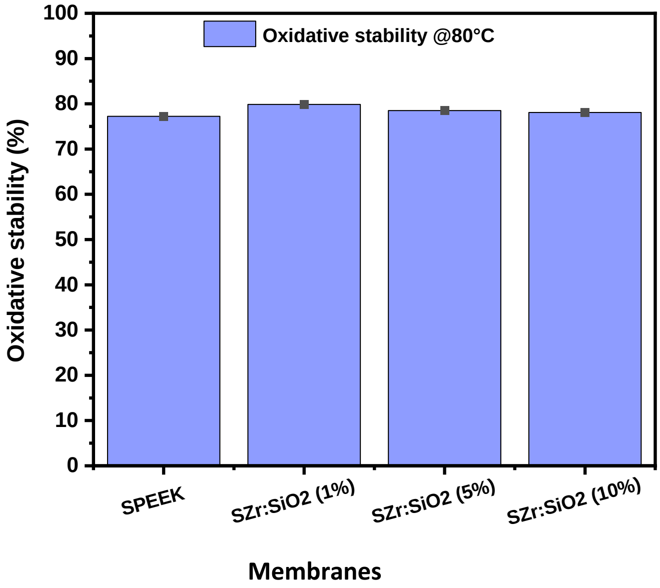

**Fig. 7.18:** Oxidative stability of SPEEK and SPEEK-SZr:$SiO_2$ nanocomposite membranes.

### 7.11.6. Water uptake, swelling ratio and IEC of membranes.

Table 7.6 presents the specific values for water uptake (WU) and swelling ratio (SR) of both pure and hybrid membranes at low and high temperatures, with the trends illustrated in Fig. 7.19(a-b). According to the presented results, the pristine SPEEK membrane exhibited the lowest water uptake and swelling ratio. At 25 °C, the WU was 27%, and the swelling ratio was 8.03%. When the temperature increased to 80 °C, the WU rose to 57.20%, and the SR increased to 20.24%. After the addition of fillers, the WU and SR of the hybrid polymer electrolyte membranes (PEMs) showed varying degrees of increase. The most significant enhancement was observed in the SZr:$SiO_2$ (10%) membrane. At 25 °C, this membrane had a WU of 76.20% and a swelling ratio of 16.07%. At 80 °C, the WU was 60.20%, while the SR reached 42.64%. This improvement is attributed to the hydrophilic nature of the sulfonic acid groups in the fillers, which enhance water absorption [75]. It is evident that both the WU and SR increased significantly with rising temperatures. As the temperature increased, the motion of the polymer chains accelerated, resulting in a larger free volume and greater water absorption capacity of the membranes [76].

Table 7.5 clearly presents the Ion Exchange Capacity (IEC) for both SPEEK and the SPEEK-SZr:$SiO_2$ composite membranes. It indicates that increasing the SZr:$SiO_2$ ratio to 1% raised the IEC values of the membranes from 2 meq/g to 3.1 meq/g. The SZr:$SiO_2$ contributed hydrogen protons by incorporating sulfonic acid groups. However, the decrease in IEC values observed at 5% and 10% SZr:$SiO_2$ ratios was due to the formation of agglomerations within the SPEEK-SZr:$SiO_2$ composite. These agglomerations obstructed the transit pathways for water molecules, making the separation of $H^+$ more challenging.

**Table 7.5**: Proton conductivity, Water uptake and Swelling ratio of the membranes.

| **Sample** | **Proton conductivity (S/cm)** | **Water Uptake (WU) (%)** | | | **Swelling ratio (SR) (%)** | | |
|---|---|---|---|---|---|---|---|
| | | **25 °C** | **40°C** | **80°C** | **25°C** | **40°C** | **80°C** |
| SPEEK | 0.00407 | 27 | 43.9 | 57.2 | 8 | 16 | 20 |
| SPEEK-SZr:$SiO_2$ (1%) | 0.087 | 39.7 | 55 | 58.8 | 5 | 19.5 | 22 |
| SPEEK-SZr:$SiO_2$ (5%) | 0.076 | 45.9 | 56.23 | 59.77 | 8.5 | 20.9 | 24.8 |
| SPEEK-SZr:$SiO_2$ (10%) | 0.038 | 50.13 | 57.46 | 60.2 | 16.07 | 21.38 | 42.64 |

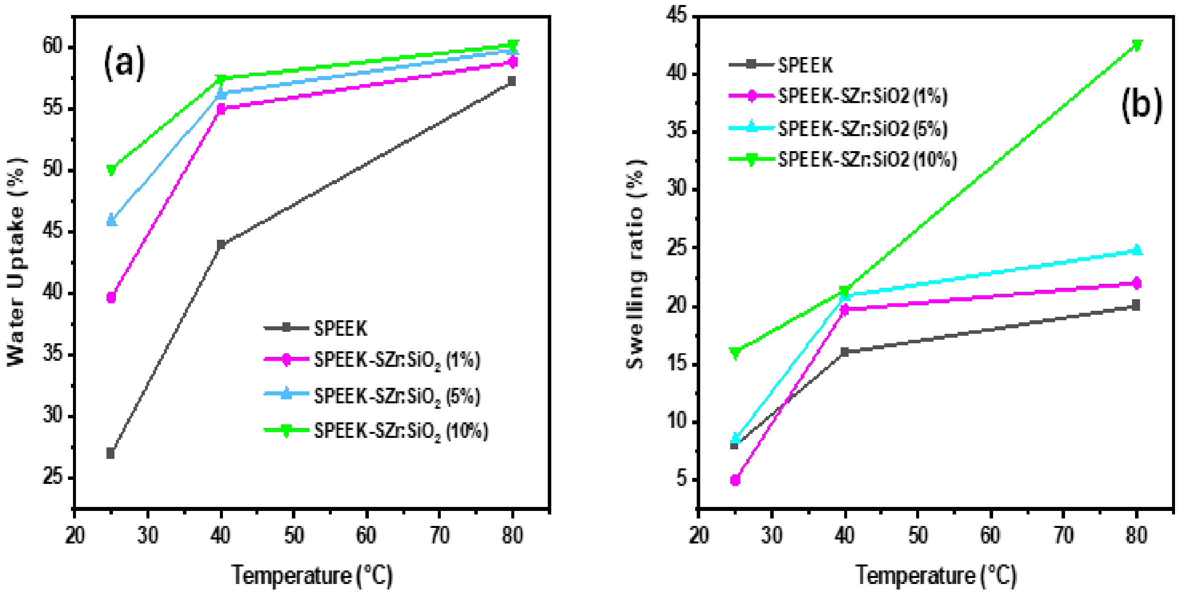

**Fig. 7.19:** (a) Water uptake and (b) Swelling ratios of SPEEK and SPEEK-SZr:$SiO_2$ composite membranes.

### 7.11.7. Proton conductivity

Fig. 7.20 summarizes the proton conductivity of pristine SPEEK and SPEEK-SZr:$SiO_2$ membranes at ambient temperature. It was not difficult to determine that the proton conductivity of the composite membrane after adding SZr:$SiO_2$ was much higher than that of the pure membrane. This was one of the primary reasons why the sulfonic acid group on SZr supplied more proton transfer sites than the pure membrane. Furthermore, the proton conductivity of the SZr:$SiO_2$ (5 and 10%) membrane has decreased. This could be due to the inclusion of too much filler, which caused aggregation and disrupted the continuity of the proton transport channel.

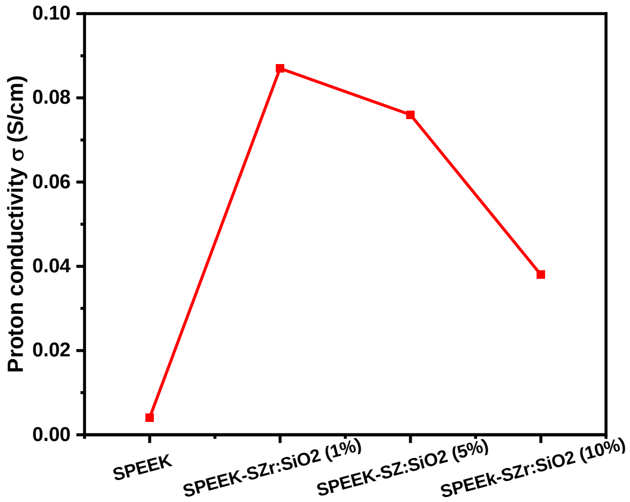

**Fig. 7.20:** Proton conductivity of SPEEK and SPEEK-SZr:$SiO_2$ composite membranes.

## 7.12. Fuel cell performance

Single cell performance. Proton conductivity is strongly linked to fuel cell performance [77]. To provide a more objective evaluation of PEM performance, all produced membranes with high proton conductivity were tested and compared to that of pristine SPEEK. The curves of the test results are displayed in Fig. 7.21 (a-b). The suitability of the developed blend membranes for fuel cell applications is investigated using a single cell investigation. The power performance and voltage drop of the membranes were assessed as a function of current density while the cell operated at ambient temperature. As shown in Fig. 7.21(a), all produced membranes had an open circuit voltage greater than 0.9 V, indicating that they have good $H_2$ and $O_2$ gas permeation resistance. The composites containing SPEEK-SZr:$SiO_2$ (1%) sample attained a peak power density of 54.69 mW/cm$^2$ with the highest current density of 1370.77 mA/cm$^2$, while the PEMFC containing SPEEK-$CeO_2$:ZrO2 (10%) and SPEEK-$CeO_2$:$SiO_2$ (5%) samples exhibited a peak power density of 40.96 and 38.94 mW/cm$^{-2}$ with the highest current density of 1297.17 and 1167.74, respectively. SPEEK-$CeO_2$:$SiO_2$ (5%) samples had the lowest current and power densities. This was mostly owing to the excessive inclusion of Ce:Si, which caused an aggregation phenomena and hindered the proton transport pathway. SPEEK-SZr:$SiO_2$ (1%) membrane, on the other hand, performs better due to increased proton conductivity achieved by a higher $SO_3H$ group per unit volume ratio [78]. In conclusion, the above investigations showed that the

SPEEK-SZr:$SiO_2$ (1%) membrane has good potential for PEMFCs. Table 7.6 summarizes several block copolymer performance results reported in the literature for comparison with the current study.

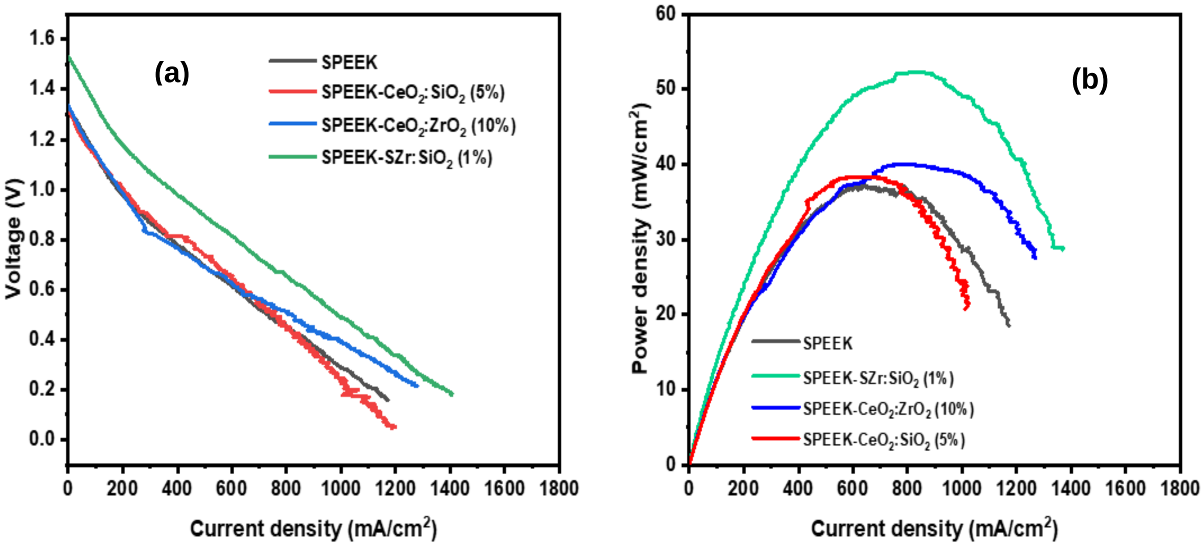

**Fig. 7.21:** (a) I-V and (b) Power density curves of SPEEK-$CeO_2$:$SiO_2$ (5%), SPEEK-$CeO_2$:$ZrO_2$ (10%) and SPEEK-SZr:$SiO_2$ (1%) composite membranes.

**Table 7.6:** Power densities of different SPEEK-based composite membranes.

| Material | Temperature °C | Power density mW/cm$^2$ | References |
|---|---|---|---|
| SPEEK-Z3 | 100 | 49.33 | [79] |
| SPEEK/SPDF-co-HFP | 30 | 43.02 | [80] |
| SPEEK-PDA/PEI@PVDF | 80 | 54.3 | [13] |
| SPEEK/PSf -8% | - | 51 | [81] |
| SPEEK | 30 | 35.20 | This work |
| SPEEK-$CeO_2$:$SiO_2$ (5%) | 30 | 38.94 | This work |

| | | | |
|---|---|---|---|
| SPEEK-$CeO_2$:$ZrO_2$ (10%) | 30 | 40.96 | This work |
| SPEEK-SZr-$SiO_2$ (1%) | 30 | 54.69 | This work |

### 7.12.1 Durability test

The OCV durability test was conducted on proton exchange membranes (PEMs) to better understand their durability. The changes in open circuit voltage (OCV) are illustrated in Fig. 7.22. The OCV decay rates observed were 0.151 V/h for SPEEK-$CeO_2$:$SiO_2$ (5%), 0.155 V/h for SPEEK-$CeO_2$:$ZrO_2$ (10%), and 0.157 V/h for SPEEK-SZr:$SiO_2$ (1%). These results indicate that the inclusion of SZr:$SiO_2$ helps mitigate membrane degradation caused by free radical attacks on PEMs, thereby extending the service life of proton exchange membrane fuel cells (PEMFCs).

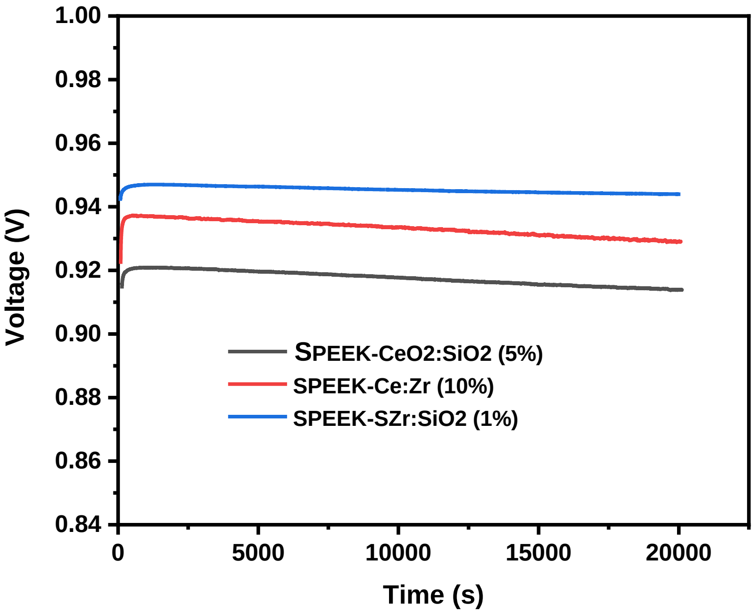

**Fig. 7.22:** The durability operation of SPEEK-$CeO_2$:$SiO_2$ (5%), SPEEK-$CeO_2$:$ZrO_2$ (10%) and SPEEK-SZr:$SiO_2$ (1%).

## 7.13. Conclusion

This study investigates the effects of introducing sulfated binary metal mixed oxide (SZr:$SiO_2$) into the SPEEK polymer matrix for application in proton exchange membrane fuel cells (PEMFCs). The research covers everything from the synthesis of the nanoparticles to the performance tests of single cells. To our knowledge, although the benefits of sulfated binary metal oxides, particularly $ZrO_2$-$SiO_2$, are recognized, there has been no prior research on incorporating SZr:$SiO_2$ nanoparticles into the SPEEK matrix as a potential candidate for PEMFCs operating at moderate temperatures. The objective of this study was to achieve simultaneous improvements in both proton conductivity and chemical stability. Different amounts of SZr:$SiO_2$ were added to a SPEEK polymer matrix to create a series of composite membranes. It was evident that nearly all properties of the hybrid membranes improved compared to the pure membrane after the filler was added. Among these, the SPEEK-SZr:$SiO_2$ (1%) membrane stood out as the most representative. In terms of oxidation stability, the SPEEK-SZr:$SiO_2$ (1%) membrane demonstrated the highest antioxidant stability at 82.87%, surpassing the pure polymer matrix membrane, which had a stability of 77.24%. Additionally, the SPEEK-SZr:$SiO_2$ (1%) membrane exhibited the highest proton conductivity of 0.087 S/cm compared to the other composites tested under the same conditions. For assessing fuel cell performance, all composite membranes that displayed the highest proton conductivity within their respective groups were selected for testing. The SPEEK-SZr:$SiO_2$ (1%) membrane also performed exceptionally well, achieving a current density of 1370.77 mA/cm$^2$ and a peak power density of 54.9 mW/cm$^{-2}$. Considering all aspects, the SPEEK-SZr:$SiO_2$ (1%) membrane shows great potential for applications in polymer electrolyte membrane fuel cells (PEMFCs).

## 7.14. References

1. Okonkwo, P.C., O.O. Ige, P.C. Uzoma, W. Emori, A. Benamor, and A.M. Abdullah, *Platinum degradation mechanisms in proton exchange membrane fuel cell (PEMFC) system: A review.* International journal of hydrogen energy, 2021. **46**(29): p. 15850-15865.
2. Jiao, K., J. Xuan, Q. Du, Z. Bao, B. Xie, B. Wang, Y. Zhao, L. Fan, H. Wang, and Z. Hou, *Designing the next generation of proton-exchange membrane fuel cells.* Nature, 2021. **595**(7867): p. 361-369.

3. Tellez-Cruz, M.M., J. Escorihuela, O. Solorza-Feria, and V. Compañ, *Proton exchange membrane fuel cells (PEMFCs): advances and challenges.* Polymers, 2021. **13**(18): p. 3064.
4. Maiti, T.K., J. Singh, P. Dixit, J. Majhi, S. Bhushan, A. Bandyopadhyay, and S. Chattopadhyay, *Advances in perfluorosulfonic acid-based proton exchange membranes for fuel cell applications: A review.* Chemical Engineering Journal Advances, 2022. **12**: p. 100372.
5. Zeng, L., X. Lu, C. Yuan, W. Yuan, K. Chen, J. Guo, X. Zhang, J. Wang, Q. Liao, and Z. Wei, *Self‐enhancement of perfluorinated sulfonic acid proton exchange membrane with its own nanofibers.* Advanced Materials, 2024. **36**(15): p. 2305711.
6. Ying, J., T. Liu, Y. Wang, M. Guo, Q. Shen, Y. Lin, J. Yu, and Z. Yu, *Perspectives on membrane development for high temperature proton exchange membrane fuel cells.* Energy & Fuels, 2024. **38**(8): p. 6613-6643.
7. Xu, M., H. Xue, Q. Wang, and L. Jia, *Sulfonated poly (arylene ether) s based proton exchange membranes for fuel cells.* International Journal of Hydrogen Energy, 2021. **46**(62): p. 31727-31753.
8. Qian, P., H. Wang, L. Zhang, Y. Zhou, and H. Shi, *An enhanced stability and efficiency of SPEEK-based composite membrane influenced by amphoteric side-chain polymer for vanadium redox flow battery.* Journal of Membrane Science, 2022. **643**: p. 120011.
9. Yang, K., D. Zhang, M. Zou, L. Yu, and S. Huang, *The Known and Overlooked Sides of Zeolite‐Extrudate Catalysts.* ChemCatChem, 2021. **13**(6): p. 1414-1423.
10. Elerian, A.F., M. Abu-Saied, G. Abd-Elnaim, and E.M. Elnaggar, *Development of polymer electrolyte membrane based on poly (Vinyl Chloride)/graphene oxide modified with zirconium phosphate for fuel cell applications.* Journal of Polymer Research, 2023. **30**(1): p. 6.
11. Darıcık, F., A. Topcu, K. Aydın, and S. Celik, *Carbon nanotube (CNT) modified carbon fiber/epoxy composite plates for the PEM fuel cell bipolar plate application.* international journal of hydrogen energy, 2023. **48**(3): p. 1090-1106.
12. Nimir, W., A. Al-Othman, M. Tawalbeh, A. Al Makky, A. Ali, H. Karimi-Maleh, F. Karimi, and C. Karaman, *Approaches towards the development of*

*heteropolyacid-based high temperature membranes for PEM fuel cells.* International Journal of Hydrogen Energy, 2023. **48**(17): p. 6638-6656.

13. Chu, J., Y. Ou, F. Cheng, H. Liu, N. Luo, F. Hu, S. Wen, and C. Gong, *Achieving better balance on the mechanical stability and conduction performance of sulfonated poly (ether ether ketone) proton exchange membranes through polydopamine/polyethyleneimine co-modified poly (vinylidene fluoride) nanofiber as support.* International Journal of Hydrogen Energy, 2024. **50**: p. 1381-1390.
14. Zhao, Y., H. Liu, X. Meng, A. Liu, Y. Chen, and T. Ma, *A cross-linked tin oxide/polymer composite gel electrolyte with adjustable porosity for enhanced sodium ion batteries.* Chemical Engineering Journal, 2022. **431**: p. 133922.
15. Wang, Y., J. You, Z. Cheng, K. Jiang, L. Zhang, W. Cai, Y.-Q. Liu, and S. Li, *A promising Al-CeZrO4/HPW-incorporated SPEEK composite membrane with improved proton conductivity and chemical stability for PEM fuel cells.* High Performance Polymers, 2021. **33**(3): p. 295-308.
16. Gashoul, F., M.J. Parnian, and S. Rowshanzamir, *A new study on improving the physicochemical and electrochemical properties of SPEEK nanocomposite membranes for medium temperature proton exchange membrane fuel cells using different loading of zirconium oxide nanoparticles.* international journal of hydrogen energy, 2017. **42**(1): p. 590-602.
17. Li, X., B. He, P. Li, and S. Tang, *In situ-doped sulfonated schiff-base networks in SPEEK composite membranes with enhanced proton conductivity.* ACS Applied Materials & Interfaces, 2023. **15**(21): p. 25584-25593.
18. Meng, X., K. Song, Y. Lv, C. Cong, H. Ye, Y. Dong, and Q. Zhou, *SPEEK proton exchange membrane with enhanced proton conductivity stability from phosphotungstic acid-encapsulated silica nanorods.* Materials Chemistry and Physics, 2021. **272**: p. 125045.
19. Rani, S., S. Verma, B. Sharma, and S. Kumar, *Tuning of structural, optical/spectral and thermal properties of cubic CeO2 nanoparticles via incorporation of zirconia.* Physica B: Condensed Matter, 2023. **661**: p. 414922.
20. Zhou, Y., A. Najar, J. Zhang, J. Feng, Y. Cao, Z. Li, X. Zhu, D. Yang, and S.F. Liu, *Effect of solvent residue in the thin-film fabrication on perovskite solar cell performance.* ACS applied materials & interfaces, 2022. **14**(25): p. 28729-28737.

21. Yousef, S., J. Eimontas, N. Striūgas, A. Mohamed, and M.A. Abdelnaby, *Pyrolysis kinetic behavior and TG-FTIR-GC–MS analysis of end-life ultrafiltration polymer nanocomposite membranes.* Chemical Engineering Journal, 2022. **428**: p. 131181.
22. Esmaeili, N., E.M. Gray, and C.J. Webb, *Non‐fluorinated polymer composite proton exchange membranes for fuel cell applications–A review.* ChemPhysChem, 2019. **20**(16): p. 2016-2053.
23. Baschieri, A., Z. Jin, and R. Amorati, *Hydroperoxyl radical (HOO•) as a reducing agent: unexpected synergy with antioxidants. A review.* Free Radical Research, 2023. **57**(2): p. 115-129.
24. Hwang, S., H. Lee, Y.-G. Jeong, C. Choi, I. Hwang, S. Song, S.Y. Nam, J.H. Lee, and K. Kim, *Polymer electrolyte membranes containing functionalized organic/inorganic composite for polymer electrolyte membrane fuel cell applications.* International Journal of Molecular Sciences, 2022. **23**(22): p. 14252.
25. Haider, R., Y. Wen, Z.-F. Ma, D.P. Wilkinson, L. Zhang, X. Yuan, S. Song, and J. Zhang, *High temperature proton exchange membrane fuel cells: progress in advanced materials and key technologies.* Chemical Society Reviews, 2021. **50**(2): p. 1138-1187.
26. Jing, J., J. Pang, L. Chen, H. Zhang, Z. Lei, and Z. Yang, *Structure, synthesis, properties and solid oxide electrolysis cells application of Ba (Ce, Zr) O3 based proton conducting materials.* Chemical Engineering Journal, 2022. **429**: p. 132314.
27. Lu, Y., S.-A. Li, and R. Qi, *Review of ionomers in catalyst layers of proton exchange membrane (PEM) modules: key parameters, characterization and manipulation methods.* International Journal of Green Energy, 2024. **21**(12): p. 2872-2897.
28. Liu, L., H. Li, and G. Avgouropoulos, *A review of porous polytetrafluoroethylene reinforced sulfonic acid-based proton exchange membranes for fuel cells.* International Journal of Hydrogen Energy, 2024. **50**: p. 501-527.
29. Mirfarsi, S.H., M.J. Parnian, S. Rowshanzamir, and E. Kjeang, *Current status of cross-linking and blending approaches for durability improvement of hydrocarbon-based fuel cell membranes.* International Journal of Hydrogen Energy, 2022. **47**(27): p. 13460-13489.

30. Xiao, F., Y.C. Wang, Z.P. Wu, G. Chen, F. Yang, S. Zhu, K. Siddharth, Z. Kong, A. Lu, and J.C. Li, *Recent advances in electrocatalysts for proton exchange membrane fuel cells and alkaline membrane fuel cells.* Advanced Materials, 2021. **33**(50): p. 2006292.
31. Kamal, M., J. Jaafar, A.A. Khan, Z. Khan, A. Ismail, M. Othman, M.A. Rahman, F. Aziz, and G.U. Rehman, *A critical review of the advancement approach and strategy in SPEEK-based polymer electrolyte membrane for hydrogen fuel cell application.* Energy & Fuels, 2024. **38**(14): p. 12337-12386.
32. Zhou, N., J. Jia, S. Zhao, D. Zhang, and M. Feng, *Interfacial enhancement of CF/PEEK composites by coating sulfonated PEEK sizing agent.* Surfaces and Interfaces, 2023. **37**: p. 102652.
33. Ranganathan, H., M. Vinothkannan, A.R. Kim, V. Subramanian, M.S. Oh, and D.J. Yoo, *Simultaneous improvement of power density and durability of sulfonated poly (ether ether ketone) membrane by embedding CeO2‐ATiO2: a comprehensive study in low humidity proton exchange membrane fuel cells.* International Journal of Energy Research, 2022. **46**(7): p. 9041-9057.
34. Li, X., T. Ye, X. Meng, D. He, L. Li, K. Song, J. Jiang, and C. Sun, *Advances in the Application of Sulfonated Poly (Ether Ether Ketone)(SPEEK) and Its Organic Composite Membranes for Proton Exchange Membrane Fuel Cells (PEMFCs).* Polymers, 2024. **16**(19): p. 2840.
35. Ali, A., A. Al-Othman, and M. Tawalbeh, *Polymer membranes: general principles and applications in fuel cells.* Polymer Membranes: Increasing Energy Efficiency, 2024: p. 115-138.
36. Cui, W., P. Sun, P. Li, L. Zhang, X. Zhi, Q. Liu, and Z. Li, *Sulfonated polyphosphazene-blended self-cross-linked polybenzimidazole-based high-temperature proton exchange membranes: high efficiency in proton transport at low humidity.* ACS Applied Energy Materials, 2022. **5**(9): p. 11526-11539.
37. Ng, W.W., H.S. Thiam, Y.L. Pang, K.C. Chong, and S.O. Lai, *A State-of-Art on the development of Nafion-based membrane for performance improvement in direct methanol fuel cells.* Membranes, 2022. **12**(5): p. 506.
38. Salarizadeh, P., M. Javanbakht, and S. Pourmahdian, *Enhancing the performance of SPEEK polymer electrolyte membranes using functionalized TiO 2 nanoparticles with proton hopping sites.* RSC Advances, 2017. **7**(14): p. 8303-8313.

39. Parnian, M.J., S. Rowshanzamir, A.K. Prasad, and S.G. Advani, *Effect of ceria loading on performance and durability of sulfonated poly (ether ether ketone) nanocomposite membranes for proton exchange membrane fuel cell applications.* Journal of Membrane Science, 2018. **565**: p. 342-357.
40. Maiti, T.K., J. Singh, J. Majhi, A. Ahuja, S. Maiti, P. Dixit, S. Bhushan, A. Bandyopadhyay, and S. Chattopadhyay, *Advances in polybenzimidazole based membranes for fuel cell applications that overcome Nafion membranes constraints.* Polymer, 2022. **255**: p. 125151.
41. Alhweij, H., E.A.C. Emanuelsson, S. Shahid, and J. Wenk, *Simplified in-situ tailoring of cross-linked self-doped sulfonated polyaniline (S-PANI) membranes for nanofiltration applications.* Journal of Membrane Science, 2021. **637**: p. 119654.
42. Al Lafi, A.G., *The sulfonation of poly (ether ether ketone) as investigated by two‐dimensional FTIR correlation spectroscopy.* Journal of Applied Polymer Science, 2015. **132**(2).
43. Aparna, M., P. Hemalatha, D. Paradesi, and D.A. Raj, *Design and development of copper trimesic acid anchored sPEEK/polyimide composite membranes for fuel cell applications.* ChemistrySelect, 2023. **8**(14): p. e202204584.
44. Chikumba, F., M. Tamer, L. Akyalçın, and S. Kaytakoğlu, *The development of sulfonated polyether ether ketone (sPEEK) and titanium silicon oxide (TiSiO4) composite membranes for DMFC applications.* International Journal of Hydrogen Energy, 2023. **48**(37): p. 14038-14052.
45. Yagizatli, Y., B. Ulas, A. Sahin, and I. Ar, *Investigation of sulfonation reaction kinetics and effect of sulfonation degree on membrane characteristics for PEMFC performance.* Ionics, 2022. **28**(5): p. 2323-2336.
46. Yılmazoğlu, M., N. Kanmaz, and P. Demircivi, *Constructing the synergistic effects of chitosan and ionic liquid on SPEEK polymer for efficient adsorption of crystal violet dye.* International Journal of Biological Macromolecules, 2024. **271**: p. 132638.
47. Dafalla, A.M., L. Wei, B.T. Habte, J. Guo, and F. Jiang, *Membrane electrode assembly degradation modeling of proton exchange membrane fuel cells: A review.* Energies, 2022. **15**(23): p. 9247.
48. Sahin, A., *The development of Speek/Pva/Teos blend membrane for proton exchange membrane fuel cells.* Electrochimica Acta, 2018. **271**: p. 127-136.

49. Rui, Z. and J. Liu, *Understanding of free radical scavengers used in highly durable proton exchange membranes.* Progress in Natural Science: Materials International, 2020. **30**(6): p. 732-742.

50. Chen, F., L. Meng, H. Liang, and J. Xu, *Enhanced oxidation stability and proton conductivity of sulfonated poly (arylene ether ketone sulfone) s via embedment of surface-modified ceria nanoparticles.* Process Safety and Environmental Protection, 2024. **185**: p. 480-491.

51. Ruan, H., S. Gao, Y. Li, S. Yu, J. Liao, E.H. Ang, Y. Xu, and J. Shen, *Optimization of the mass ratio of siloxane crosslinkers for poly (2, 6-dimethyl-1, 4-phenylene oxide) anion exchange membranes to improve acid enrichment by electrodialysis.* Journal of Membrane Science, 2024. **695**: p. 122487.

52. Rosli, N.A.H., K.S. Loh, W.Y. Wong, T.K. Lee, and A. Ahmad, *Phosphorylated chitosan/poly (vinyl alcohol) based proton exchange membranes modified with propylammonium nitrate ionic liquid and silica filler for fuel cell applications.* International Journal of Hydrogen Energy, 2022. **47**(44): p. 19217-19236.

53. Okonkwo, P.C. and C. Otor, *A review of gas diffusion layer properties and water management in proton exchange membrane fuel cell system.* International Journal of Energy Research, 2021. **45**(3): p. 3780-3800.

54. Sun, Y., S. Polani, F. Luo, S. Ott, P. Strasser, and F. Dionigi, *Advancements in cathode catalyst and cathode layer design for proton exchange membrane fuel cells.* Nature communications, 2021. **12**(1): p. 5984.

55. Harun, N.A.M., N. Shaari, and N.F.H. Nik Zaiman, *A review of alternative polymer electrolyte membrane for fuel cell application based on sulfonated poly (ether ether ketone).* International Journal of Energy Research, 2021. **45**(14): p. 19671-19708.

56. Fan, X., C. Zhong, J. Liu, J. Ding, Y. Deng, X. Han, L. Zhang, W. Hu, D.P. Wilkinson, and J. Zhang, *Opportunities of flexible and portable electrochemical devices for energy storage: expanding the spotlight onto semi-solid/solid electrolytes.* Chemical Reviews, 2022. **122**(23): p. 17155-17239.

57. Xu, Q., Z. Guo, L. Xia, Q. He, Z. Li, I.T. Bello, K. Zheng, and M. Ni, *A comprehensive review of solid oxide fuel cells operating on various promising alternative fuels.* Energy Conversion and Management, 2022. **253**: p. 115175.

58. Zhang, H., Y. Chen, C. Li, and M. Armand, *Electrolyte and anode‐electrolyte interphase in solid‐state lithium metal polymer batteries: a perspective.* SusMat, 2021. **1**(1): p. 24-37.
59. Ahmad, S., T. Nawaz, A. Ali, M.F. Orhan, A. Samreen, and A.M. Kannan, *An overview of proton exchange membranes for fuel cells: Materials and manufacturing.* International Journal of Hydrogen Energy, 2022. **47**(44): p. 19086-19131.
60. Yusoff, Y.N., N. Shaari, and S.H. Osman, *Metal oxide-based materials as an emerging platform for fuel cell system: a review.* Materials Science and Technology, 2023. **39**(16): p. 2363-2397.
61. Gao, X., J. Chen, R. Xu, Z. Zhen, X. Zeng, X. Chen, and L. Cui, *Research progress and prospect of the materials of bipolar plates for proton exchange membrane fuel cells (PEMFCs).* International Journal of Hydrogen Energy, 2024. **50**: p. 711-743.
62. Tang, J., C. Su, Y. Zhong, and Z. Shao, *Oxide-based precious metal-free electrocatalysts for anion exchange membrane fuel cells: from material design to cell applications.* Journal of Materials Chemistry A, 2021. **9**(6): p. 3151-3179.
63. Cardarelli, F., *Sulfuric Acid Digestion, Sulfuric Acid Baking, and Sulfation Roasting in Mineral and Chemical Processing, and Extractive Metallurgy*. 2022: Electrochem Technologies & Materials Inc.
64. Kirillova, S.A.e., V.I. Almjashev, and V.L. Stolyarova, *Phase equilibria and materials in the TiO2-SiO2-ZrO2 system: a review.* Наносистемы: физика, химия, математика, 2021. **12**(6): p. 711-727.
65. Liu, Y., D. Yang, L. Riekehr, H. Engqvist, L. Fu, and W. Xia, *Combining good mechanical properties and high translucency in yttrium-doped ZrO2-SiO2 nanocrystalline glass-ceramics.* Journal of the European Ceramic Society, 2022. **42**(1): p. 274-285.
66. Nurazzi, N., F. Sabaruddin, M. Harussani, S. Kamarudin, M. Rayung, M. Asyraf, H. Aisyah, M. Norrrahim, R. Ilyas, and N. Abdullah, *Mechanical performance and applications of cnts reinforced polymer composites—A review.* Nanomaterials, 2021. **11**(9): p. 2186.
67. Li, M., S. Askari, Y. Niu, T. Li, A. Zavabeti, M.S. Alivand, K.A. Mumford, C.e. Li, and R. Zhang, *One-step synthesis of SO42−/ZrO2‐SEP solid-acid catalyst for*

*energy-efficient CO2 capture.* Separation and Purification Technology, 2025. **359**: p. 130577.

68. Kumar, M., N. Sreedhar, N. Thomas, M. Mavukkandy, R.A. Ismail, T.M. Aminabhavi, and H.A. Arafat, *Polydopamine-coated graphene oxide nanosheets embedded in sulfonated poly (ether sulfone) hybrid UF membranes with superior antifouling properties for water treatment.* Chemical Engineering Journal, 2022. **433**: p. 133526.
69. Chen, W., B. Pang, X. Yan, X. Jiang, F. Cui, X. Wu, and G. He, *Oxidized black phosphorus nanosheets/sulfonated poly (ether ether ketone) composite membrane for vanadium redox flow battery.* Journal of Membrane Science, 2022. **644**: p. 120084.
70. Khan, Z., F. Ali, A. Said, U. Arif, K. Khan, N. Ali, G. Shabir, H.M. Iqbal, and M. Bilal, *Polyethylene glycol capped copper ferrite porous nanostructured materials for efficient photocatalytic degradation of bromophenol blue.* Environmental Research, 2022. **215**: p. 114148.
71. Mossayebi, Z., M.J. Parnian, and S. Rowshanzamir, *Effect of the sulfated zirconia nanostructure characteristics on physicochemical and electrochemical properties of SPEEK nanocomposite membranes for PEM fuel cell applications.* Macromolecular Materials and Engineering, 2018. **303**(5): p. 1700570.
72. Bashambu, L., R. Singh, and J. Verma, *Metal/metal oxide nanocomposite membranes for water purification.* Materials Today: Proceedings, 2021. **44**: p. 538-545.
73. Yasmin, H., S.O. Giwa, S. Noor, and M. Sharifpur, *Thermal conductivity enhancement of metal oxide nanofluids: a critical review.* Nanomaterials, 2023. **13**(3): p. 597.
74. Fang, J., J. Qiao, D.P. Wilkinson, and J. Zhang, *Electrochemical polymer electrolyte membranes*. Vol. 7. 2015: CRC Press Boca Raton, FL.
75. Sigwadi, R., T. Mokrani, M.S. Dhlamini, P. Nonjola, and P.F. Msomi, *Nafion®/sulfated zirconia oxide-nanocomposite membrane: the effects of ammonia sulfate on fuel permeability.* Journal of polymer research, 2019. **26**(5): p. 108.
76. Guo, Z., J. Chen, J.J. Byun, M. Perez–Page, Z. Ji, Z. Zhao, and S.M. Holmes, *Insights into the performance and degradation of polybenzimidazole/muscovite*

*composite membranes in high–temperature proton exchange membrane fuel cells.* Journal of Membrane Science, 2022. **641**: p. 119868.

77. Xie, D., K. Li, J. Yang, D. Yan, L. Jia, B. Chi, J. Pu, and J. Li, *High-performance La0. 5 (Ba0. 75Ca0. 25) 0.5 Co0. 8Fe0. 2O3-δ cathode for proton-conducting solid oxide fuel cells.* International Journal of Hydrogen Energy, 2021. **46**(15): p. 10007-10014.
78. Sigwadi, R., T. Mokrani, P. Msomi, and F. Nemavhola, *The effect of sulfated zirconia and zirconium phosphate nanocomposite membranes on fuel-cell efficiency.* Polymers, 2022. **14**(2): p. 263.
79. Barjola, A., J.L. Reyes-Rodríguez, O. Solorza-Feria, E. Gimenez, and V. Compan, *Novel SPEEK-ZIF-67 proton exchange nanocomposite membrane for PEMFC application at intermediate temperatures.* Industrial & Engineering Chemistry Research, 2021. **60**(25): p. 9107-9118.
80. Bagheri, A., M. Javanbakht, H. Beydaghi, P. Salarizadeh, A. Shabanikia, and H.S. Amoli, *Sulfonated poly (etheretherketone) and sulfonated polyvinylidene fluoride-co-hexafluoropropylene based blend proton exchange membranes for direct methanol fuel cell applications.* RSC Advances, 2016. **6**(45): p. 39500-39510.
81. Guhan, S., R. Muruganantham, and D. Sangeetha, *Development of a solid polymer electrolyte membrane based on sulfonated poly (ether ether) ketone and polysulfone for fuel cell applications.* Canadian Journal of Chemistry, 2012. **90**(2): p. 205-213.

# CHAPTER 8: CONCLUSIONS AND RECOMMENDATIONS

## 8.1. CONCLUSIONS

This research successfully achieved the synthesis, characterization, and application of novel non-platinum electrocatalysts for hydrogen generation and the development of SPEEK-based proton conductive membranes modified with mixed metal oxide fillers, in full alignment with the seven objectives stated in Chapter 1. The conclusions are presented below following the sequential order of those objectives.

### Objective (a): Synthesis of electrocatalyst at varying ratios

Three different mixed oxide electrocatalyst systems were successfully synthesized using coprecipitation, hydrothermal, and Stöber methods at varying compositional ratios. The $CeO_2$:$ZrO_2$ system was prepared at ratios of 1:1, 1:2, and 2:1; the $CeO_2$:$SiO_2$ system at 1:1, 1:2, and 2:1; and the SZr:$SiO_2$ system at 1:1, 1:2, and 2:1. All syntheses yielded nanocomposite materials with distinct morphological, structural, and electrochemical properties dependent on the metal oxide ratios, demonstrating that the synthesis methods were effective in producing the desired electrocatalyst compositions.

### Objective (b): Synthesis of sulfonated polyether ether ketone (SPEEK) membrane

SPEEK was successfully synthesized via post-polymerization sulfonation of PEEK using concentrated sulfuric acid at room temperature. The resulting SPEEK exhibited characteristic sulfonic acid groups confirmed by FTIR, with absorption peaks observed at 1026 and 1083 $cm^{-1}$ corresponding to S=O and O=S=O stretching vibrations. The synthesized SPEEK demonstrated adequate thermal stability up to 300 °C as confirmed by TGA analysis, making it suitable for fuel cell membrane applications. The degree of sulfonation achieved was sufficient to impart the necessary hydrophilicity and proton exchange capability to the polymer.

### Objective (c): Synthesis of SPEEK/inorganic metal oxide nanofiller composite membranes

SPEEK composite membranes incorporating $CeO_2$:$ZrO_2$, $CeO_2$:$SiO_2$, and SZr:$SiO_2$ nanoparticles at varying weight percentages (1%, 5%, and 10%) were successfully fabricated using the solution casting or recast method. FTIR analysis confirmed the formation of hydrogen bonds and electrostatic interactions between the sulfonic acid groups of SPEEK and the metal oxide nanofillers, while SEM analysis revealed that the nanoparticles were distributed within the polymer matrix. Optimal dispersion of nanofillers was observed at lower filler loadings (1-5 wt%), whereas higher loadings (10 wt%) showed some degree of agglomeration. These results confirm that the solution casting method is effective for producing homogeneous nanocomposite membranes.

### Objective (d): Characterization of as-synthesized materials

Comprehensive characterization was performed using FTIR, XRD, TGA, BET, SEM-EDS, TEM, UV-vis, CV, LSV, CA, and EIS techniques. XRD analysis confirmed the cubic face-cantered fluorite structure of ceria at 2θ values of 28.62°, 33.34°, and 47.66°, while zirconia exhibited tetragonal and monoclinic phases. The $CeO_2$:$ZrO_2$ (1:1) composite showed peak shifts towards higher 2θ values, confirming the incorporation of $Zr^{4+}$ into the ceria lattice. BET analysis revealed that the $CeO_2$:$ZrO_2$ (1:1) composition demonstrated superior surface area characteristics (63.41 $m^2/g$) compared to all other tested materials. TGA analysis showed that all composite membranes exhibited three-stage thermal degradation, with the first stage around 100 °C due to water loss, the second stage between 250-410 °C due to sulfonic acid group decomposition, and the final stage above 560 °C due to polymer backbone degradation. SEM and TEM analyses revealed mixed spherical and rod-like morphological structures, with the $CeO_2$:$ZrO_2$ (1:1) composition exhibiting a greater presence of rod-like structures that provide three-dimensional configuration advantages for catalytic activity. FTIR analysis confirmed the presence of characteristic functional groups, including S=O and O=S=O peaks for SPEEK, Ce-O and Zr-O stretching vibrations for the metal oxides, and Si-O-Si bonds for silica-containing composites.

### Objective (e): Evaluation of as synthesized electrocatalysts for hydrogen generation

All three electrocatalyst systems demonstrated viable HER activity when used as working electrodes with SPEEK binder on graphite substrates in 0.5 M $H_2SO_4$ electrolyte. Th**e** $CeO_2$:$ZrO_2$ (1:1) nanocomposite is identified as the best electrocatalyst among all those investigated in this study. This material exhibited remarkable HER efficiency with a current density of -2000 mA/cm² on a geometrical area of 0.20 cm², outperforming palladium black (which achieved -0.29 A) and showing only 2.56% deviation from platinum (which achieved -0.39 A). The superior performance of the $CeO_2$:$ZrO_2$ (1:1) electrocatalyst is attributed to its unique mixed spherical and rod-like morphology, high BET surface area (63.41 m²/g), ECSA of 4.4 cm², and pore size of 1.71 nm. The hydrogen generation rate followed first-order kinetics with a rate of $9.6 \times 10^{-5}$ A/s and a rate constant of $8.35 \times 10^{-5}$ $s^{-1}$. The SZr:$SiO_2$ (1:1) electrode demonstrated exceptional performance with a hydrogen evolution current density of -1700 mA/cm² at -0.55 V vs. RHE based on ECSA dimension, attributed to the easy exchange of electrons between the surface and aqueous hydrogen ions. The $CeO_2$:$SiO_2$ (2:1) exhibited the best HER activity among its series with a current density of -260 mA/cm² at -0.50 V vs. RHE, an ECSA of 2.0 cm², and a turnover frequency of -1.42 $s^{-1}$. In all systems, SPEEK played a dual role as both a protective membrane (Ecorr = -0.33 V vs -0.29 V) and a binder for the inorganic materials, effectively securing nanoparticles to the electrode surface through complexation between its sulfonic acid groups and the metal ions.

### Objective (f): Evaluate the conductivity of as-synthesized SPEEK/inorganic metal oxide filler membranes

The proton conductivity of the composite membranes was significantly enhanced compared to pristine SPEEK, which measured only 0.004 S/cm under standard conditions. Among the $CeO_2$:$ZrO_2$ series, the SPEEK-$CeO_2$:$ZrO_2$ (10%) composite membrane exhibited the highest proton conductivity of 0.07 S/cm, which was attributed to the increased water retention and additional proton transport pathways provided by the nanofillers. For the $CeO_2$:$SiO_2$ series, the SPEEK-$CeO_2$:$SiO_2$ (5%) membrane achieved a proton conductivity of 0.037 S/cm, with the presence of $SiO_2$ enhancing proton conductivity through its hygroscopic nature while $CeO_2$ helped reduce chemical degradation by scavenging free radicals. The SPEEK-SZr:$SiO_2$ (1%) membrane demonstrated the highest proton conductivity overall at 0.087 S/cm, which is attributable to the strong interaction between $-SO_3H$ groups and the sulfated binary metal oxide that creates new proton conduction channels. Water uptake increased with filler loading, with the SPEEK-$CeO_2$:$ZrO_2$ (10%) membrane showing the highest water uptake of 60.3% at 80 °C, while the swelling ratios remained within acceptable limits for fuel cell operation. IEC values increased from 2 meq/g for pristine SPEEK to 5.1 meq/g for SPEEK-$CeO_2$:$ZrO_2$ (10%) and 3.1 meq/g for SPEEK-SZr:$SiO_2$ (1%). Oxidative stability tests conducted in 3 ppm $Fe^{2+}$ at 80 °C revealed that SPEEK-$CeO_2$:$SiO_2$ (5%) exhibited the highest oxidative stability of 81.6% after 250 minutes, while SPEEK-SZr:$SiO_2$ (1%) achieved 82.87%, both surpassing the pristine SPEEK membrane which had a stability of 77.24%. The enhanced oxidative stability is attributed to the radical scavenging properties of $CeO_2$ nanoparticles and the orderly molecular arrangement in the composite membranes.

**Objective (g): Optimize and utility of membrane materials for fuel cell application through construction of power density curves**

For assessing fuel cell performance, all composite membranes that displayed the highest proton conductivity within their respective groups were selected for single cell testing using a membrane electrode assembly with palladium catalyst and hydrogen/oxygen gas feeds. The SPEEK-SZr:$SiO_2$ (1%) membrane outperformed all other composite membranes, achieving the highest current density of 1370.77 mA/cm² and a peak power density of 54.9 mW/cm². This superior performance demonstrates its superiority as a catalyst in fuel cells due to its high conductivity (0.087 S/cm) and excellent oxidative stability (82.87%). The SPEEK-$CeO_2$:$ZrO_2$ (10%) membrane achieved a peak power density of 40.96 mW/cm² with a current density of 1297.17 mA/cm², while the SPEEK-$CeO_2$:$SiO_2$ (5%) membrane attained 38.94 mW/cm² with 1167.74 mA/cm². All fabricated membranes exhibited open circuit voltages greater than 0.9 V, indicating good $H_2$ and $O_2$ gas permeation resistance. OCV durability tests showed decay rates of 0.151 V/h for SPEEK-$CeO_2$:$SiO_2$ (5%), 0.155 V/h for SPEEK-

$CeO_2$:$ZrO_2$ (10%), and 0.157 V/h for SPEEK-SZr:$SiO_2$ (1%), confirming that the inclusion of metal oxide fillers helps mitigate membrane degradation caused by free radical attacks, thereby extending the service life of PEMFCs.

In conclusion, all seven objectives outlined in Chapter 1 were successfully achieved. The $CeO_2$:$ZrO_2$ (1:1) nanocomposite is identified as the best electrocatalyst for hydrogen generation, demonstrating remarkable efficiency with a current density of -2000 mA/cm² and performance comparable to other materials. The SPEEK-SZr:$SiO_2$ (1%) composite membrane is recommended as the most promising candidate for PEMFC applications, exhibiting the highest proton conductivity of 0.087 S/cm, excellent oxidative stability (82.87%), and superior fuel cell performance with a peak power density of 54.9 mW/cm². Overall, this research demonstrates that SPEEK-based nanocomposite membranes modified with mixed metal oxide fillers and the developed non-platinum electrocatalysts represent innovative, cost-effective, and efficient alternatives for sustainable energy solutions, particularly in hydrogen generation and proton exchange membrane fuel cell applications.

## 8.2. RECOMMENDATIONS FOR FUTURE WORK

Based on the findings and limitations of this study, the following recommendations are proposed for future research:

- ❖ **High-temperature proton conductivity**: Investigate the effect of incorporating metal oxide fillers into SPEEK membranes and assess proton conductivity at temperatures above 100 °C to evaluate performance under elevated temperature operating conditions.
- ❖ **Fuel cell efficiency at elevated temperatures**: Evaluate the fuel cell performance of SPEEK-metal oxide nanocomposite membranes at temperatures exceeding 100 °C to determine their viability for high-temperature PEMFC applications.
- ❖ **Hydrogen quantification**: Quantify the actual volume and mass of hydrogen produced during the hydrogen evolution reaction (HER) to enable calculation of faradaic efficiency and compare theoretical vs. actual hydrogen yields.
- ❖ **Long-term durability testing**: Investigate the durability of the composite membranes under accelerated stress tests at higher temperatures (120-150 °C) and varying humidity conditions to simulate real-world operating conditions.

- **Membrane electrode assembly optimization**: Optimize the MEA fabrication process, including catalyst loading, binder composition, and hot-pressing conditions, to further improve fuel cell performance.
- **Scale-up studies**: Conduct scale-up synthesis of the best-performing electrocatalyst ($CeO_2$:$ZrO_2$ 1:1) and composite membrane (SPEEK-SZr:$SiO_2$ 1%) to evaluate reproducibility and performance at larger scales for potential commercial applications.
- **In-situ characterization**: Employ in-situ characterization techniques (e.g., operando XRD, Raman spectroscopy) during fuel cell operation to understand structural changes and degradation mechanisms under operating conditions.
- **Computational modelling**: Utilize density functional theory (DFT) and molecular dynamics simulations to understand the proton transport mechanisms and the role of metal oxide fillers at the molecular level.